JAERI-Review
2002-022

REVIEW OF JT-60U EXPERIMENTAL RESULTS IN 2000

November 2002

JT-60 Team

日本原子力研究所
Japan Atomic Energy Research Institute

本レポートは，日本原子力研究所が不定期に公刊している研究報告書です。
入手の問合わせは，日本原子力研究所研究情報部研究情報課（〒319-1195 茨城県那珂郡東海村）あて，お申し越しください。なお，このほかに財団法人原子力弘済会資料センター（〒319-1195 茨城県那珂郡東海村日本原子力研究所内）で複写による実費頒布をおこなっております。

This report is issued irregularly.
Inquiries about availability of the reports should be addressed to Research Information Division, Department of Intellectual Resources, Japan Atomic Energy Research Institute, Tokai-mura, Naka-gun, Ibarakiken 319-1195, Japan.

編集兼発行　日本原子力研究所

Review of JT-60U Experimental Results in 2000

JT-60 Team※

Department of Fusion Plasma Research
and
Department of Fusion Facility
Naka Fusion Research Establishment
Japan Atomic Energy Research Institute
Naka-machi, Naka-gun, Ibaraki-ken

(Received August 2, 2002)

The results of JT-60U experiments in 2000, from February to December, are reviewed. The performance under the full non-inductive current drive has been greatly advanced both in high β_p H-mode plasmas and in reversed shear (RS) plasmas. In the high β_p H-mode, with injection of the negative ion based neutral beam (NNB) of 360 keV and 4 MW into a high electron temperature plasma ($T_e(0) \sim 13$ keV), a high fusion triple product $n_D(0)T_i(0)\tau_E = 2.0\times10^{20}$ keVm^{-3}s has been obtained at the plasma current of 1.5 MA, and the highest value of current drive efficiency of NNB (1.55×10^{19} A/W/m^2) has been achieved. In RS, LHCD and NNB-CD were employed for current drive and high confinement ($HH_{y2} \sim 1.4$) at high density ($f_{GW} \sim 0.80$) has been achieved. In the 110 GHz ECRF system, two more gyrotrons have been installed in addition to the one installed in 1999 and 1.5 MW was injected into the torus for 3 s. Complete stabilization of neoclassical tearing mode (NTM), realization of high confinement plasmas with $T_e \sim T_i$, a high value (1 MA) of NNB-driven current in the high T_e regime, and measurement of localized EC driven current were achieved with the upgraded EC system. The multiple pellet injection system has been newly installed. In high power NB heated plasmas, high-field-side pellet injection was more effective than low-field-side injection, and it extended the regime of high confinement high β_p H-mode to a higher density. A new method, called CCS (Cauchy-condition surface method), for the control of the plasma position and shape in real-time became available and was found very useful especially for the control of plasma-wall clearance in LH and IC experiments. The active control of ITB strength by the switch of the injection direction of toroidal angular momentum was successfully demonstrated. In high triangularity H-mode plasmas, higher pressure and temperature at the edge pedestal were observed, which resulted in higher temperature and confinement in the core through the profile 'stiffness.' In the W-shaped divertor, a pumping slot was opened at the outer leg in addition to the inner leg to enhance the pumping

efficiency. The confinement improvement in the high density regime was attempted by using Ar and Ne injection. In ELMy H-mode (q_{95} = 3.4), HH_{y2} ~ 1 was obtained at f_{GW} = 0.65. In a configuration with the outer strike-point on the dome tile (q_{95} = 3.6), a peaked density profile was obtained and H_{89P} = 1.68 was achieved at f_{GW} = 0.80. In RS (q_{95} = 6-7) with Ne puff, H_{89P} = 1.8 and HH_{y2} = 1.2 were obtained during X-point MARFE. Helium exhaust efficiency was extended by the both leg pumping and τ^*_{He}/τ_E = 2.8 with H_{89P} = 1.2 was achieved in ELMy H-mode (q_{95} = 4.0). Impurity and Z_{eff} in the main plasma have been reduced by boronization of the first wall and by reduction of the wall temperature. The time evolution of pedestal density profile during a type I ELM was evaluated with the O-mode reflectometer. The heat flux by ELM was measured both in the SOL plasma and on the divertor plates, by reciprocating Mach probes at the X-point and the midplane and by IRTV, respectively. The results indicated convective heat transport was dominant in the SOL plasma.

Keywords:
JT-60U, High β_p H-mode, Reversed Shear, Non-inductive Current Drive, NNB, ECRF, Pellet Injection, CCS, Internal Transport Barrier, ITB Control, High Triangularity, Helium Exhaust, Impurity Reduction, ELM

※ JT-60 Team

H.Adachi[1)], H.Akasaka, N.Akino, K.Anno, M.Arai[1)], T.Arai, N.Asakura, M.Azumi, P.E.Bak[2)], M.Bakhtiari[3)], A.Chankin[4)], C.Z.Cheng[5)], S.Chiba, Z.Cui[6)], N.Ebisawa, T.Fujii, T.Fujita, T.Fukuda, A.Funahashi, H.Furukawa[1)], X.Gao[4)], N.N.Gorelenkov[5)], L.Grisham[5)], K.Haga[1)], K.Hamamatsu, T.Hamano[1)], T.Hatae, N.Hayashi, S.Higashijima, N.Hikida[1)], K.W.Hill[5)], S.Hiranai, H.Hiratsuka, T.Hiroi[1)], H.M.Hoek[4)], A.Honda, M.Honda, Y.Hoshi[1)], N.Hosogane, H.Ichige, S.Ide, Y.Idomura, K.Igarashi[1)], Y.Ikeda, A.Inoue[1)], M.Isaka, A.Isayama, N.Isei, S.Ishida, K.Ishii[1)], Y.Ishii, T.Ishijima[7)], M.Ishikawa[7)], A.Ishizawa[8)], K.Itami, T.Itoh, T.Iwahashi[1)], K.Iwasaki[1)], M.Iwase[8)], K.Kajiwara[8)], E.Kajiyama[1)], Y.Kamada, A.Kaminaga, T.Kashiwabara[1)], M.Kawai, Y.Kawamata, Y.Kawano, M.Kazawa, H.Kikuchi[1)], M.Kikuchi, T.Kimura, Y.Kishimoto, S.Kitamura, A.Kitsunezaki, K.Kizu, K.Kodama, Y.Koide, M.Koiwa[1)], S.Kokusen[1)], T.Kondoh, S.Konoshima, G.J.Kramer[4)], A.V.Krasilnikov[9)], H.Kubo, K.Kurihara, G.Kurita, M.Kuriyama, Y.Kusama, N.Kusanagi[1)], L.L.Lao[10)], P.Lee[6)], S.Lee[8)], G.Lei[6)], A.W.Leonard[10)], J.Li[4)], J.Manickam[5)] K.Masaki, H.Masui[1)], T.Matsuda, M.Matsukawa, T.Matsumoto, D.R.Mikkelsen[5)], Yukitoshi Miura, Yushi Miura, N.Miya, K.Miyachi, K.Miyata[1)], Y.Miyo, T.Miyoshi[8)], K.Mogaki, K.Mori[1)], A.Morioka, S.Moriyama, S.Nagaya, O.Naito, Y.Nakamura, T.Nakano, R.Nazikian[5)], M.Nemoto, S.V.Neudatchin[4)], Y.Neyatani, H.Ninomiya, T.Nishitani, M.Noda[1)], T.Oba[1)], M.Odamaki[1)], S.Oguri[1)], T.Ohga, A.Oikawa, T.Oikawa, M.Okabayashi[5)], T.Okabe, J.Okano, S.Omori, Y.Omori, H.Oohara, T.Oshima, N.Oyama[8)], T.Ozeki, T.Petrie[10)], G.Rewoldt[5)], J.A.Romero[2)], Y.Sakamoto, A.Sakasai, S.Sakata, T.Sakuma[1)], S.Sakurai, T.Sasajima, N.Sasaki[1)], M.Sato, M.Seimiya, H.Seki[1)], M.Seki, Y.Shibata[3)], K.Shimada, K.Shimizu, M.Shimizu, M.Shimono, K.Shinohara, S.Shinozaki, H.Shirai, M.Shitomi, M.Sueoka, A.Sugawara[1)], T.Sugie, H.Sunaoshi, Masaei Suzuki[1)], Mitsuhiro Suzuki[1)], T.Suzuki, Y.Suzuki[8)], M.Takahashi[1)], S.Takano[1)], M. Takechi[8)], S.Takeji, H.Takenaga, Y.Taki[1)], T.Takizuka, H.Tamai, Y.Tanai[1)], M.Terakado, T.Terakado, K.Tobita, S.Tokuda, T.Totsuka, R.Toyokawa[1)], K.Tsuchiya, T.Tsugita, Y.Tsukahara, T.Tuda, K.Uehara, T.Uehara[1)], N.Umeda, Y.Uramoto, H.Urano[3)], K.Urata[1)], K.Ushigusa, K.Usui, S.Wang[6)], J.Yagyu, M.Yamaguchi[1)], Y.Yamashita[1)], H.Yamazaki[1)], T.Yamazaki[1)], K.Yokokura, I.Yonekawa, R.Yoshino

1) Cooperative Staff
2) JSPS Fellow (former STA Fellow)
3) Fellow of Advanced Science
4) JAERI Fellow
5) PPPL, USA
6) MEXT Scientist Exchange Program (former STA Exchange)
7) JAERI-Univ.Tsukuba, Cooperative Doctoral Program
8) Post-Doctoral Fellow
9) TRINITI, Russian Federation
10) General Atomics, USA

2000年におけるJT-60U実験結果のレビュー

日本原子力研究所那珂研究所炉心プラズマ研究部・核融合装置試験部

JT-60チーム※

（2002年8月2日 受理）

2000年のJT-60U実験（2月～12月）の結果をレビューする。高β_p Hモードプラズマおよび負磁気シアプラズマにおいて、完全非誘導電流駆動状態での性能を大きく更新した。高β_p Hモードプラズマにおいては、高電子温度プラズマ（中心電子温度～13keV）へ360keV，4MWの負イオン源NB（NNB）を入射し、プラズマ電流1.5MAにて$2.0\times10^{20}m^{-3}keVs$の高い核融合積を得るとともに、NNBの電流駆動効率の世界最高値（$1.55\times10^{19}A/W/m^2$）を達成した。負磁気シアにおいては、低域混成波電流駆動とNNB電流駆動を用いて、高密度（グリンワルド密度の80%）にて高閉じ込め（HH_{y2}~1.4）を得た。110GHzの電子サイクロトロン波帯（ECRF）加熱装置においては、発振管（ジャイロトロン）を1999年の１本から３本へと増強し、1.5MWを3秒間真空容器内へ入射した。増強したEC装置を用いて、新古典テアリングモードの完全な安定化、電子温度とイオン温度がほぼ等しい状態での高閉じ込め、高電子温度領域における高いNNB駆動電流（1MA）、局在化したEC駆動電流の測定、などの成果を得た。連続ペレット入射装置を新たに設置した。高パワーNB加熱プラズマにおいては、高磁場側からの入射の方が低磁場側からの入射より有効であり、高閉じ込め高β_p Hモードプラズマの運転を高密度領域へ拡張した。CCS（コーシー条件面法）と呼ばれる新しいプラズマ位置・形状実時間制御法が利用できるようになり、特にLHおよびIC実験におけるプラズマと壁のクリアランスの制御に有効であった。トロイダル角運動量入力による内部輸送障壁の能動制御を実証した。高三角度のHモードにおいて、ペデスタル部で高い圧力・温度を得、分布の硬直性を通してコア部においても高い温度および高い閉じ込め性能をもたらした。W型ダイバータにおいては、従来の内側の排気溝に加えて外側にも排気溝を設け、排気効率を向上させた。アルゴンやネオンの入射により、高密度領域における閉じ込めの改善を試みた。ELMy Hモード（q_{95}=3.4）ではグリンワルド密度の65%にてHH_{y2}~1を得た。外側ストライク点をドームタイル上に置いた配位（q_{95}=3.6）では、よりピーキングした密度分布を得、グリンワルド密度の65%にてH_{89P} = 1.68を得た。負磁気シアプラズマ（q_{95}=6-7）においては、ネオンパフにより、X点MARFE中 H_{89P} = 1.8を得た。両脚排気によってヘリウムの排気効率を向上し、H_{89P} = 1.2（q_{95}=4.0）にてτ^*_{He}/τ_E = 2.8を得た。第一壁のボロン化処理と壁温の低減により主プラズマ中の不純物とZ_{eff}を低減した。Oモード反射計により、タイプIのELM中のペデスタル部の密度の時間発展を計測した。ELMによる熱流束を、X点と赤道面の可動マッハプローブを用いてSOLプラズマ中で測定するとともに、赤外テレビを用いてダイバータ板で測定し、SOLプラズマ中での熱輸送において対流による輸送が支配的であることを明らかにした。

那珂研究所：〒311-0193　茨城県那珂郡那珂町向山 801-1

※ JT-60チーム

安達　宏典[1)]，赤坂　博美，秋野　昇，安納　勝人，新井　優[1)]，新井　貴，
朝倉　伸幸，安積　正史，P.E.Bak[2)]，M.Bakhtiari[3)]，A.Chankin[4)]，C.Z.Cheng[5)]，
千葉　真一，Z.Cui[6)]，海老沢　昇，藤井　常幸，藤田　隆明，福田　武司，
船橋　昭昌，古川　弘[1)]，X.Gao[4)]，N.N.Gorelenkov[5)]，L.Grisham[5)]，芳賀　浩一[1)]，
濱松　清隆，濱野　隆[1)]，波多江　仰紀，林　伸彦，東島　智，疋田　繁紀[1)]，K.W.Hill[5)]，
平内　慎一，平塚　一，広井　俊和[1)]，H.M. Hoek[4)]，本田　敦，本田　正男，
星　芳幸[1)]，細金　延幸，市毛　尚志，井手　俊介，井戸村　泰宏，五十嵐　浩一[1)]，
池田　佳隆，井上　昭[1)]，井坂　正義，諫山　明彦，伊世井　宣明，石田　真一，
石井　和宏[1)]，石井　康友，石島　達夫[7)]，石川　正男[7)]，石澤　明宏[8)]，伊丹　潔，
伊藤　孝雄，岩橋　孝明[1)]，岩崎　慶太[1)]，岩瀬　誠[8)]，梶原　健[8)]，梶山　英一[1)]，
鎌田　裕，神永　敦嗣，柏原　庸央[1)]，河合　視己人，川俣　陽一，河野　康則，
椛澤　稔，菊池　弘[1)]，菊池　満，木村　豊秋，岸本　泰明，北村　繁，狐崎　晶雄，
木津　要，児玉　幸三，小出　芳彦，小岩　素直[1)]，石仙　茂晴[1)]，近藤　貴，木島　滋，
G.J.Kramer[4)]，A.V.Krasilnikov[9)]，久保　博孝，栗原　研一，栗田　源一，
栗山　正明，草間　義紀，草薙　直人[1)]，L.L.Lao[10)]，P.Lee[6)]，S.Lee[8)]，G.Lei[6)]，
A.W.Leonard[10)]，J.Li[4)]，J.Manickam[5)]，正木　圭，増井　浩史[1)]，松田　俊明，
松川　誠，松本　太郎，D.R.Mikkelsen[5)]，三浦　幸俊，三浦　友史，宮　直之，
宮地　謙吾，宮田　克行[1)]，三代　康彦，三好　隆博[8)]，藻垣　和彦，森　活春[1)]，
森岡　篤彦，森山　伸一，永谷　進，内藤　磨，中村　幸治，仲野　友英，R.Nazikian[5)]，
根本　正博，S.V.Neudatchin[4)]，閨谷　譲，二宮　博正，西谷　健夫，野田　政明[1)]，
大場　俊夫[1)]，小田巻　昌良[1)]，小栗　滋[1)]，大賀　徳道，及川　晃，及川　聡洋，
M.Okabayashi[5)]，岡部　友和，岡野　潤，大森　俊造，大森　栄和，大原　比呂志，
大島　貴幸，大山　直幸[8)]，小関　隆久，T.Petrie[10)]，G.Rewoldt[5)]，J.A.Romero[2)]，
坂本　宜照，逆井　章，坂田　信也，佐久間　猛[1)]，櫻井　真治，笹島　唯之，
佐々木　昇[1)]，佐藤　稔，清宮　宗孝，関　宏[1)]，関　正美，柴田　泰成[3)]，
島田　勝弘，清水　勝宏，清水　正亜，下野　貢，篠原　孝司，篠崎　信一，
白井　浩，蔀　守正，末岡　通治，菅原　章博[1)]，杉江　達夫，砂押　秀則，
鈴木　昌栄[1)]，鈴木　光博[1)]，鈴木　隆博，鈴木　善雄[8)]，高橋　正己[1)]，高野　正二[1)]，
武智　学[8)]，竹治　智，竹永　秀信，滝　義秋[1)]，滝塚　知典，玉井　広史，
棚井　豊[1)]，寺門　正之，寺門　恒久，飛田　健次，徳田　伸二，戸塚　俊之，
豊川　良治[1)]，土屋　勝彦，次田　友宣，塚原　美光，津田　孝，上原　和也，
上原　聡明[1)]，梅田　尚孝，浦本　保幸，浦野　創[3)]，浦田　一宏[1)]，牛草　健吉，
薄井　勝富，S.Wang[6)]，柳生　純一，山口　将男[1)]，山下　睦樹[1)]，山崎　晴幸[1)]，
山崎　武[1)]，横倉　賢治，米川　出，芳野　隆治

1) 業務協力員
2) JSPS フェロー（旧 STA フェロー）
3) 特別研究生
4) 原研リサーチフェロー
5) PPPL, USA
6) MEXT 研究員交換プログラム（旧原子力交流制度研究員）
7) 連携大学院生，筑波大学
8) 博士研究員
9) TRINITI, RF
10) GA, USA

This is a blank page.

Contents

目次

1. Overview of the Experiments in 2000

1.1 Core Plasma

Full non-inductive current drive has been achieved in a high performance high β_p H-mode plasma with 1.5 MA and in a high confinement reversed shear (RS) plasma. In the high β_p H-mode, with injection of the negative ion based neutral beam (NNB) of 360 keV and 4 MW into a high electron temperature plasma ($T_e(0)$ ~ 13 keV), a high fusion triple product $n_D(0)T_i(0)\tau_E = 2.0\times10^{20}$ keVm^{-3}s has been obtained, and the highest value of current drive efficiency of NNB (1.55×10^{19} A/W/m^2) has been achieved. In the RS case, LHCD and NNB-CD were employed and high confinement (HH_{y2} ~ 1.4) at high density (f_{GW} ~ 0.80) has been achieved. In the 110 GHz ECRF system, two more gyrotrons have been installed in addition to the one installed in 1999 and 1.5 MW was injected into the torus for 3 s. Complete stabilization of neoclassical tearing mode (NTM), realization of high confinement plasmas with T_e ~ T_i, a high value (1 MA) of NNB-driven current in the high T_e regime, and measurement of localized EC driven current were achieved with the upgraded EC system. The newly installed pellet injection system extended the regime of high confinement high β_p H-mode to a higher density. The active control of ITB strength by the switch of the toroidal momentum injection direction was successfully demonstrated. In high triangularity H-mode plasmas, higher pressure and temperature at the edge pedestal were observed, which resulted in higher temperature and confinement in the core through the profile 'stiffness.' The time evolution of pedestal density profile during a type I ELM was evaluated with the O-mode reflectometer installed at the midplane.

1.1.1 Sustainment of high performance and non-inductive current drive

The full non-inductive high β_p ELMy H mode regime has been extended to the reactor relevant regime with small values of collisionality and normalized gyroradius. The record values of the fusion product under full non-inductive current drive ($n_D(0)\tau_E T_i(0)$ = 2.0×10^{20}m^{-3}skeV) and the neutral beam current drive efficiency (η_{CD} = 1.55×10^{19}A/m^2/W) have been demonstrated at 1.5 MA with N-NB injection (360keV, 4MW). High stability (β_N =2.5) and high confinement (HH_{y2} = 1.4) were also obtained.

The density range in the high β_p ELMy H-mode regime with high confinement, high β_N and high fraction of non-inductive current drive, has been extended with high field side pellet injection and NNB injection. The pellet injected discharge has a high pedestal pressure compared with the gas fuelled discharges and the pedestal temperature does not decrease even at high pedestal density. At low q_{95} = 3.4, β_N = 2.8-2.9 has been sustained for 4 s, determined with hardware limitations. The pedestal pressure increases with increasing core confinement.

In RS plasmas, full non-inductive current drive with high confinement (HH_{y2} ~ 1.4) and with high density (f_{GW} ~ 0.80) has been achieved by using LHCD and NNB-CD at I_p = 0.9 MA, B_{t0} = 2.5 T and q_{95} ~ 6.9. High values of β_N (~2.2) and bootstrap current fraction (~61%) were also obtained. With the injection of LHCD, expansion of ITB was observed and the stored energy was increased accordingly.

Extension to a low q regime was attempted in RS plasmas with NB heating, where a full non-inductive current drive with high beta (β_N ~ 2) and high confinement (HH_{y2} ~ 2.2) had been achieved before by bootstrap current and off-axis NBCD in a high q regime (q_{95} ~ 9). High beta (β_N ~ 2) was sustained for longer than $5\tau_E$ in a low q regime (q_{min} ~ 2.5, q_{95} ~ 5.5) while high confinement (HH_{y2} >~ 1.5) was sustained only for ~τ_E. The latter was restricted by the confinement degradation phenomena encountered during a high confinement phase.

The magnetic shear was scanned between a weak positive shear (typical high β_p mode) and a strong negative shear (typical RS plasma) to see if an optimum point exists from the viewpoints of stability and confinement. In the zero shear region, confinement higher than that in the high β_p mode was obtained while the stability was not improved from that in the RS mode. A localized reversed shear region was formed due to the bootstrap current in "weak shear" plasmas. Major collapses seem to be related to q(0) ~ integer.

Formation of RS plasma with a low ramp rate of 0.2 MA/s was attempted by using NB, EC or LH to address the issue of formation of RS in a super-conducting machine, where the low ramp rate is favorable to reduce AC power loss in super-conducting coils. The scenario with LH was most successful and ρ_{qmin} of 0.7 was sustained with only 1.8 MW of LH power up to 1.2 MA.

The regime of NNB current drive experiment, in which N-NB driven current was precisely measured by MSE in a low density plasma with small bootstrap current fraction, was extended to higher T_e reaching $T_e(0)$~10 keV by utilizing EC. Measured NNB driven current reached 1 MA with $\eta_{CD} = 1 \times 10^{19} A/m^2/W$ and agreed with the theoretical prediction.

In the EC wave injection system for local heating and current drive, the number of gyrotrons (110 GHz) was increased from one to three. In 2000, 1.5 MW was injected into the torus for 3 s. The EC driven current, which was expected to be very localized, was measured with MSE and the measured profile agreed with a theoretical result.

The current profile control by combination of LH and EC injection was also attempted, where the profile of hard X-ray (driven current) changed according to the EC injection angle.

1.1.2 Confinement and transport

Extensive studies on ITBs have been performed including effects of electron heating, ITB control through the toroidal angular momentum injection and the threshold power of ITB formation.

To address the issue of improved confinement under dominant electron heating regime, which is expected in fusion reactors, confinement properties of high β_p mode and RS plasmas under electron heating were studied. Both in high β_p mode and RS plasmas, confinement enhancement relative to the L-mode (H_{89P}) was found not to change drastically and to be good enough, during the electron heating dominant phase. In the RS case, ion temperature T_i and electron density n_e profiles were almost unchanged, while, in the high β_p mode case, gradients in T_i and n_e profiles were reduced. The pedestal might have increased during the electron heating phase and contributed to maintaining the overall confinement.

The dependence of formation of ITB on the plasma current I_p and the toroidal rotation V_t was examined in RS plasmas. On the toroidal rotation, the results would suggest that V_t could affect ITB formation. On the plasma current, no conclusive results were obtained since not only I_p but also the current profile differed.

The active control of ITB strength by the switch of the injection direction of toroidal angular momentum was successfully demonstrated. The T_i gradient degraded by co-injection was recovered by counter and balanced injection. The change in radial electric field E_r shear of outer half region of the ITB layer (near the ITB foot) was important to control the ITB strength of the whole ITB region. This suggests a non-local nature in relations between the E_r shear and the reduction of transport.

Confinement properties of reversed shear plasmas were investigated under the discharge conditions of nearly balanced momentum injection, L-mode edge and NB heating. The stored energy was found to be strongly correlated with B_p^{foot} rather than I_p, and was proportional to $(B_p^{foot})^{1.5}$, where B_p^{foot} is a poloidal magnetic field at the ITB foot.

Dynamic behavior of transport and heat propagation were studied in normal and reversed shear plasmas with ITBs, which revealed a combination of various fast and slow time scale processes. Abrupt variations of $\chi_{e,i}$ (ITB-events) are wide (30-40% of plasma minor radius) in normal and reversed shear plasmas with weak ITBs while they are localized near the ITB foot in RS plasmas with a strong ITB.

As for the H-mode, the L-H transition threshold power in ITB plasmas and the dependence of pedestal pressure and confinement on the triangularity were studied.

The L-H transition threshold power in plasmas with an ITB was found to be substantially higher than the conventional scaling established for plasmas without an ITB. This is because electron densities are lower in ITB plasmas and the criteria for the edge density and temperature to induce the L-H transition is similar. The degradation of the quality of ITB resulted in the increase of edge density and thus inducing the L-H transition.

The high triangularity (δ) H-mode plasmas without an ITB were produced to investigate the dependence of confinement on the triangularity. The thermal confinement in high δ ($\delta \sim 0.45$) H-mode plasmas was substantially higher than low δ ($\delta \sim 0.20$) H-mode plasmas.

This is because of higher pressure and temperature at the edge pedestal, which results in higher core temperature through the profile 'stiffness.' In the high δ high β_p H-mode with an ITB, further increase in the pedestal pressure was obtained.

1.1.3 MHD instabilities and high energy ions

Stability of RS plasmas was studied focusing on the resistive MHD modes. It was found that the radially localized resistive interchange mode led to a major collapse through nonlinear mode coupling with a tearing mode in the positive shear region.

The stabilizing effects of wall were demonstrated in RS plasmas. Both of resistive (tearing) and ideal modes were stabilized by the wall when the wall was close enough to the plasma surface (typically d/a < 1.3, where d is the wall radius and a is the plasma radius) and high beta plasmas exceeding the no-wall beta limit were obtained. Resistive wall modes were observed in these high beta plasmas, whose growth rate was large when the edge safety factor was close to an integer value.

Complete stabilization of a neoclassical tearing mode, NTM, with m/n = 3/2 was achieved by using upgraded EC system. In this experiment, the first harmonic O-mode wave was used and the estimated driven current density was about twice as large as the bootstrap current density. The region of appearance of NTM was investigated and it was found that NTMs with n = 2 and n = 3 are observed only in the region of $\beta_p > 0.6$ and $q_{95} < 4.5$. Disappearance of NTM with m/n = 2/1 was observed in plasmas with N-NB injection, probably due to smaller pressure gradient at the q =2 surface at a fixed total pressure.

The influence of MHD instabilities on NNB current drive performance was investigated. In a low density, low beta plasma, a burst-like instability, which was believed due to the pressure of fast ions injected by NNB, caused a reduction of neutron yield and a increase of loop voltage evaluated with MSE inside ρ = 0.3. This indicates the loss of fast ions carrying the current. The reduction of neutron yield was also observed during the NTM in high beta plasmas.

The time evolution of pedestal density profile during a type I ELM was evaluated with the O-mode reflectometer installed at the midplane. The position of cut-off layer, which was located near the shoulder of the pedestal, was found to move about 7 cm inward during 100-350 μs. The burst of divertor D_α singal was delayed by 105-195 μs from the density collapse. Asymmetric structure of density collapse in the poloidal direction was suggested.

Instabilities with a frequency sweep in the frequency regime of Alfvén eigenmode were studied by using NNB. Abrupt large amplitude events (ALEs) often appeared during the fast frequency sweeping mode and a large drop of neutron emission rate and a significant increase in fast neutral particle fluxes were observed during ALEs.

1.1.4 Plasma control and disruption

A new method for the control of the plasma position and shape in real-time became available in 2000. This method employs a novel plasma-shape reproduction technique, called the Cauchy-condition surface (CCS) method, with which the shape of the separatrix is calculated every 1 ms. One of the merits of CCS is that it can deal with various plasma position and shape accurately while the available region of the conventional function parameterization method (FPM) is restricted inside the equilibrium database. By using CCS, it has become possible to control the clearance δ_0 between the plasma surface and the wall, which is very important for LH and IC experiments, in a wider range.

A system for real-time NTM detection and EC wave injection has been developed. The amplitude of electron temperature perturbation by NTM was successfully evaluated in real-time and EC wave was injected.

The process of termination of runaway electron current generated at the plasma disruption was investigated in detail. Intensive heat pulses to the inner divertor plates were observed. The halo current during the runaway termination was small and increased after the termination.

1.2 Divertor and Boundary Plasmas

Since H-mode confinement degradation below n_{GW} (the Greenwald density) is a critical issue in ITER-FEAT, large efforts are devoted to produce high density plasmas with good H-mode confinement in JT-60U. Ar injections were found to be useful to increase plasma densities in ELMy H-mode in 1999. Ar injection experiments were refined and continued in 2000. In those experiments, the radiation loss from the edge plasma was controlled by a feedback technique using Ar puffing and divertor pumping. It was found that HH_{y2} remained near unity in the range of $n_e < 0.65\ n_{GW}$. HH_{y2} was about 50% higher than that in the plasmas without Ar injection at $n_e = 0.65\ n_{GW}$.

In the process to minimize deuterium gas puffing by producing high density plasmas in the near-limiter configurations, the ITB was found in a few ELMy H-mode discharges with Ar gas puffing in 1999. In 2000, the outer strike-point location was scanned from the outer target plates to the dome plates to find out the condition to produce the ITB. The peaked density profile with the ITB was obtained when the outer strike point was located on the dome tiles. The best data was $H_{89P} = 1.68$ after ripple loss correction at $0.8\ n_{GW}$. The total radiation fraction was 85% of the input power and the divertor plasmas were detached.

In the reversed shear plasmas, neon and deuterium gas puffings were applied and high confinement ($H_{89P} \leq 1.8$) was obtained during X-point MARFE. It demonstrated separation of the ITB from the strong radiator in the boundary plasma. Impurity accumulation was not significant, since the neon and carbon density profiles were similar to electron density profiles.

Helium exhaust was investigated with He beam injection of $P_{He\text{-}NB} = 1.4$ MW (equivalent to 85 MW α heating) for 3 s into ELMy H-mode discharges ($I_P = 1.4$ MA, $B_t = 3.5$ T, $q_{95} = 4.0$, $P_{NB} = 16$ MW, $V_P = 58\ m^3$). In one of those discharges, $\tau^*_{He} = 0.36$ s and $\tau^*_{He}/\tau_E = 2.8$ with an H-factor ($\equiv \tau_E/\tau_E^{ITER\text{-}89P}$) = 1.2 were achieved. As a result, the helium exhaust efficiency in the divertor-closure configuration was extended by 45% as compared to the one with the inner-leg pumping. Impurity transport study was also carried out for He in the reversed shear plasmas. Diffusivity of He was in the same order with the neoclassical transport inside the ITB, which made He exhaust difficult in the low divertor recycling conditions.

Repetitive HFS (high magnetic field side) and LFS (low magnetic field side) pellet injections were carried out to extend plasma operation regime toward the high density and to explore the pellet enhanced performance (PEP) mode. The plasma densities just after each pellet injection, n_e^{peak}, reached up to $1.8 \times n_{GW}$ in the OH plasmas with LFS pellet injections. In high power NB heated plasmas, HFS pellet injections were more effective than LFS pellet injections for density increase due to slow density decays. Improvement in confinement due

to E×B drift of pellet clouds was not obvious yet. The Pellet enhanced performance (PEP) mode trial was carried out with hydrogen NB, hydrogen gas and hydrogen pellets. The ITB in the density profile was associated with central pellet deposition and the reversed magnetic shear, which was produced by injection of pellet simultaneous with low power NB heating as low as 1 MW.

Impurity and Z_{eff} in the main plasmas have been reduced by boronization of the first wall and by reduction of the wall baking temperature. Durability of boronization effect was investigated in L-mode discharges with an identical condition, which were repeated before and after boronization. The oxygen fraction (n_O/n_e) in the main plasma decreased from ~ 1.5% to ~ 0.7 % by boronization. The plasma effective charge (Z_{eff}) was successfully reduced due to reduction in carbon content in the L-mode and reversed shear plasmas by lowering the baking temperature from 270°C, usual baking temperature, to 150 and 80°C. The measured chemical sputtering yield was reduced from 15 % at 270°C to 10 % at 150°C and 5 % at 80°C, respectively. The CH_4/CD_4 yield was not apparently dependent on the baking temperature, while the C_2H_x/C_2D_x yield was clearly dependent.

In order to understand the origin of the carbon due to chemical sputtering and the screening of methane in the SOL and divertor plasmas, the carbon density was measured by CXRS system and analyzed in the discharges with CH_4 gas puffing. The analysis suggested that carbon ions in the main plasma were mainly originated from chemically sputtered hydrocarbon at the divertor plates.

Volume recombination in detached divertor plasmas was studied by observation of Balmer lines of hydrogen atoms and continuum. Recombination fluxes to divertor plates were estimated by Hε line emission. It was found that the ratio of the recombination flux to the divertor ion flux increased up to 0.5 in the inner divertor and 0.3 in the outer divertor, respectively during the X-point MARFE.

Reciprocating Mach probes installed at both the X-point position and midplane position were used to measure plasma flows in ELMy H-mode discharges and, for the first time in JT-60U, OH discharges with pellet injections. The SOL plasma flow in the ELMy H-mode plasma was compared with ELM heat flux to the divertor plates measured by IRTV with fast sampling data(250μs per profile). It was found that the period of peak heat fluxes by ELMs corresponded to the enhanced SOL plasma flows which carried the convective heat fluxes. As for pellet perturbation, increase in $j_{s,up}^{Xp}$ (ion saturation current on the up-stream side of the X-point Mach probe) by a pellet was roughly 30-50% near the separatrix and $T_{e,up}^{Xp}$ (electron temperature on the up-stream side of the X-point Mach probe) did not change. While large and rapid peaks in $j_{s,up}^{Xp}$ near X-point was found, no change in $j_{s,up}^{mid}$ (ion saturation current on the up-stream side of the midplane Mach probe) was observed for LFS pellet injections. It might be caused by local increase in the plasma density.

2. Sustainment of High Performance and Non-inductive Current Drive

2.1 Enhanced performance of the high β_p ELMy H-mode with high NNB current drive efficiency

Y. Kamada and the JT-60 Team

Abstract

In the high βp ELMy H mode regime, characterized by the weak magnetic shear, discharges with a high integrated performance have been sustained near the steady-state current profile solutions under full non-inductive current drive with a proper current profile driven by N-NB and bootstrap current. The full non-inductive high βp ELMy H mode regime has been extended to the reactor relevant regime with small values of collisionality and normalized gyroradius. Record values of the fusion product under full non-inductive current drive ($n_D(0)\tau_E T_i(0)$ =2.0x10^{20}m^{-3}skeV) and the neutral beam current drive efficiency (η_{CD}=1.55x10^{19}A/m^2 /W) have been demonstrated.

1. Introduction

With the main aim of providing physics basis for ITER and the steady-state tokamak reactor, JT-60U has been optimizing operational concepts and extending discharge regimes toward simultaneous sustainment of high confinement, high β_N, high bootstrap fraction, full non-inductive current drive (full-CD) and efficient heat and particle exhaust utilizing variety of heating, current drive, torque input and particle control capabilities. In the two advanced operation regimes, the reversed magnetic shear and the weak magnetic shear (high-β_p) ELMy H modes characterized by both internal (ITB) and edge transport barriers and high bootstrap current fractions f_{BS}, discharges have been sustained near the steady-state current profile solutions under full noninductive current drive [1]. Figure 1 shows the strategy of the JT-60U high-β_p H mode development. Based on the early development for high β_N and full-CD at low current and for high fusion product at high current, we have been extending the high integrated performance regime towards the reactor relevant plasma regime with small values of collisionality, normalized gyroradius by increasing B_t, I_p and heating power.

2. Achievement of high integrated performance with NNB current drive

With N-NB injection (360keV, 4MW), the full non-inductive high-βp ELMy H-mode regime was successfully extended to the higher I_p regime (=1.5MA). Figure 2 shows time evolution and typical profiles of the discharge (E36715) with high confinement enhancement over the ITER H-mode scaling HH_{y2}=1.4 and high β_N=2.5 under full noninductive current drive obtained near the steady state current profile solution. The main parameters are listed in Table I. The noninductive current drive was achieved mainly by on-axis current drive by NNB (608kA, 40% of I_p), broad current drive by P-NB (255kA,17%) and off-axis bootstrap

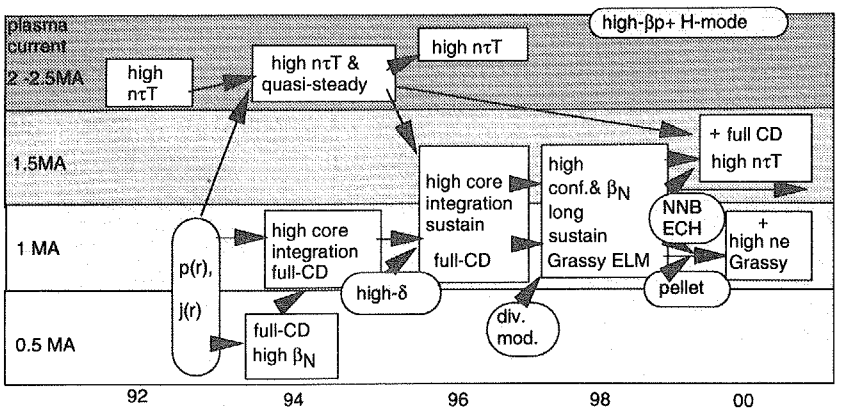

Fig.1 Strategy of high-β_p H mode development

current (760kA, 51%) (see Fig.5 a)). In the later phase of the N-NB pulse, the safety factor at the plasma center q(0) stays almost constant suggesting saturated current profile evolution. In this phase, the fast ion distribution has also reached steady state according to the 3-D OFMC calculations. Since the NB current drive efficiency increases with $T_e(0)$, on-axis ECH was applied and $T_e(0)$ reached 13keV, and then the record N-NB η_{CD} of 1.55×10^{19} A/m^2/W was achieved. Current drive capability of the N-NB system in JT-60U has been extended to the reactor relevant regime (Fig.3, see also Sec.2.7). The N-NB injection phase in E36715 was free from any significant MHD instability except for type-I ELMs. We have shown experimentally that onset conditions and mode numbers of the tearing mode are determined by local ∇p at the mode rational surfaces. The stable discharge E36715 was sustained with reduction of ∇p at the q=2 surface (Sec.4.4). Figure 4 shows the integrated performance for E36715 (1.5MA/3.7T) and another discharge achieved previously at 1MA/3T. The figure consists of 7 axes: HH_{y2}, β_N, f_{BS} (fraction of bootstrap current to plasma current I_p), f_{CD} (fraction of non-inductive driven current to I_p), fuel purity, ratio of radiated power to absorbed heating power, and line averaged electron density normalized by the Greenwald density limit. The full scale for each axis represents one of the ITER-FEAT steady-state operation design examples. These discharges satisfy the requirements for HH_{y2},f_{BS} and f_{CD}. However, for density and radiation power, in particular, further improvement is needed. For these parameters, an improved integrated performance has been achieved by pellet injection (see Sec.2.2).

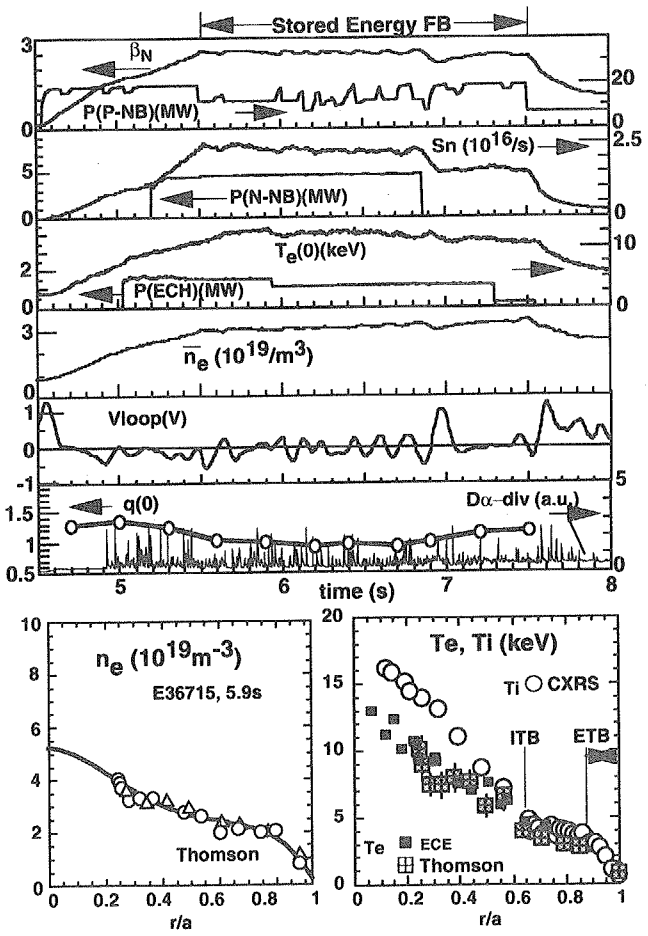

Fig.2 Time evolution and profiles of the high β_p ELMy H-mode discharge E36715 in which HH_{y2}=1.4 and β_N=2.5 were sustained under full non-inductive current drive with N-NB (1.5MA, 3.74T,q_{95}=4.75).

Table I. Achieved Parameters

shot	E36715
Mode	High-β_p ELMyH full-CD NNB inj.
time (s)	6.4
I_p (MA)	1.5
B_t (T)	3.74
P_{aux}^{abs}(MW)	15.3
a (m)	0.79
R (m)	3.22
δ_x	0.36
κ_x	1.54
q_{95}	4.75
W (MJ)	5.98
dW_{dia}/dt (MW)	0
S_n (10^{16}/s)	2.2
Z_{eff}	3.06
$n_e(0)$ (10^{19}m^{-3})	5.0
$n_D(0)$ (10^{19}m^{-3})	3.0
$\bar{n}_e$ (10^{19}m^{-3})	3.1
$\bar{n}_e/n_{GW}$	0.41
$T_i(0)$	17.5
$T_e(0)$	12.7
τ_E (s)	0.39
H_{89PL}	2.95
HH_{y2}	1.40
β_N	2.51
β_p	1.97
β_t(%)	1.26
f_{BS}	0.51
f_{BD}	0.57(NNB 0.40)

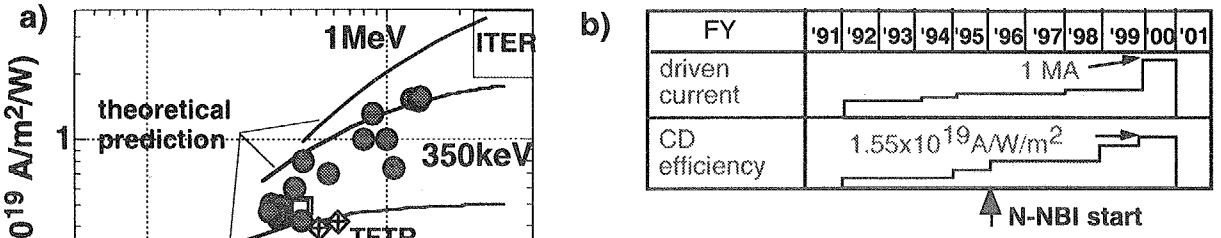

Fig.3. a) N-NB current drive efficiency (η_{CD}) approaching the ITER regime. b) Progress of neutral beam current drive efficiency in JT-60U.

Figure 5 compares profiles of driven current j , magnetic shear s, safety factor q and ion temperature T_i for a) the weak positive shear case E36715 (Fig.2, fully noninductive) and b) the flat shear case (partially noninductive). Current profiles were controlled by a) combination of central N-NB and EC current drive (CD) and bootstrap current, and b) ohmic and bootstrap currents without NBCD. The measured q-profiles or the current profiles in the saturated phase stay near the steady-state solutions calculated by the ACCOME code. By modification of the external current drive profile together with proper combination with bootstrap current, JT-60U has thus sustained high confinement advanced modes near the steady state current profile solutions in the weak positive shear configurations. Based on the JT-60U high β_p mode experience, the ITB is formed in the low shear region; typically s<1. In discharges shown on Figs 5 a) and b), this criterion was held and wide radii satisfying this condition were sustained. The ITB radius often coincides with the q=2 or 3 surface. This, however, cannot apply to the conditions of the *initial* formation condition of ITB in JT-60U, which can occur at an inner region where q<2 and s<1, and then the ITB radius expands and is stagnated near the q=2 surface or s~1.

JT-60U has extended the advanced operation regime toward the reactor relevant parameter regimes. In the high β_p ELMy H-mode regime, $\beta_N H_{89PL}$ ~7 has been sustained for ~1.3s (~3τ_E) with full noninductive CD and $\beta_N H_{89PL}$ ~5.5 for ~2.8s (~12τ_E) at q_{95}=3.3 (Fig.6 a). For sustainment of high $\beta_N H_{89PL}$ values, high triangularity operation (δ>0.3 –0.4) is essentially important in addition to current and pressure profile optimization [3].

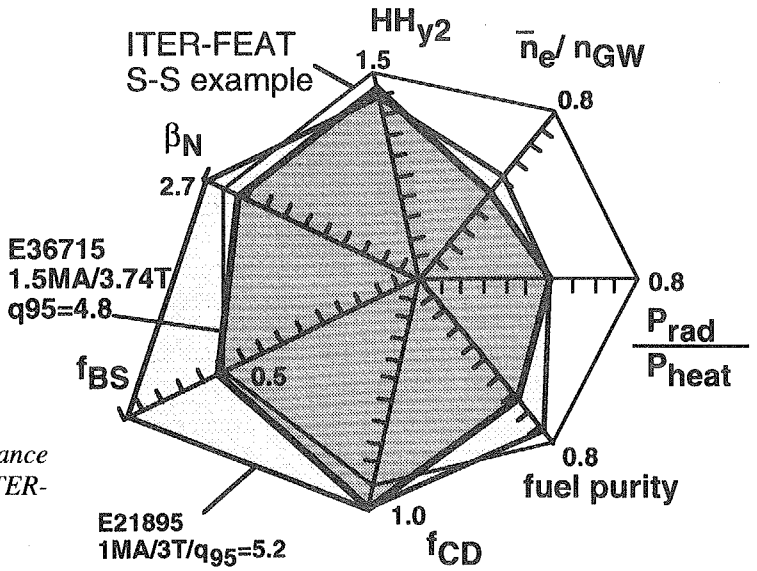

Fig. 4 Achieved integrated performance relative to the target values in the ITER-FEAT steady-state operation.

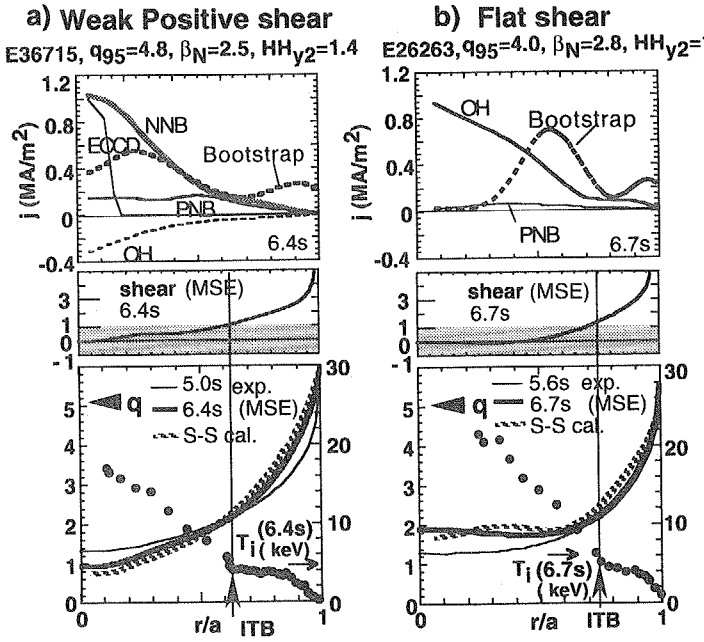

Fig.5 High β_p mode profiles with ITBs sustained near the steady-state current profile solutions by active current drive control: a) the weak positive shear (full noninductive: N-NB central CD + P-NB broad CD + bootstrap; E36715 in FIG.3), b) the flat shear (bootstrap + OH ; not full noninductive). a) and b) shows driven current profiles calculated with ACCOME, measured magnetic shear profiles, measured q-profiles in the early phase (thin solid lines), measured q-profiles in the saturated phase (bold solid lines), steady-state q-profiles (ACCOME: Steady-State cal. ,bold hatched lines) and $T_i(r)$ with ITBs.

JT-60U has increased plasma current and toroidal field in developing high-β_N full noninductive CD plasmas . Figure 6b) demonstrates the significance of this research direction on the ν_e*(collisionality) - ρ_{pi}*(normalized poloidal gyroradius) plane. Since behavior of the key physics processes, such as stability, transport and bootstrap current are determined by these non-dimensional parameters, it is necessary to demonstrate the required performance at sufficiently low values of ν_e* and ρ_{pi}* close to the reactor operational regimes. The JT-60U high-β_N full noninductive CD regime has accessed ν_e*~0.01-0.02 and ρ_{pi}*~0.07-0.1. These values are close to those for the ITER-FEAT steady-state reference design; ν_e*~ν_e*$_{ITER}$ and ρ_{pi}*~3-4 ρ_{pi}*$_{ITER}$.

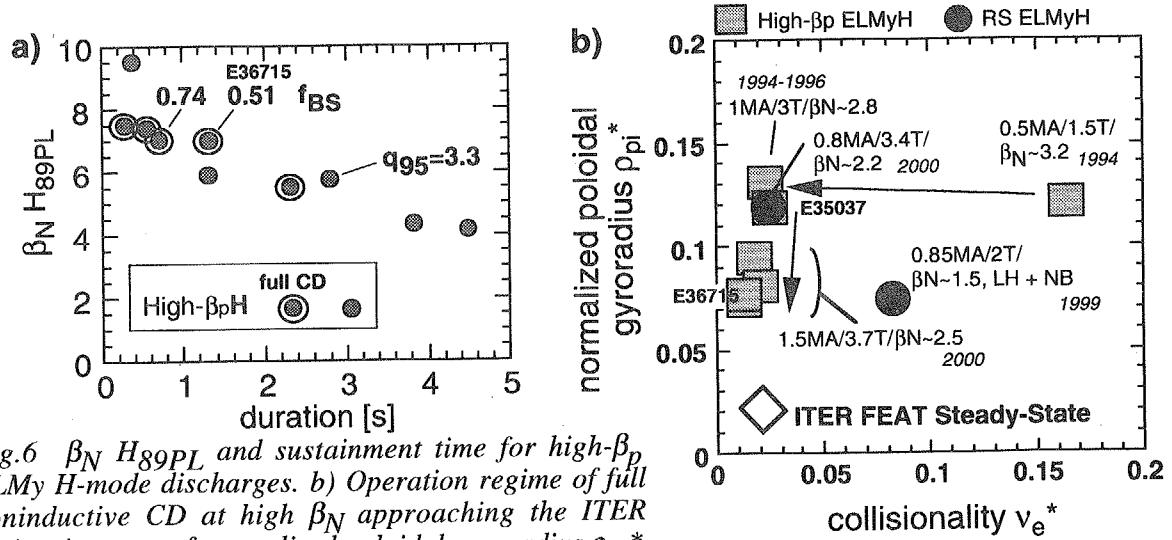

Fig.6 β_N H_{89PL} and sustainment time for high-β_p ELMy H-mode discharges. b) Operation regime of full noninductive CD at high β_N approaching the ITER regime in terms of normalized poloidal gyroradius ρ_{pi} and collisionality ν_e*.*

REFERENCES

[1] Y. Kamada and the JT-60 Team, 18th IAEA Int. Conf. Fusion Energy, 2000, Sorrento, IAEA-CN-77/OV1/1, Nucl. Fusion 41, 1311 (2001).

2.2 Extended operation regimes of quasi-steady high βp ELMy H-mode discharges with high integrated performance

Y, Kamada, H. Takenaga, A. Isayama, T, Hatae and the JT-60 Team

Abstract

With the high field side pellet injection and NNB injection, JT-60U has successfully extended the density range in the high β_p ELMy H-mode regime with a favorable integrated performance; high confinement, high β_N and high fraction of noninductive current drive.The pellet injected discharge has a high pedestal pressure compared with the gas fuelled discharges and the pedestal temperature does not decrease even at high pedestal density. At low q_{95}=3.4, β_N=2.8-2.9 has been sustained for 4s determined with hardware limitations. The pedestal pressure increases with increasing core confinement. The full non-inductive operation has been demonstrated with grassy ELMs.

2.2.1. Extended density regime with high confinement and enhanced pedestal pressure

In order to achieve the high integrated performance discussed in Sec.2.1, the critical issue is extension of the density range of the high confinement modes. For this purpose, JT-60U has been optimizing the operation scenario of the high β_p ELMy H-mode with multiple pellet injection and NNB injection into high triangularity discharges.

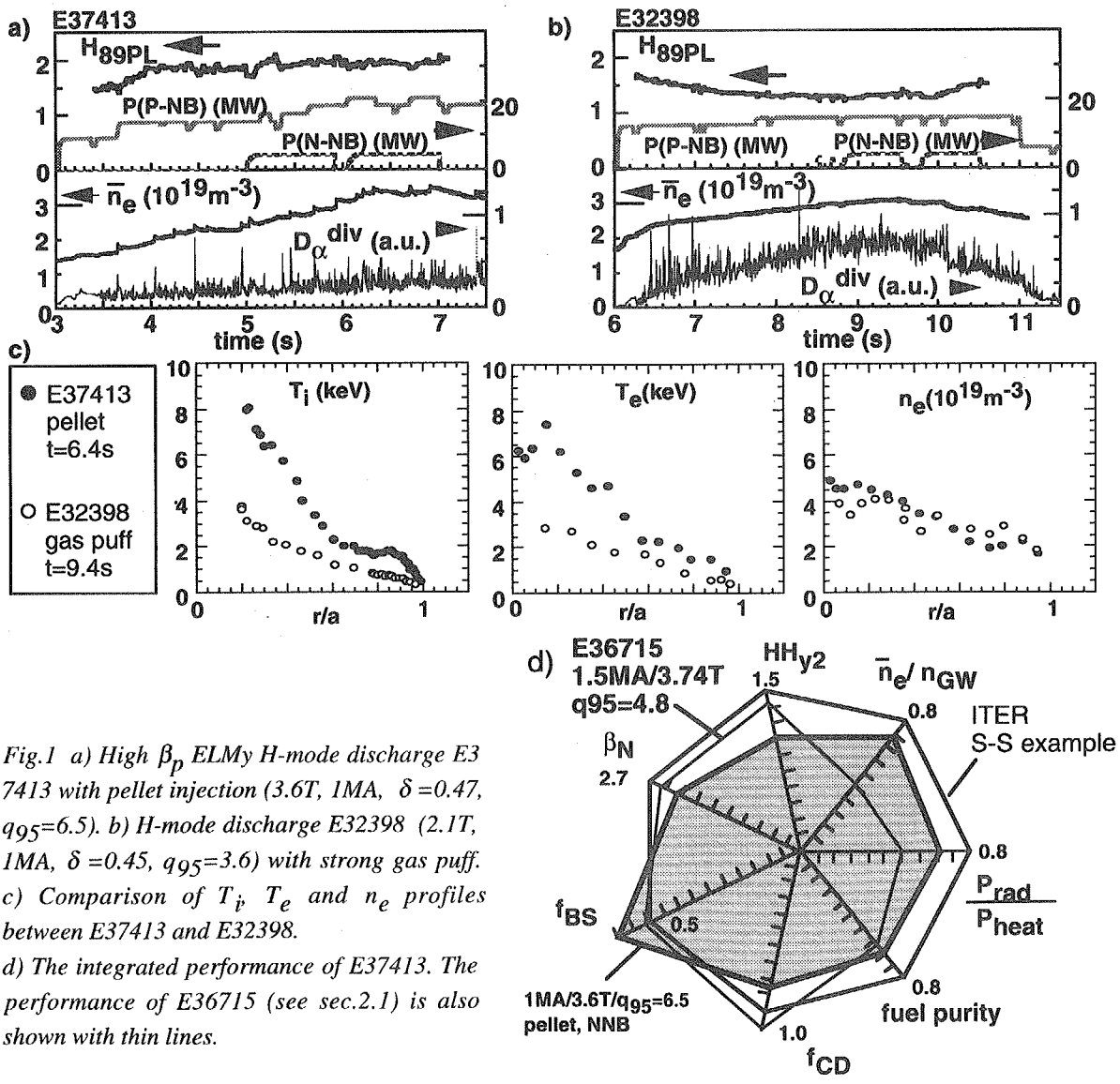

Fig.1 a) High β_p ELMy H-mode discharge E3 7413 with pellet injection (3.6T, 1MA, δ =0.47, q_{95}=6.5). b) H-mode discharge E32398 (2.1T, 1MA, δ =0.45, q_{95}=3.6) with strong gas puff. c) Comparison of T_i, T_e and n_e profiles between E37413 and E32398.
d) The integrated performance of E37413. The performance of E36715 (see sec.2.1) is also shown with thin lines.

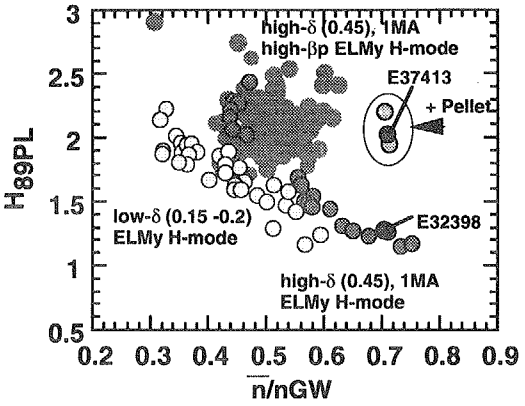

Fig.2 Extended high confinement - high density range by high triangularity and pellet injection.

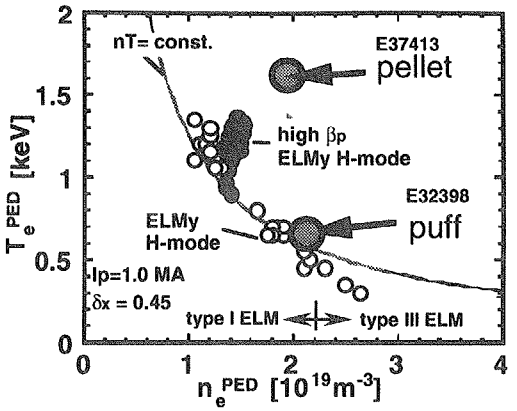

Fig.3 Pedestal temperature and density for 1MA discharges at fixed triangularity δ=0.45.

With the high field side pellet injection, JT-60U has successfully extended the density range in the high β_p ELMy H-mode regime with a favorable integrated performance. Figures 1 (a) and (b) compare two discharges ; one with pellet injection and the other with gas fueling. We adopted high triangularity (δ~0.47), since high-δ is beneficial to achieve high pedestal pressure. In addition, we injected NNB which can keep a centrally peaked heating profile even at high density. In the pellet injected discharge, the H-factor stays almost constant even with increasing density. On the other hand, the H-factor decreases with density in the gas fueled discharge. Figure 1(c) shows that the pellet injected discharge has remarkably high temperature. Compared with the discharge E36715 treated in Sec.2.1.1, the integrated performance was improved in terms of density, radiation power and purity (Fig.1(d)). In the pellet injected discharge, HH_{y2}=1.05 together with β_N=2.2 and f_{BS}~60% was achieved at n_e/n_{GW}~0.7. Without pellets, n_e/n_{GW}~0.6 was the upper density limit to achieve HH_{y2} >1. Figure 2 shows that the high confinement discharge regime expands to higher n_e/n_{GW} with pellet injection and high δ. The remarkable difference between the two discharges treated in Fig.1 appears in the pedestal parameters. Figure 3 shows that the pedestal pressure (~n_e^{PED}xT_e^{PED}) stays roughly constant for the standard H-mode with type I ELMs (open circles). In the high β_p ELMy H-mode (small closed circles), the pedestal pressure can be higher than that of the

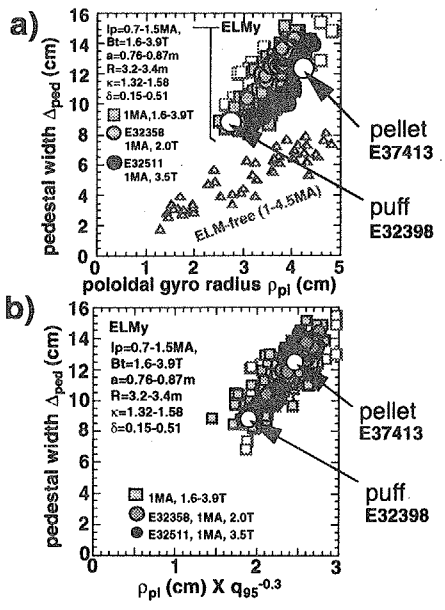

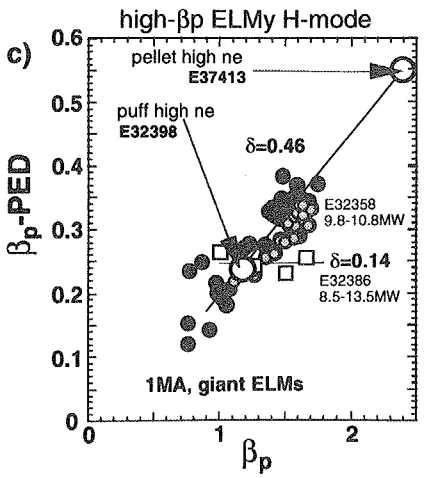

Fig.4 a) Pedestal width Δ_{ped} versus poloidal gyro radius ρ_{pi}. b) Δ_{ped} versus $q_{95}^{-0.3}$. c) Increasing pedestal β_p (β_p-PED) with total β_p at high δ. At low δ, β_p-PED is almost constant.

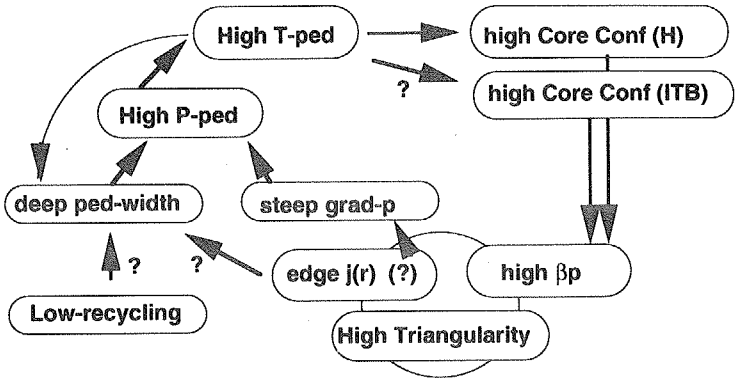

Fig.5 Correlations of the pedestal and core parameters based on JT-60U observations.

standard H-mode. The pedestal temperature in the pellet injected discharge E37413 is higher than that of the gas fueled reference discharge E32398 by more than a factor of 2 (large closed circles) and the pedestal width is wider. Figures 4(a) and (b) show that the pedestal width of these two discharges follows the pedestal width scaling [2]. We found that the edge stability limit for type I ELMs are improving with increasing β_p in the high δ regime. Figure 4(c) shows the pedestal β_p, defined by the ratio of the pedestal pressure to the poloidal field, increases with increasing total β_p at high $\delta\tilde{}$0.46. The two discharges E37413 and E32398 follows this relationship. On the other hand, β_p-PED seems almost constant at low-δ (open squares). In the case of high δ, the pedestal pressure limited by type I ELMs increases with β_p, which may be due to improved edge stability. Figure 5 summarizes correlations among pedestal and core parameters observed in JT-60U. For a steep pedestal pressure gradient, high δ and high β_p are required. The steep grad-p enhances pedestal pressure. The high pedestal pressure allows a high pedestal temperature at a high pedestal density. The high pedestal temperature widens the pedestal width. The wide pedestal width enhances the pedestal pressure and the pedestal temperature. High pedestal temperature improves the core confinement in the standard ELMy H-mode as observed in the high density ELMy H-mode and in the Ar puff experiments [1].

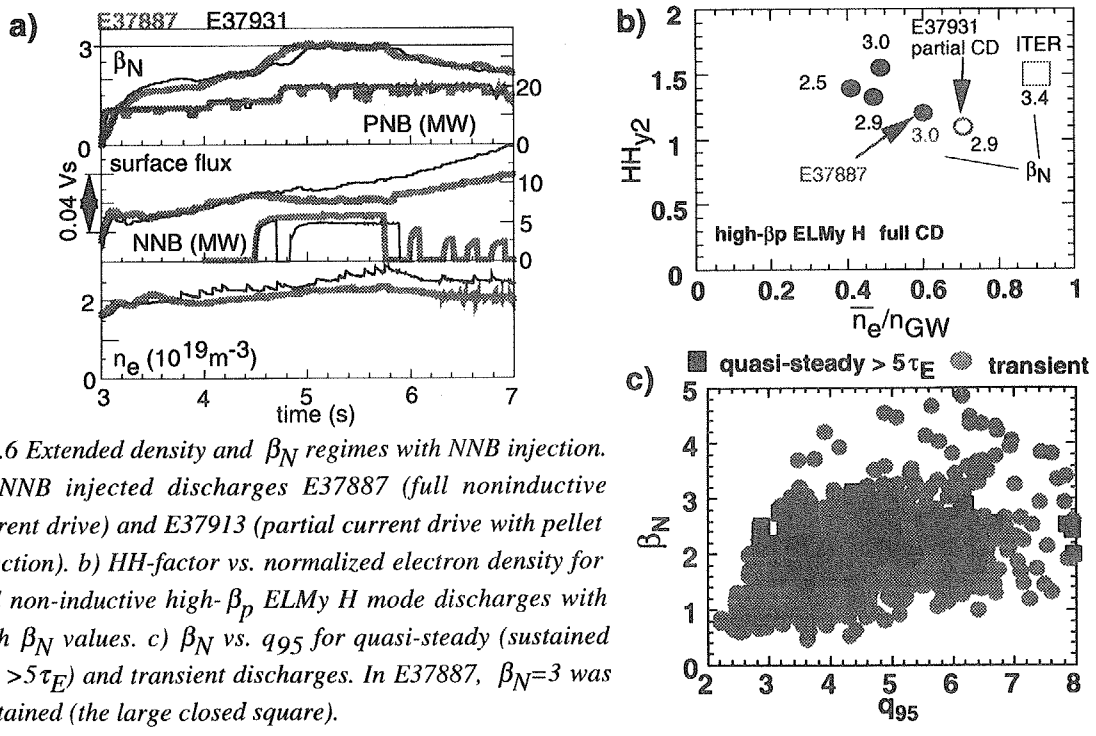

Fig.6 Extended density and β_N regimes with NNB injection. a) NNB injected discharges E37887 (full noninductive current drive) and E37913 (partial current drive with pellet injection). b) HH-factor vs. normalized electron density for full non-inductive high-β_p ELMy H mode discharges with high β_N values. c) β_N vs. q_{95} for quasi-steady (sustained for >5τ_E) and transient discharges. In E37887, β_N=3 was sustained (the large closed square).

Fig.7 Extended period of high β_N at a low q_{95}~3.4 (high β_p ELMy H-mode at 1MA, 2.1T and δ~0.41).

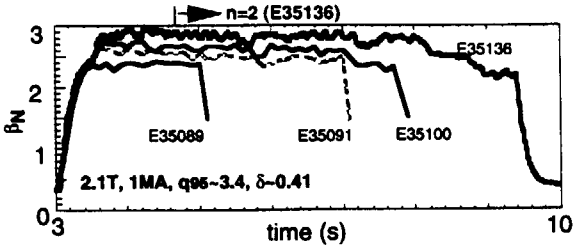

2.2.2. Enhanced β_N and high integrated performance with grassy ELMs

Towards extension of the integrated performance, JT-60U has been increasing sustainable density under full noninductive current drive. At δ=0.43, I_p=1MA, B_t=3.6T and q_{95}=4.5, we have demonstrated full noninductive current drive by NNB injection together with β_N=3.0, HH_{y2}=1.2 and at n_e/n_{GW}~0.6 (E37887, see bold lines in Fig.6 (a)). Figure 6 (b) shows the HH_{y2} factor versus the Greenwald parameter together with β_N values. Figure 6 (c) shows β_N vs. q_{95} for quasi-steady (sustained for $>5\tau_E$) and transient discharges. In E37887, β_N=3 was sustained (the large closed square). In the quasi steady discharges, the sustainable β_N is limited by the neoclassical tearing modes. It has been demonstrated that reduction of the pressure gradient at the low-n resonant surface improves the sustainable β_N as discussed in Sec.2.1. In JT-60U, the sustainable duration of high β_N values has been also successfully extended. As shown in Fig. 7 β_N=2.8- 2.9 was sustained for 4sec at a high triangularity δ=0.41. The sustainable duration has reached the hardware limitations; excitation time limit of the poloidal field coils for high δ shaping. At higher values of δ =0.5 and q_{95}=6.9 (1MA/3.6T), we have also demonstrated full noninductive current drive with grassy ELMs (Fig.8). In this case, high confinement performance HH_{y2}=1.2 was achieved at n_e/n_{GW}~0.6. For Grassy ELMs, the peak heat load onto the divertor plates is 1/4 ~ 1/5 of that for the Giant ELMs.

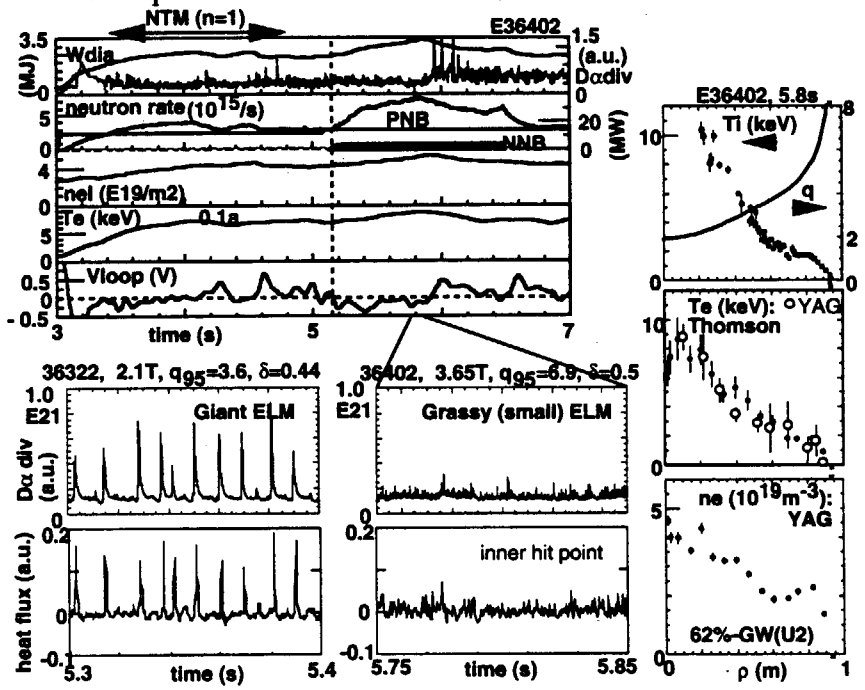

Fig.8 Evolution and profiles for the grassy ELMy full non-inductive discharge E36402 (3.6T, 1MA, δ=0.50, q_{95}=6.9). Particle and heat flux on the divertor plates for the Giant ELMy discharge E36332 are shown for comparison.

REFERENCES

[1] Y. Kamada and the JT-60 Team, 18th IAEA Int. Conf. Fusion Energy, 2000, Sorrento, IAEA-CN-77/OV1/1, Nucl. Fusion **41**, 1311 (2001).

[2] Y. Kamada, et al.,Plasma Phys. Control. Fusion **41**, 1371 (1999)

[3] Y. Kamada, et al., Plasma Phys. Control. Fusion **42**, A247 (2000)

2.3 Non-inductive sustainment of high confinement reversed shear plasma at high normalized density regime [4]

S. Ide, M. Seki, T. Fujita, T. Suzuki, T. Hatae, O. Naito, Y. Kamada and the JT-60 team

On the ITER steady state operational phase, a target plasma is expected to have a high confinement feature with high normalized pressure, full non-inductive current drive with high bootstrap current fraction, high normalized density at low safety factor regime. One example is; confinement enhancement factor to H-mode; $HH_{98(y,2)} \sim 1.5$, $\beta_N \sim 2.7$ - 3, $f_{BS} \sim$ 54%, electron density normalized to Greenwald density; $f_{GW} \sim 0.83$ and $q_{95} \sim 4.1$. Toward the realization of ITER steady state operation, it is important to demonstrate such a high performance plasma in an existing tokamak. A reversed magnetic shear (RS) plasma is expected to be one of the most convincing candidates for the ITER steady state operation. One of the most important key issues in RS research towards steady state operation is full current drive with a proper current profile. On JT-60U, this has been explored by using non-inductive current drive by lower hybrid wave (LHCD)[1-3]. Assessing high performance with parameters which are relevant to the ITER steady state operation, as shown above, has been aimed at, and recently such a plasma is demonstrated by utilizing LHCD and negative ion source based NBI (N-NBI).

The experiment was carried out in a deuterium plasma, $I_p = 0.9$ MA, $B_{t0} = 2.5$ T and q_{95} ~ 6.9. The target plasma was initially produced with P-NBI to increase stored energy high enough, then at the current flat top N-NBI ($P_{inj} \sim 2.4$ MW) and LHCD ($P_{inj} \sim 4$ MW with duty 90% on-off power modulation) were injected, $P_{PNB,\,inj} \sim 6.5$ MW. With the injection of LHCD, expansion of ITB was observed and stored energy was increased accordingly. Around the maximum performance, $HH_{98(y,2)} \sim 1.4$, $\beta_N \sim 2.2$, $f_{BS} \sim 61\%$, $f_{GW} \sim 0.80$ were simultaneously obtained.

The role of LHCD on modification of the ITB location was investigated in a similar discharge but without N-NB. Modification of the current profile during LHCD was confirmed. The location of the ITB was found to move in accordance with the movement of the location of q minimum.

Reference

[1] S. Ide et. al., Plasma Phys. Controlled Fusion, **38**, 1645 (1996).

[2] S. Ide et. al., Proc. of the 16th IAEA Fus. Energy Conf. Montreal, Vol. **3**, 253 (1997).

[3] S. Ide et. al., Nucl. Fusion, **40**, 445 (2000).

[4] S. Ide et. al., J. of Plasma Fusion Res. SERIES, **4**, 99 (2001).

2.4 Extension to low q regime of high confinement reversed shear plasmas [1]

T. Fujita, Y. Kamada, S. Ide, S. Takeji, Y. Sakamoto, A. Isayama,
T. Suzuki, T. Oikawa, T. Fukuda, the JT-60 Team

High confinement of HH_{98y2} ~ 2.2 was sustained for 2.7 s ($6\tau_E$) in an ELMy H-mode reversed shear plasma with high bootstrap current fraction of ~80% maintaining large radius of q_{min} (ρ_{qmin}) and that of ITB [2]. However, low I_p (0.8 MA) and high q (q_{95} ~ 9) operation was required to sustain large ρ_{qmin} with available power (2 MW) of co-tangential off-axis beam and with attainable beta (β_N ~ 2). Though stationary sustainment of the q profile is not expected in a lower q regime at present, q values (q_{min} and/or q_{95}) are supposed to affect the MHD stability significantly in RS plasmas and hence lower q operation was attempted to address this issue.

In a higher current regime (3.7T, 1.35 MA, q_{95} ~ 5), H_{89P} ~2 (HH_{98y2} ~1.2) and β_N ~1.6 were sustained for 3 s though the q_{min} continued to decrease gradually. The q_{min} passed through q = 3 successfully with β_N ~ 1.5 and was located between q = 2 and q = 3 for the sustainment period, which was in contrast to q_{min}>3 in the discharge described in the experiments in a high q regime (q_{95} ~ 9). The discharge entered a higher confinement state during the stored energy feedback control and H_{89P} ~2.7 (HH_{98y2} ~1.5), β_N ~1.8, W_{dia} ~ 3.9 MJ, $n_e(0)$ ~ 5×10^{19} m^{-3} and $T_i(0)$ ~ 12 keV were obtained. However, the confinement returned to the previous level again and hence the duration of this high confinement was ~0.5 s (~τ_E). In a lower toroidal field regime (2.2T, 0.8MA, q_{95} ~ 5.6), β_N ~2 was sustained for 1.6 s (~5 τ_E) but the duration of high confinement (HH_{98y2} ~ 1.6) phase was limited to ~0.4 s (~$1.2\tau_E$), which was also due to the abrupt confinement degradation. This type of confinement degradation was often observed and may be related to the change radial electric field shear [3].

As a result, high beta (β_N ~ 2) was sustained for longer than $5\tau_E$ in a low q regime (q_{min} ~ 2.5, q_{95} ~ 5.5) while high confinement (HH_{y2} >~ 1.5) was sustained only for ~τ_E. Long sustainment of HH_{98y2} >~ 1.5 in a low q regime has been prevented by the confinement degradation phenomena that were encountered during a high confinement phase. The mechanism of this confinement degradation will be investigated to extend the high confinement in a low q regime.

References

[1] Fujita, T., et al., Nucl. Fusion **42**, 180 (2002).
[2] Fujita, T., et al., Phys. Rev. Lett. **87**, 085001 (2001).
[3] Sakamoto, Y., et al., Nucl. Fusion **41**, 865 (2001).

2.5 Weak magnetic shear plasma

T. Fujita, Y. Kamada, S. Ide, S. Takeji

1. Introduction

In JT-60U, two approaches for advanced operation with internal transport barriers (ITBs) have been explored; the high β_p mode [1] and the reversed shear (RS) plasma [2]. The RS plasma is characterized by a very high H-factor (H_{89}~3), but achievable β_N is moderate (β_N <~ 2-2.5) except in wall stabilized cases [3] and steady-operation is not easy because the current profile tends to change according to the penetration of inductive current. The impurity accumulation and confinement of α particles may be problems in a reactor. The high β_p mode, which has typically a weak positive shear, is characterized by high stability (high β_N) sustained for a long duration [4], but the H-factor is lower than RS. The weak reversed shear configuration is considered promising for steady state advanced operation, but high confinement with a weak reversed shear has not been routinely obtained in JT-60U. Here, we scan magnetic shear between a weak positive and a strong negative shear and see if an optimum point exists from the viewpoints of stability and confinement. If a quasi-steady high β_N & high H-factor plasma with a weak negative (or positive) shear in a central region is developed, this q profile will be kept stationarily or at least longer than RS by the bootstrap current.

2. Magnetic shear scan and global performance

Our first target was to establish a 1 MA weak shear plasma with high q_{95}. High q_{95} was employed to enhance the bootstrap current fraction. Typical parameters were as follows; working gas was deuterium, plasma current (I_p) was 1 MA, toroidal field (B_t) was 3.65-3.81 T (1 shot with 2.68 T), q_{95} ~6.5 (4.5 for 2.68 T), plasma volume ~58 m^3, triangularity at the separatrix ~0.45, target electron density ~1.5×10^{19} m^{-3} (several shots with 0.4-$1.1\times10^{19}m^{-3}$), and main heating power was 14 MW NB (6.5 units). All discharges entered H-mode with type I ELMs during the main heating.

The target safety factor (q) profile was scanned by changing preheating power, I_p ramp rate and the time of main heating. Waveforms and profiles of typical discharges with weak-positive shear (E37765), nearly-zero-shear (E37748) and reversed-shear (E37751) are shown in Figs. 1 and 2. In these three discharges, the waveform of plasma current was the same as shown in Fig. 1 (a). In E37765 (weak positive shear), the main heating started at t = 5.9 s (0.7 s into the current flattop) and preheating of 1 MW (half unit) started 0.9 s before the main heating. In E37751 (reversed shear), the main heating started 0.4 s earlier and the preheating power was 3 MW (1.5 units). In E37748, the time of main heating and preprogrammed power and duration of preheating were the same as those in E37751, but the current penetration was faster because of frequent break down of NB unit for preheating and lower main heating power. The stored energy saturated in E37765 as shown in Fig. 1 (b), while collapses were observed in the other two discharges as shown in Figs. 1 (c) and (d). In Fig. 2, radial profiles

of ion temperature (T_i), q and magnetic shear (s = (ρ/q)dq/dρ) in three discharges are shown (ρ is the normalized minor radius). In E37765, q is a monotonically increasing function of ρ with q(0) ~2. The ITB foot is located at ρ ~ 0.55-0.6 where s ~1. In E37748, q was nearly flat within ρ ~0.55-0.6 and the ITB foot was located at ρ ~0.6-0.65. In E37751, a reversed shear was formed and q_{min} was located at ρ ~0.5-0.55 and the ITB foot was at ρ ~0.55-0.6. The gradient of T_i in the ITB was enhanced as the magnetic shear was changed from weak positive to negative. The shape of profile was also changed from a 'parabolic type' ITB to a 'box type' ITB.

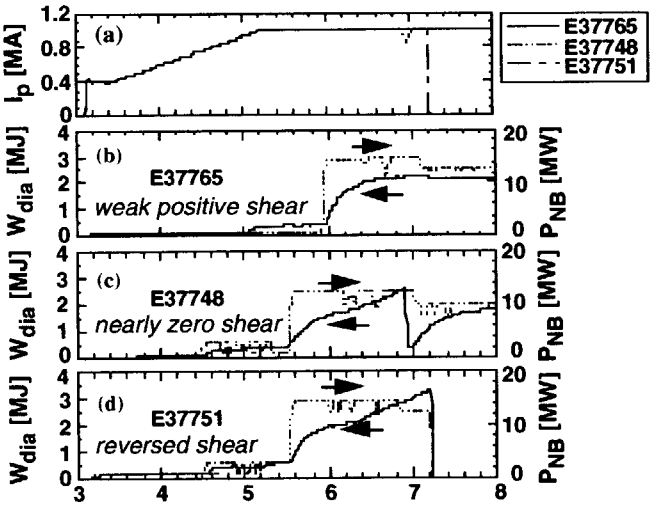

Fig. 1. Waveforms in three discharges for magnetic shear scan. (a) Plasma current for three discharges. (b) Plasma stored energy and NBI power in E37765. (c) Those in E37748. (d) Those in E37751.

The H-factor was H_{89} ~1.8 in E37765, H_{89} ~2.2 in E37748 and H_{89} ~2.9 in E37751. The confinement was enhanced as the shear became more negative or the ITB became steeper. In Fig. 3, H_{89} and β_N are plotted against average magnetic shear evaluated in ρ = 0.3-0.6. The magnetic shear was scanned from s = −0.7 to 0.3. In Fig. 3, data from a typical high β_p H-mode plasma with I_p = 1 MA and B_t = 3.6 T, where no preheating was applied, are also plotted. The magnetic shear scanned in this experiment covers the typical high β_p H-mode

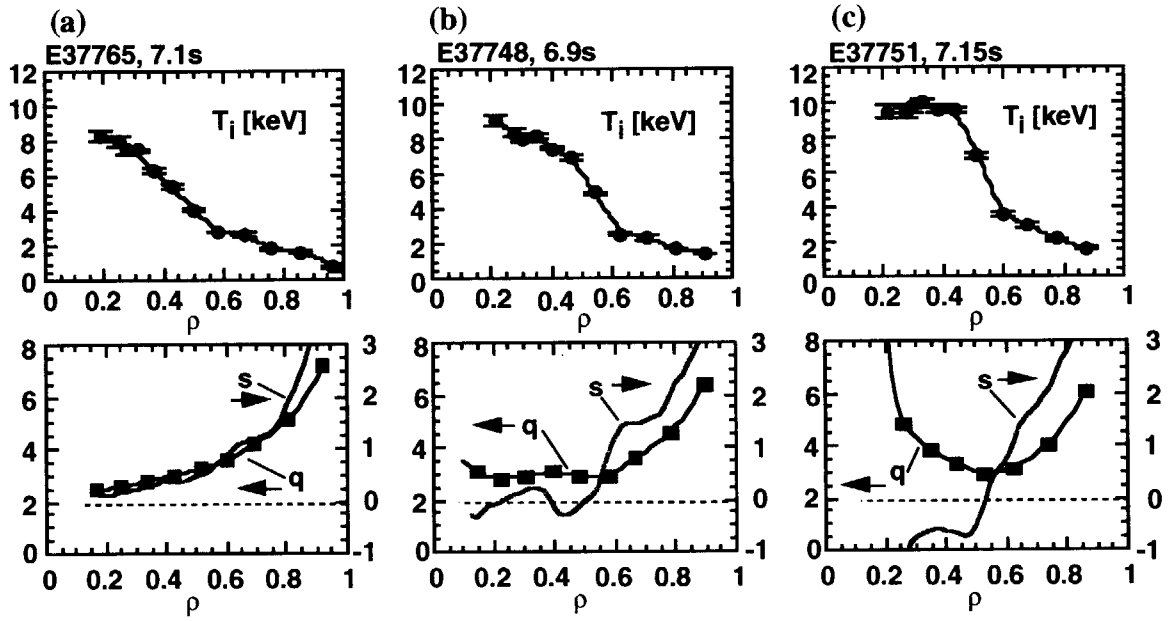

Fig. 2. Ion temperature profile (top) and q and s profiles (bottom) in (a) weak positive shear, (b) nearly zero shear, and (c) reversed shear plasmas.

regime and obtained H_{89} and β_N in that regime are also close to the typical values in high β_p H-mode of the same plasma current and the toroidal field. Figure 3 (a) indicates that the confinement was enhanced as the magnetic shear was reduced.

The β_N at the collapses (crosses in Fig. 3 (b)) seems to increase as the magnetic shear was reduced, but it should be noted that the heating power was almost fixed in these discharges. As the shear was reduced β_N was enhanced because of confinement improvement. Hence, the tendency shown in Fig. 3 (b) does not necessarily imply the improvement of stability in the negative shear if the conditions of collapse depend strongly on q profiles, the value of q_{min} for instance, rather than β_N. However, it is true that the collapses were encountered at relatively low beta (β_N ~1.5-2) in a nearly zero shear regime and the improvement of stability was not obtained in this region compared to the reversed shear region. The stability remains a problem in the nearly zero shear plasma as well as in the reversed shear plasma.

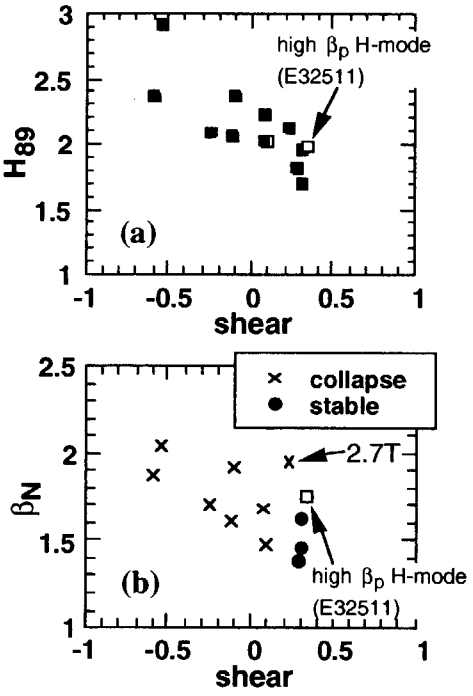

Fig. 3. (a) H factor (H_{89}) and (b) normalized beta (β_N) as a function of magnetic shear averaged in ρ = 0.3-0.6. In (b), crosses denote β_N at a collapse while solid circle without collapses. The toroidal field was 3.65 -3.81 T except for one shot. Open rectangles denote the data of a typical high β_p H-mode plasma.

3. Collapses in nearly zero shear plasmas

An example of collapses in a nearly zero shear plasma is shown in Fig. 4. Here, two mini collapses at t = 6.81 s and 7.05 s followed by a large collapse at t = 7.26 s with β_N ~1.5 were observed. The influence of mini collapses was observed mainly near the ITB as shown in Figs. 4 (b) and (e), which was similar to barrier localized modes (BLMs) [5] previously observed in the high β_p mode. MSE angles (γ_{MSE}) were also changed. This seems to be caused by j(r) not by $E_r(r)$ since both of γ_{MSE} from co-NB and ctr-NB moved in the same direction. The q and j profiles just before and just after a mini collapse are shown in Figs. 4 (f) and (g). A narrow current peak, attributed to the bootstrap current in the ITB, appeared before a collapse and it caused a local negative shear around ρ = 0.6 as shown in Fig. 4 (f). After a mini collapse, the gradient in the ITB was reduced and the local peak in j and the local negative shear disappeared. After that, the ITB grew again, the local negative shear appeared, and a collapse was triggered again.

Fluctuations in electron temperatures, whose growth time was ~1-10 ms, were observed at the ITB before mini collapses. They were observed both at the high-field-side and at the low-field-side with out-of-phase, which denotes m (poloidal mode number) = odd. On the other hand, n (toroidal mode number) =1 was strong in the saddle-coil signal. Hence m/n=3/1 is speculated, but q at the ITB seems larger than 3. Precursors with similar features were

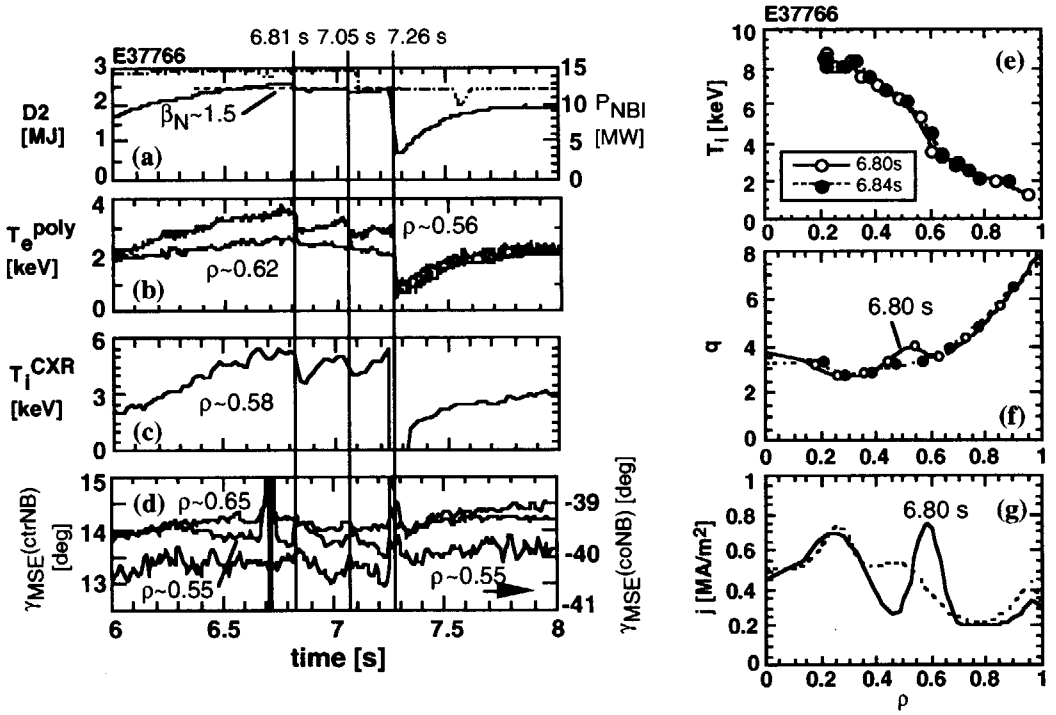

Fig. 4. Successive mini collapses observed in a nearly zero shear plasma. (a)-(d): Waveforms. (a) Stored energy (solid line) and NBI power (dotted line), (b) electron temperature at ρ ~0.56 and ρ ~0.62, (c) ion temperature at ρ ~0.58, and (d) MSE polarization angle viewing a counter beam (ρ ~0.55 and ρ ~0.65) and a co beam (ρ ~0.55). In (d), the upper direction corresponds to a larger poloidal field for both of co and counter beams. (e)-(g): Profiles at t =6.80 s (solid line) and 6.84 s (dotted line). (e) Ion temperature, (f) q, and (g) current density.

observed before major collapses. Collapses seem to become major ones when q(r) was flat near the axis and q_{min}(~q(0)) became integer; 3 (for q_{95} ~6.5) or 2 (for q_{95} ~4.5). It will be necessary to adjust q(0) between integers and to sustain q(0) stationary by raising β_p (bootstrap current fraction) in order to suppress collapses and maintain high confinement.

4. Summary

The magnetic shear was scanned between a weak positive and a strong negative shear or between the typical high β_p mode and the typical RS with the same configuration, I_p and B_t, n_e(target) and P_{NB}. In the zero shear region, confinement higher than that in the high β_p mode was obtained while the stability was not improved from that in the RS mode. A localized reversed shear region can be formed due to the bootstrap current in "weak shear" plasmas, which may be related to collapses. Major collapses seem to be related to q(0) ~integer. It will be necessary to adjust q(r) carefully to keep the stability in the weak shear region.

References

[1] Koide, Y., et al., Phys. Rev. Lett. **72**, 3662 (1994).
[2] Fujita, T., et al., Phys. Rev. Lett. **78**, 2377 (1997).
[3] Takeji, S. et al., 4.2 in this volume.
[4] Kamada, Y., et al., Nucl. Fusion **39**, 1845 (1999).
[5] Takeji, S. et al., Phys. Plasmas **4**, 4283 (1997).

2.6 Reversed shear plasma with low current ramp-up rate

T. Fujita, S. Ide, Y. Kamada, T. Suzuki, T. Oikawa, M. Seki, K. Kajiwara, Y. Ikeda

1. Introduction

In JT-60U, reversed shear plasmas are usually generated under a fast current ramp with NB heating to retard the current penetration into the plasma core [1]. The ramp rate is typically 0.4-0.6 MA/s. In a super-conducting machine, however, a lower ramp rate, 0.2 MA/s for example, is required or at least favorable to reduce AC power loss in super-conducting coils. To address this issue, formation of reversed shear plasma with a low ramp rate of 0.2 MA/s was attempted by using NB, EC and LH.

2. Results

The experiments were done using hydrogen gas and hydrogen beam. We attempted three scenarios to establish a reversed shear plasma with a low ramp rate; (a) high power NB (+EC) heating to raise the electron temperature and to enhance the bootstrap current, (b) EC injection into a low density plasma to raise the electron temperature and (c) LH injection for off-axis current drive and electron heating. Our target was to establish a 1.2 MA reversed shear plasma with a large radius of q_{min}, >~50% of plasma minor radius. The current ramp rate was 0.2 MA/s and the initial plasma current was set 0.4-0.5 MA, which resulted in the duration of current ramp of 3.5-4.0 seconds.

2.1 High power heating

Seven units (~ 8.2 MW) of NB, 3 tangential and 4 on-axis perpendicular, were injected and the line-averaged electron density (n_e-bar) was raised to ~$1\times10^{19}m^{-3}$ at t = 3.6 s (0.5 s after the plasma break down) to establish strong ITBs. EC of 0.4-0.8 MW was also injected to raise the electron temperature. When high power heating was continued, collapses were observed at t = 4.4-4.9 s with β_N ~ 0.9. This seems to be related to q_{min}~5. In the discharge shown in Fig. 1, the NB power was stepped down to 5.9 MW (5 units) after t = 4.2 s, then β_N was reduced to ~0.5 and no collapses were observed. However, the locations of q_{min} and ITB foot moved inward after the power step down and they were located at ρ ~0.45 at t = 4.9 s as shown in Figs. 1 (e) and (f), where ρ is the normalized radius. The normalized radius of q_{min}, ρ_{qmin} continued to move inward after that and it was 0.3 when the plasma current reached 1.1 MA (q_{95} = 5.4) as shown in Fig. 1 (f) (t = 6.98 s). Higher beta and/or higher electron temperature are required to keep a large ρ_{qmin}. Since the available number of shots were limited, the waveform of NB power was not optimized yet and we would be able to increase the power and beta without suffering collapses; for instance high power heating after passing through t = 4.9 s. However, low beta collapses tend to happen in reversed shear plasmas with

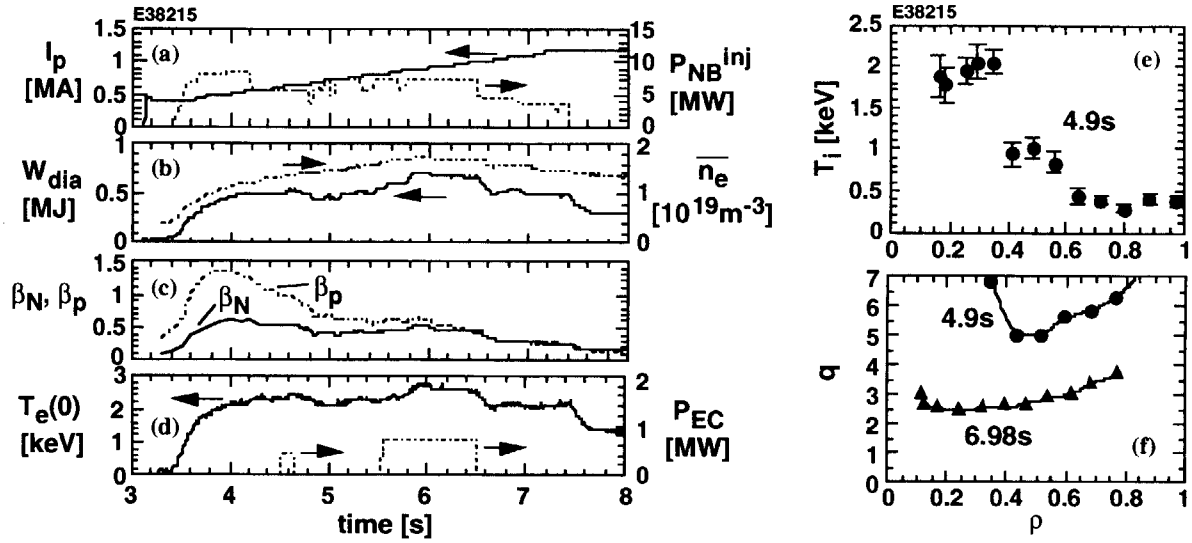

Fig.1. Waveforms (left) and profiles (right) of an RS plasma with high power heating and low I_p ramp rate. (a) Plasma current I_p (solid line) and NB power (dashed line). (b) Plasma stored energy W_{dia} (solid line) and line-averaged electron density (dashed line). (c) Normalized beta β_N (solid line) and poloidal beta β_p (dashed line). (d) Central electron temperature $T_e(0)$ (solid line) and EC power (dashed line). (e) Ion temperature profile at t = 4.9 s. (f) q profiles at t = 4.9 s (circles) and 6.98 s (triangles). The working gas was hydrogen. The toroidal field at the plasma center was 3.6 T.

hydrogen gas and hence β_N would be restricted <~1 and no significant improvements would be expected. This scenario is suitable to attempt in the operation with deuterium gas and deuterium beams where higher β_N can be sustained.

2.2 EC heating

In the discharge shown in Fig. 2, EC (110 GHz, O-mode) of 0.4-0.8 MW was injected for t = 3.4 –4.9 s into the central region of a low density (n_e-bar ~$0.4\times10^{19}m^{-3}$) plasma. The NB power was 3.4 MW (three tangential units). Due to the EC heating, high $T_e(0)$ of ~5 keV was obtained and ρ_{qmin} of 0.45 was sustained at the end of EC pulse (t = 4.9 s) as shown in Fig. 2 (f) in spite of low beta (β_N ~ 0.3). After that, high power NB heating was applied and ρ_{qmin} ~ 0.3-0.4 was obtained at the end of current ramp (1.2 MA, q_{95} = 4.7) though strong shear reversal seems to be restricted in a narrow region of ρ<0.2. The q profile at t = 6.98 s was different from that in the discharge shown in Fig. 1 though q profiles at t = 4.9 s were almost similar in two discharges. This is considered to be due to slightly higher heating power after t = 4.9 s in the discharge shown in Fig. 2.

2.3 LH current drive

The reversed shear configuration was obtained by LH alone during current ramp in JT-60U [2] though this technique has not been employed routinely after that. Recently, reversed shear was obtained in JET by using LH during the current ramp [3]. In the discharge shown in Fig.

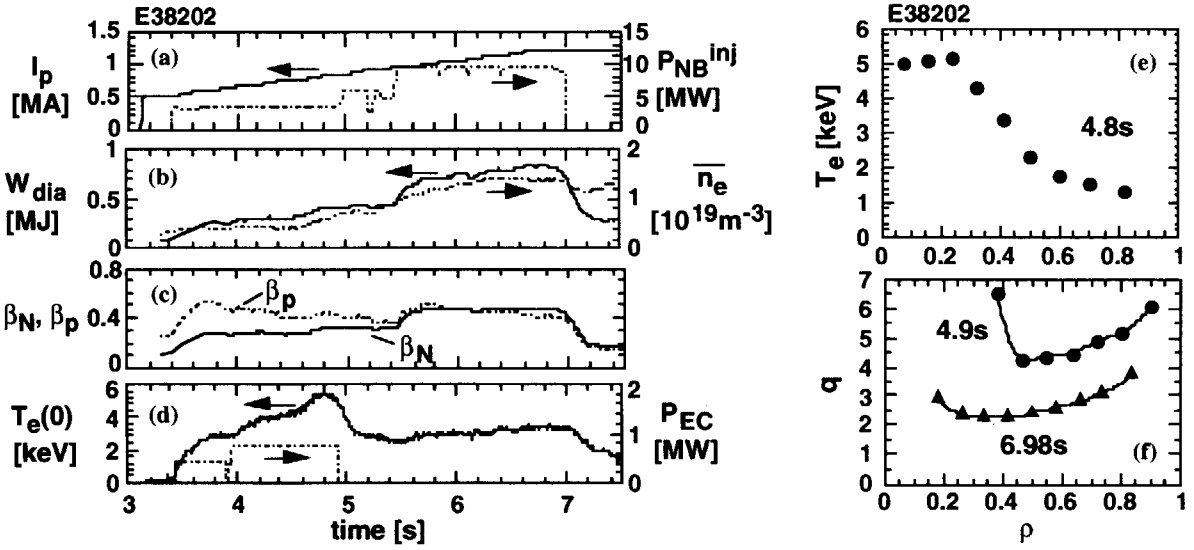

Fig.2. Waveforms (left) and profiles (right) of an RS plasma with EC heating and low I_p ramp rate. (a) Plasma current I_p (solid line) and NB power (dashed line). (b) Plasma stored energy W_{dia} (solid line) and line-averaged electron density (dashed line). (c) Normalized beta β_N (solid line) and poloidal beta β_p (dashed line). (d) Central electron temperature $T_e(0)$ (solid line) and EC power (dashed line). (e) Electron temperature profile at t = 4.8 s. (f) q profiles at t = 4.9 s (circles) and 6.98 s (triangles). The working gas was hydrogen. The toroidal field at the plasma center was 3.6 T.

3, LH of 1-1.8 MW was injected into a low density (n_e-bar ~0.65×10^{19} m^{-3}) plasma for t = 3.5 s to 7.6 s. The refractive index parallel to the magnetic field line ($N_{//}$) of injected LH wave was ~1.6 for a horizontal antenna and ~2.4 for an upper antenna. These values are the same as those used for sustainment of reversed shear plasma [4]. NB was injected only for MSE measurements (half unit, 0.6 MW). The large ρ_{qmin} of 0.6-0.7 (though q was very flat in ρ = 0.55-0.85) was successfully sustained during LH injection. At the end of current ramp, a reversed shear configuration with ρ_{qmin}~0.7 and q_{min}~4 was obtained (Fig. 3 (g)). The ITB foot was located at ρ~0.55 as shown in Figs. 3 (e) and (f). The q_{min} and q_{95} (~ 6.4) were higher than those in discharges shown in Figs. 1 and 2 because of larger plasma volume for LH coupling (~80 m^3 compared to ~60 m^3 in discharges shown in Fig. 1 and 2).

3. Discussion

Figure 4 shows time evolution of ρ_{qmin} in three discharges discussed above. In E38215 (high power heating) and E38202 (EC heating), ρ_{qmin} continued to decrease during I_p ramp. In E38174 (LH current drive), large ρ_{qmin} was sustained as long as LH was injected while it decreased rapidly after t=7.6 s when LH injection was stopped. Therefore it is clear that the LH current drive was effective to sustain large ρ_{qmin}. Though it may be possible to obtain larger ρ_{qmin} in "high power heating" or "EC heating" scenario if higher beta in the former scenario (in deuterium discharges) or higher power and longer EC pulse in the latter scenario is available, the scenario with LH is attractive because ρ_{qmin} of 0.7 was successfully sustained

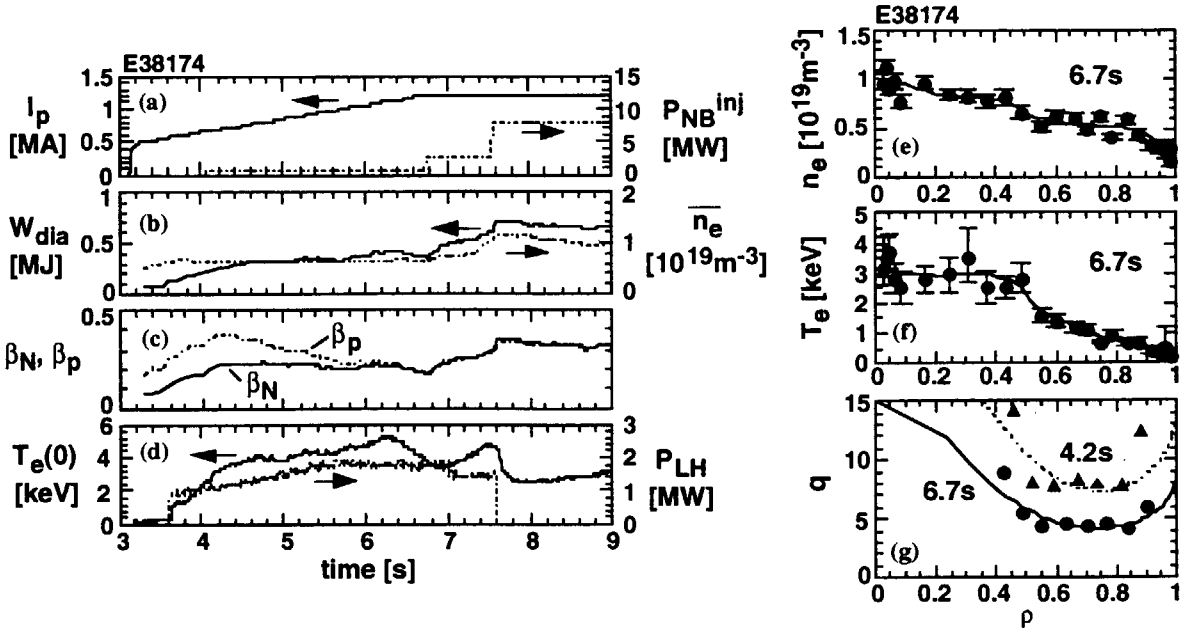

Fig.3. Waveforms (left) and profiles (right) of an RS plasma with LH current drive and low I_p ramp rate. (a) Plasma current I_p (solid line) and NB power (dashed line). (b) Plasma stored energy W_{dia} (solid line) and line-averaged electron density (dashed line). (c) Normalized beta β_N (solid line) and poloidal beta β_p (dashed line). (d) Central electron temperature $T_e(0)$ (solid line) and LH power (dashed line). (e) Electron density profile at t = 6.7 s. (f) Electron temperature profile at t = 6.7 s. (g) q profiles at t = 4.2 s (triangles) and 6.7 s (circles). The working gas was hydrogen. The toroidal field at the plasma center was 3.6 T.

with only 1.8 MW. It is noted, however, that MHD activities were observed when q_{min} passed through 5 in E38174, which caused tentative decrease of ρ_{qmin} at t = 6 s as shown in Fig. 4. In another series of experiments in a low q regime (with a higher I_p ramp rate), collapses with q_{min} = 4 and 3 were observed. On the other hand, in the previous experiments [2], q_{min}<4 was obtained without collapses, which indicates a possibility of stable path to a low q regime. Optimization to establish a scenario to a low q regime without collapses will be done in future.

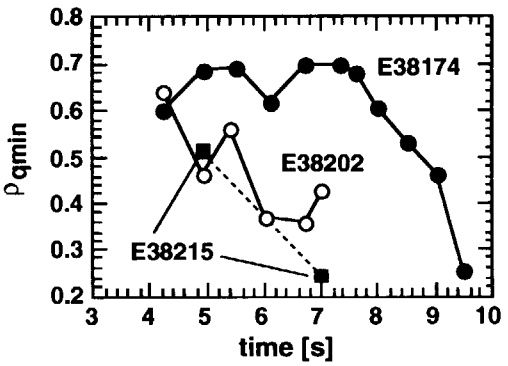

Fig.4. Evolution of normalized radius of q_{min}, ρ_{qmin} in three discharges; E38215 (high power NB heating, closed rectangulars), E38202 (EC heating, open circles) and E38174 (LH current drive, closed circles).

References

[1] Fujita, T., et al., Nucl. Fusion **39**, 1627 (1999).
[2] Ide, S., et al., in Fusion Energy 1996 (Proc. 16th Int. Conf. Montreal, 1996), Vol. 3, IAEA, Vienna (1997) 253.
[3] Challis, C. D., et al., Plasma Phys. Control. Fusion **43**, 861 (2001).
[4] Ide, S., et al., Nucl. Fusion **40**, 445 (2000).

2.7 MA-class N-NB current drive in high electron temperature [1]

T. Oikawa, Y. Kamada, A. Isayama, N. Umeda, M. Kawai and M. Kuriyama

The current profile driven by high energy neutral beam has been experimentally identified and agreed with the theoretical prediction, and current drive efficiency was increased with electron temperature and beam energy [2]. In these former results, however, plasma temperature was relatively low ($T_e(0) \lesssim 5\mathrm{keV}$). To increase reliability of the design for ITER and prospect for the future reactor use, evaluation of N-NB current drive capability in higher electron temperature regime has been conducted.

In order to evaluate N-NB driven current in high electron temperature regime of $T_e(0) \sim 10\mathrm{keV}$, we adopted newly installed ECRF. For precise measurement of N-NB driven current, a low density L mode plasma was employed to reduce the bootstrap current and co- and counter-directional tangential P-NBIs have been balanced to vanish P-NB current drive. Measured N-NB driven current profile has been confirmed to agree with the theoretical prediction by the OFMC code [1]. Figure 1 shows comparison of the measured N-NB driven current I_{NNB}(exp.) with the calculated one I_{NNB}(calc.) An agreement over a wide range from 0.1MA to 1MA has been shown. Experimentally measured N-NB driven current reached up to 1MA at $T_e = 10\mathrm{keV}$. This value is a record of NB current drive in JT-60U. Corresponding current drive efficiency η_{CD} was $1 \times 10^{19}\mathrm{Am}^{-2}\mathrm{W}^{-1}$ as shown in Fig. 2. Confirmation of N-NB current drive capability with high accuracy over a wide range of electron temperature reaching ~10keV and $\eta_{\mathrm{CD}} \sim 1 \times 10^{19}\mathrm{Am}^{-2}\mathrm{W}^{-1}$ shows validity of theoretical prediction and gives more confidence to the design of high energy neutral beam for ITER.

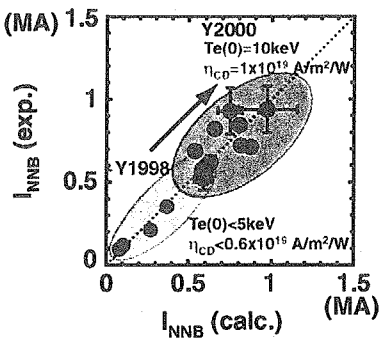

Figure 1: *Comparison of N-NB driven current I_{NNB}(exp.) with I_{NNB}(calc.).*

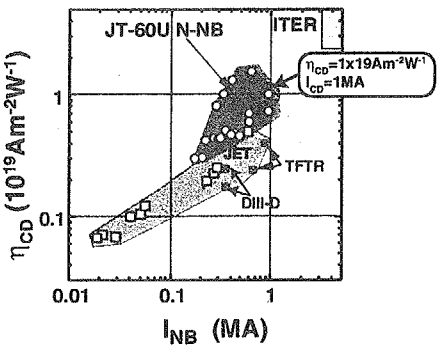

Figure 2: *Current drive efficiency η_{CD} versus driven current I_{NB} for N-NB(330-370keV) and P-NB(85keV).*

References

[1] Oikawa, T., et al., Nucl. Fusion **41**, 1575(2001).

[2] OIKAWA, T., et al., Nucl. Fusion **40**, 435(2000).

2.8 Measurement of EC driven current by motional Stark effect polarimetry [1]

T. Suzuki, S. Ide, T. Oikawa, T. Fujita, A. Isayama, Y. Ikeda, K. Kajiwara, K. Ushigusa

Current profile control is essential for high performance tokamak plasmas. For example, neo-classical tearing mode (NTM) limits achievable poloidal beta. For the suppression of NTM, current drive in a layer (within about 10% of minor radius) thinner than magnetic islands is effective. Theory predicts that current drive by EC waves (ECCD) has remarkable property of local current drive, which enables suppression of NTM. While the suppression of NTM depends on the width of EC driven current layer, experimental validation of theoretical EC driven current profile is underway in the world. In this study, emphasis is put on the experimental measurement of EC driven current.

EC driven current is estimated from internal magnetic field measurement by motional Stark effect (MSE) polarimetry and new magnetic equilibrium reconstruction technique [2]. The new equilibrium reconstruction code (MSE SELENE) enables determination of magnetic flux and toroidal current in the plasma. Time derivative of poloidal magnetic flux leads to inductive electric field in the plasma (Faraday's law). Assuming neo-classical resistivity, the electric field gives current density induced by the EC driven current. Non-inductive current is the difference between the total current and inductive current. Subtracting bootstrap current and beam driven current from the non-inductive current, EC driven current is obtained. The EC driven current density fairly agrees with a theoretical result from ray-tracing method and Fokker-Planck simulation, when EC waves are absorbed around ρ~0.25 (ρ: normalized minor radius). EC driven current density was about 1MA/m^2, and the width of the EC driven current layer was 9% of minor radius.

For current profile control, EC driven current against absorption position of EC waves is investigated. The analyses have detected the change in driven current profile, when absorption positions of EC waves are changed. Insufficient resolution of MSE polarimetry produced error in EC driven current density, for near-axis (ρ~0.1) current drive. Small EC driven current density was the cause of error for the off-axis case (ρ~0.4).

[1] T. Suzuki, et al., Plasma Phys. Control. Fusion, **44** 1 (2002).

[2] T. Fujita, et al., Review of JT-60 Experimental Results in 2000 (this issue), JAERI, Ibaraki, (2002).

2.9 Current profile control by injection of LH with EC

M. Seki and Y. Ikeda

The Lower Hybrid Current Drive (LHCD) is useful not only for sustainment of plasma current in steady state but also for control of plasma current profile aiming at good energy confinement. Especially the reverse magnetic shear plasma supported by LHCD shows improved confinement with internal transport barrier [1]. The current profile control has been successfully performed by changing adjacent phase difference to obtain a proper phase velocity of LH-wave corresponding to the position of driven current. However it will be difficult to change the phase velocity by controlling the phase difference at a higher working frequency as 5-10 GHz in a next generation LHCD antenna. Therefore a new current profile control method is required such as by changing injection angle of EC-wave during LH-wave injection with a fixed phase velocity [2].

Control of current density profile j(r) was performed by combination of LH and EC injection in this campaign. The j(r) estimated from hard x-ray profiles was obtained as a function of magnetic field and injection angle of EC. Experimental conditions are shown in Fig.1. The injection angles of EC were 30 to 51 degrees in the poloidal direction. The EC power was ~700 kW of X-mode at 110 GHz, and the LH power was ~1000 kW at 2 GHz. The plasma current was 1 MA and the toroidal magnetic field was 3 T at the center. The fundamental resonance position of injected EC wave, R_{ce}, was located at the high-field-side edge as indicated in Fig.1. The injected EC wave should couple with LH-driven fast electrons via resonance condition including Doppler effect and relativistic effect at R_{res} in the Fig.1. The comparison of hard x-ray signal profiles during LHCD alone with those during LHCD + EC injection is shown in Fig. 2 for the two injection angles of 51degree (on-axis) and 39 degree (off-axis). As expected, energetic electrons with several hundreds keV in the central part increased in the on-axis case. This is consistent with the fact that the path of injected EC wave intersects with the resonance radius R_{res} at the central part of plasma volume. Results for off-axis case are understood well in the same way.

Thus control of current profile was successfully done by changing the injection angle of EC under the fixed phase velocity of LHCD. In the next generation LHCD system, the current profile control will be performed by changing only the injection angle of EC without the phase control.

References

[1] S. Ide, T. Fujita, T. Suzuki and M. Seki, JAERI Review 2000-035, pp. 15-17, (2001).

[2] M. Seki, O. Naito, T. Kondoh, S. Ide, Y. Ikeda and JT-60 team, JAERI Review 2000-035, pp. 22-23, (2001).

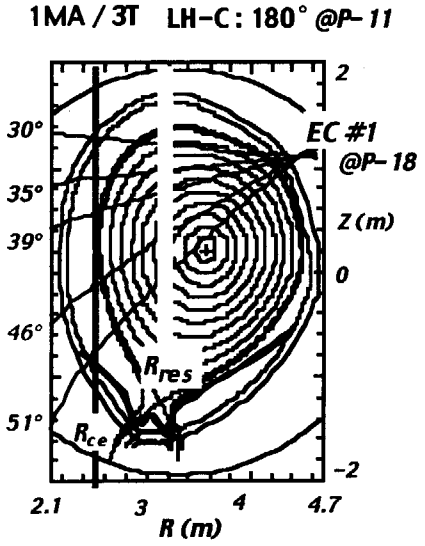

Fig. 1. Experimental conditions.

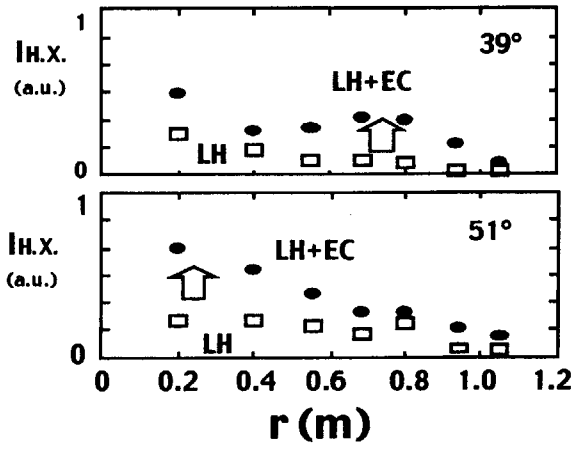

Fig. 2. Hard x-ray profile with 2 injection angles of EC.

2.10 Study on high bootstrap current fraction plasma

X. Gao, A. Isayama, Y. Kamada, K. Ushigusa, T. Fujita, and T. Suzuki

Abstract

A new experimental regime was studied for achieving high fraction of the bootstrap current in the JT-60U hydrogen discharges recently. The high poloidal beta (up to 3.61) plasma was obtained at a very high edge safety factor (I_p = 0.3 MA, B_t = 3.65 T, q_{eff} = 25 ~ 35) region, and the bootstrap current fraction f_{BS} was estimated about 38% ~ 40% by the ACCOME code calculation correspondingly. It is shown that there was no MHD limit to retard the increasing of β_p and f_{BS} parameters in this new regime.

1. Introduction

A bootstrap current is usually induced in a high poloidal beta (β_p) plasma with a steep pressure gradient and results in the production of a hollow profile in the current density. The fraction of the bootstrap current (f_{BS}) is roughly proportional to the normalized beta (β_N) and the edge safety factor (q_{eff}): $f_{BS} \sim \varepsilon^{1/2} \beta_p \sim \varepsilon^{-1/2} \beta_N q_{eff}$, where ε = a/R is the inverse aspect ratio. It is one of key parameters for the steady state tokamak fusion reactor [1]. However, the high f_{BS} plasma within the high β_N and normal edge safety factor q_{eff} (< 7 ~ 9) region is usually limited by the MHD instability due to the β_N (~3) limit in the JT-60U high β experiments [1,2]. The enhancement of f_{BS} is strongly affected by the β_N limit (MHD limit) in the previous experiments [1-4]. It is thought that a higher edge safety factor with a lower β_N may be helpful for increasing the fraction of the bootstrap current without MHD limit in the experiment. Therefore it is a new experimental regime to achieve high f_{BS} plasmas at a very high edge safety factor and moderate β_N (under the β_N limit) condition. Recently the high f_{BS} plasma at a very high edge safety factor (q_{eff} = 25 ~ 35) was studied preliminarily in the JT-60U hydrogen discharges in 2000.

2. Experimental results

The operational parameters in the new experimental region for high β_p plasma are: plasma current I_p = 0.3 MA, toroidal field B_t = 3.65 T, average density = 0.9 ~ 1.1x10^{19} m^{-3}, plasma volume = 57 ~ 58 m^3, the effective safety factor at the edge q_{eff} = 25 ~ 35. Figure 1 is a diagram of normalized beta β_N and the edge safety factor q_{eff} of the experimental new data (I_p = 0.3 MA, and B_t = 3.65 T) in JT-60U. The reference discharges with different current (0.35 MA at 3.65 T) and different toroidal field (B_t = 2.5 T, 2.0 T at 0.3 MA of plasma current) are also plotted in Fig.1. The high β_p plasma with β_N = 1, q_{eff} = 33.2 (shot No.E038355, 8.0 s) is achieved, and the highest value of β_p is 3.61 as shown in Fig.1. Figure 2 is a typical waveform

of the discharge. Plasma current is kept at 0.3 MA for several seconds by the current ramp-down from 0.5 MA. The injected power of P-NBI is 12.5 MW, and the N-NBI power is about 4 ~ 4.5 MW. It shows a clear non-inductive current plasma phase that the loop voltage is less than 0 V in Fig.2. There is no MHD limit to prevent the increasing of β_p and f_{BS} parameters in this new regime. However, increasing of the store energy of plasma (up to 0.4 MJ) is retarded due to the break down of N-NBI power. The average density in this shot is about $1x10^{19}$ m^{-3}, and the plasma confinement is still in the L-mode level [5]. In JT-60U, the published data shows that high β_N plasma always appears within the high H factor and a good confinement [1]. A further increase of β_N and f_{BS} in this regime should be obtained in JT-60U deuterium discharges with improved confinement. Figure 3 is the profiles of the beam driven current $j_{CD}(r)$, the bootstrap current $j_{BS}(r)$, ohmic current $j_{OH}(r)$ and the total plasma current j(r) in the experiment. The total current profile is measured by the MSE diagnostic, and the bootstrap current profile is calculated by the ACCOME code. The fraction of the bootstrap current is about 38 ~ 40% of the total plasma current in Fig.3.

3. Summary

In conclusion, the high f_{BS} plasma at a very high edge safety factor (q_{eff} = 25 ~ 35) was studied preliminarily in the JT-60U hydrogen discharges in 2000 [6]. The high beta (β_N ~ 1, β_p ~ 3.61) plasma was obtained at a very high edge safety factor region, and correspondingly the bootstrap current fraction (f_{BS}) was about 38% ~ 40% by the ACCOME code calculation. It was clearly shown that there was no MHD limit to retard the increasing of β_p and f_{BS} parameters in this new regime. Therefore there is still much room for increasing the β_N before reaching the MHD limit in this experiment. It is expected that the further increasing of β_N and f_{BS} in this regime will be achieved by increasing the density and the NBI power in JT-60U deuterium discharges in the near future.

References

[1] Kamada, Y., et al., Nucl. Fusion, **34**, 1605 (1994).
[2] Neyatani, Y., et al., Plasma Phys. Control. Fusion, **37**, 741 (1995).
[3] Ozeki, T., et al., Nucl. Fusion, **33**, 1025 (1993).
[4] Ishida, S., et al., Phys. Rev. Lett. **68**, 1531 (1992).
[5] Fukuda, T., et al., Nucl. Fusion, **37**, 1199 (1997).
[6] Gao, X., et al., Chinese Phys. Lett. **18**, 931 (2001).

Captions

Fig.1 The diagram of normalized beta β_N and the edge safety factor q_{eff}.

Fig.2 A typical waveform of the high f_{BS} discharge (shot No.E038355).

Fig.3 The profiles of the beam driven current $j_{CD}(r)$, the bootstrap current $j_{BS}(r)$, ohmic current $j_{OH}(r)$ and the total plasma current $j_{Total}(r)$.

Figures

Fig.1

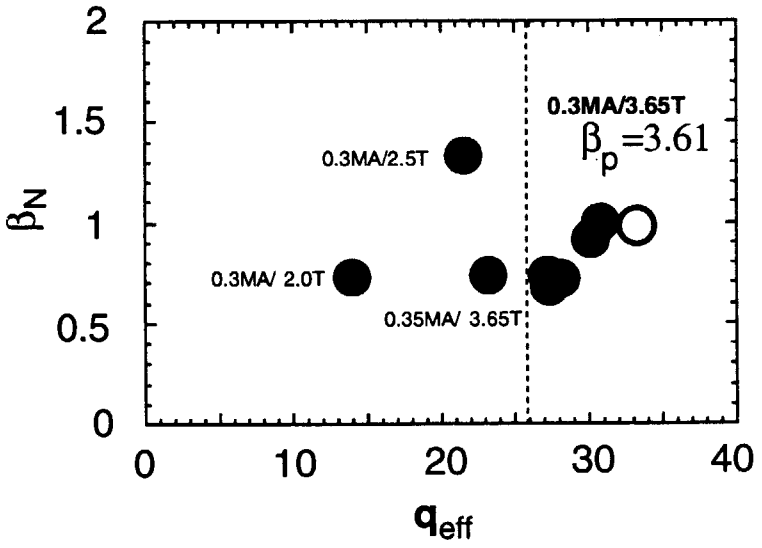

Fig.2

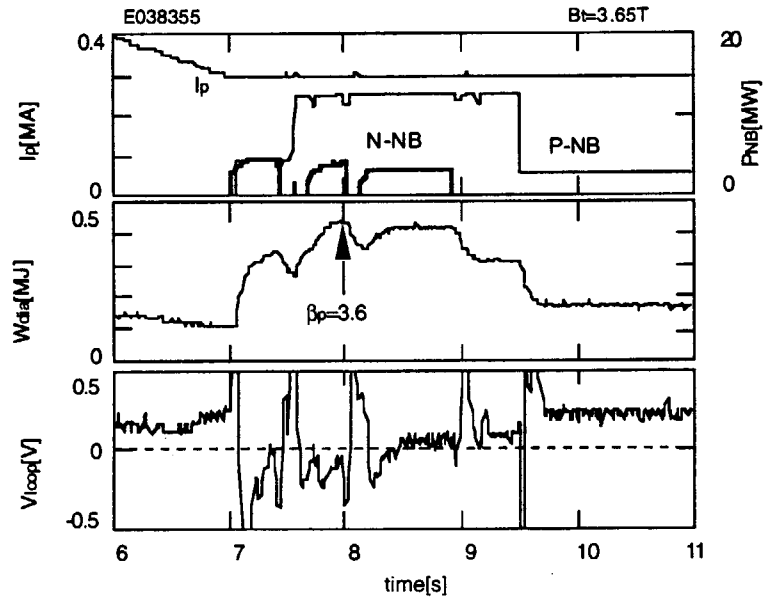

Fig.3

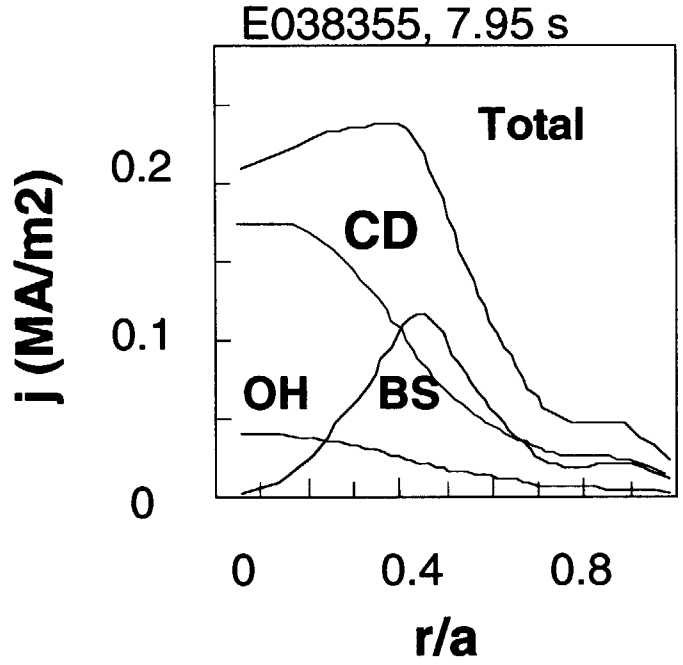

2.11 Current profile measurement during co/counter LHCD

X.Gao, O.Naito, K.Ushigusa, Y.Ikeda, M.Seki, Y.Kamada, and S.Ide

1. Introduction

A change in the plasma internal inductance during LHCD has been observed in many machines [1]. In order to understand the effect of LHCD on profile control, the MSE diagnostics or Li-beam probe diagnostic were used in co-direction LHCD experiments to measure the current profile in many tokamaks. Although the current drive efficiency of the counter-direction current drive by LHW was studied in Ref. [2], the effects of reversed current drive on the current profile were not discussed. Recently, the current profile j(r) in co/counter LHCD with A-unit was studied systematically with MSE measurement at wave phase $\Delta\phi = 30^0$ and $\Delta\phi = 210^0$ in JT-60U. The result is compared with the HX profile and the plasma internal inductance derivative. The direct measurement of the current profile on counter-LHCD experiment is reported for the first time in this paper.

2. Experiments

Figure 1 shows the wave spectrum of LHW at phase $\Delta\phi = 30^0$ and $\Delta\phi = 210^0$ used in the JT-60U LHCD experiment. Figure 2 shows experimental dependence of the peaking factor of HX profile and the derivative of the internal inductance (dl_i/dt) on different LH wave phases. The open circles and squares are old data by the phase scan in JT-60U, and the closed circles and closed squares are new data with j(r) measurement in 2000. The co-direction LHCD data is denoted by circle symbols, and the counter-direction LHCD data is by square symbols in Fig.2.

The main plasma parameters in this experiment are: plasma current I_p = 1.2 MA, toroidal field B_t = 3 T, the plasma volume ~ 80 m^3, the injected LH power = 1.5 MW, the average density ~ 0.8×10^{19} m^{-3}. Figure 3 shows current profiles measured by the MSE diagnostics before and during LHCD for four typical cases in JT-60U. Comparing the current profile (Fig.3) with the derivative of the internal inductance on $\Delta\phi = 30^0$ (Fig.2), a hollow current profile (E038178 in Fig.3) is consistent with a slightly negative value of dl_i/dt (closed circle at $\Delta\phi = 30^0$ in Fig.2) during co-LHCD. There is almost no change in the current profile (E038157 in Fig.3) on counter-LHCD discharge, and it is consistent with $dl_i/dt \sim 0$ (closed square at $\Delta\phi = 30^0$ in Fig.2) during counter-LHCD. However in comparison of the j(r) profile (Fig.3) with the dl_i/dt on $\Delta\phi = 210^0$ (where $210^0 = -150^0$ in Fig.2), the measured j(r) profiles for neither co-LHCD (E038176) nor counter-LHCD (E038158) cases are consistent well with the internal inductance derivative. Here the calculation of the internal inductance was done

using the Shafranov Λ and the poloidal beta by the diamagnetic measurement, $\beta_p^{perpendicular}$, assuming $\beta_p^{parallel} = \beta_p^{perpendicular}$; $l_i = 2 \times (\Lambda + 1 - \beta_p^{perpendicular}) = 2 \times [(\beta_p^{parallel} + l_i/2) - \beta_p^{perpendicular}]$. This should be done carefully during LHCD due to the possible pressure anisotropy and lack of direct measurement on the parallel component of poloidal beta $\beta_p^{parallel}$. The result for the co/counter LHCD at $\Delta\phi = 210^0$ case is not clear yet, because the HX profiles of E038176 and E038158 at $\Delta\phi = 210^0$ (where $210^0 = -150^0$ in Fig.2) are also abnormal compared with the old previous data, suggesting a problem in the LHW system.

3. Summary

Co/counter LHCD with A-unit at wave phases of 30 degrees and 210 degrees were studied with MSE measurement. The HX profile is in a qualitative agreement with the measured current profiles. The behaviors on the derivative of the internal inductance, which is calculated with the assumption of $\beta_p^{parallel} = \beta_p^{perpendicular}$ during LHCD, can not be explained well by the current profile measurement for the co/counter LHCD at $\Delta\phi = 210^0$ case. It must be studied experimentally again in the near future. The direct measurement of the current profile is very important for understanding the effort of LHCD on current profile control.

References

[1] Ushigusa, K., "Lower Hybrid Current Drive in Tokamak Plasmas", JAERI 1339, 1999.
[2] Leuterer, F., et al., Nucl. Fusion, **31**, 2315 (1991).

Captions

Fig.1 The LH wave spectrum of the refractive index of waves $N_{//}$ at $\Delta\phi = 30^0$ and 210^0.

Fig.2 The experimental dependence of HX peaking factor and the derivative of the internal inductance on different wave phases during co-direction (circles) and counter-direction (squares) LHCD.

Fig.3 Current profiles measured by MSE diagnostics during LHCD (dotted line) and the target ohmic plasma (solid line).

Figures

Fig.1

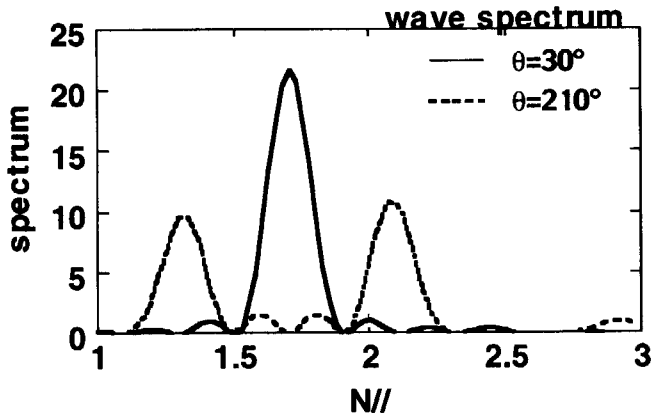

Fig.2

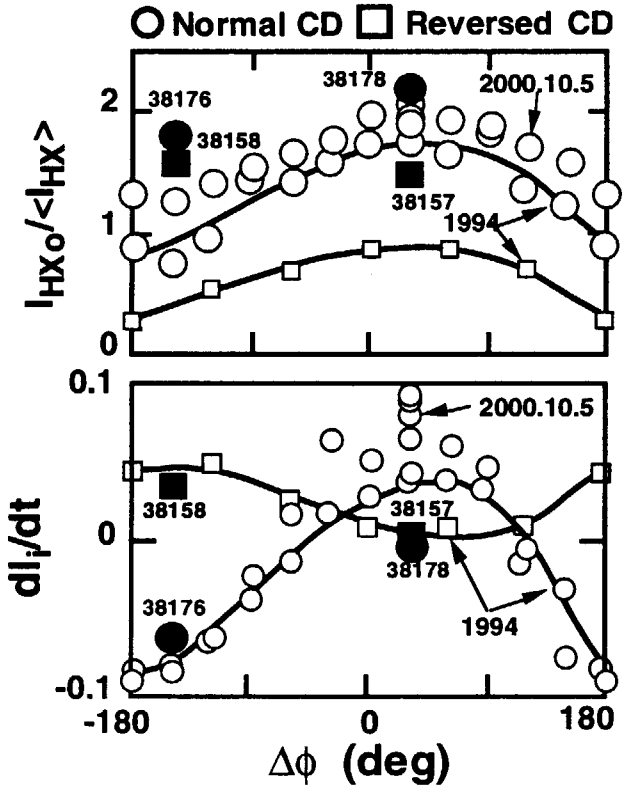

Fig.3

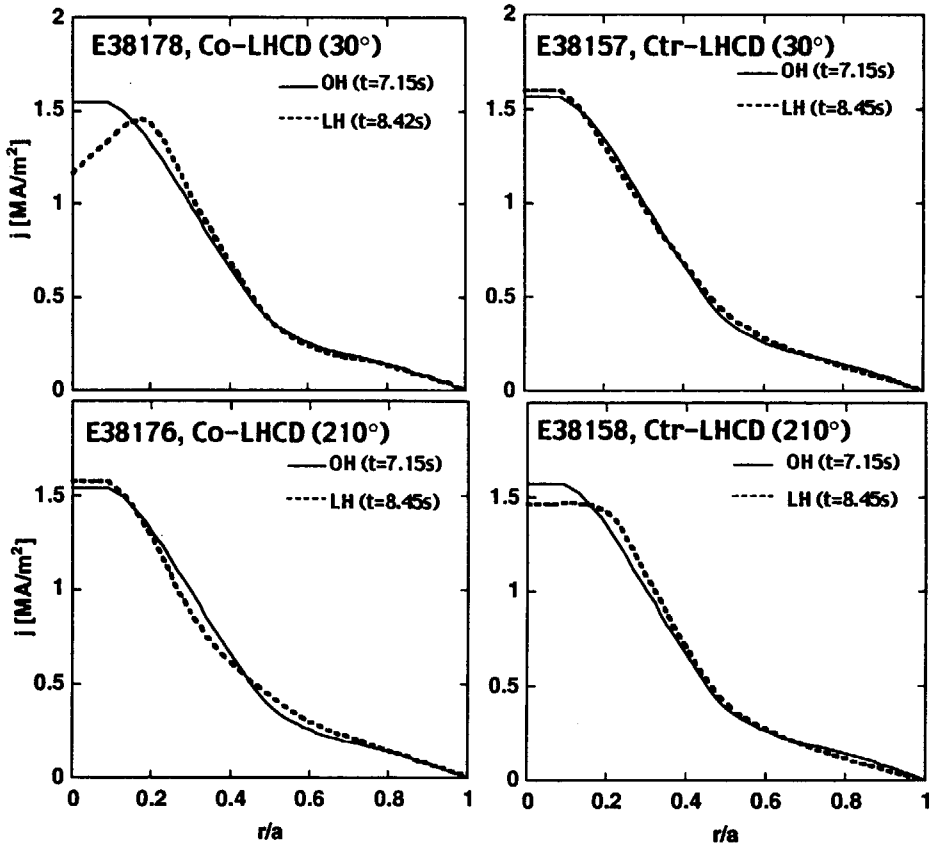
E38178, Co-LHCD (30°)
OH (t=7.15s)
LH (t=8.42s)
E38157, Ctr-LHCD (30°)
OH (t=7.15s)
LH (t=8.45s)
E38176, Co-LHCD (210°)
OH (t=7.15s)
LH (t=8.45s)
E38158, Ctr-LHCD (210°)
OH (t=7.15s)
LH (t=8.45s)
j [MA/m²]
r/a
0
0.5
1
1.5
2
0.2
0.4
0.6
0.8

3. Plasma Confinement and Transport Barrier

3.1 Improved confinement in electron heating/low fueling dominant regime

S. Ide, T. Fujita, Y. Kamada, A. Isayama, T. Suzuki, Y. Sakamoto and the JT-60 team.

1. Introduction

On a research toward steady state operation of a fusion plasma, sustainment of high performance plasma is one of the key issues. To date, various kinds of confinement improved plasmas have been developed and investigated in tokamak devices worldwide. However, in many experiments such high performance plasmas are obtained by positive-ion based neutral beam injection (P-NBI) heating whose beam energy is ranging from several tens of keV to about hundred keV. Therefore, in such plasmas, heating power is initially absorbed by ions, thus the ion temperature (T_i) tends to be higher than the electron temperature (T_e). On the other hand, plasmas in the ITER or future reactors, T_e is higher than T_i since predominant electron heating by fusion α particle. It is theoretically expected that $T_e/T_i > 1$ is a destabilizing factor to the ion temperature gradient (ITG) micro-instability, which is expected to be responsible for the confinement degradation. Therefore, it is important to investigate confinement improvement in such a condition.

On the JT-60U tokamak, various kinds of heating systems are installed and therefore is potentially suitable to investigate improved confinement in electron heating dominant regime. Especially, the electron cyclotron range of frequencies (ECRF) heating directly heats electrons without particle fueling. Power from the negative-ion based NBI (N-NBI) also mainly goes into electrons due to higher acceleration energy, $\geq$ ~350 keV, and fueling is lower than that of P-NBI but not zero. The study had been continued, previously the ITBs in RS plasmas of moderate confinement improvement under $T_e/T_i > 1$ were investigated and found to be robust in such a condition [1]. One of the main objectives in this year was to demonstrate good enough confinement under electron heating both in RS and high β_p plasmas.

2. Experimental result

2.1 High β_p plasma

High β_p mode is one of typical confinement improved modes on JT-60U. The main heating scheme is P-NBI, and T_i is quite high compared to T_e especially in high performance discharges.

In the experiment, the target plasma was chosen as I_p = 1 MA so that the fraction of

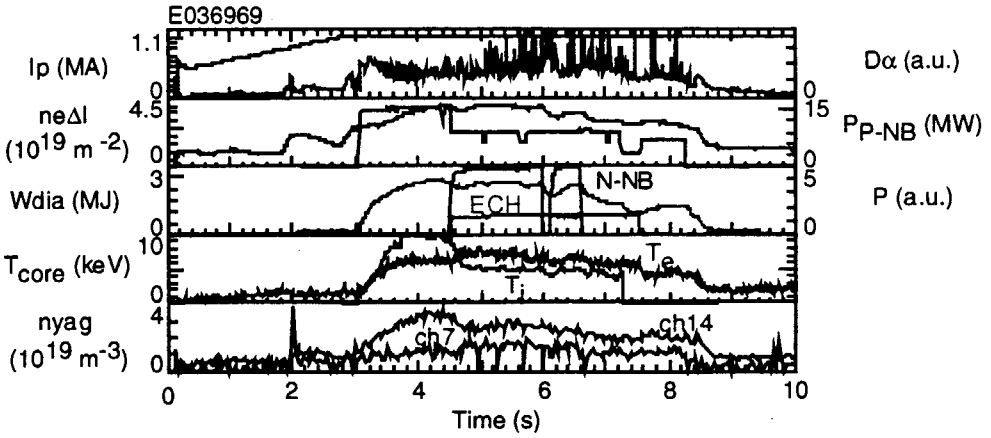

Fig.1 Typical waveform. I_p = 1 MA, B_t = 3.63 T. Deuterium discharge.

available electron heating power can be comparable to or higher than ion heating power, since at this lower plasma current a high β_p mode can be operated relatively with lower input power. The toroidal field at plasma center (B_{t0}) of 3.6 T was chosen so as to set the fundamental electron cyclotron resonance near the plasma center.

In Fig.1 shown are typical waveforms of the discharge. As shown in the figure, high β_p mode target plasma was formed by P-NBI heating as usual. Then P-NB power was stepped down and ECRF and N-NB powers were injected instead. Profiles of T_e, T_i and n_e are shown in Fig.2. In the target, at 4.3 s, T_i is much higher than T_e as an usual high β_p discharge (Fig.2 a). On the other hand, during electron heating dominant phase T_e in the core region increases to reach T_i as shown in Fig.2 b). The density in the core region became lower as shown in Fig.2 c). The confinement enhancement was evaluated both for the target (4.3 s) and the electron heating (5.5 s) phases as H_{89P} = 2.6/$HH_{98(y,2)}$ = 1.1 and H_{89P} = 2.3/$HH_{98(y,2)}$ = 1.0 respectively.

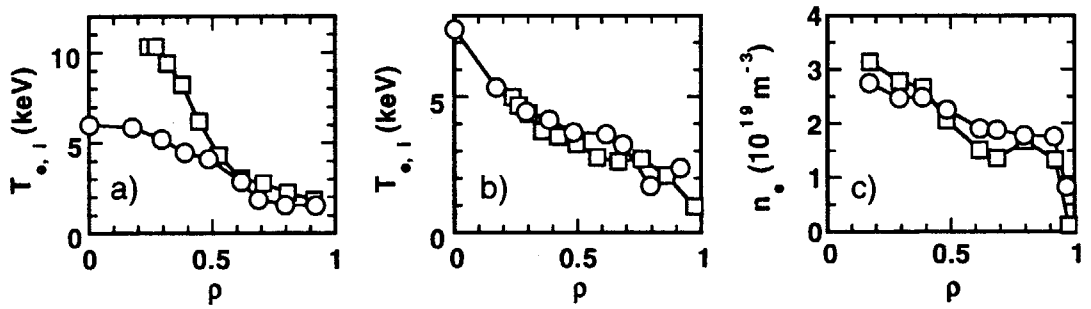

Fig.2 Comparison of the T_e (circles) and T_i (squares) profiles, a); at 4.3 s and b); at 5.5 s. c) Comparison of the density profile at 4.3 s (squares) and 5.5 s (circles).

2.1 RS plasma

In an RS plasma, T_e is relatively close to T_i compared to high β_p mode, but still T_e is lower than T_i in usual discharges with P-NB heating.

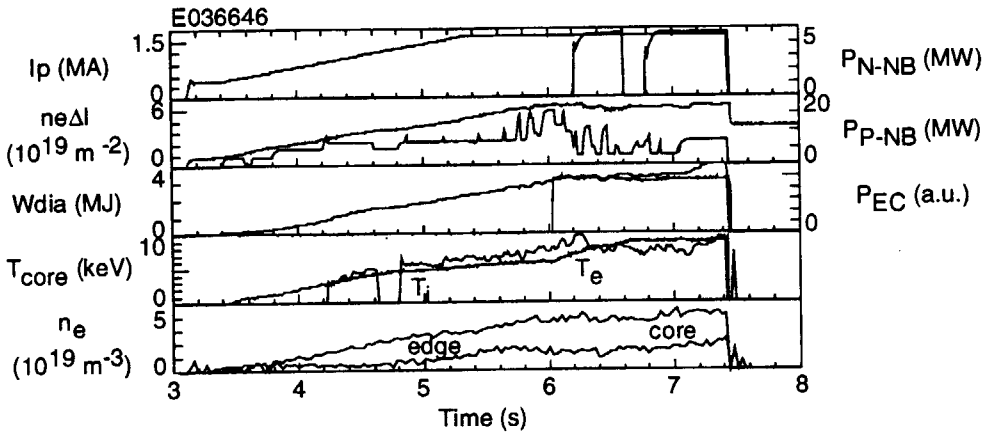

Fig.3 Typical waveform. I_p = 1.35 MA, B_t = 3.7 T. Deuterium discharge.

In the experiment, the target plasma was I_p = 1.35 MA and B_{t0} = 3.7 T for the central ECH. Typical waveforms are shown in Fig.3. Similar to the high β_p mode experiment, P-NB power was stepped down to be replaced by the ECH and N-NB powers. In this discharge, T_i and n_e did not change drastically even when the heating scheme was switched mainly to electron heating and low fueling ones. Profiles of T_e, T_i and n_e are shown in Fig.4. As shown in Fig.4 a), T_i in the core region is higher than T_e at 6 s before ECRF and N-NB injection started. At 7 s, later phase of the electron dominant heating, T_e in the core region exceeded T_i as shown in Fig.4 b). On the other hand, the density profile was almost identical at 6, 7 and 7.4 s as plotted in Fig.4 c).

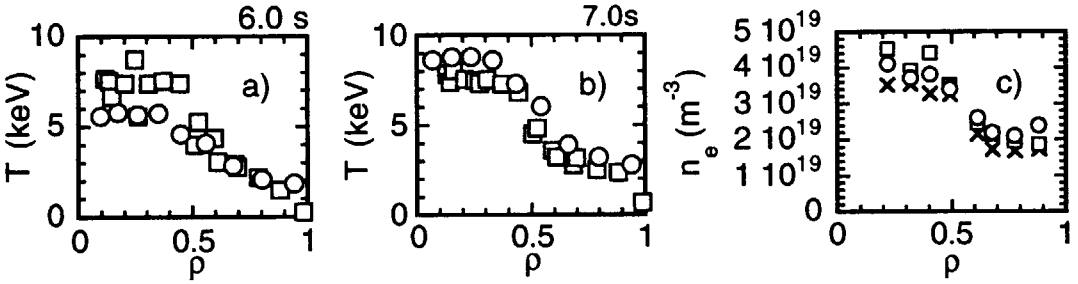

Fig.4 a) The Te (circles: ECE polychrometer, diamonds; YAG Thomson) and Ti (squares) profiles in the target, at 6 s. b) Those during the electron heating phase, 6 s. c) Density profile at 6 s (croses), 7 s (squares) and 7.4 s (circles).

The confinement enhancement was evaluated both for the target (5.6 s) and the electron heating (7.0 s) phases as $H_{89P} = 2.4/HH_{98(y,2)} = 1.3$ and $H_{89P} = 2.9/HH_{98(y,2)} = 1.5$ respectively.

3. Discussion and Summary

Both in the high β_p and RS plasmas, confinement enhancement relative to the L-mode (H_{89P}) was found not to change drastically and to be good enough, during the electron heating dominant phase. In the RS case, T_i and n_e profiles were observed to be almost unchanged. On the other hand, in the high β_p case, gradients in T_i and n_e profiles were reduced. It seems that ITB still remains in both profiles but is quite weak. Pedestal might have increased during the electron heating phase, and contributed to keeping the overall confinement. Careful consideration would be necessary to conclude if confinement improvement remains under electron dominant heating in a high β_p plasma. And further experiments are required

Reference

[1] Ide S. and the JT-60 team, Phys. Plasmas 7, 1927 (2000).

3.2 On ITB formation condition in a reversed shear plasma

S. Ide, T Fukuda, T. Suzuki, Y. Sakamoto, T. Fujita and the JT-60 team

1. Introduction

Formation of internal transport barrier (ITB) is a key issue for confinement improvement and steady state operation with high bootstrap current fraction. Therefore study of conditions required for ITB formation is one of crucial objectives in fusion plasma research both for physics understanding and designing a device based on advanced tokamak operation. For the study, several experiments were carried out in order to investigate which parameter is important for ITB formation in reversed magnetic shear (RS) plasmas. In this report, results of these experiments are presented.

2. Experimental result

2.1 Effect of toroidal rotation on ITB formation

Theories based on ITG mode suppression by ExB shearing suggest that plasma rotation can affect ITB. Therefore it is important to figure out how toroidal torque input affects ITB formation. On this motivation, ITB formation in an RS plasma in which major fraction of the input power was provided by tangential beams was compared between co- and counter-injection cases. The experiments were done at B_{t0} = 3.8 T, the working gas was deuterium. ITB was intended to be formed during I_p ramp-up.

Temporal evolutions of I_p, P_{NB} and T_i at around ITB foot (see Fig.2) are plotted in Fig.1, (a); the counter parallel beam injection case, and (b); the co parallel beam injection case. In the waveform of P_{NB}, shown by hatching is the fractional power by parallel beams. In the counter injection case, separation of T_i evolution between adjacent channels is clearly seen showing evolution of the ITB. With closer look, it is found that the separation started even before 4.1 s when the injected power stepped up to the maximum. On the contrary, ITB was not formed, or at least not clearly visible, before 4.4 s in the co injection case, even though

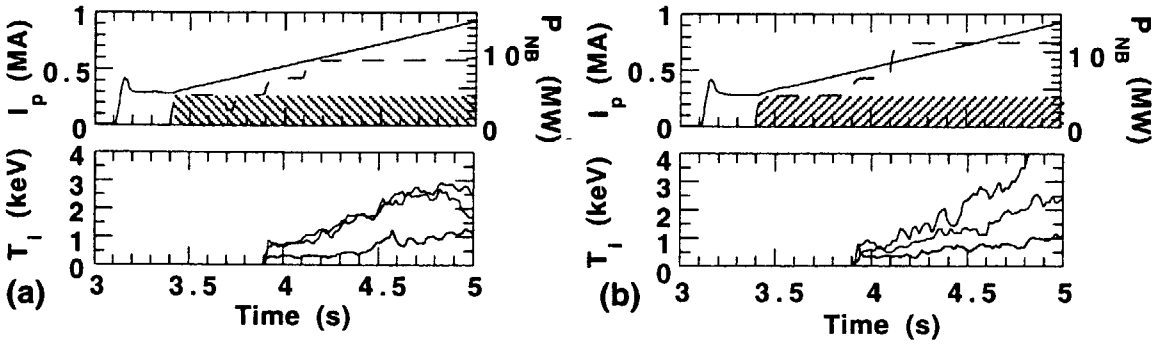

Fig.1 Temporal evolutions of I_p (upper box, solid line), P_{NB} (upper box, dashed line) and T_i (channels. 15, 17 and 18, cf. Fig.2) in the lower box.. (a); the counter parallel beam injection case. (b); the co parallel beam injection case.

the power reached the maximum which is higher than that in the counter injection case.

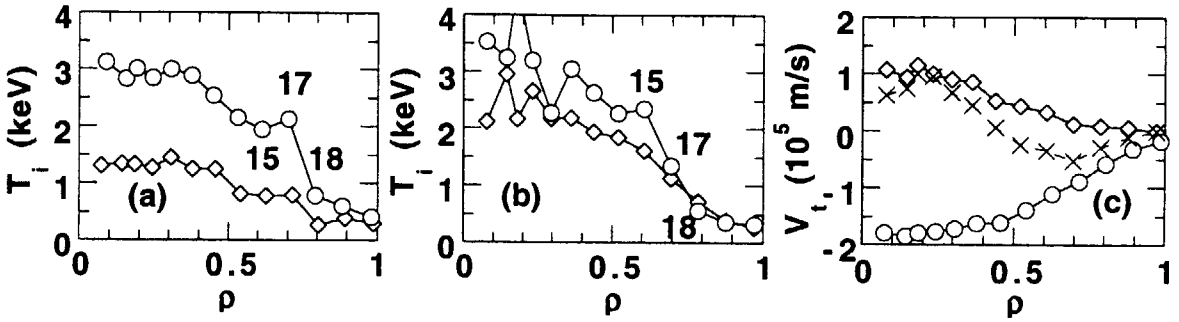

Fig.2 (a) T_i profiles at 4.06 (diamonds) and 4.5 s (circles) in the counter injection case. (b) Those at 4.4 (diamonds) and 4.5 s (circles) in the co injection case. The figures, 15, 17 and 18, are the channel number (cf. Fig.1). (c) V_t profiles at 4.06 s with counter injection (circles), 4.05 (diamonds) and 4.4 s (crosses) with co injection.

Snapshots of the T_i profile are helpful to confirm this. As shown in Fig.2 (a), a steep gradient in T_i is already formed at $\rho \sim 0.8$ at 4.06 s and the gradient evolves to a clearer ITB at the same position. The profile at 4.5 s is shown for a reference, as seen in Fig.1 (a), the ITB grows further up to ~ 4.8 s. On the other hand in the co injection case (Fig.2 (b)), even at 4.4 s the profile looks quite smooth suggesting ITB was not formed yet. And at 4.5 s an ITB seems to start growing at $\rho \sim 0.8$. It should be noted that the location is almost the same as in the counter case. The V_t profile at ~4.05 s is clearly different between the counter (open circles) and co (open diamonds) injection cases as shown in Fig.2 (c). It shold be noted that, other parameters look similar between the discharges. One parameter which is expected to be important but not compared yet is the q profile. Since the main MSE diagnostics is measuring along one of the counter beams, the measurement along a co beam is not well established yet. The q profile at 4.06 s in the counter injection discharge is shown in Fig.3 as a reference. It is found that the ITB is located near q_{min} location. However, it is not clear if the ITB locates in the negative or the positive shear region, since spatial resolution is not enough in both the T_i and the q measurement. The V_t profile at 4.4 s in the co injection case is shown as well in Fig.2 (c). At the outer region the plasma started rotating in the counter direction due to larger ripple loss by larger P_{NB}. Although it looks as if gradient in V_t at the ITB foot is approaching the same value of that at 4.06 s in the counter injection case, dependence in the absolute value of the V_t gradient is not clear.

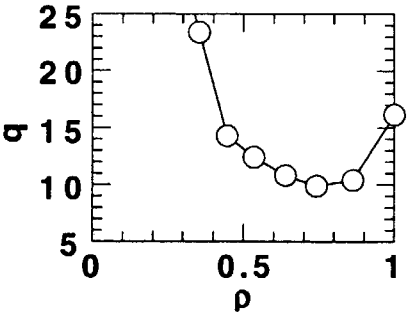

Fig.3 The q profile at 4.06 s in the counter injection case.

2.2 Effect of the plasma current

The second one is to investigate if power necessary to form ITB depends on I_p. I_p is an important factor not only for physics understanding but also from a view point of designing a new machine. Dependence on B_t, one of the other important parameters, had been found to be small already [1]. The experiments were carried out with deuterium discharges. The plasma configuration was chosen so that upper tangential beams passed through near the plasma center.

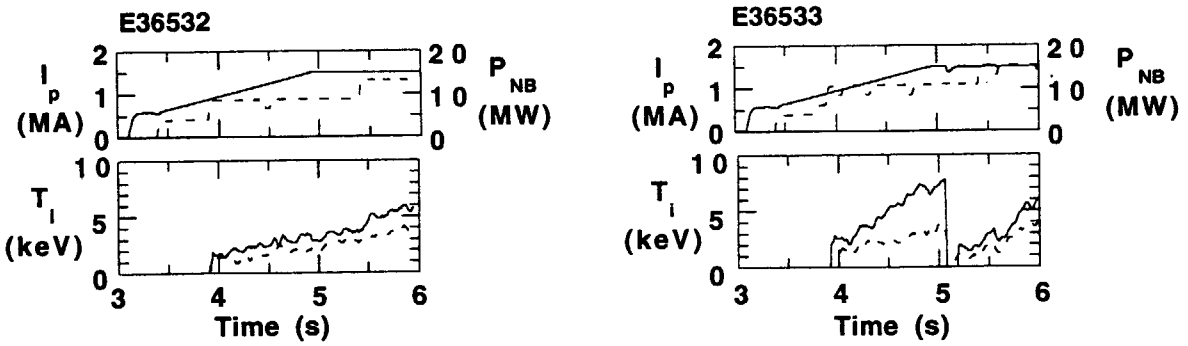

Fig.4 Temporal evolution of I_p, P_{NB} and T_i at the core (solid line) and peripheral (dashed line) region for lower (left) and higher (right) injection discharges..

In discharges with I_{p0} = 0.6 MA and dI_p/dt = 0.6 MA/s, sufficient amount of power was necessary in order to obtain clear ITB. As shown in Fig.4, when about 10.5 MW of NB power was injected T_i in the core region took off, while it did not when injection power was about 8.5 MW. It should be noted that both the co and counter central tangential beams were used so that the input torque was as balanced as possible at least in the central region. And in E36533, co peripheral tangential beam was injected from 3.8 s just for additional power. Absorbed power estimated using the OFMC code is 6.0 MW and 4.7 MW respectively. For comparison, discharges with I_{p0} = 0.3 MA and dI_p/dt = 0.4 MA/s were also tried. The NB power was scanned in these different I_{p0} discharges. In Fig.5 plotted is the net NB power, estimated assuming 70% absorption for parallel beams and 30% for perpendicular beams, against the plasma current at the timing when ITB seems to

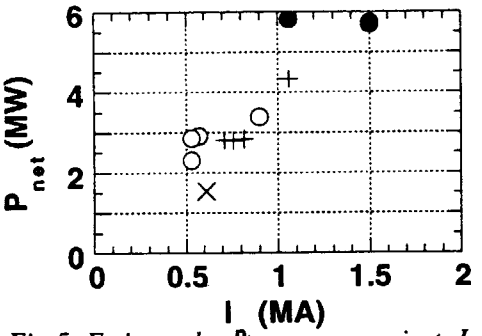

Fig.5 Estimated net power against I_p. Open and closed circles correspond to shots in which ITB was formed. Xs and crosses correspond to no ITB cases.

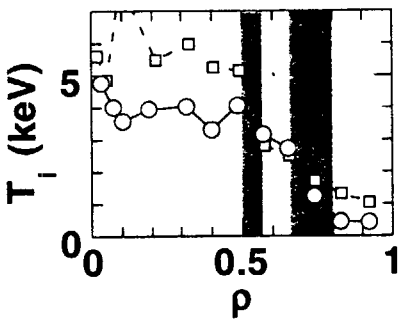

Fig.6 Comparison of Ti profiles for lower (circles) and higher (squares) I_p cases. For better recognition, profiles are taken at 4.5s when ITB had grown. Gray areas indicate ITB region, one that locates outer corresponds to the lower I_p case.

be formed. Also here, both co and counter central beams were used. Open circles correspond to the lower I_{p0} discharges in which ITB is formed and closed circles correspond to the higher I_{p0} discharges, while Xs and crosses correspond to the lower and higher I_{p0} discharges in which ITB was not formed. Crosses at around I_p = 0.7 MA correspond earlier phase of higher I_{p0} discharges when I_p was lower but the power was low as well hence no ITB was observed. It seems that the necessary power is lower for lower I_p. In this kind of experiments, all the parameters but I_p should be as similar as possible. However, location of the ITB is quite different between lower and higher I_p cases as shown in Fig.6. This may be attributed to the difference in the safety factor (q) or magnetic shear (s) profiles. They are shows in Fig.7, and look quite differently.

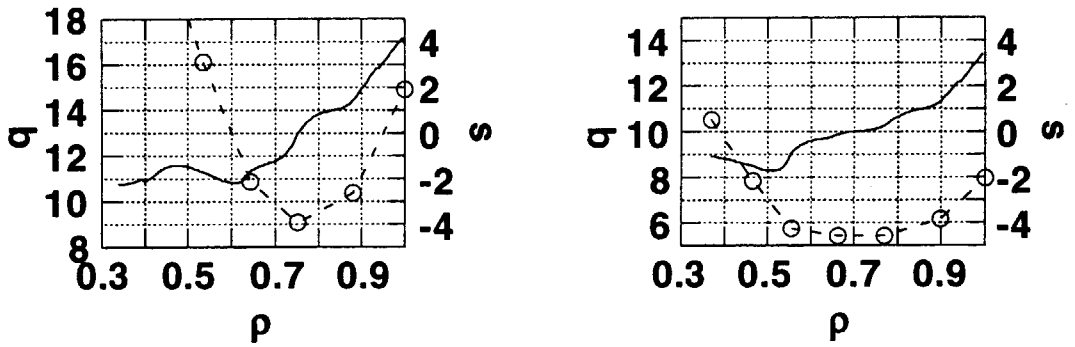

Fig.7 Comparison of q (circles and dashed line) and s (solid line) profiles for lower (left) and higher (right) I_p cases

3. Discussion and Summary

Formation of ITB was examined against I_p and V_t in RS plasmas. On toroidal rotation, the results would suggest that V_t could affect ITB formation. Although other parameters look similar, one concern is left on the q profile. Calculation suggests that absolute value of NB driven current is 1/4 – 1/5 to the total current, therefore the total current profile would not be much different. The same ITB location would support it. More systematic study would help investigate more detailed dependence such as V_t gradient. The local T_e and n_e evolution measurement by YAG-LASER Thomson scattering, which have not been obtained in the campaign, should be obtained for total understanding. The results should be analyzed relating to ExB effect. On the plasma current, the results are more complicated. Since not only I_p but also the current profile differed, thus the ITB position differed between lower and higher I_p cases. Although obtained data would give a clue to local parameter analysis, well optimized discharges would be necessary for future work.

Reference

[1] Ide S. and the JT-60 team, Phys. Plasmas 7, 1927 (2000)

3.3 Active control of internal transport barrier in JT-60U reversed shear plasmas [1]

Y. Sakamoto, H. Shirai, Y. Kamada, T. Fujita, S. Ide, T. Takizuka,
Y. Koide, T. Fukuda, T. Suzuki, T. Oikawa

Several theoretical models for transport barrier formation suggest that the ExB flow shear plays an important role in suppressing the level of the turbulence and reducing the correlation length of the turbulence. Therefore there is a possibility that the ITB can be controlled by the modification of the radial electric field, E_r, profile. Toroidal rotation as well as pressure gradient profiles affect the E_r shear profile because the E_r is coupled with plasma rotation and pressure gradient in the force balance equation. The effect of toroidal rotation has been investigated in JT-60U [2].

The demonstration of the active control of ITB strength by the switch of the toroidal momentum injection direction was successfully performed. The reversed shear plasma with the strong ITB was generated in the standard scenario with balanced injection for JT-60U, which has an L-mode edge. In a quasi-steady state phase after the current flat-top, the directions of toroidal momentum injection was only changed with the same injected NB power from initial balanced injection to co-injection, then to ctr-injection and finally to the balanced injection again. The ion temperature gradient was degraded by co-injection, then recovered by ctr- and balanced injection. The change in E_r shear of outer half region of the ITB layer (near the ITB foot) was important to control the ITB strength of the whole ITB region. This indicates that there is a non-local nature in relations between the E_r shear and the reduction of transport. The behaviors of electron temperature and electron density profiles were similar to ion temperature profile.

The demonstration of the active control of ITB strength by the change of the central heating power was also performed. In this case, ITB was recovered by the increment of the heating power, after the degradation by co-injection. Thus the self-sustainable E_r shear was formed due to the reduction of the diffusivity, and then ITB was sustained with reduced heating power.

[1] Sakamoto, Y., et al., Nucl. Fusion **41**, 865 (2001).
[2] Shirai, H., et al., Plasma Phys. Control. Fusion **42**, A109 (2000).

3.4 Scaling of ITB width in JT-60U reversed shear plasmas [1]

Y. Sakamoto, Y. Kamada, S. Ide, T. Fujita, H. Shirai, T. Takizuka,
Y. Koide, T. Fukuda, T. Suzuki, T. Oikawa

In JT-60U reversed shear plasmas, thermal and particle diffusivities decreased to the level of neoclassical value within the narrow region. Thus the ITBs were formed in ion temperature, T_i, and electron temperature, T_e, and electron density, n_e, profiles. These profiles had steep gradients for the ITB layer and reduced gradients for other regions (except for edge region), and then internal pedestals were formed. The ITB width is one of the characterized parameter for the ITB structure. Therefore the study of ITB width scaling is one of the most important issues for the physics understanding of the ITB formation and sustainment.

The ITB width became narrower with evolution of ITB in the typical high performance discharge, where the plasma current was raised, and then reached values of the ITB width is related to the ion poloidal gyroradius estimated at the ITB center. This may indicate that the lower boundary of the ITB width is related to the ion poloidal gyroradius. In order to examine the parameter dependence of ion poloidal gyroradius, which is proportional to square root of ion temperature and is in inverse proportion to poroidal magnetic field strength, the lower boundary data is extracted. As a result, the ITB width in the lower boundary is in inverse proportion to the poloidal magnetic field at the ITB, for the ion temperature fixed in ~5keV and ~10keV. The ratio of proportional coefficients in 5keV to in 10keV is almost the same to the ratio of square root of ion temperatures. On the other hand, the ITB width is proportional to square root of the ion temperature at the ITB center, for the poloidal magnetic field fixed at ~0.24T. Therefore the ITB width in the lower boundary is proportional to the ion poloidal gyroradius at the ITB center.

A radial electric field and its gradient were formed in the ITB layer, which affects the particle orbit. The effects of the radial electric field and its gradient on the motion of guiding center were numerically investigated by Escape Particle Orbit analysis Code (EPOC). The calculation results indicate the effect of radial electric field is less than 10%.

[1] Sakamoto, Y., et al., Nucl. Fusion **41**, 865 (2001).

3.5 Scaling of stored energy in JT-60U reversed shear plasmas [1]

Y. Sakamoto, T. Takizuka, Y. Kamada, T. Fujita, T. Fukuda, S. Ide, H. Shirai, Y. Koide

Confinement properties of reversed shear plasmas were investigated under the discharge conditions of B_T=4T, $0.03<\delta<0.1$, $1.7<\kappa<2.0$, $3.08\text{m}<R<3.18\text{m}$, $0.5<\rho_{foot}<0.75$, nearly balanced momentum injection, L-mode edge and NB heating. The large ITB radius and L-mode edge plasmas reduced the contribution for the stored energy from outside of ITB. Nearly balanced momentum injection excludes the effect of toroidal torque for the sake of simplicity. The stored energy, W_{dia}, was strongly correlated with I_p, and also W_{dia} increased with ρ_{foot} due to the larger improved confinement region when q_{min} was fixed. Therefore the confinement property should be characterized by a local parameter such as poloidal magnetic field at ρ_{foot}, which is written by

$$B_p^{foot} = \frac{\rho_{foot}}{R} B_T \frac{q_{eff}}{q_{foot}} \frac{\mu_0 R I_p}{2\pi a^2 B_T}.$$

where a, q_{eff} and q_{foot} are the minor radius, the effective safety factor and the safety factor at the ITB foot, respectively. The stored energy was strongly correlated with B_p^{foot} rather than I_p, and then proportional to $(B_p^{foot})^{1.5}$. In JT-60U reversed shear plasmas, the ITB width, Δ_{ITB}, becomes narrower with evolution of the ITB and the lower boundary of ITB width is proportional to the ion poloidal gyroradius at the ITB center, ρ_{pi}^{ITB}. This indicates that the transport property at the ITB layer can be characterized by the ratio of Δ_{ITB} to ρ_{pi}^{ITB}. We consider the dependence of this ratio, and then W_{dia} scaling for reversed shear plasmas was rewritten by

$$W_{dia} = 27.1 \times \left(B_p^{foot} \right)^{1.5} \times \left(\Delta_{ITB} / \rho_{pi}^{ITB} \right)^{-0.25}$$

(in MJ, T and m). The RMSE for this fit is 6.86%. It should be mentioned that W_{dia} is independent on the heating power in this scaling expression. This feature is quite strange from the viewpoint of diffusive nature. Physics mechanism of this confinement property and the effects of the toroidal momentum are the future work.

[1] Y. Sakamoto et al., J. Plasma Fusion Res. SERIES, **4**, 249 (2001).

3.6 Dynamic behavior of transport and heat propagation in normal and reversed shear plasmas with internal barriers in JT-60U [1,2]

S. V. Neudatchin, T. Takizuka , H. Shirai, T. Fujita, A. İsayama,
Y. Kamada and Y. Koide

Transport evolution in reverse shear (RS) and normal shear (NrS) JT-60U tokamak plasmas with internal transport barrier (ITB) is described as a combination of various fast and slow time scales processes. Abrupt in time and wide in space (0.3-0.4 of minor radius) variations of $\chi_{e,i}$ (ITB-events) are found in NrS plasmas. ITB-events are observed as the simultaneous rise and decay of electron and ion temperatures $T_{e,i}$ in two zones. ITB-events widths are generally similar for weak ITBs in RS and NrS plasmas while profiles of χ_e jump ($\delta\chi_e$) at ITB-event in RS plasmas with strong ITB are localized near ITB "foot" in narrower region. In various RS pulses studied up to now, the maximum of the abrupt variation in the heat flux is always located near the position of q_{min} and heat flux variation is always extended into the positive shear region [1].

New sources of HPP (Heat Pulse Propagation) are found in RS plasmas. We observe symmetric picture of slow HPP (with values of the electron dynamic heat diffusivity $\chi_e^{HP} \approx 0.1 m^2/s$) in 3 cases. ITB-event induced electron inward HPP and sawtooth-like crash induced outward HPP are studied, both propagated throughout the strong ITB in the RS zone. ITB formation in positive shear zone of RS plasmas is described as series of ITB-events. For the last ITB-event, the region of strong (~20 keV/s) T_e rise is initially well localized (~4 cm) in space. Outward HPP is analyzed in the region with ~8 cm width fully located in positive shear space zone. Values of χ_e^{HP} as low as $\sim 0.1 m^2/s$ are found. A similar low value of the ion dynamic heat diffusivity (close to the neoclassical one) is obtained for ion HPP. Important consequence of HPP analysis is the absence of electron and ion "heat pinch" in the ITB region [1,2].

Fast response of T_e to ELM-induced H-L back transitions (seen as T_e decay correlated within 2ms with abrupt rise of Hα) is found well inside the weak ITB in the RS region, suggesting edge-core interplay across q_{min} in ms timescale. The T_e decay is interpreted as abrupt appearance of the negative $\delta\chi_e$ at global H-L transition [1].

References

[1] Neudatchin, S. V., Takizuka, T., Shirai, H., et al., 2000 IAEA Fusion Energy Conference (Sorrento, 2000) IAEA-CN77/EXP5/01.

[2] Neudatchin, S. V., Takizuka, T., Shirai, H., et al., Plasma Phys. Control. Fusion **43**, 661 (2001).

3.7 Compatibility conditions of the edge and internal transport barriers in JT-60U

T. Fukuda, T. Takizuka, T. Fujita, Y. Sakamoto, Y. Kamada and S. Ide

1. Introduction

In order to establish the steady-state operation in fusion experimental reactors, it is required to achieve high bootstrap fraction and improved confinement, in addition to the superior stability characteristics, which is relevant to high normalized beta. Therefore, it is necessary to induce the L-H transition and produce the secondary transport barrier at the edge plasma region of a plasma with internal barrier. Consequently, the plasma pressure profile is flattened to improve the global stability boundary. However, it has been known in our previous experience in JT-60U that the L-H transition threshold power is much higher in high performance discharges with strong internal transport barrier (ITB) than that is predicted by the scaling law. The speculative interpretation we thereby made at first was that the loss power to the edge region is reduced transiently, due to the substantial reduction of the transport coefficient in the core. However, even in the case of small dW/dt, the plasma edge often stayed in L mode. Conversely in H mode plasmas, the efficiency of central heating is reduced and impedes the formation of ITB, as reported in the DIII-D experiments. The degree to which the central heating efficiency is reduced seems to be less and the internal barrier is formed without as much difficulties in H mode plasmas in JT-60U. This is seemingly due to the fact that the heating beams are near perpendicular to the magnetic field in JT-60U, which can enhance the central heating, whereas in DIII-D, the beams are injected tangentially. Another relevant issue may be that an increase of edge density in the plasma edge is more predominant in DIII-D, in comparison with JT-60U, which makes the heating power deposit more in the edge region. Therefore, it is an important issue of investigation to resolve the compatibility conditions of edge and internal transport barrier.

The global feature of L-H transition with and without the internal barrier is first reviewed in this paper, with emphasis on the averaged density and magnetic field that are the most influential elements of L-H transition criteria. The edge density and temperatures, of which intimate relation to the global threshold power has been documented in JT-60U [1-3], are then looked into to resolve the causality of mutual dependence of formation conditions formed in the core and edge. The criteria for the formation condition of ITB itself, where the role of local magnetic shear at the barrier as well as the influence of intensive central heating is recently disputed is out of the scope of this paper and will be not be herein discussed.

2. L-H transition threshold power in plasmas with internal barrier

It is known and pervasively accepted that the L-H threshold power scales with the magnetic field (B_t), as indicated in the detailed systematic investigations performed in JT-60U for plasmas without the internal barrier, and the result of which is plotted in Fig. 1 (a) as a func-

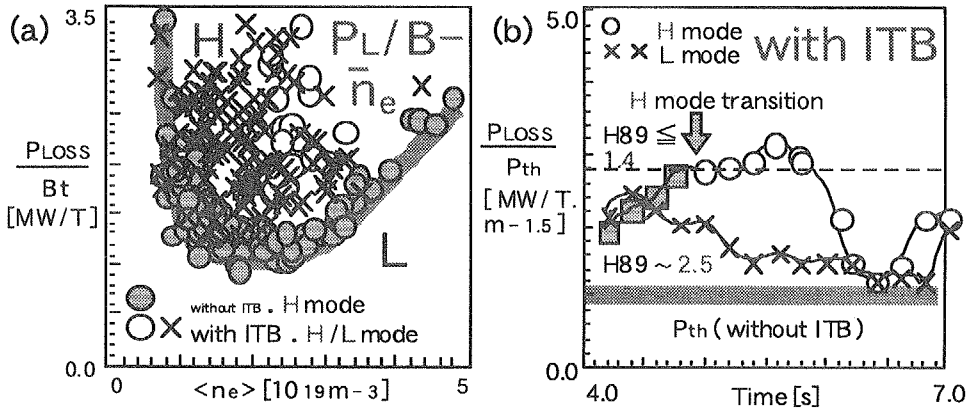

Fig. 1 (a) The dependence of heating power (absorption power with the derivative of the stored energy subtracted) normalized by B t on line averaged density. Open and solid circles are respectively for H mode with and without ITB (internal transport barrier), and the cross indicates L mode with ITB. (b) Temporal evolution of the heating power normalized by the L-H transition threshold scaling for plasmas with ITB. Open circles and shaded squares are for H89 ≤ 1.4, and crosses are for H89 ~ 2.5.

tion of the line averaged density ($<n_e>$). Here, the L-H threshold power is accordingly normalized by B_t and overlaid with the results for plasmas with internal barrier. The lower boundary of H mode data has practical significance, as the rest in the upper region with higher normalized threshold power is relevant to the cases with larger amount of impurities and malign effect of edge neutral particles. It is obvious that the plasmas with internal barrier has higher threshold power compared to those without. The temporal evolution of the heating power normalized by the threshold scaling that was established in JT-60U for plasmas without the internal barrier is shown in Fig. 1 (b). The open circles and squares are for plasmas with the confinement enhancement factor relative to 89P L mode scaling (H89) below 1.4, respectively corresponding to the H and L mode phase. On the other hand, crosses are for H89 around 2.5, which stayed in L mode throughout the discharge. General observation is that higher the H89 is, namely better the quality of the internal barrier is, loss power to the edge is reduced. It should be noted here that plasmas stay in L mode at normalized heating power above unity, and the L-H threshold is increased by more than a factor of two. However, the conventional L-H threshold scaling does not separate the core transport and L-H transition physics, and it is naturally expected that the condition for the edge barrier formation is modified as the core transport is changed. Therefore, it is necessary to focus on the edge plasma parameters for the comprehension of the compatibility condition of the barrier formation in the core and edge.

3. Edge quantities at L-H transition in plasmas with internal barrier

The edge ion temperature (T_i^{95}) is plotted against the edge density (n_e^{95}) both at 95% normalized toroidal flux in Fig. 2 (a) for plasmas with and without the internal barrier. Although integrated understanding was not straightforward in the discussion of the L-H power threshold, the L and H mode data is clearly separated both for plasmas with and without the internal barrier in this edge parameter diagram. It indeed indicates that the edge density of plasmas with internal barrier is extremely low, even if the averaged density is moderately

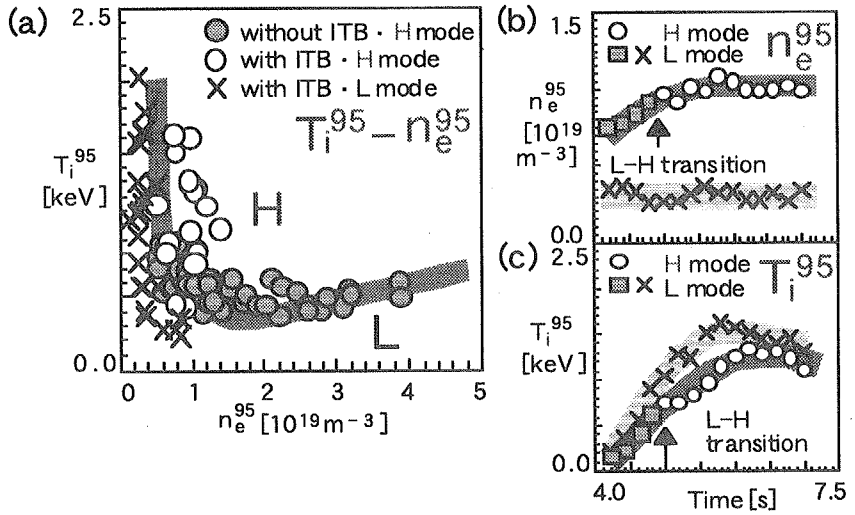

Fig. 2 (a) The relationship between the edge ion temperature and density. Open and solid circles are respectively for H mode with and without ITB, and the crosses indicate L mode with ITB. Temporal evolution of the (b) edge density and (c) temperature. Open circles and shaded squares are respectively for H and L mode with H89 ≤ 1.4, whereas the crosses are for L mode with H89 ~ 2.5.

high, and the plasma therefore stays in L mode, similar to the case in low density plasmas without the internal barrier. The low density boundary is situated at around $n_e^{95} = 0.5 \times 10^{19}$ m^{-3}, which increases the L-H threshold power, and it is shown that a small increase of density actually produces the H mode at the boundary. An increase of the threshold power at low density has been interpreted in terms of the edge neutral density in JT-60U. On the other hand, the edge ion temperature is high due to the applied heating power above the conventional threshold. The dynamic evolution of the edge density and temperature of the very same pulse depicted in Fig. 1 (b) is plotted in Fig. 2 (b) and (c). The pulse with lower H89, namely reduced barrier quality, has higher edge density, whereas it stayed at very low value in the improved confinement plasma with H89 of 2.5. The difference in temperature is less, and edge ion temperature is slightly higher for the case with lower edge density. The consequence of this observation is that an increase of the edge density can induce the L-H transition in plasmas with internal barrier, either by additional fueling in the edge or reducing the barrier quality.

4. Control of L-H transition in plasmas with internal barrier

One of the straightforward methods of instantaneously increasing the edge density is to apply the strong pulsed gas puff. However, this approach has not been effective in JT-60U, seemingly either due to the increased opacity to the neutrals at higher densities or enhanced particle diffusivity outside of the ITB region. The additional gas puff experiment was performed using the gas valve in the main plasma region. However, It has been also documented that gas puffing from the private region of divertor neither reduces the L-H threshold power by a significant amount in JT-60U. The alternative technique is to delay the formation of ITBs, after the L-H transition, which is not practically effective in DIII-D, as aforementioned in the previous section. The fast rampdown of the plasma current is also suggested to reduce

the L-H threshold power, expecting the role of edge magnetic shear. However, it was not obvious in JT-60U, the amount of reduction in the L-H transition threshold power less than 10% even for the case of rampdown at 2 MA / s. The most appropriate method, which enables the L-H transition in plasmas with internal barrier is to control its quality, in terms of ω_{ExB} / Γ[4] which is the ratio of shearing rate to the growth rate of assumed instability. The experimental procedure often employed in JT-60U is to inject unidirectional tangential beams, in order to modify the toroidal flow velocity profile and resulting radial electric field profile. It provides the gradual increase of the edge density, as shown in Fig. 3, accompanied by the reduction of the temperature gradient at the internal barrier.

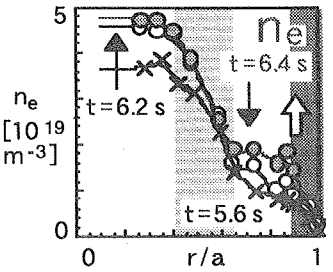

Fig. 3 The evolution of density profile at the modification of the barrier quality. 5.6 s is right before the start of unidirectional beam injection which continues till 6.3 s.

5. Conclusion

Having in mind that it is prerequisite to seek for the compatibility conditions of internal and edge transport barriers to establish the steady state high performance plasmas with superior stability characteristics in a fusion experimental reactor, the L-H transition power threshold was investigated in plasmas with internal barrier. It was hereby found that it is substantially higher than the conventional scaling established for plasmas without the internal barrier. However, the criteria for the edge density and temperature to induce the L-H transition is similar between the cases with and without the internal barrier, and the edge density is extremely low in plasmas with strong internal barrier, which substantially increases the heating power to attain the H mode. Thus, the L-H transition threshold power scaling, which does not separate the core transport and transition physics, is not generally applicable for plasmas with internal barrier. It was shown that the degradation of the quality of the transport barrier, in terms of the changes of toroidal rotation profile or equivalently the radial electric field distribution, results in the increase of edge density and thus inducing the L-H transition. Therefore, it is concluded that the degree to what extent the threshold power is modified depends on the quality of the internal barrier, indicating that the additional "hidden" parameter is present in plasmas with internal barrier.

References

[1] Fukuda, T., et al., Nucl. Fusion **37**, 1199 (1997).
[2] Fukuda, T., et al., Plasma Phys. Control. Fusion **40**, 827 (1998).
[3] Fukuda, T., et al., Plasma Phys. Control. Fusion **42**, A289 (2000).
[4] Fujita, T., et al., Nucl Fusion **39**, 1627 (1999).

3.8 H-mode edge structure in JT-60U high density improved confinement plasmas [1]

T. Fukuda, K. Tsuchiya, T. Hatae, H. Urano, Y. Kamada, Y. Sakamoto, S. Sakurai,
H. Takenaga, H. Kubo, N. Asakura, T. Fujita and T. Takizuka

Sustainment of the improved confinement at high density is one of the serious issues of concern especially in large tokamaks, and it is therefore considered as one of the urgent topics of R&D in ITER. Accordingly, intensive investigation has been carried out in various tokamaks to resolve how the collisional edge degrades the core confinement. It is also urged to understand how the H mode quality is degraded and edge pedestal structure is modified at high density. In this respect, the physics of edge pedestal structure produced at the L-H transition is revisited, based on the experimental results accumulated in JT-60U. Various features of edge pedestal structure and its interaction with the internal structure has also been investigated. The reduction of edge temperature is generally observed with an increase of the edge density in ELMy H mode plasmas in JT-60U, which results in the decrease of central temperature as well as the degradation of global confinement. In regard to the properties of edge E_r shear in high-density plasmas, the role of neutral particle has been investigated. On the other hand, the influence of edge magnetic shear on the barrier formation in the plasma interior and edge was also studied, and it has been addressed that the magnetic shear effect is less dominant at the edge than in the interior. As to the issue of how the collisional edge is linked to the core confinement degradation, it is being explored in terms of the profile "stiffness," of which detailed investigation is in progress, incorporating the ITG based fluid simulation.

The study of density dependence of the L-H threshold power has also been intensively carried out, and significant increase of the threshold power was documented in JT-60U and ASDEX-U. Substantial difference in the scaling is produced between the cases when the high density data are treated as a scatter or as a systematic tendency. The causalities of increased L-H threshold power at high density, exceeding the ITER scaling have also been looked into emphasizing the edge parameters.

It was thereby found that the substantial increase of the L-H threshold power at high density is related to the nonlinear increase of edge density, which significantly raises the edge collisionality. As to the quality of the edge barrier, the width of the E_r shear layer is reduced in high density ELMy H mode, which corroborates the decrease of the pedestal width. The interaction between the internal and edge structure has also been studied in JT-60U, where the effectiveness of the active control of internal barrier has been manifested to increase the edge density and induce the L-H transition. In addition, it is expected that the role of edge neutral particles on L-H transition and sustainment of the edge barrier quality is subtle.

References

[1] Fukuda, T. et al., J. Plasma Fusion Res. SERIES, **4**, 243 (2001).

3.9 High triangularity ELMy H-mode plasmas with highly improved energy confinement in JT-60U

H. Urano†, Y. Kamada, H. Shirai, T. Takizuka, T. Fukuda, T. Hatae and H. Kubo
†Graduate School of Engineering, Hokkaido University

1. Introduction

ELMy H-modes are currently considered the most promising plasma operating regime of enhanced confinement with a proven capability for steady state performance in a future reactor-size magnetic fusion experiment. In order to achieve the required fusion yield, any next-step machine needs to operate at a high density. The projection of the performance of ELMy H-mode plasmas to ITER-FEAT [1,2] also shows that the plasma density required to achieve a high fusion power gain is near the Greenwald density limit, n^{GW}. However, it has generally been seen that core confinement quality is diminished continuously as the density is increased by gas fuelling in many devices [3-9]. It has been seen that the temperature at the pedestal shoulder imposed by regular ELM events may play a role as a boundary condition in determining the profile of the core temperature [5,10-16]. High triangularity discharges, in which the critical edge pressure gradient can be raised, are therefore expected to bring in the high improved energy confinement of the plasma core [17-22]. The improved energy confinement has also been achieved in high β_{pol} discharges [23,24]. An increase in the H-mode edge pressure gradient on the outerboard midplane is observed with increasing the poloidal beta, β_{pol}, due to high power additional heating [24].

2. Experiments

The experiments were performed at the plasma current, I_p = 1.0 MA. The toroidal magnetic field, B_t = 2.1 T and q_{95} = 3.5-3.7. The neutral beam (NB) injection power, P_{NBI}, for deuterium plasma was in the range of 9.0-11.5 MW at the relevant time of analysis. With deuterium gas puffing, $\bar{n}_e$, was varied on a shot by shot basis from 1.8×10^{19} to 3.1×10^{19} m^{-3}. Elongation, κ, of 1.38 to 1.44 and triangularity at the separatrix, δ_x, of 0.45 to 0.49 were fixed. The plasma volume, V_p, was in the range of 55-56 m^3. The plasma major radius, R_p, and the minor radius, a_p, were in the ranges of 3.32-3.33 m and of 0.80-0.82 m, respectively. In order to assess the effects of triangularity, low triangularity discharges were also carried out at δ_x = 0.20.

3. Thermal energy confinement properties

Figure 1 displays the H_H-factor based on the predictions of the IPB98(y,2) scaling as a function of $\bar{n}_e/n^{GW}$. For reference, figure 3 also includes data from the density scan experiments of the low triangularity ELMy H-mode (I_p = 1.8 MA, B_t = 3.0 T, q_{95} = 3.0, δ_x = 0.16 and P_{NBI} = 8-13 MW) [13]. It is seen most clearly that the thermal energy confinement is improved by high triangularity discharges at a given density. At low densities, the discharge in steady state is characterized by type-I ELMs. When the density is increased further to 50 % of n^{GW} in the high triangularity experiments, a transition from type-I to type-III ELMs occurs.

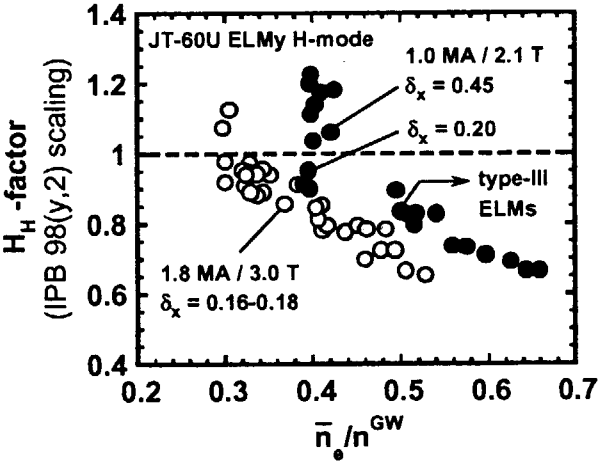

Fig. 1 H_H-factor for ELMy H-mode discharges in JT-60U as a function of $\bar{n}_e/n^{GW}$.

Profiles of n_e, T_e and T_i for low and high triangularity plasmas with P_{NBI} = 9.0 MW at a fixed density of f_{GW} ~ 0.40 are shown in figure 2(a), (b) and (c). It is seen in figure 2(a) that the density

profiles are similar in either case. It is the fact that the core temperature is also improved by a factor of ~ 1.3 as well as the peripheral temperature (see figure 2(d)) by high triangularity discharge that is of most significance because the plasma shaping affects strongly edge toroidal magnetic flux surfaces as seen in figure 2(c). Thus, there seems to exist a large transport structure where the core temperature is determined by a boundary value through the profile stiffness, such as ion temperature gradient (ITG) driven turbulence modes [25-28]. Since the temperature at the shoulder of the H-mode pedestal is raised by high triangularity, the core temperature may be increased due to the effect of profile stiffness.

4. Pedestal characteristics

As seen in figure 2(c), triangularity affects directly the edge toroidal magnetic flux surfaces. In this section, the pedestal structure imposed by the ELM activities is examined for the case of low and high triangularity. A comparison of the pedestal characteristics between low and high triangularity ELMy H-mode plasmas is shown as a diagram for the pedestal density and temperature in figure 3(a). At a fixed I_p of 1.0 MA, the high triangularity ELMy H-mode plasmas produce the pedestal temperature higher than that of low triangularity plasmas at a given density. Besides, it is seen in high triangularity plasmas that the pedestal pressure tends to decrease gradually with density. Figure 3(a) also shows a time trace of the pedestal for a high β_{pol} ELMy H-mode discharge with ITB in the core with high power heating. On the high triangularity configuration, it can be seen that the high β_{pol} H-mode plasma reaches the higher critical pedestal pressure. Related to this respect, the dependence of the poloidal beta at the pedestal, β_{pol}^{ped}, upon triangularity is plotted in figure 3(b). A comparison of standard ELMy H-modes without ITB between low and high triangularity discharges indicates that β_{pol}^{ped} tends to increase gradually with increasing triangularity. In high β_{pol} H-mode plasmas, although the improvement of the pedestal confinement is seen over a wide range of triangularity, the increase in β_{pol}^{ped} is larger in high triangularity plasmas. High β_{pol} H-mode therefore displays its potential on the pedestal confinement at high triangularity.

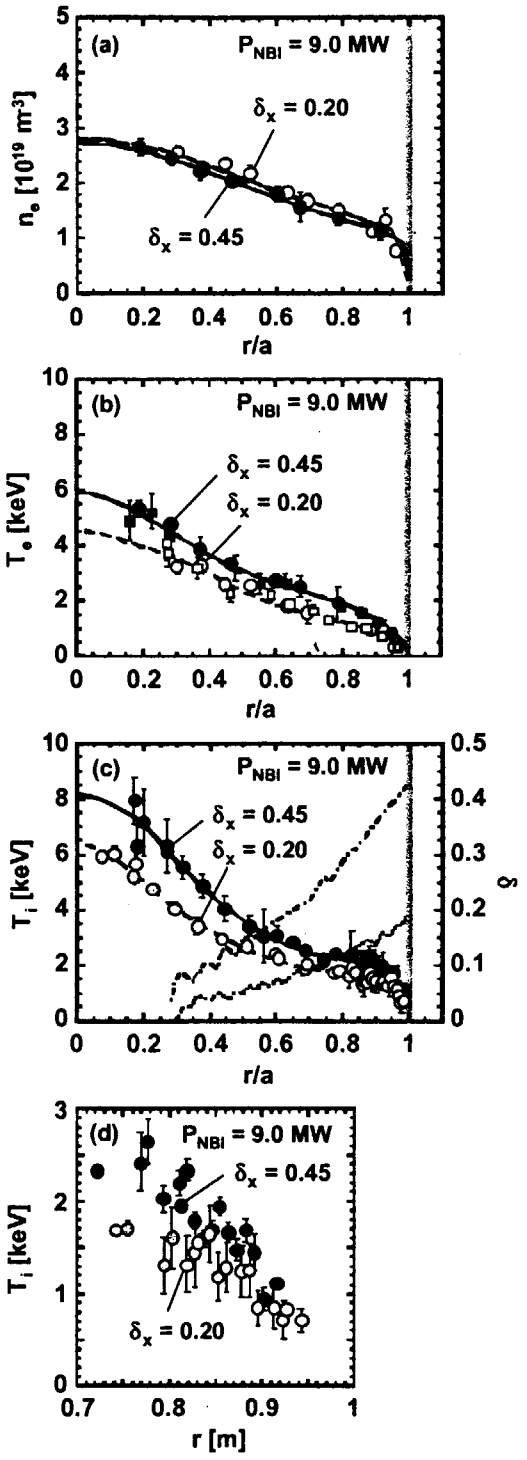

Fig. 2 Profiles of (a) n_e, (b) T_e and (c) T_i for low and high triangularity discharges at a fixed density (f_{GW} ~ 0.40). (d) The pedestal T_i profiles are also shown.

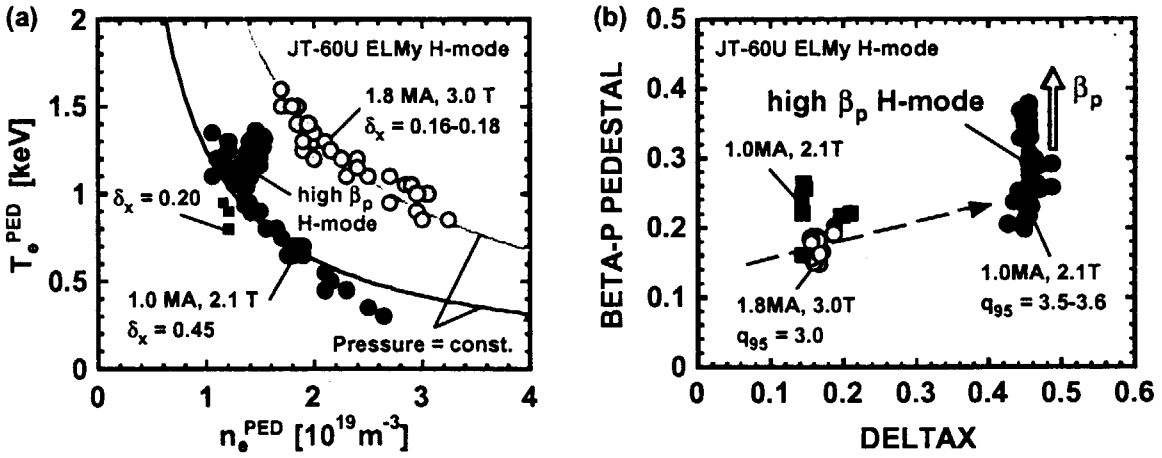

Fig. 3 (a) Diagram of (n_e^{ped}, T_e^{ped}) space for ELMy H-mode plasmas (b) Dependence of the poloidal beta at the pedestal on triangularity.

5. Boundary condition for thermal energy confinement

It has been identified in many tokamaks that the thermal energy confinement in H-mode plasmas depends strongly upon the temperature at the shoulder of the H-mode pedestal [11,16-19]. In the standard ELMy H-mode without ITB, $H_H^{IPB98(y,2)}$ increases approximately proportional to the pedestal temperature as shown in figure 4. At a fixed I_p of 1.0 MA, the trends of the enhancement factors of thermal energy confinement are conformed consistently with low and high triangularity cases. This result could be expected from the profile similarity in the temperature. The core temperature increases in roughly proportion to the pedestal temperature for each species, independent of triangularity. The core T_i and T_e at r/a ~ 0.3 increase from 2.0 to 7.6 keV and from 2.0 to 5.0 keV almost linearly with T_i^{ped} from 0.5 to 2.2 keV and with T_e^{ped} from 0.3 to 1.4 keV, respectively. Higher triangularity plasma has the higher temperature at the pedestal shoulder determined by the ELM activities at a given density, which in turn leads to an increase in the core temperature, resulting in the improvement of the energy confinement of H-mode plasmas.

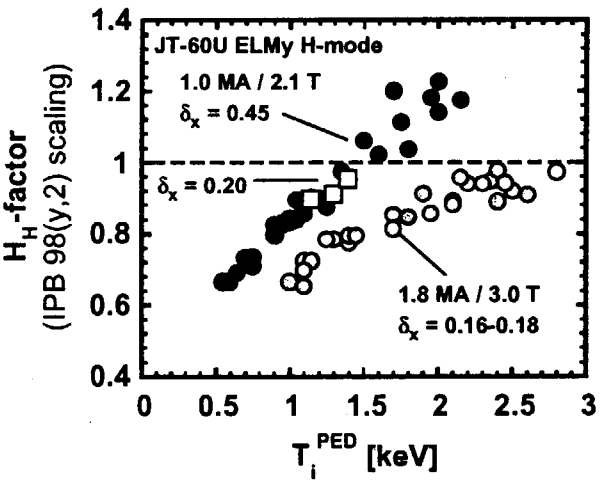

Fig. 4 Dependence of the H_H-factor on the pedestal temperature for low and high triangularity plasmas.

6. Discussions

In the previous section, the experimental results indicate the pedestal temperature might be a key boundary factor for the energy confinement through the profile similarity in the temperature. It is considered that the critical pedestal pressure for the ELMs is raised since the stability near the plasma boundary is improved by high triangularity. Besides, high β_{pol} H-mode plasmas produced the even higher pedestal pressure. This result can be explained that the stability at the edge region, where triangularity becomes higher, is improved further when a large Shafranov shift due to the high β_{pol} discharge increases a local magnetic shear in the bad curvature region and shortens the connection length between the good and bad curvature regions.

7. Conclusions

The density scans of the energy confinement and pedestal properties in high triangularity ELMy H-mode plasmas ($\delta_x \sim 0.45$) were carried out in JT-60U. High triangularity discharges produced the higher pedestal pressure, at which higher pedestal temperature was obtained at a given density. The core temperature increases in roughly proportion to the pedestal temperature for each species, independent of triangularity. High β_{pol} H-mode plasmas due to high power heating produced further high pedestal confinement. The improvement of the edge stability by triangularity leads to higher pedestal temperature, which in turn raises the core temperature, and thus the high thermal energy confinement is obtained.

References

[1] R. Aymar: Plasma Phys. Control. Fusion **42** (2000) B385.
[2] Y. Shimomura, et al.: Nucl. Fusion **41** (2001) 309.
[3] JET Team: Nucl. Fusion **39** (1999) 1687.
[4] G. Saibene, et al.: in Controlled Fusion and Plasma Physics (Proc. 25th Eur. Conf. Prague, 1997), Vol. 22C, European Physical Society, Geneva (1997) 341.
[5] W. Suttrop, et al.: in Fusion Energy 1998 (Proc. 17th Int. Conf. Yokohama, 1998), Vol. 2, IAEA, Vienna (1999) 777.
[6] O. Gruber, et al.: Nucl. Fusion **39** (1999) 1321.
[7] N. Asakura, et al.: Plasma Phys. Control. Fusion **39** (1997) 1295.
[8] Y. Kamada, et al.: Plasma Phys. Control. Fusion **41** (1999) B77.
[9] H. Urano, et al.: in Controlled Fusion and Plasma Physics (Proc. 27th Eur. Conf. Budapest, 2000), ECA Vol. 24B, European Physical Society, Geneva (2000) 956.
[10] M. Greenwald, et al.: Nucl. Fusion **37** (1997) 793.
[11] W. Suttrop, et al.: Plasma Phys. Control. Fusion **39** (1997) 2051.
[12] W. Suttrop, et al.: Plasma Phys. Control. Fusion **40** (1998) 771.
[13] H. Urano, et al.: Nucl. Fusion **42** (2002) (in press).
[14] G. Janeshitz, et al.: in Controlled Fusion and Plasma Physics (Proc. 26th Eur. Conf. Maastricht, 1999), Vol. 23J, European Physical Society, Geneva (1999) 1445.
[15] D. R. Mikkelsen, et al.: in Fusion Energy 2000 (Proc. 18th Int. Conf. Sorrento, 2000), IAEA-CN-77/EXP5/20.
[16] F. Ryter, et al.: in Fusion Energy 2000 (Proc. 18th Int. Conf. Sorrento, 2000), IAEA-CN-77/EX2/2.
[17] Y. Kamada, et al.: in Fusion Energy 1996 (Proc. 16th Int. Conf. Montreal, 1996), Vol. 1, IAEA, Vienna (1997) 247.
[18] G. Saibene, et al.: Nucl. Fusion **39** (1999) 1133.
[19] J. Stober, et al.: in Controlled Fusion and Plasma Physics (Proc. 26th Eur. Conf. Maastricht, 1999), Vol. 23J, European Physical Society, Geneva (1999) 1401.
[20] W. Suttrop, et al.: Plasma Phys. Control. Fusion **42** (2000) A97.
[21] T. H. Osborne, et al.: Plasma Phys. Control. Fusion **42** (2000) A175.
[22] J. Stober, et al.: Plasma Phys. Control. Fusion **42** (2000) A211.
[23] Y. Kamada, et al.: Plasma Phys. Control. Fusion **36** (1994) A123.
[24] T. H. Osbone, et al.: Plasma Phys. Control. Fusion **40** (1998) 845.
[25] M. Kotschenreuther, et al.: Phys. Plasmas **2** (1995) 2381.
[26] C. Petty, et al.: Phys. Rev. Lett. **83** (1999) 3661.
[27] A. Dimits, et al.: Phys. Plasmas **7** (2000) 969.
[28] G. Tardini, et al.: in Controlled Fusion and Plasma Physics (Proc. 27th Eur. Conf. Budapest, 2000), ECA Vol. 24B, European Physical Society, Geneva (2000) 1148.

3.10 Edge plasma parameters at the L-H transition under different divertors in JT-60U

K. Tsuchiya, T. Fukuda, H. Takenaga, N. Asakura, Y. Kamada,
T. Takizuka, K. Itami, T. Fujita and the JT-60 Team

1. Relation between the edge parameter and L-H transition power threshold [1]

After the modification of the divertor geometry into W shape, we have observed remarkable reduction in the L-H transition threshold power (P_{th}) and a shift of low density L-H transition boundary [2] toward higher density, in comparison with the previous open geometry. Although the core radiation power was also reduced in the W-shaped divertor, it was not sufficient to account for the amount of reduction in P_{th}. Therefore, the edge plasma quantities, which are considered to be intimately related to the L-H physics, were comparatively investigated between the W-shaped and open divertor. Here, the discussions are limited to the range of densities above the lower boundary, below which P_{th} substantially increases.

It was thereby found that the edge T_i right before the L-H transition is lower for the W-shaped divertor, which is consistent with the reduced P_{th}. The edge ion collisionality $\nu_i{}^*{}_{95}$ [3] evaluated at 95% volume averaged flux surface is also notably higher at around 1.0-1.3 for the W-shape, whereas it was around 0.6-0.7 for the open divertor. Ref. 4 predicts $\nu_i{}^*{}_{95}$ is around unity at the L-H transition, if the effect of neutral particles is neglected. This paper is aimed at resolving the physics of reduced P_{th} at L-H transition in W-shaped divertor, speculating that the compression of the neutral particles near the X-point ($n_0{}^X$), due to the closure of the divertor geometry, might have enhanced the collisional scattering of trapped ions to induce the negative E_r [5]. A substantial increase in $n_0{}^X$ was indeed documented by the DEGAS code analysis. In addition, it was observed that $n_0{}^M$, which can increase P_{th} by the charge exchange process, is slightly lower for the W-shape. Here, $n_0{}^M$ stands for the mid plane neutral particle density. As a consequence, $n_0{}^X/n_0{}^M$ is larger in the W-shaped divertor for the same edge density ($n_e{}^{95}$), which may indicate the relevance of neutral particle compression in the reduction of P_{th} in the W-shaped divertor.

2. Influence of the X-point height on the L-H transition threshold power

We have also carried out a dedicated experiment to resolve the X-point height (X_p) dependence of P_{th}, where X_p was varied 0.37 m to 0.18 m. Here, X_p = 0.18 m means that the X-point is sitting on the septum top in the divertor. The range of $n_e{}^{95}$ was fixed at 1.0 -1.5 $\times 10^{19}$ m^{-3}. The changes in P_{th} were subtle except for the case of X_p = 0.18, where remarkable reduction in P_{th} was observed. Similar observation is made at JET [6]. It is expected that abundant neutrals near the X-point is playing a decisive role also in this case, in terms of the scattering loss of trapped ions.

[1] Tsuchiya K., et al., in Fusion Energy Conference 2000 (Proc. 18th Int. Conf. Sorrento, 2000), IAEA, Vienna (2001) IAEA-CN-77/EXP5-26.
[2] Fukuda, T., et al., Nucl. Fusion **37**, 1199 (1997).
[3] Hirshman, S. and Sigmar, D., Nucl. Fusion **21**, 1079 (1981).
[4] Shaing, K., et al., Phys. Plasmas **2**, 1801 (1995).
[5] Toda, S., Plasma Phys. Control. Fusion **39**, 301 (1997).
[6] Horton, L., et al., Proc. 26th EPS Conf. on Plasma Physics and Controlled Fusion Research (Maastrricht, Holland, 1999) P1.021.

3.11 Understanding of the H-mode pedestal characteristics using the multi-machine pedestal database [1]

T. Hatae, M. Sugihara[1], A. Hubbard[2], Y. Igitkhanov[1], Y. Kamada,
G. Janeschitz[1], L. Horton[3], N. Ohyabu[4],T. Osborne[5], M. Osipenko[6],
W. Suttrop[3], H. Urano[7], H. Weisen[8]

With use of a multi-machine pedestal database, essential issues for each regime of ELM Types are investigated. They include (i) understanding and prediction of pedestal pressure during Type I ELMs which is a reference operation mode of a future tokamak reactor, (ii) identification of the operation regime of Type II ELMs which have small ELM amplitude with good confinement characteristics, (iii) identification of upper stability boundary of Type III ELMs for the access to the higher confinement regimes with Type I or II ELMs, (iv) relation between core confinement and pedestal temperature in conjunction with the confinement degradation in high density discharges. Scaling and model based approaches for expressing pedestal pressure are shown to roughly scale the experimental data similarly well and initial predictions for the future reactor case could be performed by them. It is identified that q and δ are important parameters to obtain the Type II ELM regime. A theoretical model on Type III ELMs is shown to reproduce the upper stability boundary reasonably well. It is shown that there exists some critical pedestal temperature, below which the core confinement starts to degrade. It is also shown that improved pedestal conditions for good confinement in high density discharges is possible by increasing the plasma triangularity.

[1] Hatae T. et al., Nucl. Fusion **41**, 285 (2001).

---

[1] ITER Joint Central Team, Garching, Germany

[2] MIT Plasma Science and Fusion Center, Cambridge, MA,USA

[3] Max Planck Institut für Plasmaphysik, Garching, Germany

[4] National Institute for Fusion Science, Gifu-ken, Japan

[5] General Atomics, San Diego, USA

[6] Kurchatov Institute, Moscow, Russia

[7] Hokkaido University, Hokkaido, Japan

[8] Centre de Recherches en Physique des Plasmas, Ecole Polytechnique Fédérale de Lausanne, Switzerland

4. MHD Instabilities and High Energy Ions

4.1 Resistive interchange modes in reversed shear discharges

S. Takeji, S. Tokuda, T. Fujita, T. Suzuki, A. Isayama, Y. Ishii,
T. Matsumoto, Y. Kamada, T. Ozeki, The JT-60 Team

1. Introduction

A reversed shear discharge has inherent potential as an ultimate non-inductive steady-state tokamak discharge since a reversed magnetic shear configuration is consistent with large bootstrap current fraction [1]. Operation at high β is indispensable for simultaneous achievement of large bootstrap current fraction with high fusion power density. Understanding of resistive MHD instabilities which limit tokamak operation in the lower β regime than the ideal stability limit is crucially important for achievement of a high β steady-state reversed shear discharge. Resistive interchange instabilities were reported as a triggering event of disruption in negative central shear discharges in DIII-D, while the mechanism leading to disruption was not made clear [2]. Resistive interchange instabilities were found to appear in JT-60U as radially localized MHD bursts in the negative magnetic shear region near the internal transport barrier [3]. The resistive interchange mode is benign to the internal transport barrier and results neither in major collapse nor in degradation of confinement of the reversed shear discharges. On the other hand, we found that the resistive interchange mode leads to major collapse through nonlinear mode coupling with a tearing modes in the positive shear region.

In this paper, details of the process of a major collapse led by the resistive interchange mode are described.

2. A Process of Major Collapse by Resistive Instabilities

Time evolution of T_e during a process of a major collapse in low β regime ($\beta_N = 0.77$) is shown in Fig. 1(a). As described later, the major collapse occurs in the stable state against ideal modes. Three thermal quenches are observed one after another in the process of a major collapse. Before the first thermal quench at $t = 6.1083$s, a growing mode appears near the normalized plasma minor radius, ρ, ~ 0.51. Electron temperature abruptly decreases inside $\rho \sim 0.5$ and abruptly increases outside $\rho \sim 0.5$ by the first thermal quench. After the first thermal quench, a global $m/n = 3/1$ mode, which mode numbers were identified by Mirnov analysis, appears with amplitudes much larger than the growing mode near $\rho \sim 0.51$ and lasts for 2.6 ms, then the second thermal quench occurs at $t = 6.111$s. The T_e profile is flattened after the second thermal quench and the third thermal quench occurs at $t = 6.1133$s to complete the process of the major collapse. Since the first thermal quench is a key event leading to the major collapse, we pay attention to the first thermal quench in Sections 3 and 4 to understand the causal mechanism of the major collapse. Magnetohydrodynamic behavior after the first thermal quench is also discussed in Section 5.

3. Details of the First Thermal Quench

Figure 1(b) shows enlarged waveforms of T_e before the first thermal quench. Radial profiles of T_e, q, and the perturbation amplitude of T_e divided by the local T_e gradient, $\tilde{T}_e/\nabla T_e$, just before the first thermal quench are shown in Figs. 1(c) and 1(d), respectively. Here, $\tilde{T}_e$ is the difference between the maximum and the minimum in the last one cycle of the T_e perturbations before the first thermal quench ($6.107\text{s} \lesssim t \lesssim 6.1083\text{s}$).

A growing T_e perturbation appears at $t \sim 6.105$s in the large ∇T_e region ($\rho = 0.47 \sim 0.54$) near the inner $q = 3$ surface with the growth time of $\gamma^{-1} \sim 0.5$ms in the linear growth phase. The growth time $\gamma^{-1} \sim 0.5$ms is considered to be that of resistive instabilities by the same reason described in the previous section. Growth of the T_e perturbation amplitude saturates before the first thermal quench. No evidence of magnetic islands (phase inversion of T_e perturbations between adjoining channels) is found near $\rho \sim 0.51$ within the spatial resolution of ~2 cm.

On the other hand, phase inversion is observed between T_e perturbations at $\rho = 0.71$ and $\rho = 0.73$ near the outer $q = 3$ surface. Since the T_e perturbations is localized near the outer $q = 3$ surface, we regard the T_e perturbations as an $m/n = 3/1$ magnetic islands on the outer $q = 3$ surface. The $m/n = 3/1$ magnetic islands exist before growing of the resistive mode near $\rho \sim 0.51$. It was not confirmed when the $m/n = 3/1$ tearing mode became unstable. The oscillation period is not the same between the $m/n = 3/1$ tearing mode near $\rho = 0.71$ and the resistive mode near $\rho \sim 0.51$ until $t \sim 6.1064$s. Moreover, no clear T_e perturbations are observed in the region $\rho = 0.58 \sim 0.65$ even just before the first thermal quench. Therefore, the $m/n = 3/1$ tearing mode near $\rho = 0.71$ and the resistive mode near $\rho \sim 0.51$ are different modes; i.e. each mode is localized around the corresponding rational surface and grows independently of each other.

For the last two cycles just before the first thermal quench, however, these T_e perturbations oscillate with the same frequency. The *phase matching* behavior of the perturbations between spatially separated modes and the following first thermal quench resulting in formation of a global $m/n = 3/1$ mode suggest that mode coupling of two modes, i.e. an inner mode (a resistive mode at the large ∇T_e region) and a tearing mode at the outer $q = 3$ surface, in the nonlinear growth phase is the route to the first thermal quench.

4. Stability Analysis of the First Thermal Quench

Stability analyses of ideal and resistive instabilities were carried out to identify instabilities triggering the first thermal quench in the particular discharge discussed in Fig.1 by using equilibria reconstructed consistently with the experimental data. In addition to the ERATO-J code [4] and the BETA code [5], we used the MARG2D code for ideal low n kink modes and resistive (tearing) mode analyses [6]. The linear stability code MARG2D can identify a stable state against ideal low n kink modes and calculates a stability parameter of tearing modes, Δ', including the effects of finite β, toroidal geometry in the free boundary condition. Evaluation of the stability criterion, D_R, was done following the expression given in Ref.[7].

Plasma parameters just before the first thermal quench are $\beta_N = 0.77$, $\beta_p = 0.70$, $q_{min} = 2.1$ and $q^* = 4.85$. Here, q^* ($= 5a^2 B_T/(2RI_p)[1 + \kappa^2(1 + 2\delta^2 - 1.2\delta^3)]$; B_T: toroidal magnetic field, R: major radius, κ: elongation, δ: triangularity) is a safety factor near the plasma edge. The difference between q^* and q_{95} is usually less than several percent of q^*.

First, we confirmed that the equilibrium just before the first thermal quench is stable

against an ideal $n = 1$ kink and high n ballooning modes. Figure 2 shows eigenfunctions of the stable ideal $n = 1$ mode calculated by the MARG2D code in the free boundary condition. It is revealed that Δ' is positive (destabilizing) only at the outer $q = 3$ surface ($\Delta'_{3,\mathrm{out}} > 0$) and Δ' at any other mode rational surfaces with respect to $n = 1$ such as $q = 4$ and $q = 5$ were negative (tearing modes are stable). On the other hand, it is also revealed that the stability criterion of resistive interchange modes is broken ($D_\mathrm{R} > 0$) near the inner $q = 3$ surface (Fig. 2). Considering the above-mentioned experimental evidence and the results of the stability analyses, we conclude that the growing mode in the large ∇T_e region near the inner $q = 3$ surface is the resistive interchange mode. Now, we found a remarkable fact that the localized resistive interchange mode in the negative shear region leads to the first thermal quench through a mode coupling in the nonlinear phase with a tearing mode in the positive shear region.

5. MHD Behavior After the First Thermal Quench

Figure 3 shows time evolution of T_e perturbations in the process of the major collapse and T_e profiles just before and after the first thermal quench. Since the plasma equilibrium after the first thermal quench is unknown, the radial position of each channel is given by the major radius, R (m). After the first thermal quench, the T_e profile changes drastically near the large ∇T_e region and the internal transport barrier is destroyed. Then, the change of T_e profile extends to the wider radial region accompanying a global $m/n = 3/1$ mode within 240 μs, which is longer than the typical time scale of ideal instabilities and shorter than the typical one of resistive instabilities. The amplitude of higher $n(\geq 2)$ modes is less than 10% of that of $n = 1$ mode. The global $m/n = 3/1$ mode lasts for 2.6ms which is longer than the growth time of the resistive interchange mode in the linear phase. The waveforms of T_e after the first thermal quench suggests existence of magnetic islands near the innermost channel ($R = 3.741$m) in the early phase ($t \sim 6.1086$s) and growth of magnetic islands near the outermost channel ($R = 4.033$m) until occurrence of the second thermal quench (Fig. 3(a)).

The MHD behavior throughout the first thermal quench suggests that the nonlinear coupling of a resistive interchange mode with a tearing mode evolves in the time scale longer than that of ideal instabilities but shorter than that of resistive instabilities without the contribution of higher Fourier harmonics ($n \geq 2$).

6. Conclusion

Resistive interchange instabilities were studied in JT-60U. It is found that radially localized resistive interchange mode leads to major collapse through nonlinear mode coupling with a tearing mode in positive shear region.

References

[1] T. Ozeki, *et al.*, in *Plasma Physics and Controlled Nuclear Fusion Research*, Würzburg, 1992 (IAEA, Vienna, 1993), Vol.2 p187.
[2] M.S. Chu, et al., Phys. Rev. Lett. **77** (1996) 2710.
[3] S. Takeji, et al., to appear in Nucl. Fusion.
[4] T. Tsunematsu, et al., Comput. Phys. Commun. **19** (1980) 179.
[5] M. Azumi, et al., in *Plasma Physics* (Proc. 6th Int. Conf. Lausanne, 1984), Vol. 1, CEC, Brussels (1984) 375.
[6] S. Tokuda, T. Watanabe, Phys. Plasmas **6** (1999) 3012.
[7] A.H. Glasser, et al., Phys. Plasmas **18** (1975) 875.

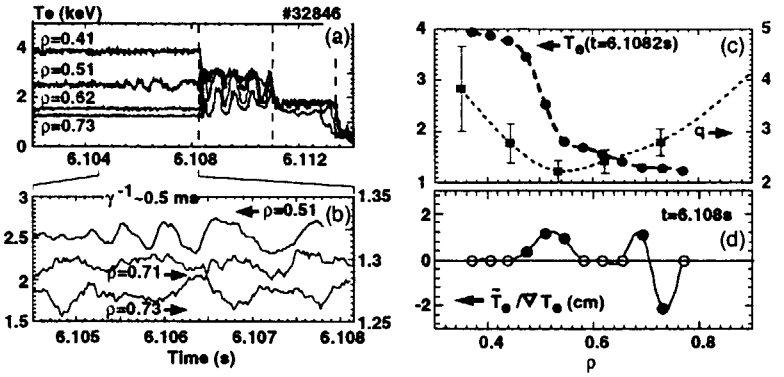

Fig.1. *Time evolution of electron temperature, T_e, (a) during the process of a major collapse, and (b) just before the first thermal quench. The vertical broken lines show the times of the first, second and third thermal quenches. Radial profiles of electron temperature T_e, q are shown in (c) and a radial profile of amplitude of T_e perturbations normalized by the local T_e gradient, $\tilde{T}_e/\nabla T_e$, just before the first collapse is shown in (d). Here, closed circles mean ECE channels on which obvious perturbations were observed, while open ones mean ECE channels on which observed perturbations were in the noise level.*

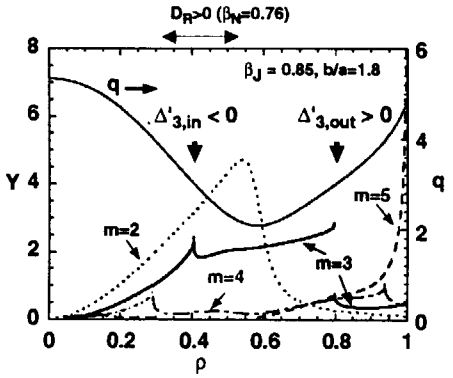

Fig.2: *Eigenfunctions of $m = 2 \sim 5$ ($n = 1$) modes calculated by the MARG2D code in the free boundary condition ($d/a = 1.8$; d: wall radius, a: plasma minor radius). A q-profile employed in this analysis is shown ad a solid line. Here, $\beta_N = 1.11$ and $q_{edge} \sim 4.87$.*

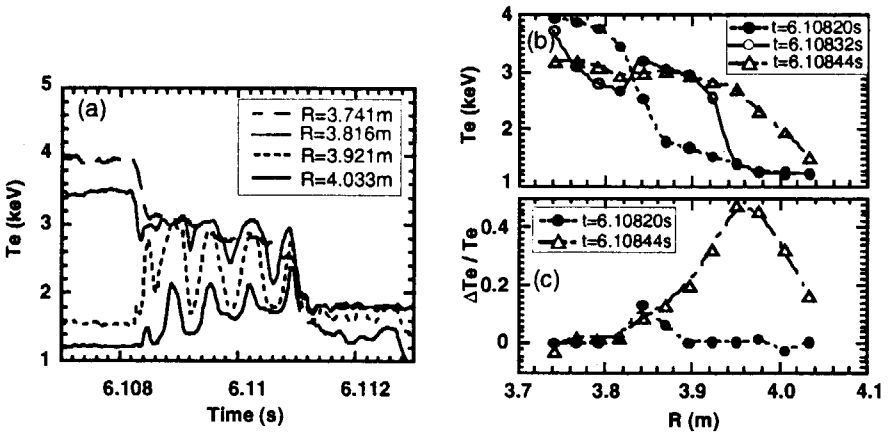

Fig.3: *(a) Enlarged waveforms of T_e in the process of a major collapse and time evolution of radial profiles of (b) T_e and (c) relative change of T_e, $\Delta T_e/T_e$, by the first collapse.*

4.2 Wall stabilization experiments on JT-60U

S. Takeji, S. Tokuda, T. Fujita, T. Suzuki, A. Isayama,
Y. Sakamoto, S. Ide, Y. Kamada, G. Kurita and The JT-60 Team

1. Introduction

Wall stabilization of ideal low n (n: toroidal mode number) kink modes is crucially important in reversed shear discharges for the high β discharges such that $\beta_N > \beta_N^{no-wall}$, since $\beta_N^{no-wall}$ of reversed shear configurations is relatively lower than those of conventional tokamak configurations [1]. Here, β_N is the normalized β and $\beta_N^{no-wall}$ is magnetohydrodynamic (MHD) stability limit against low n kink modes with the ideal wall at infinity. Then, suppression of resistive wall modes (RWMs), which appear when $\beta_N > \beta_N^{no-wall}$ owing to the finite resistivity of the wall, is required for further improvement of the achievable β and for the steady state [2]. Resistive wall modes are ideal external kink modes with the reduced growth rate of the order of τ_w^{-1} by the wall, here τ_w is the penetration time of magnetic field into the resistive wall [3]. Here, results of wall stabilization experiments and MHD characteristics of RWMs on JT-60U are described [4].

2. Improvement of Achievable Beta by Wall Stabilization

Plasma performance of JT-60U reversed shear discharges was often limited by MHD instabilities which result in major collapse in the wide β_N regime. Figure 1 shows β_N at the time of major collapses as a function of q^* in reversed shear discharges. In the case of L-mode edge discharges with the plasma shape of $d/a \sim 2$ (here, d: the distance from the magnetic axis to the outer wall, a: the plasma minor radius), the achievable β_N is lower than 2.3. The upper boundary of the achievable β_N was confirmed to be consistent with $\beta_N^{no-wall}$ of an $n = 1$ kink mode. The achievable β_N was improved up to 2.6 in discharges with an H-mode edge. Relatively higher β_N was also achieved in discharges with the plasma shapes of $d/a < 1.3$.

Enhancement factors of the achievable β_N, $E_W = \beta_N/\beta_N^{no-wall}$ were estimated for two discharges; i.e. one is an L-mode edge discharge with $d/a \sim 2.0$ and the other is a discharge with $d/a < 1.3$. In the case of the former discharge (#24715), the achieved β_N is 2.02 and evaluated $\beta_N^{no-wall}$ by using the ERATO-J code is ~ 2.2, then $E_W \sim 0.92$. On the other hand, in the case of the later discharge (#35167), the calculated $\beta_N^{no-wall}$ is ~ 2.2 while the achieved β_N was 2.6, then we obtained $E_W \sim 1.18$. Thus, the wall-stabilization of ideal low n kink modes was confirmed in the discharge with $d/a < 1.3$.

It is also remarkable that major collapses in the lower β_N region hardly occur in the case of discharges with $d/a < 1.3$. A possible reason is that resistive (tearing) instabilities which can relate to major collapse at the low β_N region are stabilized by the wall. We investigated the effect of boundary conditions on Δ' numerically by using the MARG2D code [5]. Figure 2 shows dependence of Δ' at the inner $q = 3$ surfaces ($\Delta'_{3,in}$) and Δ' at the inner $q = 3$ surfaces ($\Delta'_{3,out}$) on the parameter d/a. It was confirmed that $\Delta'_{3,out}$ changes from positive to negative with decreasing d/a, while significant change is not observed on $\Delta'_{3,in}$ by changing d/a. Since the outer $q = 3$ surface is close to the plasma surface, $\Delta'_{3,out}$ is affected by the boundary condition more strongly. The critical value of d/a to make $\Delta'_{3,out}$ negative (stabilizing) is $d/a \sim 1.4$. This result means that free-boundary modes play an important role for stability of resistive (tearing) modes at the outer mode rational surfaces and resistive (tearing) modes can be stabilized by a conducting wall as well as ideal low n kink modes.

Another theoretical analysis based on the large aspect ratio, cylindrical model has shown that tearing modes can be stabilized by the resistive wall, provided the plasma rotation frequency exceeds τ_w^{-1} (τ_w is the magnetic field penetration time into the wall) and a characteristic tearing growth rate [6]. Estimated τ_w of the JT-60U wall is about 10 ms and a characteristic tearing growth time, τ_R, is the order of millisecond or much longer. Since the typical toroidal rotation frequency, f_{tor}, of JT-60U's reversed shear discharges is several kilohertz and thus is much larger than both of τ_w^{-1} and τ_R^{-1}, wall-stabilization of tearing modes is expected by the actual plasma rotation. Resistive wall modes are, however, not stabilized by such a actual plasma rotation as mentioned below.

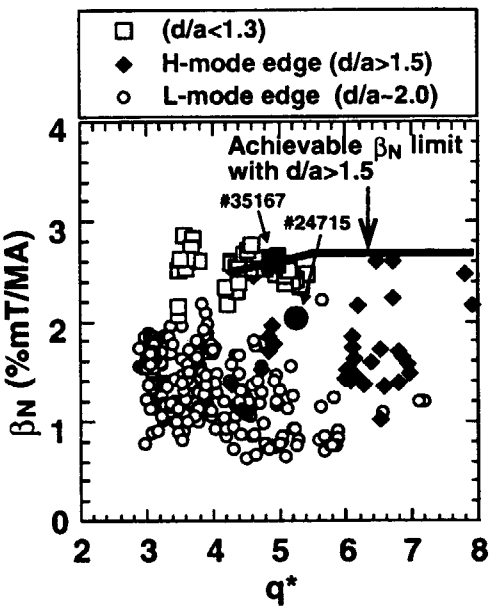

Fig.1. *Occurring region of disruptions or major collapses in the $\beta_N - q^*$ plane in several type of JT-60U reversed shear discharges. Open circles are data with the L-mode edge with the plasma shape $d/a \sim 2.0$. Closed diamonds are ones in discharges with the H-mode edge with the plasma shape $d/a > 1.5$, and open squares are ones obtained in discharges with the plasma shape $d/a < 1.3$. The large circle and square are typical discharges with the L-mode edge with the plasma shape $d/a \sim 2.0$ and with the plasma shape $d/a < 1.3$, respectively. The evaluated enhancement factor, E_W, was 0.92 for the former discharge and was 1.18 for the later discharge.*

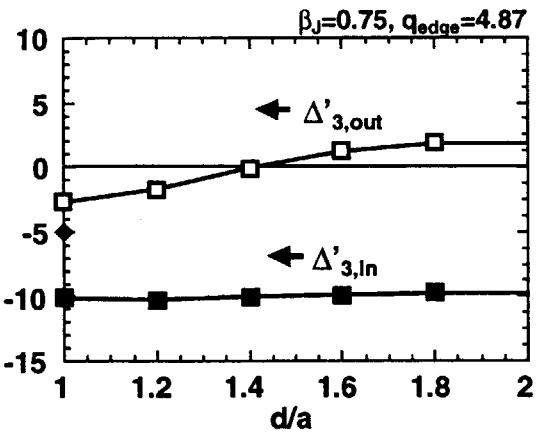

Fig.2. *Dependence of stability parameter of tearing modes, Δ', on the ratio d/a. Here, $\Delta'_{3,in}$ and $\Delta'_{3,out}$ are Δ' at the inner and outer $q = 3$ rational surfaces, respectively.*

3. Parameter Dependence of Growth Rate of RWM

The wall-stabilized high β_N reversed shear discharges are almost always terminated by disruption accompanied with n=1 modes which are attributed to RWMs at $\beta_N > 2.4$ (Fig.3). No significant reduction of the plasma toroidal rotation frequency (~4 kHz near the outer rational surfaces) is observed under the condition that $E_W > 1$. Dependence of the growth rate of the $n = 1$ modes on the plasma volume, V_p, (larger V_p corresponds to smaller d/a) and on the edge safety factor, q^* ($= (5a^2B_T/2RI_p[1 + \kappa^2(1 + 2\delta^2 - 1.2\delta^3)]$, here, B_T is toroidal field, R is major radius, I_p is plasma current, κ is elongation and δ is triangularity) are investigated to reveal characteristics of the wall stabilization effects and the RWM. We confirmed that the

growth rate of the $n = 1$ is much larger than τ_W^{-1} ($\tau_W \sim 10$ ms) with $V_p < 70m^3$ ($d/a > 1.3$) and reduces to $\sim \tau_W^{-1}$ with $V_p > 72m^3$ ($d/a < 1.3$) (see Fig.4(a)). We also confirmed for the data with $V_p > 72m^3$ that the growth rate is enhanced when q^* is close to integer values such as $q^* = 4$ or 5 (see Fig.4(b)). These results clearly shows that the wall stabilization is effective when the plasma surface is close enough to the wall (typically $d/a < 1.3$) but is ineffective if the safety factor near the edge (q^*) is close to an integer value.

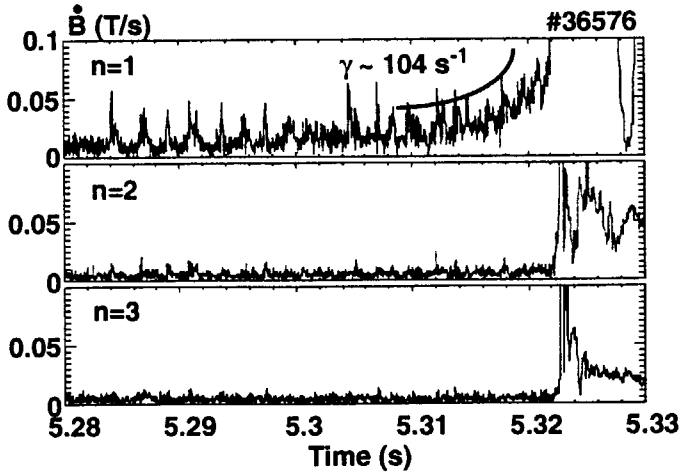

Fig.3. *Time evolution of $n = 1, 2$ and 3 components of perturbed magnetic field measured by a saddle-loop array.*

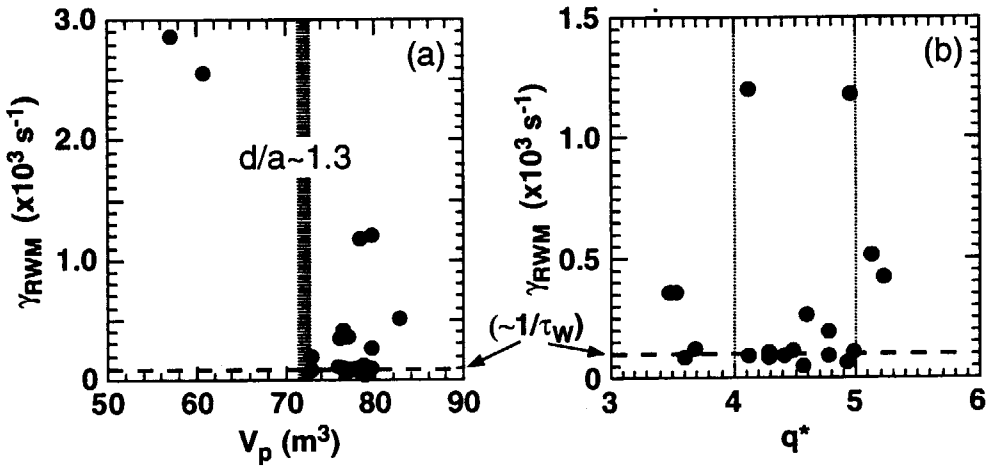

Fig.4. *Dependence of growth rate of the $n = 1$ RWMs, γ, on (a): plasma volume, V_p ($\sim d/a$) and on (b): q^*.*

4. Performance of Wall-stabilized Reversed Shear Discharges

As above-mentioned, by pushing plasmas close to the wall ($d/a < 1.3$), the achievable β_N is improved up to 2.85 owing to the stabilizing effect of the wall (see Fig.1). Such high β_N reversed shear discharges have other suitable characteristics for the advanced tokamak operation. One is that the bootstrap current fraction is more than 60% (the plasma current I_p=1.0 MA, the safety factor near the plasma edge q^* ($\sim q_{95}$) ~ 5) with the poloidal beta $\beta_p \sim 2$. The other is that the confinement does not degrade in the high normalized density regime of $n_e/n_{GW} \sim 1$. Figure

5 shows dependence of the confinement improvement factor, H_{89P}, on the electron density normalized by the Greenwald density, n_e/n_{GW}. The confinement parameter H_{89P} seems to be increasing with increase in the electron density n_e/n_{GW}. This tendency is expected to be due to the internal transport barrier is reversed shear discharges and is different from that of normal shear discharges such as the high-β_p H-mode. If the neutral beam power loss by the toroidal ripple is taken into account, H_{89P} is 3.2 at $n_e/n_{GW} \sim 0.8$.

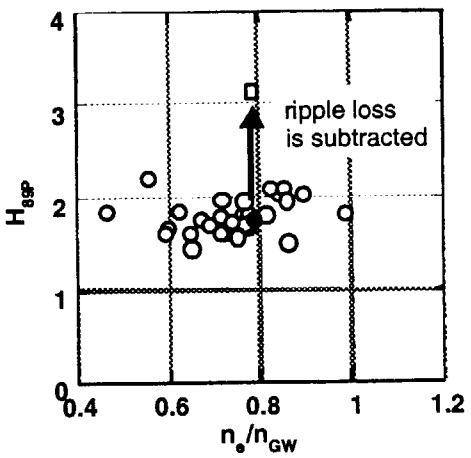

Fig.5. *Confinement improvement factor, H_{89p}, versus electron density normalized by the Greenwald density, n_e/n_{GW}.*

5. Conclusions

Wall stabilization of reversed shear discharges were demonstrated on JT-60U. It is confirmed that both of resistive (tearing) and ideal modes can be stabilized by the wall when the wall is close enough to plasma surface (typically, $d/a < 1.3$) and high β discharges with $\beta_N > \beta_N^{no-wall}$ were obtained. Resistive wall modes were observed in the high β discharges and it is also confirmed that the wall stabilization is effective when the plasma surface is close enough to the wall (typically $d/a < 1.3$) but is ineffective if the safety factor near the edge (q^*) is close to an integer value. Wall-stabilized high β reversed shear discharges have suitable characteristics for the advanced tokamak (steady state with full non-inductive current drive) operation; i.e. simultaneous achievement of high bootstrap current fraction more than 60% with high confinement at the high normalized density regime.

References

[1] J. Manickam, *et al.*, Nucl. Fusion **39** (1999) 1819.
[2] E.J. Strait, *et al.*, Nucl. Fusion **39** (1999) 1977.
A.M. Garofalo, *et al.*, Nucl. Fusion **40** (2000) 1491 and papers cited therein.
[3] A. Bondeson, *et al.*, Phys. Rev. Lett. **72** (1984) 2709.
[4] S. Takeji, *et al.*, Nucl. Fusion to appear.
[5] S. Tokuda, Watanabe, T., Phys. Plasmas **6** (1999) 3012.
[6] A. Bondeson, M. Persson, Nucl. Fusion **28** (1988) 1887.

4.3 Complete stabilization of a tearing mode in steady state high β_p H-mode discharges by the first harmonic electron cyclotron heating / current drive [1, 2]

A. Isayama, Y. Kamada, S. Ide, K. Hamamatsu, T. Oikawa,
T. Suzuki, Y. Neyatani, T. Ozeki, Y. Ikeda and K. Kajiwara

Tearing mode stabilization experiment using EC wave was started in 1999 [3]. In JT-60U, the stabilization experiments have been performed using the first harmonic O-mode EC wave, which is the same as in ITER [4]. Complete stabilization was not achieved in 1999 although magnetic perturbations and electron temperature perturbations were decreased during EC injection [5].

In 2000, two gyrotrons were newly installed. Design value of the total generation power was increased to 3 MW, which corresponds to the injection power of about 2.3 MW [6]. Furthermore, control system for the steerable mirror was modified so that the mirror angle can be changed during a discharge. Stabilization experiment was performed in the similar way as in 1999, where the mode location was estimated from profiles of electron temperature perturbations and safety factor. Mode location was also identified by scanning the steerable mirror during a discharge. By fixing the mirror angle at the optimum one, a neoclassical tearing mode with m/n=3/2 was completely stabilized. In a typical discharge where the complete stabilization was achieved, EC driven current density is calculated to be about 0.15 kA/m^2, which is about twice as large as bootstrap current density. Total EC driven current is calculated to be about 25 kA, which is 2% of plasma current. Stored energy and neutron emission rate were higher (by 12% and 18% respectively) for the case with EC wave injection than that without EC wave injection, which suggests that the reduction of the stored energy and the neutron emission rate was recovered by the tearing mode stabilization. It was found that only partial stabilization was achieved in the higher beta region. A possible reason is that EC driven current is not enough to compensate the 'missing' current.

References

[1] Isayama A *et al.*, Plasma Phys. Control. Fusion **42**, L37 (2000).
[2] Isayama A *et al.*, Nucl. Fusion **41**, 761 (2001).
[3] Ikeda Y *et al.*, Fusion Eng. Design **53**, 351 (2000).
[4] ITER Physics Basis Editors *et al.*, Nucl. Fusion **39**, 2137 (1999).
[5] Isayama A *et al.*, J. Plasma Fusion Res. SERIES **3**, 94 (2000).
[6] Ikeda Y *et al.*, Proc. 18th IAEA Conf. Sorrento (2000), IAEA-CN-77/EXP4/03.

4.4 Characteristics of neoclassical tearing modes in high β_p H-mode discharges [1]

A. Isayama, Y. Kamada and T. Ozeki

In order to sustain a high beta and high confinement plasma, it is important to investigate the characteristics of neoclassical tearing modes (NTMs) because they limit the achievable beta. Onset condition of NTMs in high β_p H-mode discharges, such as density dependence of onset β_N, has been investigated [2]. In 1999, collisionality dependence of onset β_N normalized by Larmor radius was investigated, and it was found that dependence of ion Larmor radius ρ_{i*} is stronger than that of electron collisionality ν_{e*} ($\beta_N/\rho_{i*} \propto \nu_{e*}^{0.36}$) [3].

In 2000, dependence of mode number on discharge condition has been investigated using database containing more than 250 high β_p H-mode discharges. It was found that NTMs with n=2 (m is typically 3) and n=3 (m is thought to be 4 or 5) are observed only in the region of β_p>0.6 and q_{95}<4.5. Existence of the lower limit of β_p suggests a characteristic of NTM: NTMs are not destabilized in a low beta region because of small bootstrap current. Existence of the upper boundary of q_{95} can be understood by considering the relation between the pressure and the safety factor profiles: in low-q discharges, mode rational surfaces for 4/3, 3/2 and 5/3 modes are located in the region of 0.3<ρ<0.7, where steep pressure gradient, which suggests the existence of high bootstrap current, is also observed; in high-q discharges, on the other hand, the mode rational surfaces are not located in this region.

In some discharges, neoclassical tearing mode is not observed even when the value of β_N/ρ_{i*} exceeds the threshold for the mode onset. This fact suggests that there is another factor which determines the onset of neoclassical tearing modes. Effects of the profiles on the mode onset have been investigated by comparing between the high β_p H-mode discharges with and without NNB. It was found that by replacing a part of PNB power with NNB an m/n=2/1 mode was suppressed in spite of higher beta. One of the reasons is considered to be a difference in pressure profiles: by injecting NNB, pressure gradient at 0.3<ρ<0.7 was decreased and thus bootstrap current was decreased. This fact suggests that the beta limit for NTM can be improved by pressure profile optimization using NNB.

Hysteresis in beta value has been investigated in detail. It is found that in a fixed discharge condition (I_p=1.5MA, B_t=3.6T, q_{95}=3.8, δ=0.19, κ=1.5) the normalized beta at the mode onset β_N^{on} is about 3 times as large as that at the mode disappearance β_N^{off} : $\beta_N^{on} \approx 1.6$ and $\beta_N^{off} \approx 0.5$. Hysteresis in ion temperature gradient at the mode rational surface, which is a good measure of pressure gradient, is also found: the ion temperature gradient at the mode onset is about twice as large as that at the mode disappearance.

References

[1] Isayama A *et al.*, Nucl. Fusion **41**, 761 (2001).
[2] Isayama A *et al.*, Plasma Phys. Control. Fusion **41**, 35 (1999).
[3] Isayama A *et al.*, JAERI-Research 2000-035, pp.50-53.

4.5 Influence of MHD instabilities on N-NB current drive [1]

T. Oikawa, A. Isayama and Y. Kamada

Current drive capability of N-NB has been experimentally evaluated in the high electron temperature regime ($T_e = 10\mathrm{keV}$) and confirmed to agree with the theoretical prediction [1]. This validity of theoretical prediction for N-NB current drive was concluded for MHD-quiescent plasmas. However, various instabilities such as sawtooth, beam driven instability and neoclassical tearing mode (NTM) appear in tokamak plasma. Here, influences of beam driven instability and NTM on current drive are briefly summarized. Details are described in Ref. [1].

1 Beam driven instability

In the low density plasmas with beam pressure of N-NB comparable to thermal pressure, a burst-like instability sometimes appeared. Reduction in neutron yield was observed at a large burst activity in the pulse E036546 ($\overline{n}_e \sim 0.65 \times 10^{19}\mathrm{m}^{-3}$). This instability was considered to occur in the central region ($\mathrm{r/a} < 0.3$) from the observations that loop voltage inside $\mathrm{r/a} = 0.3$ and T_e at $\mathrm{r/a} = 0.3$ increased just after burst. Observed reduction in central T_e was too small to explain increase in loop voltage. Thus, increase in loop voltage indicated loss of non-inductive current. In this discharge, bootstrap current and P-NB current drive were negligibly small because of low pressure and β_p and balanced injection of tangential P-NB. Consequently, it can be considered that reduction in non-inductive current was caused by loss of N-NB fast ions carrying current. Lost driven current of N-NB inside $r/a < 0.3$ was estimated in maximum to be $\sim 40\mathrm{kA}$ corresponding to 7% of total N-NB driven current. In most cases in other discharges with similar instabilities, clear influence on plasma as in the case mentioned here was not observed. Thus, reduction in N-NB driven current was not serious in present experiments. However, with higher beam pressure and different safety factor profile, there is a possibility that degradation of current drive caused by the instability can not be negligible.

2 Neoclassical tearing mode

In high beta discharges, neoclassical tearing instability appears when the normalized beta reaches the onset level. Reduction of the neutron production rate or saturation of its increase were observed during the instability. From comparison of the measured neutron yield with the calculated one by the transport code, we can discuss the influence of the instability on fast ions. We have concluded as :

· Reduction of neutron yield indicates loss or redistribution of fast ions.
· Influence for N-NB ions was larger than that for lower energy beam.
· Influence on beam ions was enhanced with increasing activity of instability.

References

[1] Oikawa, T., et al., Nucl. Fusion **41**, 1575(2001).

4.6 Collapse of density pedestal by giant ELM on JT-60U

N Oyama, K Shinohara, Y Kamada, Y Miura, T. Oikawa and S. Takeji

The effect of instantaneous heat and particle pulse on divertor due to the individual ELM pulses is now recognized as one of the critical issues. However, the mechanism and characteristics of an ELM pulse are not clear, because diagnostics with high spatial and time resolutions are required for detailed observation of each ELM pulse. Recently, two channels of the O-mode heterodyne reflectometer system have been installed at midplane on JT-60U to measure the behavior of cut-off density positions, that enable the observation of such fast phenomena as ELMs in good time and spatial resolution. The O-mode reflectometer system successfully measured the phase change of reflected signal without any kind of filtering correction. Observed phase change shows the density profile deformation together with the time scale of each ELM phase, precursor in density fluctuation and consequences such as D_α burst and SOL density increase.

From the phase evolution of reflected signal, an ELM event can be classified into the precursor phase, collapse phase, recovery phase and relaxation phase. The typical time scale of each phase is 200-500 μs, 100-350 μs, 200-500 μs and 6-10 ms, respectively. Due to a collapse of pedestal structure in a density profile by one ELM, a certain density layer, located near the shoulder of the pedestal, moved about 7 cm inside the plasma in collapse phase. The cut-off layer reached 10 cm inside the separatrix, which corresponded to twice the pedestal width of ~5 cm. However, we did not obtain the inner information such as the radial extent suffering from ELMs and how fast the ELM effects reach the inner plasma. In the relaxation phase, the increase of SOL density was observed in both reflectometer and interferometer as a result of enhancement of recycling at the divertor region due to the ELM heat load. The finite time delay between reflectometer signal and D_α signal was observed and varied in a range of 105 to 195 μs (average 148 μs). Since the connection length, L_c, is about 28 m, mean velocity of ELM pulse, v_{ELM}, is simply estimated to be 1.9×10^5 m/s. When we assume $v_{ELM} = C_s$, the mean temperature of ELM pulse is estimated to be 370 eV, which corresponds to 1/8 of the pedestal temperature. A precursor that has the displacement gradually growing up to ± 1 cm in a density profile is clearly observed in the reflectometer signal, though there is no clear precursor in magnetic fluctuation. Although the pedestal collapse reached 10 cm inside of the separatrix, the different response on the density signal between reflectometer and FIR interferometer was observed. From the evaluation of particle loss and supply during an ELM, a poloidal structure in an ELM event, such as a localized structure on the low-field side of the plasma, is supposed as one of the possible structures.

Reference

N Oyama. *et al.*, Plasma Physics and Controlled Fusion, **43** (2001) 717.

4.7 Alfvén eigenmodes driven by energetic ions in JT-60U

K. Shinohara, Y. Kusama, M. Takechi, A. Morioka, M. Ishikawa, N. Oyama, K. Tobita, T. Ozeki, S. Takeji, S. Moriyama, T. Fujita, T. Oikawa, T. Suzuki, T. Nishitani, T. Kondoh, S. Lee, M. Kuriyama, the JT-60 Team
G. J. Kramer[1], N. N. Gorelenkov[1], R. Nazikian[1], C. Z. Cheng[1], G. Y. Fu[1], A. Fukuyama[2]

Instabilities in the Alfvén Eigenmodes (AEs) range of frequencies can cause enhanced loss of α particles in burning plasmas with a high α particle pressure gradient and can prevent the plasma from sustaining the fusion burn. The enhanced α loss may also damage the first wall. The understanding of the enhanced fast particle loss caused by AEs is one of the most important issues for an operation of fusion reactors.

Instabilities with frequency chirping in the frequency range of AEs have been found in the N-NB injection with high beam energy of ≈360 keV in JT-60U. Our experiments were performed with energetic ion parameters similar to those of α particles expected for ITER: 0.1 % < $<\beta_h>$ < 1% and $v_{b//}/v_A \approx 1$. One type of the observed instabilities, the Slow FS (frequency sweeping) mode, appears with the frequency inside the Alfvén continuum spectrum and its frequency increases to a gap frequency of TAE on the equilibrium change time scale of ≈ 200 ms. The frequency of Slow FS modes seems to correlate with the equilibrium parameters of bulk plasma. Another type of the observed instabilities, the Fast FS mode, appears with its frequency in the TAE gap. Most of Fast FS modes consist of several branches with fast frequency chirping; the mode changes its frequency by 10 - 20 kHz in 1 - 5 ms. During the Fast FS mode, abrupt large-amplitude events, ALEs, often appear. ALE has a large amplitude, which reaches up to $\tilde{B}_\theta/B_\theta \approx 10^{-3}$ at the first wall, and a very short time scale of 200 - 400 μs. Large drop of neutron emission rate and significant increase in fast neutral particle fluxes are observed during these ALEs. The loss of energetic ions increases with the amplitude of $\tilde{B}_\theta/B_\theta$. The loss appears when the magnitude of magnetic fluctuation is larger than ≈ 10^{-4} at the first wall. Energy dependence of fast neutral particle fluxes is newly observed by using a CX-NPA. The energy dependence is consistent with the wave-particle resonance condition. This suggests that "mode particle pumping" loss mechanism is plausible for explaining the observed energetic ion loss.

We observed AE activity near/in the ITER relevant domain in terms of $<\beta_h>$ and $v_{b//}/v_A$. This result indicates a basic message that AE can be destabilized when necessary conditions are satisfied in the ITER relevant domain, even though there remains differences between the case of ITER and that of N-NB experiments in JT-60U, e.g. the profile of β_h of our

[1] Princeton Plasma Physics Laboratory
[2] Kyoto University

experiment is more peaked one, the velocity distribution of α particles is isotropic. One of the necessary conditions found in JT-60U N-NB experiments is a low shear q-profile, which might not appear in a normal operation scenario but will likely appear in an advanced operation scenario.

References

[1] K. Shinohara, *et. al*, Nucl. Fusion **41**, 603 (2001).

[2] K. Shinohara, *et. al*, Alfvén eigenmodes driven by energetic ions in JT-60U, in Fusion Energy (Proc. 18th Int. Conf. Sorrento), IAEA-F1-CN-77/EXP2/5, Vienna, 2000, IAEA.

[3] N. N. Gorelenkov, *et. al*, Fast particle effects on the internal kink, fishbone and Alfvén modes, in Fusion Energy (Proc. 18th Int. Conf. Sorrento), IAEA-F1-CN-77/TH6/1, Vienna, 2000, IAEA.

4.8 Nonlinear interaction between MHD instability driven by NNBI and energetic particles

M. Takechi, K. Shinohara, M. Morioka, Y. Kusama, S. Takeji, Y. Shibata, M. Ishikawa

1. Introduction

The MHD instabilities driven by alpha particles or energetic particles generated from neutral beam injection (NBI) or from ion cyclotron heating eject the energetic particles before their thermalization and lead to degradation of the efficiency of heating and current drive by energetic particles. It has been reported that MHD instabilities driven by energetic particles generated from Negative ion source NBI (NNBI) have been observed in JT-60U plasmas [1, 2]. It has been reported that the reduction of neutron emission rate coincides with the MHD instabilities. Moreover, the MHD instabilities have nonlinear characteristics such as bursting modulation of amplitude and rapid frequency sweep [1.2]. This reduction of D-D neutron emission is dominated by reduction of beam-thermal reaction in the NNBI case. Therefore stabilization of the MHD instabilities can be explained by prompt loss or redistribution of energetic particles.

In the case of Alfvén eigenmodes (AEs), the destabilization term is written as follows

$$\gamma_f \propto \beta_f(\frac{\omega_{*f}}{\omega}-\frac{1}{2})F(v) \qquad (1)$$

where β_f, ω_{*f}, ω and F are, the beta value, the drift frequency of energetic particles, the mode frequency and fraction of energetic particles related to destabilization in the velocity space, respectively. Prompt loss and redistribution of energetic particles decrease β_f and ω_{*f}, respectively. The simplest model of the modes is a simultaneous differential equation, which is called predator-prey relationship as follows

$$\frac{da}{dy}=na \qquad (2)$$

$$\frac{dn}{dy}=1-a \qquad (3)$$

where, a, n and y are the normalized amplitude, the normalized population of high energy particles and the normalized time, respectively. The numerical solutions of the equation are sinusoidal as shown in Fig. 1 (a). The interval of the period increases as the amplitude of the mode increases as shown in Fig. 1 (b). We compare this prediction of the interaction between the mode and energetic particles with experimental observations. We use the amplitude of magnetic fluctuation instead of that of instabilities and the neutron emission rate instead of the population of the energetic particles.

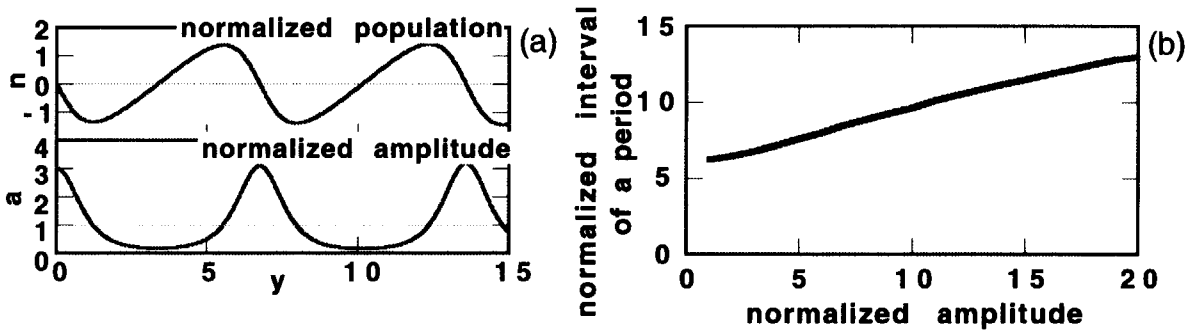

Fig. 1 Typical solutions of eqs. (2) and (3). (a) Time evolution of the normalized population of energetic particles and the normalized amplitude of the instability. (b) The normalized interval of a period increases gradually as the normalized amplitude of the instabilities increases.

2. Experimental setup

The magnetic fluctuations are measured with usual Mirnov coils and digitized at a 0.5 or 1 MHz sample rate. We calculate and plot the mode number and the direction of mode propagation (Fig. 2 (b)) in the range of whole possible frequency and time in addition to the usual calculation of power spectral density (PSD) of the magnetic fluctuation (Fig. 2 (a)). This new plotting method helps us to identify the modes even if many modes are observed intricately.

3. Experimental results

We investigate an NNB injected plasma with a low toroidal magnetic field B_t in order to increase the ratio of beam velocity to Alfvén velocity and the beta value of high energetic ions β_h. Furthermore, the plasma current is relatively low (I_p < 1 MA) in order to emphasize the reduction of the confinement of energetic particles. The 360 keV and 80 keV deuterium neutral beams are injected into a deuterium plasma. Injected power of the Negative NBI is P_{NNBI} ~ 3.8 MW and that of Positive NBI is P_{PNBI} ~ 2 MW. B_t = 1.2 T and I_p = 0.6 MA. With the OFMC code $<\beta_h>$ and β_{hpeak} are calculated to be ~0.9 % and ~5 %, respectively. Figure 2 (a) shows the temporal evolution of contour plot of PSD of the magnetic fluctuation. As shown in Fig. 2 (a), it is difficult to identify observed instabilities with presumable MHD instabilities. To avoid this difficulty, we calculate cross correlation between the signals of two magnetic probes separated about 40 degree in the toroidal direction. When the coherence is sufficiently high (larger than 0.9 in this paper), we plot the respective symbols corresponding to the mode number and the propagation direction. The most intense fluctuation, which is detected from 4.2 to 5.5 s at the frequency range of 40-60 kHz in Fig. 2 (a), has a toroidal mode number of n = 1 and propagates in the co-direction. The mode is presumed to be AE because the frequency of the mode is related to the Alfvén velocity, and the direction of propagation is consistent with that of the AE. The other modes with n=2 or n=3 are detected in the frequency range higher than n=1 mode. The modes are also presumed to be AE modes. Moreover, many modes can be detected. But we cannot identify all of the modes.

The intense n = 1 mode has the two features in its nonlinear temporal evolution. One is bursting modulation of amplitude

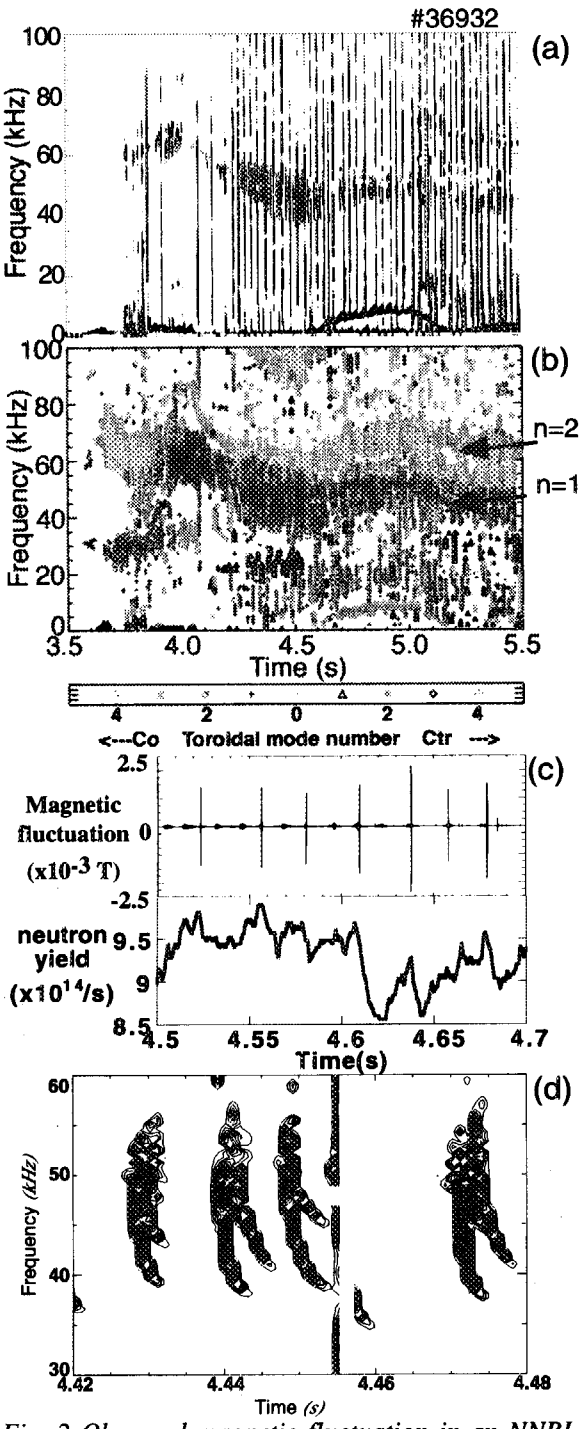

Fig. 2 Observed magnetic fluctuation in an NNBI heated plasma with B_t=1.2 T and I_p=0.6 MA. (a) A contour plot of the amplitude. (b) Toroidal mode number and direction of propagation. (c) A filtered magnetic fluctuation calculated by Fourier decomposition and neutron yielding. (d) Detail of the temporal evolution of the mode frequency.

which correlates with a drop of neutron emission rate as shown in Fig. 2 (c). The other is the rapid frequency sweep shown in Fig.2 (d). Hole and clump pair creation in the particle distribution function is responsible for this frequency chirping [3]. Surprisingly, the amplitude of this instability reaches ~10^{-3} T at the vacuum vessel. According to a numerical calculation, this value of magnetic instability is predicted to be sufficiently large to affect confinement of high energetic particles [4]. The drop of the neutron emission rate is $\Delta s/s$ ~ 8 % and larger than following experimental results and the intervals of bursts are ~30 ms and are relatively long.

The MHD instabilities driven by energetic particles are also observed in NNB injected plasmas with a higher toroidal field and a higher plasma current. They seem to affect the plasma performance. Figure 3 shows the contour plot of the magnetic fluctuation in the integrated high performance plasma with high β_p mode. The 390 keV NNBI of ~5.4 MW and PNBI of ~20 MW were injected into the plasma of B_t = 2.1 T and I_p = 1.0 MA. To achieve the large fraction of noninductive current drive the plasma current is set to be relatively low. $<\beta_h>$ and β_{hpeak} are estimated by OFMC code ~0.65 % and ~3 %, respectively. Figure 3 (a) seems to be very similar to Fig. 2 (a) in terms of bursting modes. However, in contrast with the burst in Fig. 2 (a) which consists of a single mode of n = 1, the burst in the Fig. 3 (a) consists of many modes, which have different toroidal mode numbers ranging n=3 to 8 as shown in Fig. 3 (b). Thus, the new plotting method is powerful for such instabilities. The fluctuation of lower frequency has a lower toroidal mode number, such as n = 3 in Fig.3 (b). The modes are also presumed to be AEs because the frequencies of the modes are ranging in the predicted Alfvén gap frequency, and the directions of propagation of the observed modes are also consistent with that of the AE. The reduction rate of neutron emission rate and the amplitude of

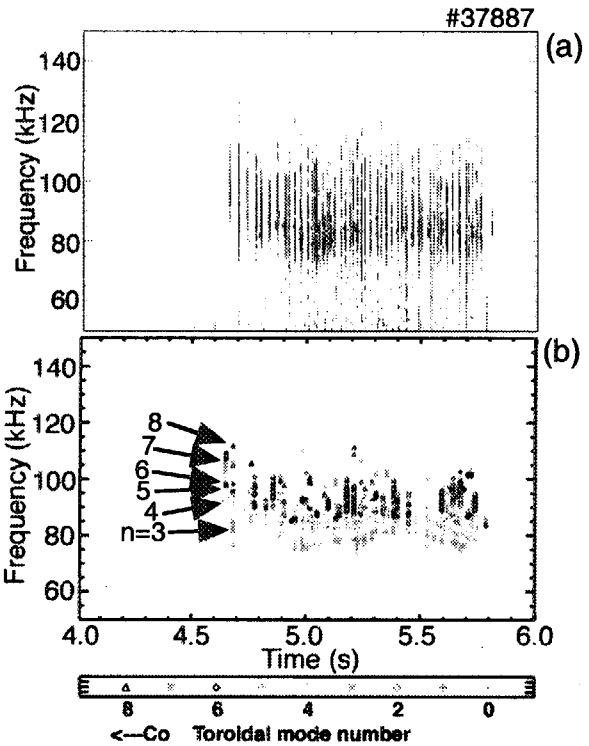

Fig. 3 Observed magnetic fluctuation in an NNBI heated high β_p mode plasma. (a) A contour plot of the amplitude. (b) A plot of toroidal mode number and direction of propagation.

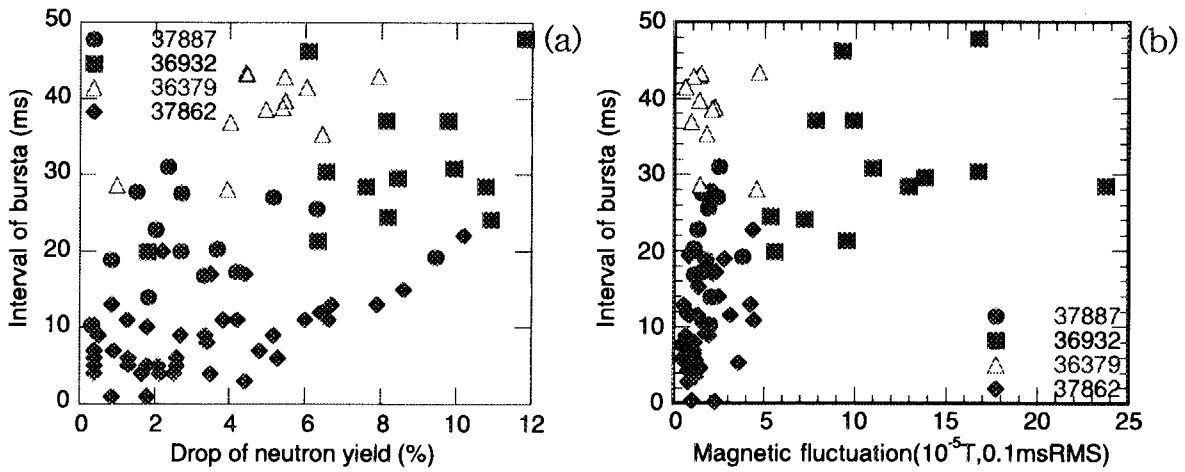

Fig. 4 Interval of bursts of magnetic fluctuations as a function of neutron drop (a) and magnetic fluctuation averaged 0.1 ms (b).

the magnetic instability are relatively smaller than those in the previous low B_t/I_p plasma; $\Delta s/s \sim 3$ % and B ~10^{-4} T. The intervals of bursts ~20 ms is relatively shorter than that in the previous plasma. This is consistent with the prediction discussed in chap. 2.

The drop of neutron emission rate and the amplitude of magnetic fluctuations seem to be related to interval of bursts, but they are widely scattered (Fig 4). The injected neutral beam power in the shot of #36379 is half to 2/3 of that in other shots. Therefore the beam fueling rate in #36379 is as small as the beam power. The scatter will be reduced taking into account of such difference in beam fueling. The longer the interval between the bursts of the modes are, the more affected by the modes energetic particles are. If the deposition power of NNBI does not change so much, we can easily estimate the influence of the mode on the confinement of energetic particles from the interval of bursts.

The AEs are also observed in RS plasmas in spite of relatively low $<\beta_h>$ (Fig. 5). Continuous AE modes are observed in an RS plasma of B_t = 2.7 T and I_p = 1.0 MA from 6.2 s to 7.7 s. To avoid the minor collapse responsible for the interchange mode only half unit of NNBI was injected. Therefore, $<\beta_h>$ and β_{hpeak} are fairly low; ~0.12 % and ~0.8 %, respectively. The observed mode does not seem to affect confinement of energetic particles at present. However in future we will inject much more NNBI power into plasmas in order to achieve higher performance and larger non-inductive driven current. In these experiments, we must pay much attention to the interaction between the mode and energetic particles.

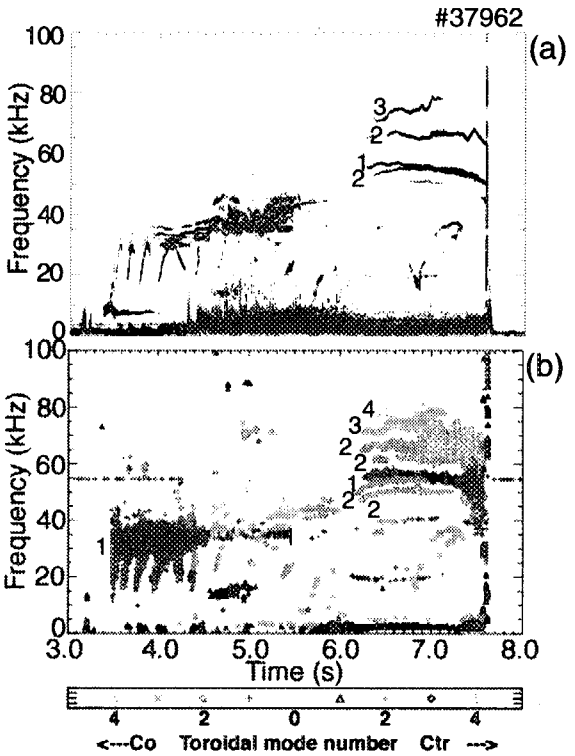

Fig. 5 Observed magnetic fluctuation in an NNBI heated plasma with reversed magnetic shear. (a) A contour plot of the amplitude. (b) A plot of toroidal mode number and direction of propagation.

4. Conclusion and summary

We investigate the nonlinear interaction between the MHD mode driven by energetic particles generated by NNBI and energetic particles. The interval of the burst is related to the mode amplitude as predicted by nonlinear interaction, so-called predator-prey relation ship, if we take difference of beam fueling rate into account. We can immediately estimate the influence of the mode on the confinement of energetic particles from the interval of bursts from experimental results. However the relation in JT-60U is not so clear in contrast to results of DIII-D and PBX [3]. The reasons are considered as follows. (1) When we consider the interaction between MHD modes and energetic particles, only prompt loss of energetic particle is taken into account. Redistribution may play a significant role for interaction between the MHD mode and energetic particles in JT-60U. (2) Many modes are destabilized at the same time or alternatively. We cannot calculate with Eqs. 2 and 3 in such a situation any more.

References

[1] Y. Kusama, *et al.*, Nucl. Fusion **39** (1999) 1837
[2] K. Shinohara, *et. al*, Nucl. Fusion **41** (2001) 603
[3] W. W. Heidbrink, *et al*, Phys. Fluids B **5** (1993) 2176
[4] Y. Todo, private communication.

4.9 Analysis of charge exchange neutral particle energy spectrum during N-NB heating by using OFMC code

A. Morioka and M. Suzuki

1. Introduction

The negative ion based neutral beam (N-NB) injector is utilized for plasma heating and current drive in JT-60U. The N-NB injector is also planned to be employed in ITER. The energy of injected neutral beam has exceeded 350 keV in the JT-60U N-NB system. It is important to study the behavior of fast ions generated by N-NB for efficient plasma heating with N-NB. In JT-60U, the high-energy neutral particles have been measured by charge exchange neutral particle analyzers (CX-NPAs). However, in large tokamaks, the measured energy spectrum by the CX-NPA is not necessarily equal to that of fast ions and a numerical calculation is required to relate them. We used the orbit following Monte Carlo code (OFMC) [1] to calculate the charge exchange neutral particle energy spectrum in N-NB heated plasmas.

2. Measurement

High-energy neutral particles injected by N-NB are ionized in plasmas by charge exchange reaction and ionization reaction. The ionized particles collide with ions and electrons in the plasma. In this process, the energetic ions experience pitch-angle scattering and slowing down. Most of these ions are thermalized. However, some of the fast ions are neutralized by charge exchange reaction in the plasma. Neutral particles thus generated have information on fast ions. The behavior of fast ions has been assessed by using the CX-NPA.

The energy spectrum of charge exchange neutral particles is based on line integration along the line of sight of CX-NPA. The measured flux at the energy E ($\Gamma_{meas.}(E)$) of charge exchange neutral particles is given by

$$\Gamma_{meas.}(E) = \xi \bullet \int n_0 \bullet n_i \bullet < \sigma v >_{cx} dl$$

where ξ is the probability that charge exchange neutrals escape from the plasma without being re-ionized, n_0 is the neutral particle density, n_i is the fast ion density, and $<\sigma v>_{cx}$ is the cross section of charge exchange reaction. In a large tokamak, the probability of reionization of charge exchange neutrals is not negligible (namely ξ is less than unity) and it is difficult to estimate ξ. We cannot obtain the energy distribution of fast ions directly from the measured spectrum of CX-NPA.

3. Calculation

We use the orbit following Monte Carlo code (OFMC) to calculate the energy spectrum of charge exchange neutral particles during N-NB heating. In OFMC, orbits of many test particles are followed during its slowing-down process. We calculate the probability that each test particle at each step of slowing-down process experience charge exchange reaction, escapes from the plasma, and enters into the slit of CX-NPA by

$P_{cx}\, P_{ni}\, \Delta\Omega$.

Here P_{cx} is the probability that the fast ion experience charge exchange reaction on the line of sight of CX-NPA, P_{ni} is the probability that charge exchange neutrals escape from the plasma without being re-ionized, and $\Delta\Omega$ is the probability that the velocity vector of fast ion is directed to the entrance slit of CX-NPA. We calculate P_{cx}, P_{ni} and $\Delta\Omega$ for each step of slowing-down process of each test particle and add them to obtain the energy spectrum. The calculated spectrum is shown in Fig.1. Now we can calculate the expected charge exchange neutral particle with the OFMC code.

We will compare the calculated energy spectrum of charge exchange neutral particles with the measured one.

Reference

[1] K. Tani, et al., J. Phys. Soc. Jpn. **50**, 1726 (1981).

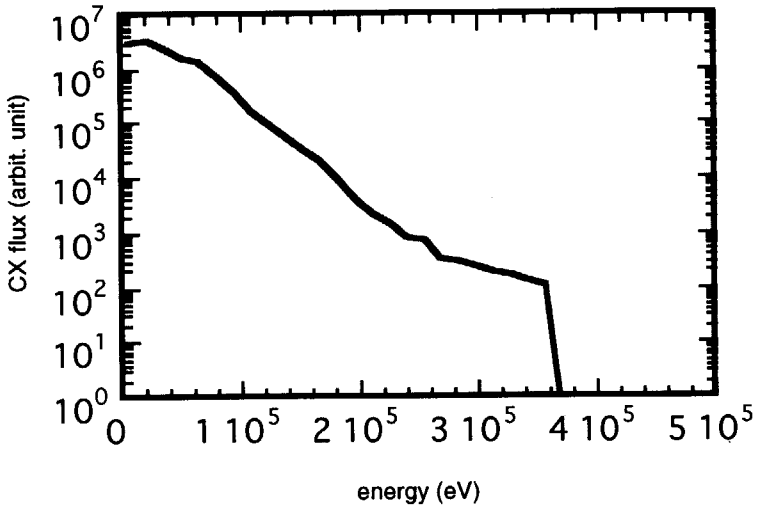

Fig.1 . The calculated CX energy spectrum with N-NB heating by OFMC-code (E032359 (t=4.5 s)).

5. Plasma Control and Disruption

5.1 JT-60 plasma shape real-time reproduction system based on the Cauchy-condition surface method

Y.M. Miura, K. Kurihara, Y. Kawamata, T. Fukuda, Y. Hoshi,
O. Kiyoshi, T. Kakefuda, K. Akiba, S. Takashima

1. Introduction

Accurate control of plasma position and shape is needed from the viewpoint of advanced plasma control, effective RF heating, and protection of in-vessel devices such as the divertor dome. The function parameterization method (FPM) has been used for JT-60 plasma real-time control, in which the parameters of plasma position and shape are calculated through the formulas statistically determined using the method of least-squares from the numerical database of plasma equilibria. This method, however, has the problem that the accuracy significantly deteriorates for a plasma outside the operating region covered by the equilibrium database.

In order to solve the problem and to meet the performance required for advanced plasma control, a new plasma shape real-time reproduction system has been developed. In this system, a novel plasma reproduction technique, called the Cauchy-condition surface (CCS) method [2], has been applied to real system for the first time. This method is based on analytical exact solution of Maxwell's equations, where a Cauchy condition (both Dirichlet and Neumann conditions) be identified on the hypothetical surface located inside a plasma.
For the specific problem, the Cauchy condition of the magnetic field and flux are calculated from the actual signals of magnetic sensors and poloidal field coil currents. After identification of the Cauchy condition, the magnetic flux can be calculated at any points outside the CCS. A separatrix, for example, can be searched for as a magnetic flux contour passing an X point.

As compared with FPM, the CCS method has the following advantages: (a) accurate detection of various plasma position and shape parameters is possible in the broader operational region (no need to make database); (b) reproduction accuracy can be improved corresponding to the increase in the number of sensors. In addition, this method uses only "straight forward" calculation while proper positioning filaments is necessary for "the filament current approximation (FCA) method" commonly used for full shape reproduction. Thus (c) this method is preferable for real-time control system.

2. Real-time system

The newly developed real-time control system consists of five processors connected by PCI- bus system. The CPU is Alpha processor 21164 (500-MHz) with 512-MB memory. This memory size permits to employ the "table-look-up" method for extreme reduction of computing time. First, the current weight centroid position (R_J, Z_J) of plasma is calculated in a 250-μs cycle by the CPU#1. This determines the CCS position. Second, an X-point position X_p is searched for as a saddle point of the magnetic flux by the CPU#2.

Consecutively, CPU#2 and CPU#3-5 trace the contour lines in their own zone in the vacuum vessel in parallel. After this, the contour lines are composed into a continuous separatrix line. The parameters such as plasma center position R_p, triangularity δ, clearance δ_0 between the vacuum vessel wall and plasma surface, are also calculated every 1 ms.

3. Application

Figure 1 shows the experimental results using this system. A comparison between the results of the CCS and full-equilibrium calculation (FAME) shows a good agreement in R_p and Z_J control except for X_p. Figure 2 shows the strike points calculated by the CCS and the same full-equilibrium code (FBEQU) as FAME. In this figure, peak positions of the ion saturation current and C II line emission are indicated. These results suggest that the CCS calculation gives closer positions to the measured peak points of heat flow than FBEQU. In the FBEQU, internal inductance l_i is provided by the FCA calculation, which might be a reason for the large error of FBEQU.

4. Summary

The new real-time reproduction system has been started to work in the experiment. The plasma shape and parameters are calculated at a 1-ms cycle. The other parameters such as magnetic axis position, lambda value and plasma current, are under consideration.

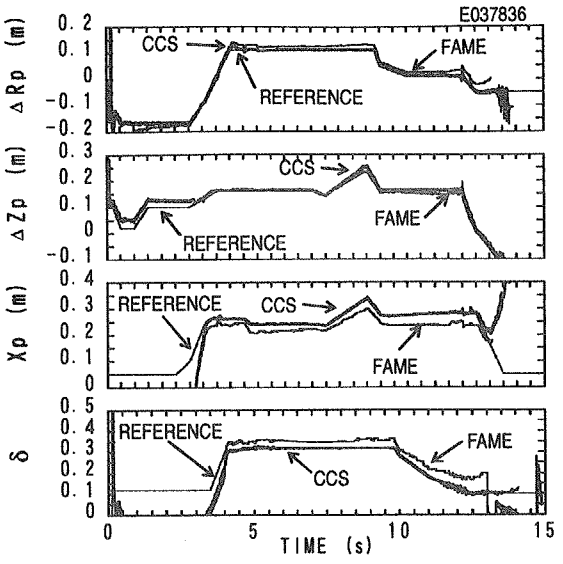

Fig1 Experimental results using the CCS real-time control system

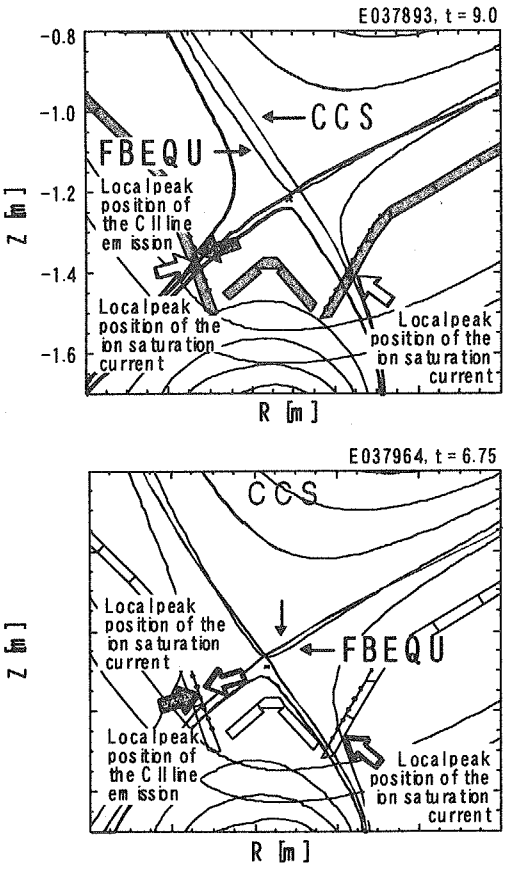

Fig.2 Comparison of strike points calculated by the CCS and fully-equilibrium calculation (FBEQU), and ones measured by the ion saturation current and C II line emission.

Reference

[1] Miura M. Y. Kawamata., Fukuda T. and Kurihara K., JAERI-Research 98-039, 19 (1998)

[2] Kurihara K., Fusion Eng. and Design **51-52**, 1049 (2000)

5.2 Development of a real-time NTM detection and EC injection system

A. Isayama, T. Oikawa, T. Fukuda and S. Sakata

1. Introduction

In high β_p H-mode discharges, neoclassical tearing modes (NTMs) such as m/n=3/2 and 2/1 appear and limit the achievable beta [1-5]. Here m and n are poloidal and toroidal mode numbers, respectively. Theoretical simulation on ITER shows that electron cyclotron (EC) power needed to stabilize an NTM can be reduced if the EC wave is injected in an early phase of the mode growth [6], indicating the importance of real-time NTM stabilization. Experimental results in JT-60U show that the structure of magnetic island can be measured using the heterodyne radiometer [7] and that a 3/2 NTM can be completely stabilized by using the 110 GHz ECRF system [8], which encourages to develop a real-time NTM stabilization system. In this section, a system description for the real-time NTM detection and EC wave injection is given. Initial experimental result and prospects for real-time detection of mode location are also described.

2. Real-time NTM Detection and EC Injection System

Schematic diagram of the signal transmission between the heterodyne radiometer system (HRS) and the real-time processor (RTP) [9] is shown in Fig. 1. ECE signal measured by the HRS is first sent to an electrical-to-optical (EO) converter through coaxial cables with bayonet Neil-Concelman (BNC) connectors. Frequency range of the EO converter is 0 to 20 kHz, which is enough to measure the electron temperature perturbations caused by NTMs because typical frequency of the perturbations is less than 10 kHz. After being transmitted through 200 m optical fibers whose transmission loss is much smaller than that of coaxial cables, the signals are sent to an optical-to-electrical (OE) converter in a cubicle located at an electromagnetically isolated area, and converted to electric signals as an input to the RTP.

Algorithm to evaluate a perturbation level of electron temperature is needed to be as simple as possible to reduce the calculation time. We consider the standard deviation of the signal as a measure of the perturbation level, which are defined as follows:

$$M = \left[\frac{1}{N}\sum_{n=1}^{N}(T_n - m)^2\right]^{1/2} / m \quad , \qquad m = \frac{1}{N}\sum_{n=1}^{N} T_n \quad .$$

Here, T_n is electron temperature in the n-th channel, and m is the average of the temperature. N is the number of data to be calculated in a step, and it is set at 100. This method is advantageous in that the perturbation level can be evaluated without calculating a frequency spectrum. The perturbation level can be evaluated even when the output of the HRS is not calibrated because the standard deviation is normalized by the average of the signal. The

average m is also used for electron temperature feedback control. There are three steps in one cycle of the calculation: initialization, data acquisition and calculation. Calculation time in each step is measured to be about 0.5 ms, 1 ms and 0.5 ms, respectively.

Figure 2 shows an example of the display to set the experimental conditions. In this display, the following conditions are designated: (1) whether the feedback system is used or not, (2) when to start the feedback, (3) when to quit the feedback, (4) how to monitor the signals, (5) location to be monitored, (6) channel to be monitored, (7) when to quit the EC injection, (8) criterion for starting EC injection, (9) criterion for quitting EC injection, and (10) EC pulse width. The fourth item specifies how the signal is referred to, namely, either the channel nearest to a specified position is monitored, or a specified channel is monitored. The value in the fifth item is referred to in the former case, and the value in the sixth item is referred to in the latter case. In the discharge shown in Fig. 2, channel 3 is used for monitoring the electron temperature perturbations. The seventh item specifies when to quit the EC wave injection: whether the EC wave injection should be stopped when the perturbation level reaches below the specified level, or the EC wave should be injected for a specified duration. The value at the ninth item is referred to in the former case, and the value at the tenth item is referred to in the latter case. In the discharge shown in Fig. 2, the EC pulse width is set at 2000 ms.

3. Application to Experiment

Typical waveforms in a real-time NTM detection and EC injection experiment are shown in Fig. 3. Plasma parameters are as follows: plasma current I_p=1.5 MA, toroidal field B_t=3.6 T, major radius R=3.2 m, minor radius a=0.77 m, safety factor at the 95% flux surface q_{95}=3.9, elongation κ=1.6, triangularity δ=0.20. EC injection angle is set at 43°, which is optimum to stabilize a 3/2 NTM in this configuration. Neutral beams of 19 MW are injected at t=4.8 s, and a 3/2 NTM starts to grow at t=5.7 s, as shown in Fig. 3(a). As the amplitude of magnetic perturbations with n=2 increases, the perturbation level (Fig. 3(b)) also increases. Note that the perturbation level is not equal to zero even without NTMs because a perturbation level of about 1.3% corresponds to the noise level. When a perturbation level exceeds the designated criterion, which is 2% in this discharge, a control signal to inject EC wave is turned on (Fig. 3(c)). In this discharge, EC wave is injected about 200 ms after the mode onset. Although power and pulse width of the EC wave were not enough to stabilize the NTM due to insufficient conditioning of gyrotrons, it is shown that the feedback system functions satisfactorily.

The EC injection angle is fixed at the optimum in the above experiment. However, mode location also has to be identified in real-time because it can be changed during a discharge. In general, mode location can be identified by measuring amplitude or phase of

electron temperature perturbations. When electron temperature fluctuations near a magnetic island are measured, reduction of the amplitude is observed at the center of the island, and phase inversion is observed across the center of the island at the same time . Thus, there are two ways to find out the mode location. We investigated the possibility identifying the mode location by evaluating the amplitude of electron temperature fluctuations using the above system. Figure 4(a) shows amplitude profiles of electron temperature perturbations in shot E37774. As shown in this figure, decrease in amplitude is observed near the position of channel 5. According to a phase profile of the electron temperature perturbations evaluated by using fast Fourier transform (Fig. 4(b)), phase inversion is observed across channel 5, which suggests that the center of the island is located at this position. Although it is found that signals in each channel are needed to be smoothed to improve the signal-to-noise ratio, this result shows that mode location can be also identified in real-time with minor modifications of the present system.

4. Summary

System for real-time NTM detection and EC wave injection was developed. In 2000, amplitude of electron temperature perturbations was successfully evaluated in real-time, and EC wave was injected about 200 ms after the mode onset. It was also shown that the mode location can be identified with minor modifications of this system.

References

[1] Kamada Y *et al.*, *Plasma Physics and Controlled Nuclear Fusion Research 1995* (Proc. 15th Int. Conf., Seville, 1994) vol.1 (IAEA, Vienna) 1995 p.651.

[2] Kamada Y *et al.*, *Fusion Energy 1996* (Proc. 16th Int. Conf., Montreal, 1996) vol.1 (IAEA, Vienna) 1997 p.247.

[3] Kamada Y *et al.*, Nucl. Fusion **39**, 1845 (1999).

[4] Isayama A *et al.*, J. Plasma Fusion Res. SERIES **3**, 94(2000).

[5] Isayama A *et al.*, Nucl. Fusion **41**, 761 (2001).

[6] Pustovitov V D *et al.*, Proc. 18th IAEA Conf. Sorrento (2000), IAEA-CN-77/ITERP/07.

[7] Isayama A *et al.*, Plasma Phys. Control. Fusion **42**, L37 (2000).

[8] Isayama A *et al.*, Plasma Phys. Control. Fusion **41**, 35 (1999).

[9] Sakata S, Koiwa M, Aoyagi T and Matsuda T, 'Development and Upgrade of New Real Time Processor in JT-60 Data Processing System', JAERI-Tech 2000-43 (2000) (in Japanese).

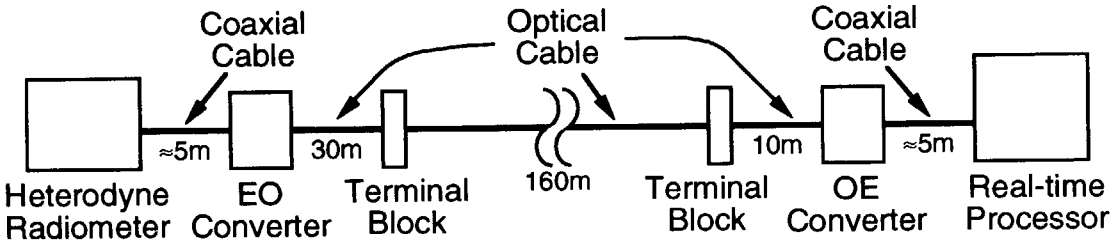

Fig. 1: Schematic diagram of the feedback system.

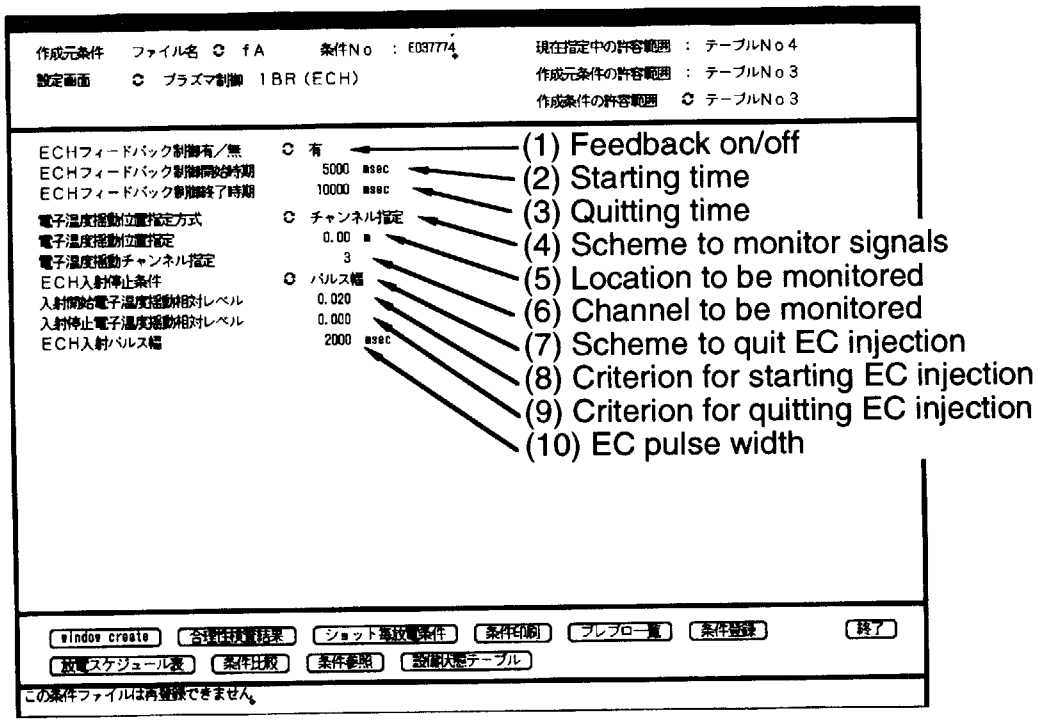

Fig. 2: Display on the control terminal.

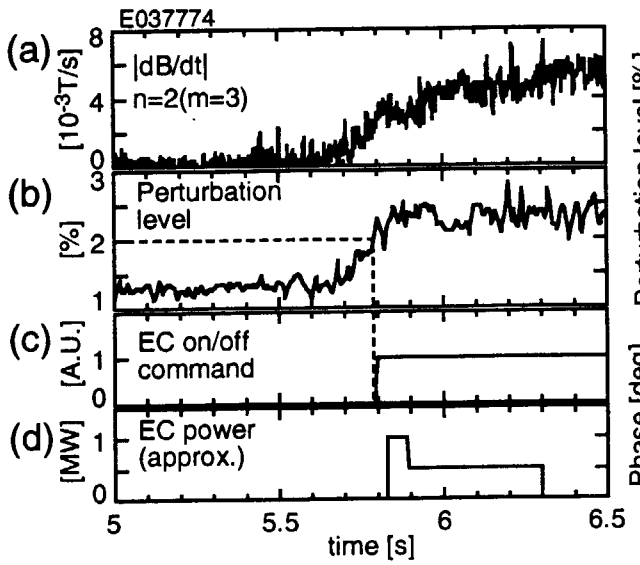

Fig. 3: Waveforms of (a) magnetic perturbations with n=2 measured by saddle coils, (b) perturbation level, (c) EC on/off command and (d) EC injection power.

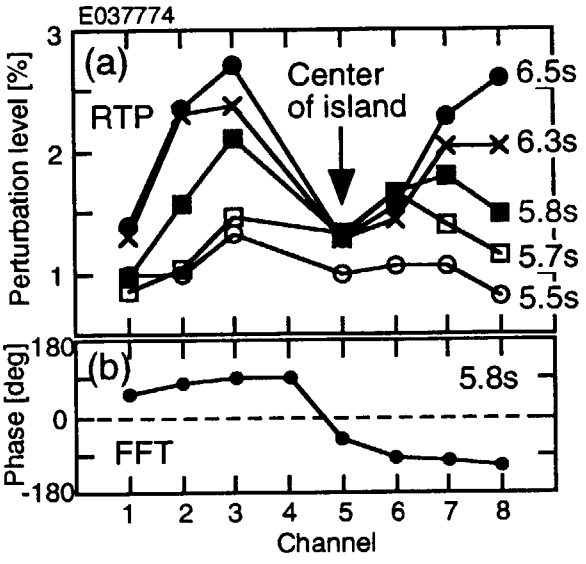

Fig. 4: Amplitude (a) and phase (b) of electron temperature perturbations.

5.3 Runaway current termination at the plasma disruption [1]

H. Tamai, R. Yoshino, S. Tokuda, G. Kurita, Y. Neyatani, M. Bakhtiari[1],
R. R. Khayrutdinov[2], V. Lukash[3], M. N. Rosenbluth[4]

The runaway current, generated at the plasma disruption should be avoided and suppressed in order to mitigate the plasma wall interaction. Shutdown of runaway electron current is successfully performed during the simulated vertical plasma displacement event, where the surface safety factor, q_s, of the limiter plasma decreases. For all shots with runaway electron generation, runaway current starts to decrease with the appearance of spikes in magnetic fluctuations, and disappears before q_s decreases to 2.

Many spikes in magnetic fluctuation appeared during the runaway termination. The dominant mode of the spikes in the magnetic fluctuations is m=3/n=1. The first magnetic fluctuation with a fast growth rate of about $3x10^4s^{-1}$ is followed by repeated magnetic fluctuations whose growth rates are slowed down to about $5x10^3s^{-1}$. Those fluctuations with slow growth rate decay and terminate the runaway current.

Corresponding to the loss of runaway electrons by magnetic fluctuations, heat flux pulses are measured at the inner divertor plates, which indicates the wall interaction with the runaway electrons. Power is deposited on the divertor plates in intensive pulses with a duration of the order of hundred micro seconds, not as a constant heat load, during the current decay.

Halo current, measured by the Rogowski coils, during the runaway termination is small, and increases after the runaway termination ($q_s< 2$) with a dominant toroidal mode of n=1. The temporal behaviour of halo current well agrees with the DINA-code analysis.

References

[1] H. Tamai, *et al.*, "Runaway Current Termination in JT-60U", IAEA-CN-77/EX9/2, paper presented at 18th Conf. on Fusion Energy, Sorrento, 2000. [Nuclear Fusion *in Press*]

---

[1] Utsunomiya University, Utsunomiya, Japan.
[2] Troitsk Institute, Moscow, Russia.
[3] Kurchatov Institute, Moscow, Russia.
[4] General Atomics, San Diego, USA.

6. High Density and Improved Confinement

6.1 Impurity behavior in high performance radiative discharges of JT-60U [1]

S. Sakurai, H. Kubo, H. Takenaga, N. Asakura, H. Tamai, S. Konoshima, K. Itami, A. Sakasai, S. Higashijima, T. Sugie and JT-60 Team

Transport coefficients of impurity in reversed shear plasma were evaluated and compared with those in ELMy H-mode plasma. The diffusivity was significantly reduced (~1/10) at the ITB region in the reversed shear plasma. An inward pinch velocity of -3m/s was also observed at the ITB region. The inward pinch velocity increases for higher Z impurities. Radiation loss inside ITB was consistent with bremsstrahlung from carbon and oxygen impurities and less than 15% of absorbed heating power, but Ar enhanced radiation loss inside ITB due to high electron density and strong line emission from Ar ions inside ITB.

The effect of Ar seeding to the main plasma was investigated in ELMy H-mode plasmas. The radiation loss was enhanced at not only divertor region but also the main plasma edge (≥0.7a) and SOL. The total radiation power inside the separatrix remained ≤30% of the total absorbed heating power. Therefore, the mantle radiation did not significantly affect energy confinement and higher edge temperature and thermal component of stored energy were maintained up to $0.7n^{G}$.

On the contrary, low edge temperature in a strong D_2 fueling case degraded thermal component of stored energy. Therefore, fueling of D_2 gas should be minimized to maintain confinement improvement, but a large fueling rate might be needed to exhaust He ash and impurity by puff and pump. The ELM frequency was significantly affected by impurity seeding and D_2 fueling. In low Bt cases, the ELM frequency quickly dropped just after Ar seeding when radiation enhancement was not large yet. The total heat load on the outer target plate did not change significantly when the ELM frequency decreased to 1/2~1/3. Therefore time integrated ELM heat load was reduced with reduced frequency at outer target plate. The heat load on the inner target plate has not been measured yet.

[1] Sakurai S., et al., J. Nucl. Matter. **290-293**, 1002 (2001).

6.2 High radiation and high density ELMy H-mode plasmas seeded with Ar [1]

H. Kubo, S. Sakurai, N. Asakura, S. Konoshima, H. Tamai, S. Higashijima, A. Sakasai, H. Takenaga, K. Itami, K. Shimizu, T. Fujita, Y. Kamada, Y. Koide, H. Shirai, T. Sugie, T. Nakano, N. Oyama, H. Urano[1)], T. Ishijima[2)], K. W. Hill[3)], D. R. Ernst[3)], A. W. Leonard[4)]

1) Graduate School of Engineering, Hokkaido University, Sapporo, 060-8628, Japan
2) Graduate School of Engineering, Nagoya University, Nagoya, 464-8603, Japan
3) Princeton Plasma Physics Laboratory, P.O. Box 451, Princeton, NJ 08543, USA
4) General Atomics, P. O. Box 85608, San Diego, CA, 92186-5608, USA

The ITER FEAT design requires ELMy H-mode plasmas with a high radiation loss power fraction at high density. The high radiation loss power fraction is needed for mitigating the severe problem of concentrated power loading of the divertor plates. Controlled injection of impurity gases is a promising technique for enhancement of radiation loss power. The confinement is degraded in the high density range in large tokamaks, and this degradation is a critical issue for the ITER FEAT design. By injecting impurities, the confinement has been improved with high radiation loss power in the high density range in some tokamaks. In ELMy H-mode plasmas of JT-60U,. Ar, which is being considered for injection into ITER-FEAT, has been injected into the main chamber for confinement improvement and radiation loss enhancement due to a radiating mantle at high density.

The radiation loss power from an edge region of the main plasma was controlled with a feedback technique using Ar puffing and divertor pumping. With the feedback control, quasi-stationary ELMy H-mode plasmas were sustained in the region of $P_{rad}^{tot} < 0.8\ P_{net}$, where P_{rad}^{tot} and P_{net} are the total radiation loss power and the net heating power, respectively. When the Ar density was higher than 0.5% of the electron density, the $HH_{98(y,2)}$ remained near unity in the range of $n_e < 0.65\ n_{GW}$. The $HH_{98(y,2)}$ was about 50% higher than that in the plasmas without Ar injection at $n_e = 0.65\ n_{GW}$. An Ar concentration of 0.5% corresponded to about a 9% reduction in the ion density. The improvement in confinement more than compensated for the deuterium density reduction by the impurity contamination, resulting in ~50% higher neutron production rates. The confinement was improved in both the pedestal and core regions. In the discharges with Ar injection, D_2 gas puffing rate to increase the electron density was low, D_α line intensity remained low, and type-I ELMs were maintained even at the high density. It seemed that by Ar injection the ion temperature at the pedestal was kept higher at high density and the confinement improvement was kept due to the high ion temperature at the pedestal.

References

[1] Kubo H., et al., Nucl. Fusion **41**, 227 (2001).

6.3 Ne injection into reversed shear plasmas [1]

H. Kubo, S. Sakurai, N. Asakura, K. Shimizu, K. Itami, S. Konoshima,
Y. Koide, T. Fujita, H. Takenaga, S. Higashijima, K. W. Hill[1)]
1) Princeton Plasma Physics Laboratory, PO Box 451, Princeton, NJ 08543, USA

The reversed shear plasma is a promising candidate for advanced steady-state tokamak operation. Heat removal by radiation from controlled injection of impurity gases is a useful technique for mitigating the severe problem of concentrated power loading of the divertor. Compatibility between the internal transport barrier (ITB) and a detached divertor plasma has been demonstrated by radiation enhancement using Ne injection in JT-60U reversed shear plasmas [2]. In order to extend such an operation toward high confinement, Ne and Ar have been injected into reversed shear plasmas with high confinement. On the other hand, impurity accumulation inside the ITB is a concern in reversed shear plasmas. Radiation enhancement and impurity behavior have been studied in the high confinement reversed shear plasmas.

High confinement ($H_{89PL} > 2$) with an ITB and high radiation loss power fraction ($P_{rad}/P_{net} > 0.7$) were simultaneously obtained with Ne and Ar injection. By Ne injection into the divertor, the radiation loss power was enhanced in the divertor due to an X-point MARFE, and the divertor plasma was detached [3]. With the divertor plasma detachment, the ITB became more pronounced, and the H_{89PL} increased from 1.2 to 1.6. Ar injection into the main chamber, however, resulted in excessive radiation loss enhancement inside the ITB [4].

In the reversed shear discharges with Ne injection, the ITB was clearly seen in the profiles of the electron density, electron temperature and ion temperature. The Ne and C density profiles were similar to the electron profile. Therefore, it seemed that impurity accumulation was not significant. From the time evolution of the Ne density profile after Ne injection, the inward velocity and diffusion coefficient for Ne were derived to be ~ 3 m / s and ~ 0.5 m^2 / s at the ITB, respectively. The inward velocity obtained using neoclassical transport calculations was ~ 2 m / s, and it seemed to be consistent with the experimentally derived inward velocity. However, the diffusion coefficient obtained using the neoclassical transport calculations was ~ 0.07 m^2 /s, and it was smaller than the experimentally derived diffusion coefficient.

References

[1] Kubo H., et al., Proc. 28th EPS Conf. on Controlled Fusion and Plasma Physics, Funchal, Vol. 25A, 1353 (2001).
[2] Itami K., et al., Fusion Energy 1996, Montreal, Vol. 1, 385 (1996).
[3] Itami K., et al, J. Plasma and Fusion Research **77**, 1027 (2001).
[4] Sakurai S., et al., Nucl. Mater. **290-293**, 1002 (2001).

6.4 Exploring high density operation of Ar seeded ELMy H-mode plasma (RI mode trials)

N. Asakura, H. Kubo, S. Sakurai, K. Itami, H. Tamai, H. Konoshima

Degradation of the enhancement factor of energy confinement is observed in the high density ELMy H-mode plasmas, where large deuterium gas puff rate is required. Impurity seeding such as argon (Ar) has been found to increase the radiation fraction at the plasma edge. At the same time, small deuterium gas puff rate is enough to obtain high density H-mode plasma with relatively good energy confinement.

In 1999, a few trials were done to improve the energy confinement and to increase the plasma density for the Ar seeded ELMy H-mode plasma, where I_p=1.2MA, B_t=2.4T, q_{95}=3.6, δ=0.36, κ=1.38, P_{NB}= 17 MW. (1) gas puffing in near-limiter plasma in order to reduce the deuterium gas-puff rate during increasing the plasma density. (2) radiation feedback control for Ar gas puff with the outer strike-point on the exhaust slot to increase the pumping rate in the detached divertor. Although H-factor and radiation fraction were comparable to those in standard ELMy H-mode scenario, small ITB was observed.

In 2000, the outer strike-point location was scanned from the outer target plate to the dome plate. Since the peak particle flux shifts to the outer flux surfaces during divertor detachment, location of the outer strike point on the dome might enhance the effect of pumping impurity ions and neutrals. It is useful to plan future experiments of the radiation improved mode, which is often obtained in the limited plasma discharges of TEXTOR, DIII-D and JET.

1. Improved confinement at high density

In order to increase the plasma density up to the similar values (n_e/n^{GW} ~0.6-0.65) during near-limiter configuration (with P_{NB}= 4.3MW for 2.5 s), plasma density FB control was used in 2000. Figure 1 shows that total gas puff amount decreased from 20 to 7 Pam^3 with the saturated divertor plate and/or wall. After 6.5 s, the plasma volume was reduced and the outer strike-point moved to the dome as shown in Fig. 2. At the same time, Ar puff was injected from the lower outboard port, and P_{NB} was increased to 17 MW.

Figure 3 shows two best discharges (36915 and 37347) in 2000. Although particle recycling flux was different in the two cases, similar waveforms of density and Ar^{+14} radiation were obtained with using a radiation feed-back of Ar puff rate. After 7s, n_e was increased up to $0.8n^{GW}$ during a constant D2 gas puff rate of 8.5-9 Pam^3/s, and the profile peaking started. The ELM activity was reduced rapidly in 7.2-7.9s when Ar^{+14} radiation was increased. The ELMy H-mode plasma (37347) with relatively high H-factor (H89L =1.45 without ripple loss correction, and H89L* = 1.68 including ripple loss correction of 18%) at high density (~0.8 n^{GW}) and with the reduction of ELM activity was, for the first time, observed in JT-60U. The enhancement factor of the H-mode thermal confinement was HH(98y2) = 0.98 with some uncertainty of the impurity profile. At the same time, the total radiation fraction reached up to

85% of P_{abs}, and divertor plasma was detached. In particular, at high density operation the energy confinement was often reduced after an NB breakdown of more than 2 units such as 6.9s of 36915, suggesting that a change in heating deposition reduces the improvement.

2. Strike-point location on dome

It is found that the location of the outer strike-point is the most important operation parameter. Figure 4 (d) shows time evolution of distances from separatrix and dome surface (Dgap_3 and Dgap_4 in Fig.4(a)). The outer strike point is located on the dome side for Dgap_3 > 0 and Dgap_4 < 0, and on the dome top for Dgap_3 < 0 and Dgap_4 < 0, where uncertainty of the equilibrium fit is several mm. After decreasing x-point height from 7s, radiation of Ar ions starts increasing, and then n_e starts increasing when the strike point shifts to the dome top. On the other hand, the radiation power from Ar ions and n_e decrease after 8s since the strike point moves to the dome-side due to an insufficient capability of FB control for changing plasma beta. The ELM activity is also reduced during the strike point on the dome-top although changes in the edge profiles of temperature and density are not identified clearly. It is reproduced well, but the mechanism is not understood yet.

In future, improved FB control to fix the strike point location accurately such as CCS method (see 5.1 in this issue) will be used for maintaining the improved confinement plasma at high density.

3. Density and temperature profiles

Figure 5 shows time evolution of T_e and n_e profiles (36915) measured with YAG Thomson scattering system, which was not available in the later series of experiment (including 37347). Peaking of the n_e profile starts from 7s (NB break down) for 36915. Peaking factor, $n_e(0)/\langle n_e \rangle$, increased gradually from 1.6 (7.3s) to 1.9 (8.0s). Reduction of the peaking factor after 8s is faster than the increasing since the ELM activity exhaust deuterium and Ar ions. Central T_e decreased from 5.1 to 3.9keV, and the thermal confinement time increased.

4. H-factor

Figure 6 shows trajectories of H-factor (without correction of ripple loss) and density normalize by n^{GW} for four cases with the strike-point on dome-top. For the standard Ar puff ELMy H-mode plasmas (with strike-point on the divertor target), relatively high H-factor (~1.5 at 0.7 n^{GW}) decreases rapidly above n_e ~ 0.7 n^{GW}. One the other hand, for the strike point on the dome-top, small reduction in the H-factor is extended to n_e ~ 0.8 n^{GW} (H89L ~1.4-1.45) which is larger than H89L < 1.25 for the standard cases.

Figure 7 shows the time evolutions of plasma parameters during negative NBI of 4.3MW (only one shot). Enhancement of H-factor from 1.4 to 1.6 (without correction of ripple loss) is observed at relative high density at n_e ~ 0.7 n^{GW}. This result shows that heating of central region improves the energy confinement at high density.

5. Summary

During a series of Ar seeding experiments, the plasma configuration with the outer strike-point on the dome top was found out to maintain relatively high H-factor (HH~0.98) at high density (~0.8n^{GW}) and radiation fraction (P_{rad}/P_{abs}~0.8) using feedback control of Ar gas puff. At the high density, ELM activity became smaller and the density profile was slightly peaked, which were different from the conventional Ar-seeding results. Sustaining the high density ELMy H-mode plasma for longer duration is planned in 2001.

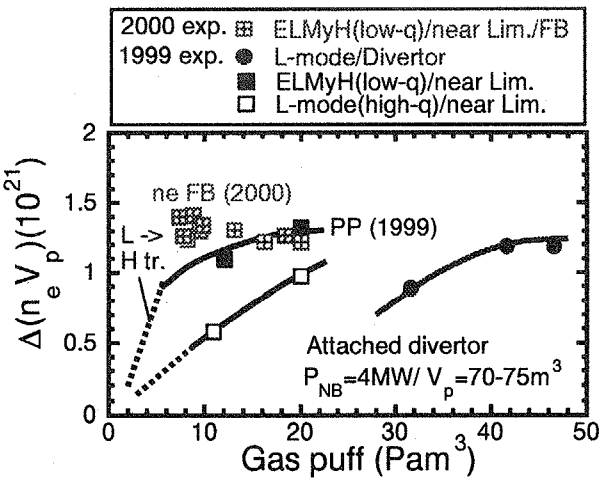

Fig1. Plasma electrons as a function of total gas puff during near limiter start-up. In 2000, density feedback control was used.

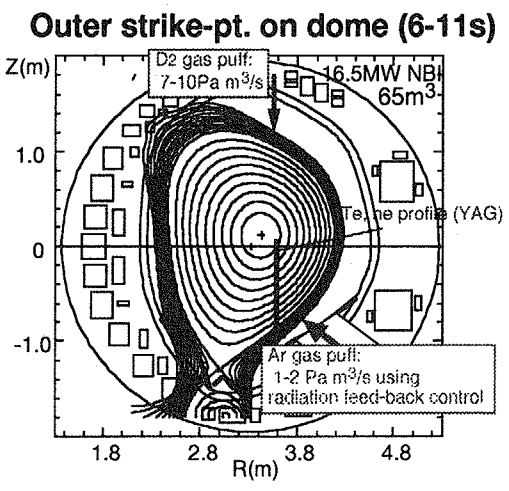

Fig2. Plasma configuration for Ar seeded ELMy H-mode with outer strike point on dome top.

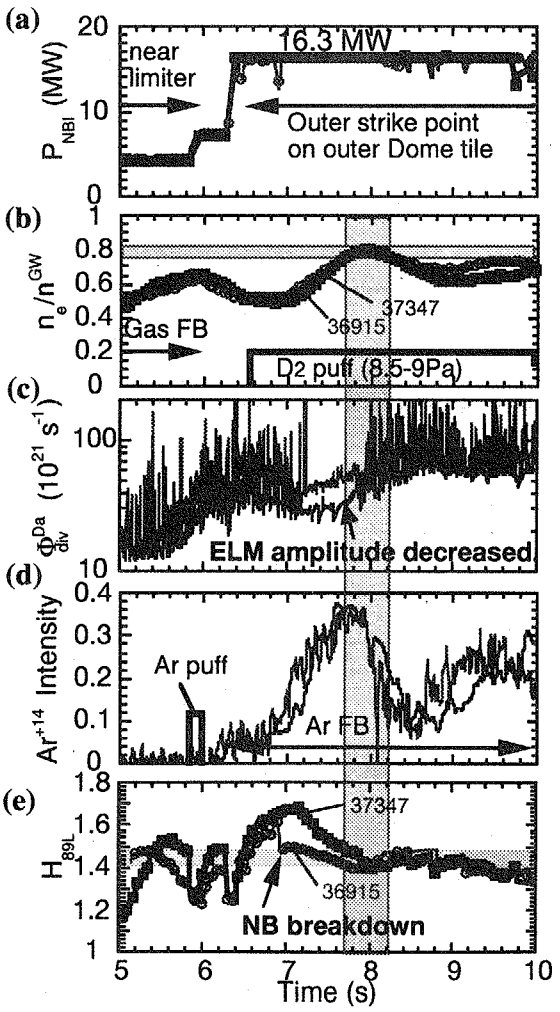

Fig3. Time evolutions of (a) NBI power, (b) electron density normalized by Greenwald density, (c) recycling flux, (d) Ar^{+14} ion radiation, (e) H-factor for 36915 and 37347.

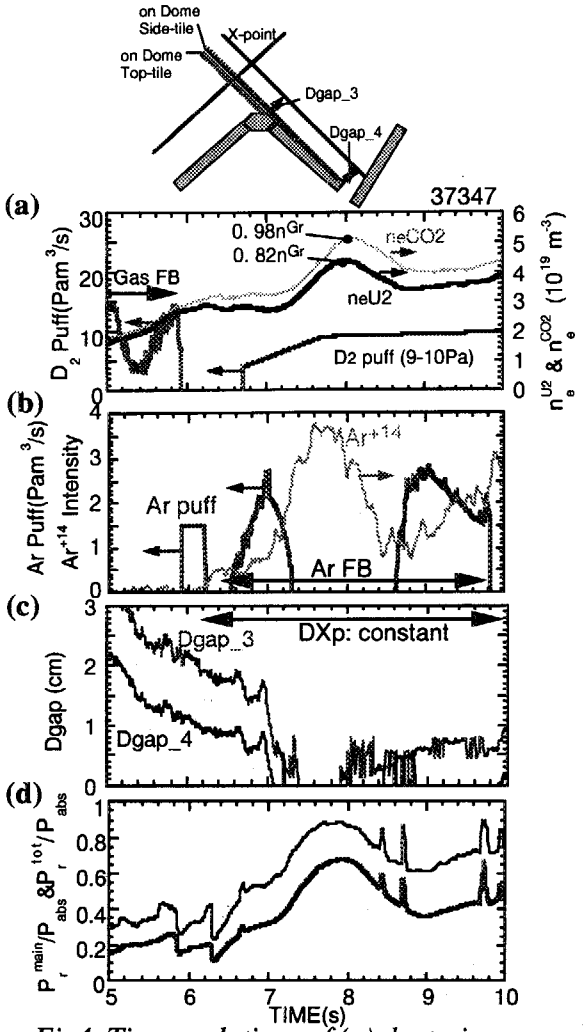

Fig4. Time evolutions of (a) dueterium gas puff rate and electron density, (b)Ar^{+14} ion radiation and Ar gas puff rate, (c) distance from dome top and side tiles, (d)radiation fractions for 37347.

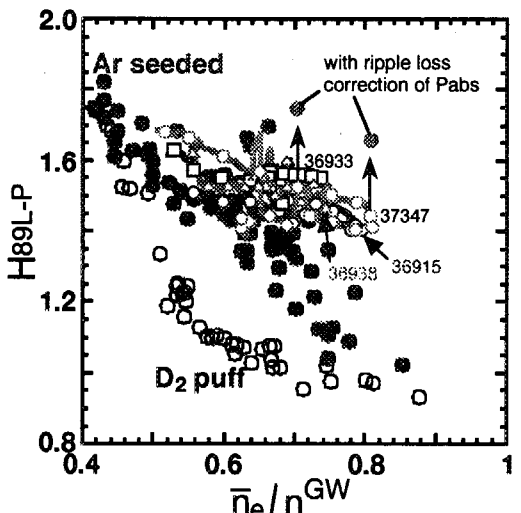

Fig6. H-factors (enhanced factor above ITER L-mode scaling) as a function of electron density normalized by Greenwald density.

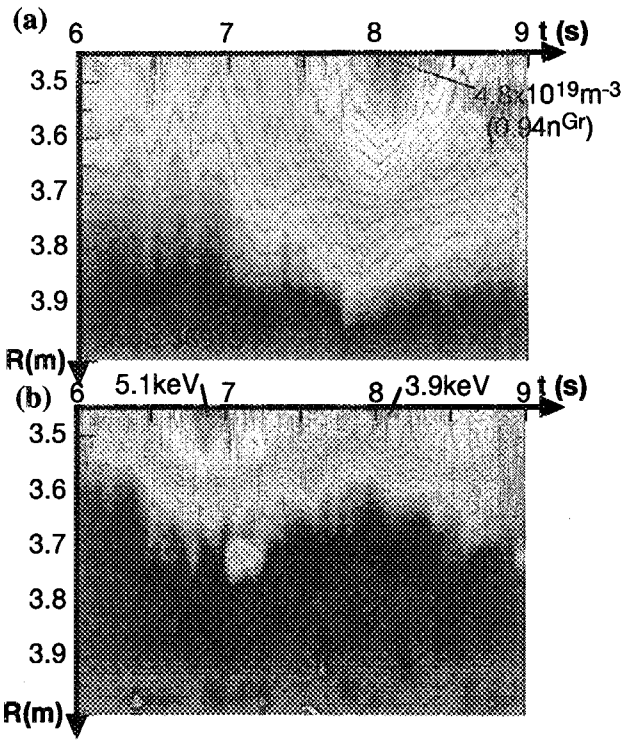

Fig5. Time evolutions of (a) electron density, (b)electron temperature profiles for 36915.

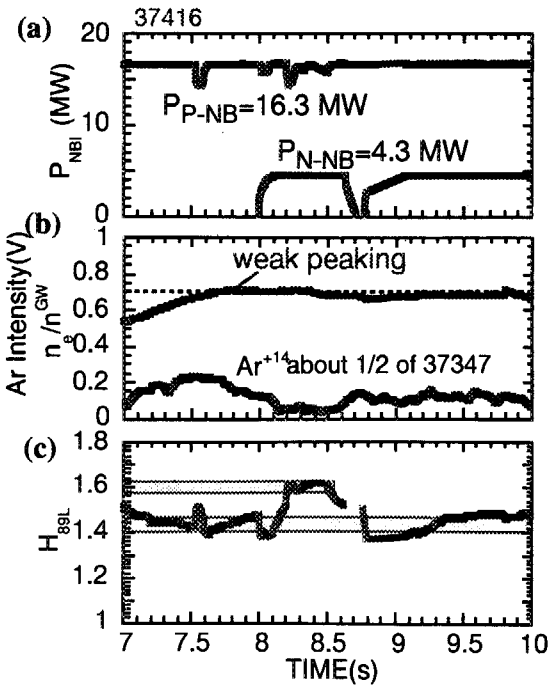

Fig 7. Time evolutions of (a) positive and negative NBI power, (b) normalized density and Ar^{+14} ion radiation, (c) H-factor for 37416 (N-NB injection case).

7. Neutral and Impurity Particle Control

7.1 Pellet injection characteristics [1]

H. Takenaga, H. Kubo, K. Itami, K. Kizu, T. Iwahashi, H. Ichige, H. Hiratsuka

1. Introduction

In order to extend the operation region to high density without confinement degradation, a multiple pellet injector has been installed with injection from the low-field-side midplane [LFS(mid)] and from the high-field-side at the top [HFS(top)]. Recently, it was found that fuelling efficiency of a high-field-side pellet is enhanced due to a radial displacement of the pellet ablatant on several tokamaks [2]. The ablation characteristics and radial displacement in JT-60U were discussed in Ref. [1], where a penetration depth deeper than the ablation depth calculated based on the neutral gas shielding model was observed for the HFS(top) pellets in NB heated plasmas and the E×B drift model [3] gives a radial displacement consistent with the measurements. In this report, peak density in the pellet injected discharges and dependence of the increment in the number of electrons on injection speed and NB heating power are discussed. Furthermore, the configuration effect is discussed for the HFS(top) pellet.

2. Pellet injector system

Figure 1 illustrates the layout of the centrifugal pellet injector system, which can inject 30-40 2.1 mm cube pellets in each discharge. So far, the injection frequency (f) of 10 Hz (designed maximum value is 20 Hz) and the injection speed (v) in the designed range of 100-1000 m/s have been achieved. The injection lines are arranged for injection from the low-field-side midplane [LFS(mid)] and the high-field-side at the top [HFS(top)]. The minimum curvature of the guide tube for the HFS(top) pellet injection is 600 mm. Deuterium (D) and Hydrogen (H) pellets were injected into D and H plasmas, respectively.

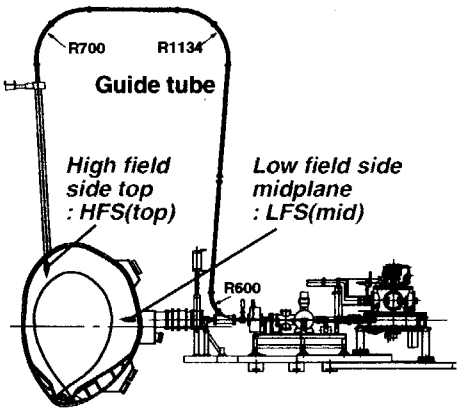

Fig. 1 Illustration of pellet injector system in JT-60U.

3. Peak density in the pellet injected discharges

Figure 2 shows the peak value of the line averaged density (n_e^{peak}) normalized to the Greenwald density (n_{GW}) as a function of plasma current (I_p) for pellet injected discharges. For the LFS(mid) D pellet injection, n_e^{peak} reaches up to $1.8 \times n_{GW}$ in the OH discharges without gas-puffing at I_p=1.2 MA. With NB heating power (P_{NB}) of >5 MW, n_e^{peak} reaches up to n_{GW} with gas-puffing for the LFS(mid) D pellet injection. For the LFS(mid) H pellet injection, n_e^{peak} is limited below n_{GW}. For the HFS(top) pellet injection, n_e^{peak} reaches up to 90% of n_{GW} in the D discharges and 65% of n_{GW} in the H discharges without gas-puffing at P_{NB}>5 MW. The

value of n_e^{peak} is limited to about 30% of n_{GW} in the region of I_p>1.5 MA without gas-puffing for both D and H discharges.

4. Characteristics of pellet injection in OH plasmas

Figure 3 (a) shows time evolution of line averaged electron density ($\bar{n}_e$) in an OH plasma (I_p=1.5 MA / B_T=3.2-3.5 T) with LFS(mid) D pellet injection (v=690 m/s, f=5 Hz), HFS(top) D pellet injection (v=120 m/s, f=10 Hz) and gas-puffing. The value of $\bar{n}_e$ increases more with LFS(mid) pellet injection compared with HFS(top) pellet injection. The actual injection frequency for the HFS(top) pellets became lower than 10 Hz. The gas-puffed plasma disrupted at t=7.5 s. The relationship between the integrated D_α emission and $\bar{n}_e$ is shown in Fig. 3 (b). With LFS(mid) pellet injection, $\bar{n}_e$ increases with small increase of D_α emission. The edge density with LFS(mid) pellet is almost the same as that with HFS(top) pellet and gas-puffing, indicating a peaked density profile. The effective particle confinement time defined as τ_p^*=Ne/($S_{pellet\ or\ gas}$ − dNe/dt), where Ne is the total number of electrons and $S_{pellet\ or\ gas}$ is the time averaged particle source due to pellet injection or gas-puffing, was estimated to be 1.2 s for both LFS(mid) and HFS(top) pellets and to be 0.6 s for gas-puffing.

The increment of the number of electrons (ΔNe) for each pellet injection estimated using 2 or 3 interferometers with a sampling time of 1 ms is shown in Fig. 4 as a function of v. For the LFS(mid) D pellet

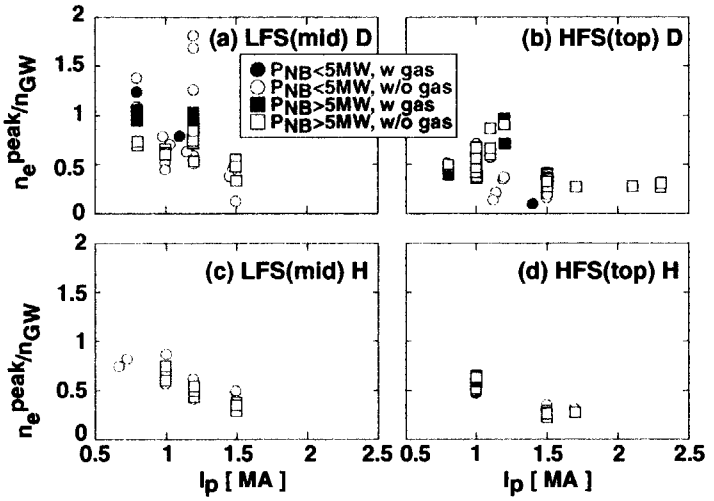

Fig. 2 Peak density in discharges with (a) deuterium LFS(mid) pellet, (b) deuterium HFS(top) pellet, (c) hydrogen LFS(mid) pellet and (d) hydrogen HFS(top) pellet injections.

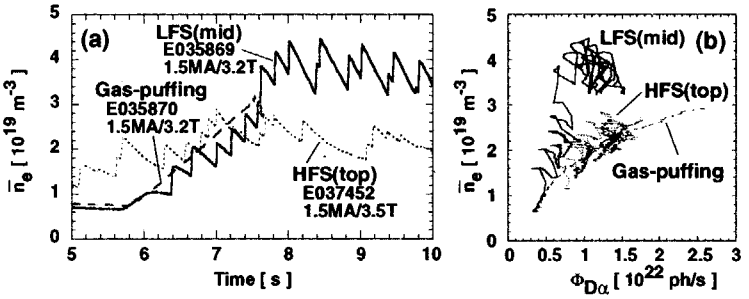

Fig. 3 (a) Wave-forms of $\bar{n}_e$ and (b) relationship between integrated D_α emission and $\bar{n}_e$ for LFS(mid) pellet (solid line), HFS(top) pellet (dotted line) and gas-puffing (dashed line).

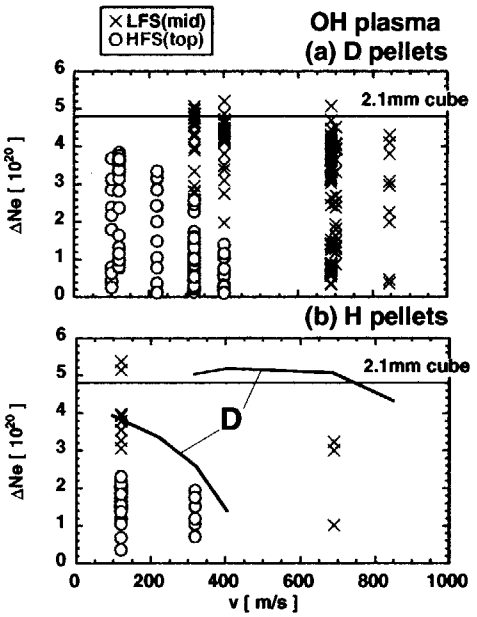

Fig. 4 ΔNe as a function of pellet injection speed for (a) deuterium pellet and (b) hydrogen pellet.

(I_p=0.8-1.5 MA / B_T=3-3.5 T), the maximum value of ΔNe is independent of v and is almost the same as the particles for 2.1 mm cube pellet. On the other hand, ΔNe for the HFS(top) D pellet (I_p=1.2-1.5 MA / B_T=3-3.5 T) decreases with increasing v, which indicates that the pellet was broken in the guide tube. At v=120 m/s, ΔNe for the HFS(top) D pellet reaches up to 80% of the particles for 2.1 mm cube pellet. For the H pellet (LFS(mid): I_p=1.5 MA / B_T=3.5 T, HFS(top): I_p=1.5-1.7 MA / B_T=3.5-3.9 T), ΔNe seems to be smaller than that for the D pellet. This could be explained by the fact that H pellet is softer than D pellet.

5. Characteristics of pellet injection in NB heated plasmas

Figure 5 shows the wave-forms of $\bar{n}_e$, fuelling rate, P_{NB} and D_α emission intensity from the inner divertor for (a) HFS(top) D pellet with v=100 m/s and f=10 Hz (I_p=1.5 MA / B_T=3.5 T) and (b) LFS(mid) D pellet with v=690 m/s and f=10 Hz (I_p=0.8 MA / B_T=3.0 T) together with gas-puffed discharges. The pellet fuelling rate was estimated from ΔNe as an averaged fuelling rate during 1 s. The value of $\bar{n}_e$ in the HFS(top) pellet discharge increases more compared with the gas-puffed discharge even with a smaller fuelling rate. The effective particle confinement time is estimated to be 0.5 s for HFS(top) pellets and 0.02 s for gas-puffing. The D_α emission increases during t=6-8 s due to pellet injection. The D_α emission in the HFS(top) pellet discharge is almost at the same level as that in the gas-puffed discharge. On the other hand, the LFS(mid) pellet is less effective in the high power heating phase, although LFS(mid) pellet injection makes higher $\bar{n}_e$ with a smaller D_α emission intensity in the low power heating phase. The density jump for each LFS(mid) pellet is larger by a factor of 2 than that for the HFS(top) pellet. However, the decay time for LFS(mid) pellets is shorter than that for HFS(top) pellets. The base density for LFS(mid) pellets is higher by only 10% than that in the gas-puffed discharge with the same total fuelling rate. The D_α spikes appear accompanied with pellet injection.

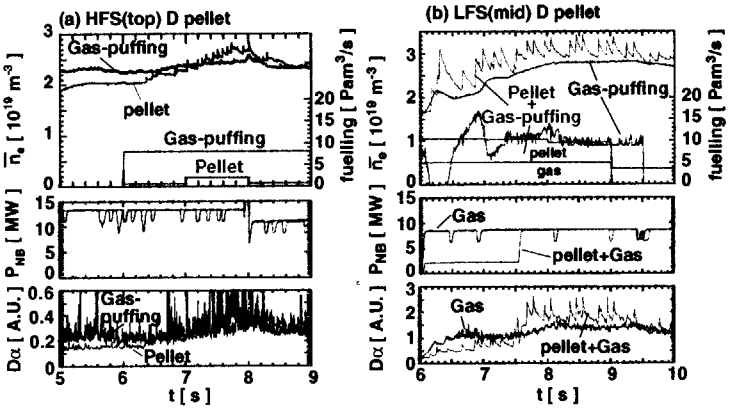

Fig. 5 Wave-forms of $\bar{n}_e$, fuelling rate, P_{NB} and D_α emission for (a) HFS(top) D pellet and (b) LFS(mid) D pellet injections.

In Fig. 6, ΔNe estimated with a sampling time of 1 ms is plotted as a function of P_{NB}. For the LFS(mid) D pellet (I_p=0.8-1.5 MA / B_T=3-3.5 T / v=690-840 m/s), ΔNe decreases with increasing P_{NB}. A large $\bar{n}_e$ spike is observed in the fast sampling data with a fast decay time of 1 ms for the high power NB heated plasma. The radial displacement due to E×B drift is consistent with the reduction of ΔNe. For the HFS(top) D pellet (I_p=1.5 MA / B_T=3.5 T / v=120 m/s), ΔNe decreases with increasing P_{NB} in the range of P_{NB}<5 MW. However, ΔNe

stays constant in the range of P_{NB}>5 MW. The jump of $\bar{n}_e$ measured with a fast sampling is smaller than that for LFS(mid) D pellets, however, a quick decrease of $\bar{n}_e$ is not observed, which is consistent with the E×B drift model. One of the explanations for the reduction of ΔNe for the HFS(top) D pellet is ablation in the SOL. The ablation model suggests a 20% loss in the SOL of NB heated plasma for HFS(top) pellets. The value of ΔNe for H pellets (LFS(mid): I_p=1.5 MA / B_T=3.5 T / v=690-1000 m/s, HFS(top): I_p=1.5-1.7 MA / B_T=3.5-3.9 T / v=120 m/s) is smaller than that for D pellets, but its dependence on P_{NB} is similar as that for D pellets.

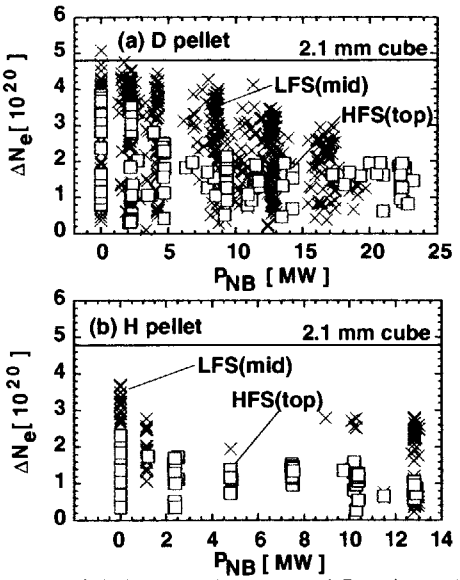

Fig. 6 ΔNe as a function of P_{NB} for (a) deuterium and (b) hydrogen pellets.

6. Configuration dependence

In order to investigate the effect of ablation position for HFS(top) pellet injection, HFS(top) D pellets were injected into three NB heated plasmas with different configurations as shown in Fig. 7. The calculated ablation position is shown in the insets. The highest $\bar{n}_e$ is obtained in the most outward-shifted plasma. However, the increase of the density is related to the fuelling rate for the pellet injection and particle confinement. The sum of ΔNe is estimated to be 2.3×10^{21} for the case (a) and 4.3×10^{21} for the case (b). In the case (c), ΔNe can not be estimated because one of the interferometers falls in the edge region. In order to investigate whether the large increase of the density in the outward shifted plasma is due to fuelling or particle confinement or E×B drift, further studies are necessary.

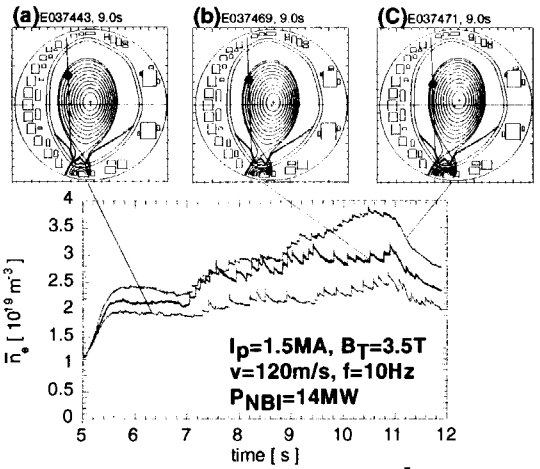

Fig. 7 Configuration dependence of $\bar{n}_e$.

7. Summary

The characteristics of high-field-side and low-field-side pellet injections are discussed. The peak density reaches up to 1.8×(Greenwald density) in OH plasmas with LFS pellet injection. In high power NB-heated plasmas, although the density jump for each LFS pellet injection is larger than that for HFS pellet injection, HFS pellet injection is more effective for density increase due to slow density decay.

References

[1] H. Takenaga and the JT-60 team, Phys. Plasmas **8**, 2217 (2001).

[2] P.T. Lang et al., Phys. Rev. Lett. **79**, 1487 (1997).

[3] P.B. Parks, W.D. Sessions, L.R. Baylor, Phys. Plasmas **7**, 1968 (2000).

7.2 Trial for pellet enhanced performance mode plasma

H. Takenaga, H. Kubo, K. Itami, T. Fujita

1. Introduction

Pellet enhanced performance (PEP) mode plasma with internal transport barriers (ITBs) has been achieved in many tokamaks [1-4]. Basic idea for the PEP-mode is as follows. A peaked density profile is formed by central particle fuelling due to pellet injection. Heating the peaked density plasma leads to a peaked pressure profile, which produces off-axis bootstrap current. Then, reversed or weak positive magnetic shear configuration is formed by the off-axis bootstrap current. ITBs are formed with the reversed or weak positive magnetic shear configuration and plasma performance is enhanced. The ITBs lead to a more peaked pressure profile, which acts as feedback to maintain the reversed or weak positive shear configuration. In DIII-D, PEP-mode was obtained with central particle deposition by pellet injection during plasma current ramp-up [4]. Pellets injected later during the current flattop with positive magnetic shear did not lead to the PEP-mode in DIII-D. In TFTR, when pellets were injected in the current flattop phase with low central shear configuration, a weak ITB was observed [3]. The PEP-mode is attractive for not only enhanced performance but also understanding of the formation mechanism of ITB. This report presents results of the PEP-mode trial experiments using low field side multiple pellet injections in JT-60U.

2. Experiments

The PEP-mode trial experiments were carried out with hydrogen NB, hydrogen gas and hydrogen pellets. The discharge scenario is based on the reversed shear discharge as well as DIII-D PEP-mode. In JT-60U, reversed shear plasma is produced using early NB heating during plasma current ramp-up phase. In the PEP-mode trial discharges, early NB heating power was reduced, in order to produce a peaked density profile by pellet injection. With low power NB heating, the low field side midplane (LFS(mid)) pellet injection is more effective for formation of a peaked density profile than the high field side top pellet injection. Therefore, the LFS(mid) pellet with an injection speed of 690 m/s and frequency of 10 Hz was used in this experiment. Figure 1 shows the plasma configuration and pellet injection line together with the FIR measuring chords (U1 and U2). The U1 and U2 chords pass around r/a=0.8 and r/a=0.2, respectively. The toroidal magnetic field is 3.5 T, the plasma volume is 65 m^3, the minor radius is 0.88 m and

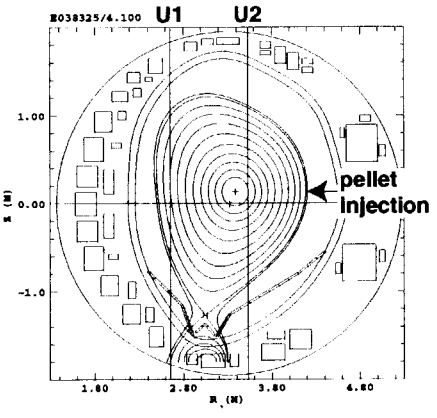

Fig. 1 Plasma configuration and pellet injection line.

the triangularity is 0.33.

3. Results and discussions

Figure 2 shows the wave-forms for (a) PEP-mode trial and (b) reversed shear discharges. In the PEP-mode trial experiments, the pre-heating power during I_p ramp-up phase (t=3.4-4.2 s) was reduced to 1.0 MW for deep deposition of the LFS(mid) pellet injection. Then, NB heating power of 6.1 MW was applied during t=4.2-5 s. In the reversed shear discharge, the pre-heating power of 8.6 MW and 6.2 MW was applied during t=3.5-4.2 s and t=4.2-5 s, respectively, to sustain the strong reversed shear configuration.

In the PEP-mode trial discharge, the central line averaged electron density for the U2 chord increases due to the pellet injections and the ratio of the central density to the edge density for the U1 chord increases up to 2.5 at t=4.3 s. The particle fuelling due to the pellet injections during t=3.4-4.3 s is evaluated to be 2.4×10^{21}, which is larger by a factor of 4 than the particle fuelling due to the NB injection during t=3.4-4.2 s in the reversed shear discharge. The ablation position is estimated to be r/a=0.25 from the time behavior of electron temperature. After the NB heating power of 6.1 MW was applied to the peaked density target, the central density decreases, because pellet ablation becomes shallow due to high temperature. The spike of the edge density becomes large with the NB heating power of 6.1 MW compared with in the low power heating phase. In the phase of NB heating power of 12.6 MW, the density profile becomes flat. In the reversed shear plasma, density is kept at a low level until t=4.5 s. Both central and edge densities increase from t=4.5 s, and the density profile becomes flat around t=5 s. Then, the central density increases and the edge density decreases.

In the PEP-mode trial discharge, the stored energy increases during t=4.3-4.7 s. In this phase, the stored energy is larger than that in the reversed shear plasma. However, the stored energy decreases during t=4.7-5.0 s. In the discharges where the increment of the density due to the pellet injections during the low power heating phase is smaller than that in Fig. 2 (a),

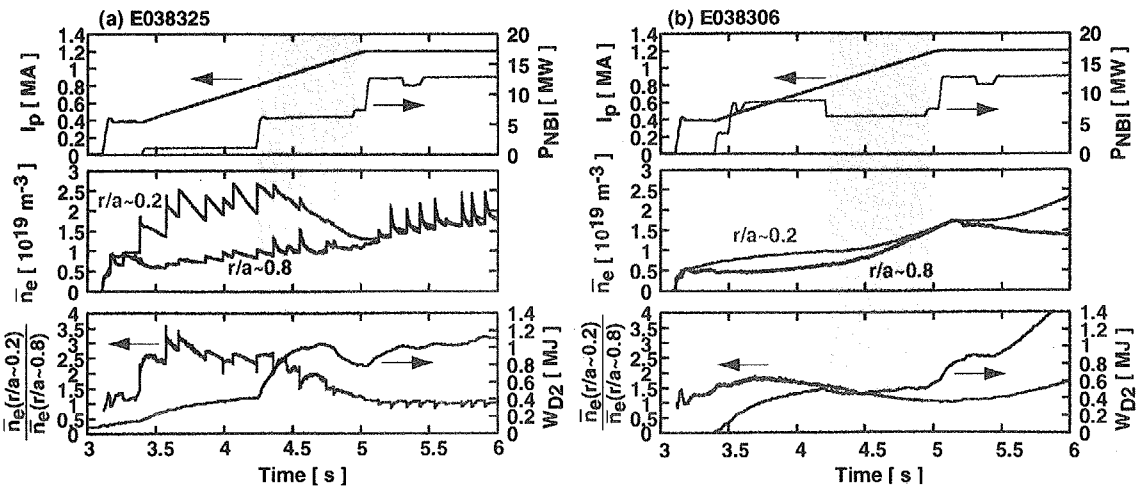

Fig. 2 Wave-forms of plasma current, NB heating power, central and edge densities, ratio of central to edge density and stored energy for (a) PEP-mode trial discharge and (b) reversed shear discharge.

the stored energy is smaller than that in Fig. 2 (a) even with higher NB heating power. In these discharges, the ratio of the central density to the edge density is less than 2.5. Therefore, the ratio of 2.5 might be marginal to increase the stored energy. In the reversed shear plasma, the ratio of the central density to the edge density is in the range of 1-1.5 during t=4.2-5 s. The stored energy quickly increases with 12.8 MW heating power, which is larger than that in Fig. 2 (a). It is noted that since the stored energy before plasma initiation is larger in Fig. 2 (a) and smaller in Fig. 2(b) than zero due to an off-set of a diamagnetic signal, the stored energy is overestimated in Fig. 2 (a) and underestimated in Fig. 2 (b), respectively.

Figure 3 shows the density, temperature and safety factor profiles in the PEP-mode trial discharge. In the density profile before 6.1 MW heating phase (t=4.1 s), ITB is observed at r/a=0.5-0.6 (see Fig. 3 (a)). At t=4.1 s, the reversed shear configuration is kept (see Fig. 3 (g)). At t=8.1 s after the NB heating with positive magnetic shear profile, where the density increases again up to the same level as at t=4.1 s due to the pellet injections, ITB is not observed (see Fig. 3 (b)). At t=4.68 s where the stored energy has a maximum value, an ITB is not observed in the electron temperature profile (see Fig. 3 (c)), but is observed in the ion

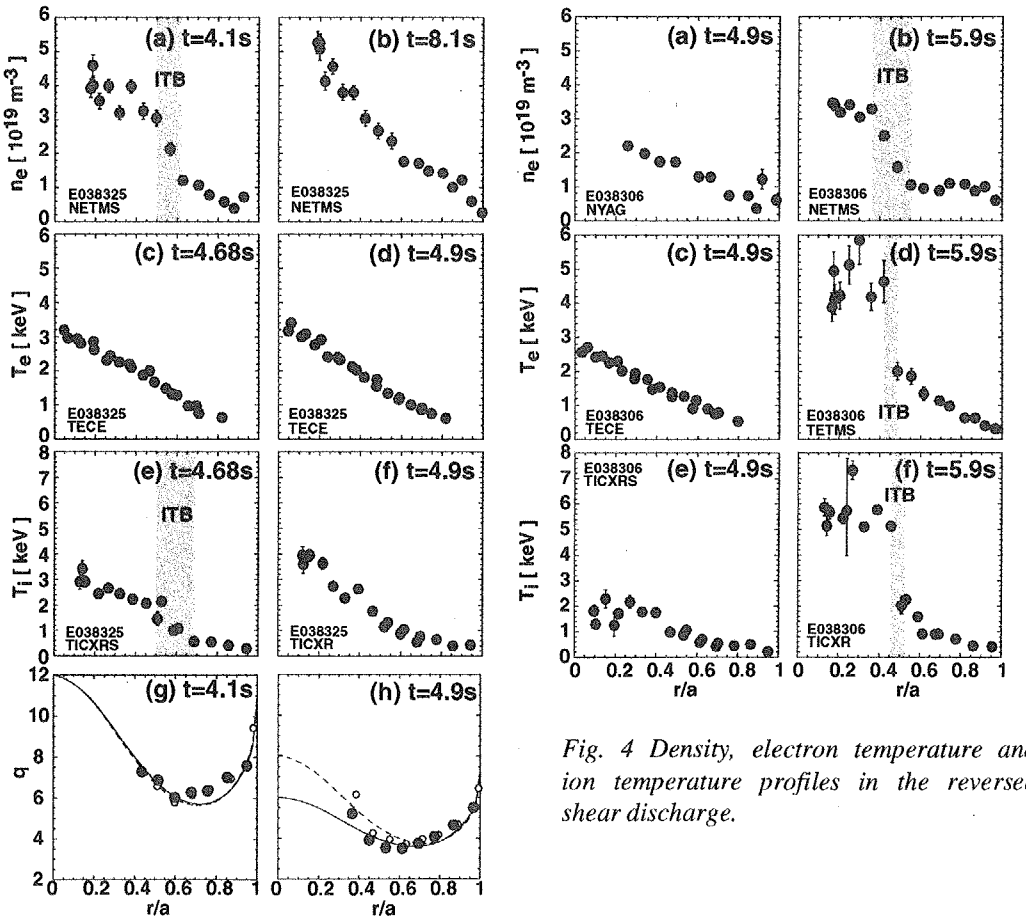

Fig. 4 Density, electron temperature and ion temperature profiles in the reversed shear discharge.

Fig. 3 Density, electron temperature, ion temperature and q profiles in the PEP-mode trial discharge. Dashed line and open circles in (g) and (h) are the data for a reference.

temperature profile around r/a=0.5-0.7 (see Fig. 3 (e)). In the discharge with a less peaked density profile during low power heating phase, ITB is observed in neither density profile nor temperature profile. At t=4.9 s where the density peaking is reduced and stored energy decreases, an ITB is not observed in both electron and ion temperature profiles (see Fig. 3 (d) and (f)), although the q profile shows negative shear configuration (see Fig. 3 (h)). Dashed line and open circles in Fig. 3 (g) and (h) show the data for a reference reversed shear discharge where similar discharge scenario as Fig. 2 (b) was adopted. In this discharge, NB heating power of 7-9 MW was applied during t=3.5-5.0 s. The q profile in the PEP-mode trial discharge at t=4.1 s is almost the same as the reference. A relatively strong reversed shear configuration is observed in the reference discharge at t=4.9 s compared with that in the PEP-mode trial discharge. The density and temperature profiles in the reversed shear discharge shown in Fig. 2 (b) are shown in Fig. 4. At t=5.9 s, ITBs are observed in all profiles (see Fig. (b), (d) and (f)). However, at t=4.9 s, no ITB is observed (see Fig. (a), (c) and (e)).

The threshold power and conditions for the ITB formation are discussed in Ref [5, 6] in JT-60U. In Ref. [5], a remarkable correlation between the gradient of electron temperature and magnetic shear at the ITB position was pointed out for onset conditions of ITB. The results obtained here indicates a possibility that a peaked density and/or local density gradient influences the ITB formation condition. As for the threshold power, ITB in the density profile is observed with very low NB heating power of 1 MW in the PEP-mode trial discharge, although an ITB is not observed in the density profile even with NB heating power of 6.2 MW in reversed shear discharges. This also suggests that the peaked density and/or local density gradient influences the ITB threshold power.

4. Summary

ITB is observed in the density profiles, when the peaked density profile is produced in the reversed shear configuration by pellet injection even with low NB heating power of 1 MW. This result indicates that the reversed magnetic shear and center particle deposition are important for density ITB formation. The following heating of 6.1 MW to the peaked density leads to ITB in the ion temperature profile and does not lead to ITB in the electron temperature profile. In reversed shear discharges without pellet injection, an ITB is not observed even with NB heating power of 6.2 MW. These results suggests that the peaked density and/or local density gradient influences the ITB threshold power.

References

[1] M. Greenwald et al., Phys. Rev. Lett. **53** (1984) 352.

[2] The JET Team (G. L. Schmidt), Plasma Physics and Controlled Nuclear Fusion Research 1988, Vol. 1 (IAEA, Vienna, 1989) 215.

[3] L. R. Baylor et al., Nucl. Fusion **37** (1997) 127.

[4] L. R. Baylor et al., Phys. Plasmas **7** (2000) 1878.

[5] Y. Koide et al., Proc. of 17th IAEA Fusion Energy Conference (1998) EXP 5/2.

[6] S. Ide and the JT-60 Team, Phys. Plasmas **7** (2000) 1927.

7.3 Efficient helium exhaust in divertor-closure configuration with W-shaped divertor of JT-60U [1, 2]

A. Sakasai, H. Takenaga, H. Kubo, N. Akino, S. Higashijima, S. Sakurai

The W-shaped divertor of JT-60U was modified from inner-leg pumping to both-leg pumping. The divertor experiments with both-leg pumping were started in February 1999. The effective pumping speed for both-leg pumping was estimated to be 15.9 m^3/s at about 0.1 Pa by using a gas filling method, which is 25% higher than the one for inner-leg pumping.

After the modification, the pumping rate was remarkably improved with both-leg pumping in a divertor-closure configuration, which means both separatrixes are closer to the divertor slots. The pumping rate was improved up to 5% with both-leg pumping in a divertor-closure configuration at the gap-in and gap-out of 0.5 cm from 3% with inner-leg pumping at $\overline{n_e} = 3.5 - 4.0 \times 10^{19}$ m^{-3}. However, the pumping rate reduced to 1% in the lower density region at $\overline{n_e} = 2.5 - 3.0 \times 10^{19}$ m^{-3}.

Helium exhaust is accomplished by condensing an argon (Ar) frost layer on the liquid helium cooled surface of three NBI cryopumps for divertor pumping between successive plasma discharges by injecting a known amount of Ar gas into the port chambers. In steady state, efficient helium exhaust was realized in a divertor-closure configuration with both-leg pumping in ELMy H-mode plasmas. Helium exhaust was investigated with He beam injection of $P_{He\text{-}NB}$ = 1.4 MW, which corresponds to He fueling rate of 1.5×10^{20} /s (equivalent to 85 MW α heating) for 3 s into ELMy H-mode discharges (I_P = 1.4 MA, B_t = 3.5 T, P_{NB} = 16 MW, V_P = 58 m^3). The He source rate (equivalent to 0.6 $Pa \cdot m^3/s$) from He beam injection is balanced by the exhaust rate with He pumping. The electron density in the main plasma has a broad profile and high edge density of $n_e = 2.5 \times 10^{19}$ m^{-3} (r/a = 0.93). The He density has the same profile as the electron density. In this discharge, τ^*_{He} = 0.36 s and τ^*_{He}/τ_E = 2.8 with τ_E = 0.13 s and an H-factor ($\equiv \tau_E/\tau_E^{ITER\text{-}89P}$) = 1.2 were achieved, well within the range generally considered necessary for successful operation of future fusion reactors, such as ITER-FEAT (i.e., τ^*_{He}/τ_E = 5). The line-averaged electron density in the main plasma is $\overline{n_e} = 3.8 \times 10^{19}$ m^{-3}, which corresponds to 0.57 of Greenwald density limit. As a result, the helium exhaust efficiency in the divertor-closure configuration was extended by 45% as compared to the one with the inner-leg pumping. In the high X-point configuration with both-leg pumping, the helium exhaust efficiency and the pumping rate of deuterium deteriorated because of the back-flow through the outer slot. The global particle confinement time τ^*_{He} in the high X_P configuration was double as compared to the one in the divertor-closure configuration. The dependence of helium exhaust on the gap is almost consistent with the pumping rate of deuterium.

References

[1] A. Sakasai et al., J. Nucl. Mater. **290-293** (2001) 957.

[2] A. Sakasai et al., the 18th IAEA Fusion Energy Conf., Sorrento 2000, EX5/5.

7.4 Helium exhaust and forced flow effects with both-leg pumping in W-shaped divertor of JT-60U [1, 2]

A. Sakasai, H. Takenaga, S. Higashijima, H. Kubo, T. Nakano, S. Sakurai, T. Fujita

The reversed shear mode with internal transport barrier (ITB) is attractive because of its high performance and a large fraction of bootstrap currents in non-inductive current drive as one of advanced tokamak operation scenarios for future steady-state tokamak reactors, such as ITER-FEAT. However, helium ash exhaust from the revered shear plasma is a matter of concern. It is very important to make clear He exhaust characteristics of reversed shear plasma because of an enhancement of He particle confinement.

By using central helium fueling with 60 keV He-beam injection, the helium removal from the core plasma inside the ITB in reversed shear plasmas (I_P = 1.0 MA, B_t = 3.5 T, δ=0.33 and P_{NB} = 7 - 10 MW) in the divertor-closure configuration was investigated for the first time. The helium density profiles inside the ITB were peaked as compared with those in ELMy H-mode plasmas. The reversed shear plasma had good confinement performance with H = 2.4 and β_N = 1.44. The He residence time inside the ITB is longer than that outside the ITB. The residence time τ^{inside}_{He} is defined by $\tau^{inside}_{He} = N^{inside}_{He}/S^{inside}_{He}$ in steady state, where N^{inside}_{He} is the total number of He ions and S^{inside}_{He} is the He source rate inside the ITB. The ratio of $\tau^{inside}_{He}/\tau_E$ was estimated to be 15. The increase in helium density inside the ITB was faster than outside the ITB and helium density profile was gradually peaked. In the case of low recycling divertor, it was difficult to achieve good helium exhaust capability in reversed shear plasmas with ITB. So, helium exhaust in reversed shear plasmas with high recycling in a divertor closure configuration as well as ELMy H-mode plasmas was investigated. In order to improve the He exhaust efficiency in the core plasma, particle recycling flux was enhanced by D2 gas puff and shallow pellet injection. As a result, the helium exhaust efficiency was improved with high recycling divertor.

A transport analysis was carried out to assess the helium exhaust properties inside the ITB. A one-dimensional, time-dependent, impurity code is employed to calculate helium ion density. The radial diffusion coefficient D(r) and the convective velocity v(r) are estimated from the results of gas puff modulation experiments. The He density has a peaked profile with ITB. The He density was reduced with increasing pumping rate as well as the one without ITB. Helium removal from the core plasma inside ITB is possible with a sufficient pumping rate.

Impurity shielding (friction force) with high-density divertor and plasma flow with puff and pump is essential to reduce impurity level in the core plasma. Carbon impurity reduction was observed by the forced flow with gas puff and effective divertor pumping. Carbon impurity level was effectively reduced with both-leg pumping.

References

[1] A. Sakasai et al., J. Nucl. Mater. **290-293** (2001) 957.
[2] A. Sakasai et al., the 18th IAEA Fusion Energy Conf., Sorrento 2000, EX5/5.

7.5 Comparison of impurity transport in ELMy H-mode, high βp mode and reversed shear plasmas [1]

H. Takenaga, A. Sakasai, H. Kubo, T. Fujita, Y. Kamada

In order to understand impurity transport in the main plasma, transport coefficients were estimated using a gas-puffing modulation technique, and these were compared with the theoretical predictions based on the neoclassical theory [2] and the turbulence model. The Multi-Mode Model (MMM) [3] is used as a turbulence model, in which the Ion Temperature Gradient (ITG) modes, Trapped Electron Modes (TEM) and drift-resistive ballooning modes, as well as a smaller contribution from kinetic ballooning modes, are included. In an ELMy H-mode plasma (I_p=1.0 MA, B_T=2.1 T, P_{NB}=11.1 MW and H_{89PL}=1.3-1.5), which has no internal transport barrier (ITB) and positive magnetic shear, helium particle diffusivity (D_{He}) is in the range of 1-2 m^2/s. In a high β_p plasma (I_p=1.5 MA, B_T=3.6 T, P_{NB}=17.5 MW and H_{89PL}=1.9), which has ITBs with a small gradient and weak positive magnetic shear, D_{He} is in the range of 1-3 m^2/s, and seems to be reduced in the ITB region. However, the reduction is less than a factor of 2. In a reversed shear (RS) plasma (I_p=1.0 MA, B_T=2.1 T, P_{NB}=7.3 MW and H_{89PL}=1.9), which has ITBs with a large gradient and reversed magnetic shear, D_{He} is in the range of 0.3-2 m^2/s, and is reduced by a factor of 5-6 in the ITB region compared with that in the inside and outside regions. In the RS plasma, D is almost the same for helium, carbon and neon, and the inward pinch velocity seems to be large for high Z species. The value of D in the ITB region of the RS plasma is higher by a factor of only 2-4 than the neoclassical value. The convection velocity in the ITB region of the RS plasma is at the same level as the neoclassical prediction (-1~-3 m/s). In the ELMy H-mode and high β_p plasmas, D_{He} is two orders of magnitude higher than neoclassical predictions, and is smaller by a factor of 3-5 than the turbulence model. The value of D for neon is almost the same as the turbulence model prediction in the ELMy H-mode plasma. The neoclassical theory predicts a small v (~0 m/s) and the turbulence model predicts the inward convection velocity in the rage of -0.3~-1.7 m/s, respectively, in the ELMy H-mode plasma. These values are in the range of uncertainty of the estimated values based on the gas-puffing modulation experiments.

References

[1] H. Takenaga and the JT-60 team, Phys. Plasmas **8**, 2217 (2001).

[2] G. Fussmann et al., Plasma Phys. Control. Fusion **33**, 1677 (1991).

[3] G. Bateman et al., Phys. Plasmas **5**, 1793 (1998).

7.6 Methane screening in the edge plasma

H. Takenaga, S. Higashijima, T. Nakano, H. Kubo, K. Itami

1. Introduction

Methane generated by chemical sputtering is one of the dominant carbon sources in JT-60U. Generation and behavior of methane in the divertor plasma have been studied in JT-60U [1, 2]. However, the contribution of the methane generated at the divertor plates to carbon contamination in the main plasma is not understood well, and it is still uncertain whether carbon in the main plasma originates in the divertor plasma or the main plasma edge. In the divertor plasma, generation of methane is larger than in the main plasma edge. However, the screening in the divertor plasma should be stronger than that in SOL. Therefore, in order to understand the origin of the carbon, it is important to evaluate the screening of methane in the SOL and divertor plasmas. In this report, the effective confinement time, which includes not only the screening effect but also particle confinement in the main plasma, is quantitatively estimated for methane puffed from the main plasma edge and the divertor plasma.

2. Experiments

Methane (CH_4) was puffed into hydrogen ELMy H-mode plasmas with an NB power of 13 MW at a plasma current of I_p=1.0 MA and a toroidal magnetic field of B_T=2.1 T. Figure 1 shows the plasma configurations together with the gas-puffing positions. The height of X-point from the dome top was 6-7 cm for the standard configuration as shown in Fig. 1 (a)-(c), and 18 cm for the high Xp configuration as shown in Fig. 1 (d). Hydrogen (H_2) was puffed from the top as shown in Fig. 1 (a), for a reference to CH_4 gas-puffing. CH_4 was puffed from the outer baffle plate as shown in Fig. 1 (b) and from the divertor plasma through the pumping slots as shown in Fig. 1 (c). CH_4 gas-puffing from the divertor plasma was also applied in the high Xp configuration.

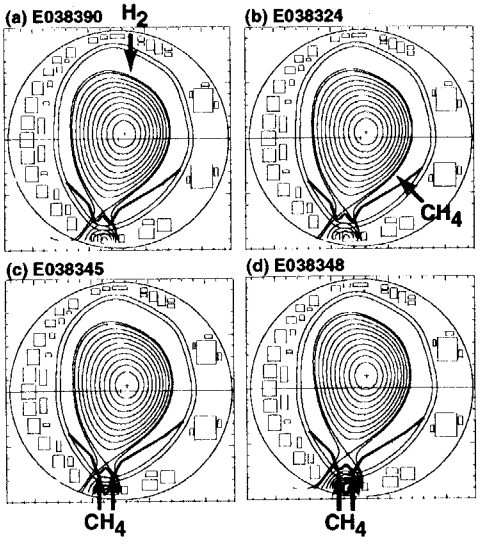

Fig. 1 Configurations and gas-puffing positions.

The carbon density in the main plasma was measured with CXRS. H_α, CII, CIV and CH band emissions from the divertor plasma were measured by a fiber array with a time resolution of 50 ms. Since the emission measurement was made at the next toroidal section of the CH_4 divertor gas-puffing, the measured values include the emissions of H, C and CH originating from the puffed CH_4.

3. Method of analysis

In order to evaluate the effective particle confinement time for CH_4 (τ_p^{CH4}), the particle balance is analyzed with and without CH_4 gas-puffing. The difference of the total number of carbon ions with and without CH_4 gas-puffing in the steady state phase can be expressed as $N_C^W - N_C^{W/O} = \tau_p^{CH4} \times S_{CH4}$, where N_C^W and $N_C^{W/O}$ are the total numbers of carbon ions with and without CH_4 gas-puffing and S_{CH4} is the CH_4 gas-puffing rate. The value of N_C^W and $N_C^{W/O}$ are estimated from Z_{eff} as $N_C=(Z_{eff}-1)/(Z^2-Z)\times N_e$, where Z_{eff} is derived from Bremsstrahlung, the total number of electrons inside the separatrix (N_e) is evaluated from the density profile measured by Thomson scattering system and Z is assumed to be 6 (only carbon impurity is considered). Thus, τ_p^{CH4} can be estimated as $\tau_p^{CH4} = (N_C^W - N_C^{W/O})/S_{CH4}$.

4. Results and discussions

Figure 2 shows time evolution of the line averaged electron density ($\bar{n}_e$), gas-puffing rate, integrated emission intensities of H_α, CII, CIV and CH band in the divertor plasma and CVI emission from CXRS measurement (I^{CXRS}) for (a) CH_4 puffed discharge from the main plasma edge (outer baffle plates) and (b) H_2 puffed discharge from the top. In the CH_4 puffed discharge, gas-puffing rate of 7 Pam^3/s is applied, which corresponds to 1.77×10^{21} carbon atoms/s and $\bar{n}_e$ increases from 1.9×10^{19} m^{-3} to 2.3×10^{19} m^{-3}. H_α, CII, CIV and CH band emissions in the divertor plasma increase, indicating the increase of carbon source from the divertor plates as the hydrogen flux increases. The increase of I^{CXRS} indicates the increase of carbon density, although beam attenuation is not considered. The value of Z_{eff} in this discharge increases from 1.7 to 1.8. On the other hand, in the H_2 puffed discharge, I^{CXRS} decreases during H_2 gas-puffing, although emissions in the divertor plasma increase. The shielding effect could become stronger with increasing $\bar{n}_e$. The value of Z_{eff} also decreases from 1.57 to 1.47.

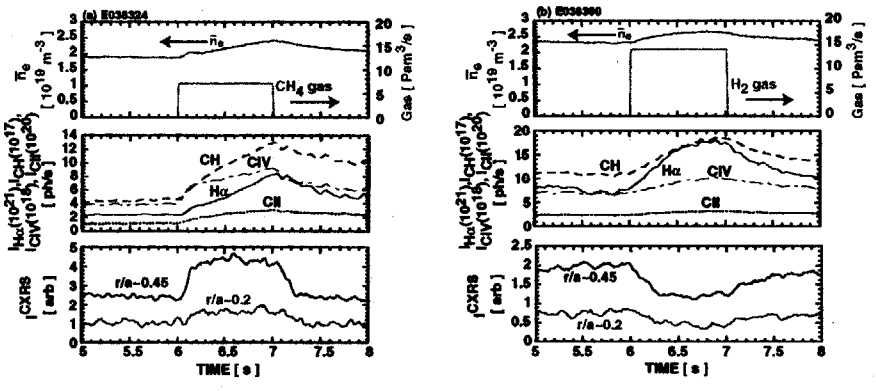

Fig. 2 Time evolution of density, gas-puffing rate, integrated emissions (H_α, CII, CIV and CH band) from the divertor and CXRS signals for (a) CH_4 and (b) H_2 puffed discharges from the main plasma edge.

Figure 3 shows time evolution of the CH_4 puffed discharge from the divertor plasma in (a) standard and (b) high Xp configurations. The emissions in the divertor plasma increase as well as in the main gas-puffing case. It is noted that these emissions include the emission of H, C and CH originating from the puffed

CH_4, as mentioned in Sec. 2. In the standard configuration, I^{CXRS} increases during t=5.6-6.0 s. However, it decreases from t=6.0 s. The shielding effect could become stronger with increasing $\bar{n}_e$. In the high Xp configuration, I^{CXRS} before gas-puffing is higher than that in the standard configuration, and gradually increases during gas-puffing. Difference of time behavior of I^{CXRS} could reflect different dependence of the shielding on $\bar{n}_e$. The value of Z_{eff} increases from 1.78 to 1.89 (at t=6.0 s) in the standard configuration and from 1.82 to 1.99 (at t=7.4 s) in the high Xp configuration.

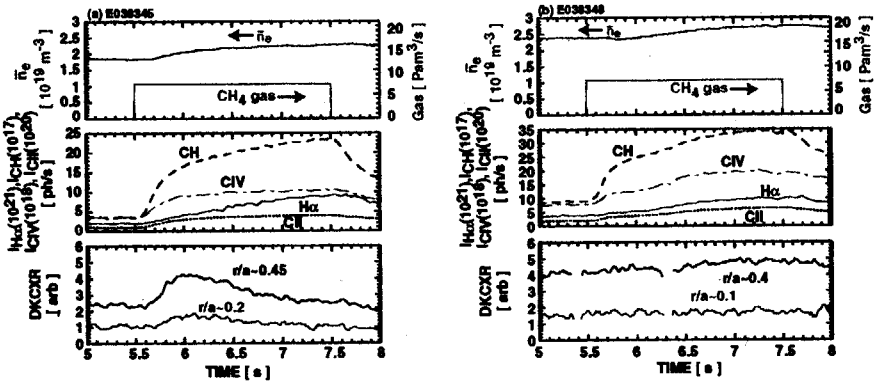

Fig. 3 Time evolution of density, gas-puffing rate, integrated emissions from the divertor and CXRS signals for CH_4 puffed discharges from the divertor region in the (a) standard and (b) high Xp configurations.

The value of Z_{eff} decreases with increasing $\bar{n}_e$ for both with and without CH_4 gas-puffing cases in the standard configuration as shown in Fig. 4. The value of Z_{eff} in the main CH_4 gas-puffing case is comparable with Z_{eff} in the divertor CH_4 gas-puffing case without divertor pumping and is larger than that with divertor pumping. With divertor pumping, puffed CH_4 might be directly pumped before CH_4 reaches to the divertor plasma. In the high Xp configuration, Z_{eff} is higher compared with Z_{eff} in the standard configuration for both with and without CH_4 gas-puffing cases. The value of Z_{eff} seems to increase with $\bar{n}_e$ in the high Xp configuration.

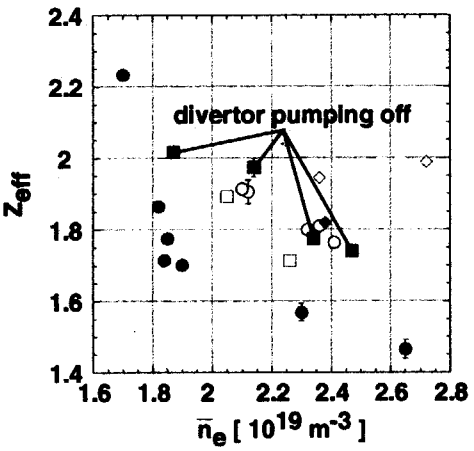

Fig. 4 Z_{eff} as a function of $\bar{n}_e$. Closed circles show the data without CH_4 gas-puffing. Open circles show the data with CH_4 gas-puffing from the main plasma edge in the standard configuration. Closed and open squares show the data with CH_4 gas-puffing from the divertor region without and with divertor pumping, respectively, in the standard configuration. Closed and open diamonds show the data for without and with CH_4 gas-puffing in the high Xp configuration. The divertor pumping is on except for closed squares.

The value of N_C calculated using Z_{eff} is shown in Fig. 5. Solid line shows $N_C^{W/O}$ and dotted lines indicate the error for $N_C^{W/O}$. The value of $N_C^{W/O}$ largely decreases in the region of $\bar{n}_e$=1.7-1.9×10^{19} m^{-3}, and gradually decreases in the high density region. The higher Z_{eff} for the divertor D_2 gas-puffing was reported compared with Z_{eff} for the main D_2 gas-puffing [3]. In this report, the same $N_C^{W/O}$ is used for both main and divertor CH_4 gas-puffing. In the high Xp configuration, $N_C^{W/O}$ is estimated only at $\bar{n}_e$=2.4×10^{19} m^{-3}, therefore, this value is used at both $\bar{n}_e$=2.4 and 2.7×10^{19} m^{-3}.

The estimated τ_p^{CH4} is shown in Fig. 6. Here, dN_C/dt is ignored, because it is much smaller than S_{CH4}. The value of τ_p^{CH4} is in the range from 4 to 8 ms in the standard configuration for both main and divertor gas-puffing cases. The value of τ_p^{CH4} for the main CH_4 gas-puffing is not so large (at least within a factor of 2) compared with τ_p^{CH4} for the divertor CH_4 gas-puffing. This result suggests a large contribution of the carbon source generated by chemical sputtering at the divertor plates to the carbon density in the main plasma. In the high Xp configuration, τ_p^{CH4} is in the range from 3 to 9 ms, which is smaller at $\bar{n}_e=2.4\times10^{19}$ m^{-3} and larger at $\bar{n}_e=2.7\times10^{19}$ m^{-3} than that in the standard configuration. This result reflects the gradual increase of the carbon density in the high Xp configuraion.

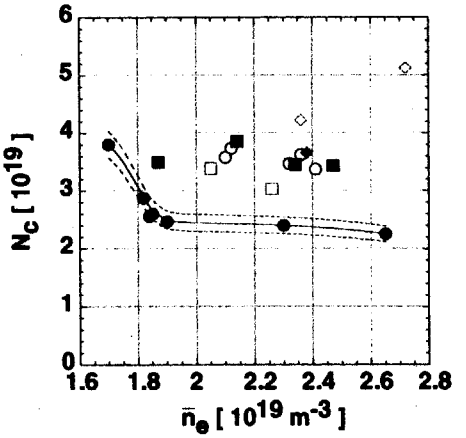

Fig. 5 N_C as a function of $\bar{n}_e$. The legend is the same as Fig. 4.

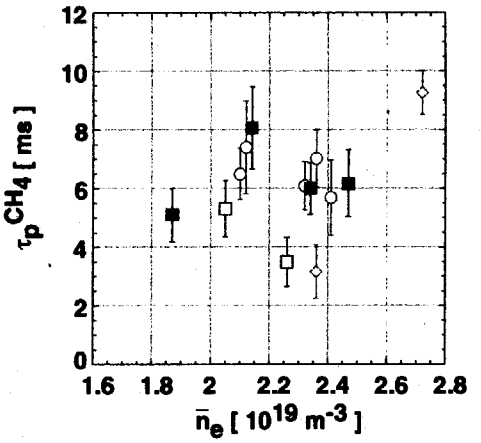

Fig. 6 τ_p^{CH4} as a function of $\bar{n}_e$. The legend is the same as Fig. 4.

Finally, $N_C^{w/o}$ is estimated using τ_p^{CH4} and the intrinsic carbon generation rate. At $\bar{n}_e=2.3\times10^{19}$ m^{-3} without CH_4 gas-puffing, the particle flux to the divertor plates is estimated to be 9.9×10^{22} /s from the target probe measurements. The total chemical sputtering yield was estimated to be 10-20% considering not only CH_4 but also C_2H_2 and C_2H_4 [2]. The total yield of carbon is estimated to be 1×10^{22} /s with 10% of the total chemical sputtering yield. Therefore, $N_C^{W/O}$ is estimated to be 4×10^{19} using τ_p^{CH4}=4 ms. This is larger by a factor of 2 than the measured $N_C^{W/O}$, suggesting a large contribution of carbon generated at the divertor plates to the carbon contamination.

5. Summary

The effective confinement time for CH_4 is estimated to be in the range of 4-8 ms in the standard configuration for both main and divertor gas-puffing cases, and in the range of 3-9 ms in the high Xp configuration. These results are consistent within a factor of 2 with the measured number of carbon ions in the main plasma, suggesting a large contribution of carbon generated at the divertor plates to the carbon density in the main plasma.

References

[1] S. Higashijima et al., J. Nucl. Mater. 266-269 (1999) 1078.

[2] T. Nakano et al., submitted to Nucl. Fusion.

[3] N. Hosogane et al., in Proc. 17th IAEA, Yokohama, 1998 IAEA-CN-69/EXP4/05.

7.7 Impurity control by boronization using deuterated decaborane

T. Nakano, S. Higashijima and H. Kubo

1. Introduction

The plasma performance in nuclear fusion experimental devices such as a tokamak can be degraded by impurities. It is therefore important to reduce impurity generation to a minimum. Especially, after a vacuum vessel is exposed to the air, main impurities are water, oxygen and oxide adsorbed to tiles and some other structures [1]. As a result, the plasma is contaminated by a large amount of oxygen impurity. Boronization is one of the methods to suppress oxygen release. Boronization covers first walls with a thin boron film and keeps oxygen in the form of boron oxide [2]. In JT-60, boronization using hydride-decaborane ($B_{10}H_{14}$) was performed to reduce oxygen impurity and particle recycling [3]. A problem of the boronization was that hydrogen originating from hydride-decaborane diluted core deuterium plasmas. About 200 tokamak discharges were necessary to reduce the hydrogen fraction to a negligible level. In 2000, boronization using deuterated-decaborane ($B_{10}D_{14}$) was introduced to minimize the number of conditioning tokamak discharges [4]. In order to investigate the durability of boronization effects, discharges with an identical condition were repeated. This report discusses the oxygen gettering efficiency and the durability of the effects of the boronization using deuterated-decaborane.

2. Experimental

Boronization was performed using a glow discharge with a mixture of helium (99%) and decaborane vapor (1%) at a baking temperature of ~ 540 K. Table 1 shows decaborane quantity, glow discharge current and measured boron film thickness for the 1st, 2nd and 3rd boronization carried out in 2000. To produce a toroidally uniform boron film, 12 gas inlets for the mixture gas were positioned at even intervals along the toroidal direction and 3 electrodes for the glow discharge were used.

In order to investigate the durability of the boronization effects, L-mode discharges with an identical condition (the plasma current 1.5 MA, the toroidal field 3.0 T, the neutral beam heating power 4.3 MW and the line averaged electron density ~ 1.5 x $10^{19}m^{-3}$) were repeated before and after boronization.

Boronization	Decaborane	Glow discharge current	Boron film thickness
1st	~ 70 g	~ 2 A	~ 135 nm
2nd	~ 20 g	~ 13 A	~ 145 nm
3rd	~ 20 g	~ 10 A	-

Table 1 Conditions of the 1 – 3rd boronization.

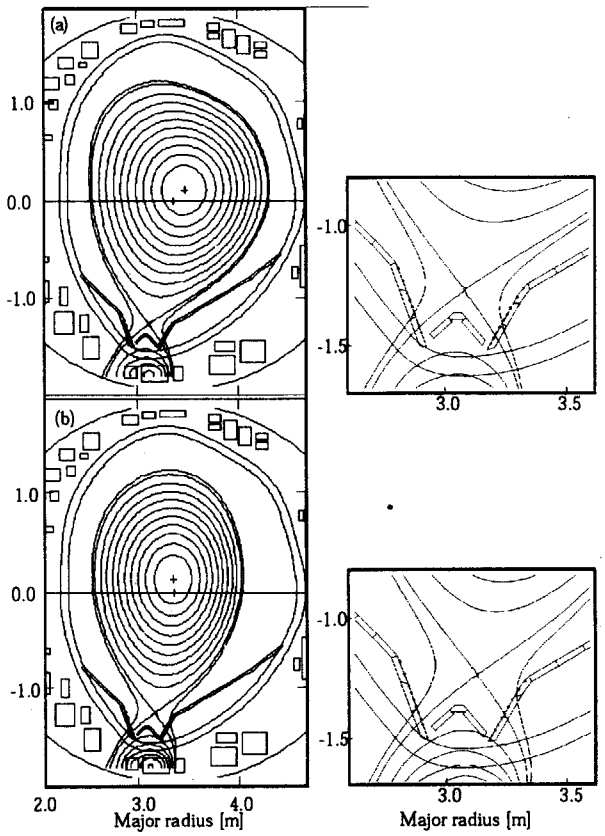

Fig. 1. Plasma configuration of the plasma and expansion around the X point (a) after the 1st and 2nd boronization, and (b) after the 3rd boronization

Figure 1 (a) shows a poloidal cross-section of the plasma after the 1st and 2nd boronization. The plasma volume was set at ~ 67 m^3 and the plasma shape was configured at a triangularity of ~ 0.3 to suppress local strong plasma-wall interactions except for the strike points on the divertor plates. The plasma configuration after the 3rd boronization was different from that after the 1st and 2nd boronization. Figure 1 (b) shows a poloidal cross-section of the plasma after the 3rd boronization. The plasma volume was set at ~ 55 m^3 and the plasma shape was configured at a triangularity of ~ 0.1.

The plasma effective charge (Z_{eff}) was evaluated from visible bremsstrahlung emission. A VUV spectrometer measured spectral lines with a transition of n = 1 − 2 of hydrogen-like boron, carbon and oxygen. The oxygen content was derived from Z_{eff} and the intensity ratio of the spectral lines with a help of C VI (n = 7 - 8) and O VIII (n = 9 - 10) emission intensities from the main plasma by charge exchange recombination spectroscopy.

3. Results and discussion

Figure 2 shows the oxygen content (n_O/n_e) as a function of shot number. The vacuum vessel was exposed to the air before the 1st and 2nd boronization and not before the 3rd. The 1st boronization using 70g of decaborane reduced n_O/n_e from ~ 1.5 % to ~ 0.7 %, and then n_O/n_e gradually increased. The plasma with n_O/n_e less than 1% were kept for ~ 400 shots. After it reached ~ 1.4 %, it decreased again. The decrease

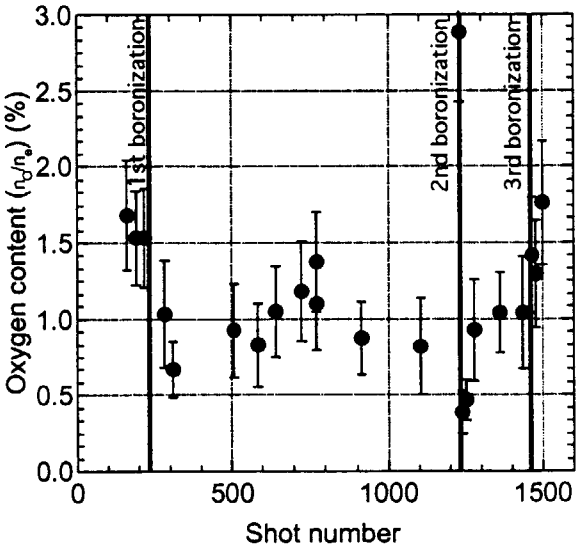

Fig. 2. Oxygen content in the main plasma as a function of shot number. Vertical lines correspond to 1 – 3rd boronization.

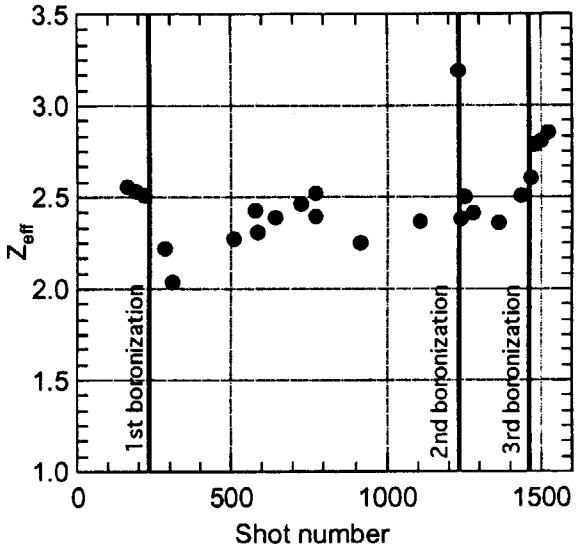

Fig. 3. Z_{eff} as a function of shot number. The trace is similar to n_O/n_e in Fig. 2.

was not due to oxygen gettering by boron burst because the strong spectral line of boron was not observed around the shot number of 800. By the 2nd boronization using 20g of decaborane, n_O/n_e decreased from ~ 2.8 % to ~ 0.5 %. The plasma with n_O/n_e ~ 1% was sustained until the 3rd boronization. The 3rd boronization was performed under the condition with n_O/n_e ~ 1%. After the 3rd boronization, n_O/n_e increased to ~ 1.5 % in contrast. Since the plasma configuration after the 3rd boronization was different from that after the 1st and 2nd boronization as shown in Fig. 1, local plasma-wall interactions took place at different parts of the first walls and the divertor plates. Oxygen might have been released from an unclean region.

The boron spectral line could be observed only within ~ 50 shots after boronization. Then the boron content (n_B/n_e) was estimated to be less than 0.2 %. The carbon content (n_C/n_e) was not dependent on boronization. A constant n_C/n_e ~ 2.5 % was observed. As a result, Z_{eff} was strongly dependent on the oxygen content. Figure 3 shows Z_{eff} as a function of shot number. The trace of Z_{eff} is similar to that of n_O/n_e. This indicates that boronization is effective in reduction of oxygen impurity, resulting in plasmas with low Z_{eff}.

4. Summary

In order to investigate the durability of boronization effects, L-mode discharges with an identical condition were repeated before and after boronization. The oxygen content (n_O/n_e) in a main plasma decreased from ~ 1.5% to ~ 0.7 % by boronization using 70 g of decaborane and from ~ 2.8 % to ~ 0.5 % by boronization using 20 g of decaborane. The plasma with n_O/n_e less than 1% was sustained for ~ 400 shots after the boronization using 70 g of decaborane. On the other hand, even after boronization, the oxygen content in the main plasma increased when the plasma shape was configured differently from the plasma shape before the boronization. This is believed to be due to local plasma-wall interactions at unclean parts of first walls. After boronization, the boron content in the main plasma decreased to a negligible level in ~ 50 shots and the carbon content in the main plasma did not change by boronization. As a result, Z_{eff} was strongly dependent on the oxygen content. Therefore, boronization is necessary to obtain high plasma purity, especially after vacuum vessel ventilation.

References

[1] Higashijima S., et al., Journal of Plasma and Fusion Research **75**, 1297 (1999) in Japanese.

[2] Reflke A., et al., J. Nucl. Mater. **212-215**, 1255 (1994).

[3] S.Higashijima, et al., J. Nucl. Mater. **220-222**, 370 (1995).

[4] Yagyu J., et al., JAERI-Tech **12** (2001) in Japanese.

7.8 Impurity reduction experiments by low baking temperatures

T. Nakano, H. Kubo, S. Higashijima and T. Fujita

1. Introduction

Carbon materials have widely been used for divertor tiles, limiters and first walls in many tokamaks because of their high thermal shock resistance, high melting point, good thermal conductivity and low atomic number. Carbon, however, has the property of strong chemical reaction with hydrogen. The chemical sputtering process is more prominent than the physical one in cold and dense divertor plasmas. The chemical sputtering yield is dependent on the temperature of carbon materials while the physical is not. The chemical sputtering yield increases with the temperature of carbon materials to 600 °C, and it has the maximal value around 600 °C [1]. In this experiment, by lowering the baking temperature of carbon first walls and divertor plates from 270 °C, usual baking temperature in JT-60U, to 150 and 80 °C, we attempt to decrease the impurity concentration of the main plasma. The chemical sputtering yield is measured at each surface temperature of the carbon divertor plates.

2. Experimental

The plasma effective charge (Z_{eff}) was measured in L-mode discharges with neutral beam (NB) heating powers of 4 and 13 MW and in reversed shear discharges with NB heating power of 10 MW at the baking temperatures of 270, 150 and 80 °C. The plasma current was 1.5MA and the toroidal field 3.0 T and the line averaged electron density ~ 1.4 and ~ 2.0 x 10^{19} m^{-3} in L-mode discharges with 4 and 13 MW NB heating power, respectively. In reversed shear discharges, the plasma current was 1.2 MA, the toroidal field 3.5 T and the line averaged electron density ~ 2.4 x 10^{19} m^{-3}. A series of experiments were carried out in a hydrogen discharge with almost the same plasma configuration, that is, plasma volume, plasma shape, the position of a null point and strike points as shown in figure 1(a) in section 7.7 of this report for the L-mode discharges.

In order to measure the chemical sputtering yield, intensities of CH (~ 431.4 nm) and C_2 (~ 516.5 nm) spectral bands in the divertor plasma, ion flux to divertor plates and temperatures of the carbon divertor plates around the strike points were measured by a spectrometer, Langmuir probes and IRTV, respectively. L-mode discharges with 4 MW NB heating power were carried out in hydrogen gas at the baking temperature of 270, 150 and 80 °C and also in deuterium gas at 270 and 150 °C. The line averaged electron density of the main plasma increased to 2.5 - 3.4 x 10^{19} m^{-3} by gas puffing. The electron density and temperature were ~ 1 x 10^{20} m^{-3} and ~ 10 eV around the strike point on the outer divertor plate. The details of measurement and analysis methods are

described in [2].

3. Results

Figure 1 shows Z_{eff} of the main plasma as a function of baking temperature in hydrogen discharges. In the L-mode discharges with 13 MW NB heating and reversed shear discharges, Z_{eff} at the baking temperature of 270 °C is higher than that at 150 and 80 °C whereas in L-mode discharges with 4 MW NB heating, Z_{eff} at the baking temperature of 270 °C is not different significantly from Z_{eff} at 150 and 80 °C. The decrease of Z_{eff} might result from the dependence of the chemical sputtering yield on the wall temperature. Therefore, the chemical sputtering yield was measured at the surface temperature of 270, 150 and 80 °C in hydrogen discharges and at 270 and 150 °C in deuterium discharges.

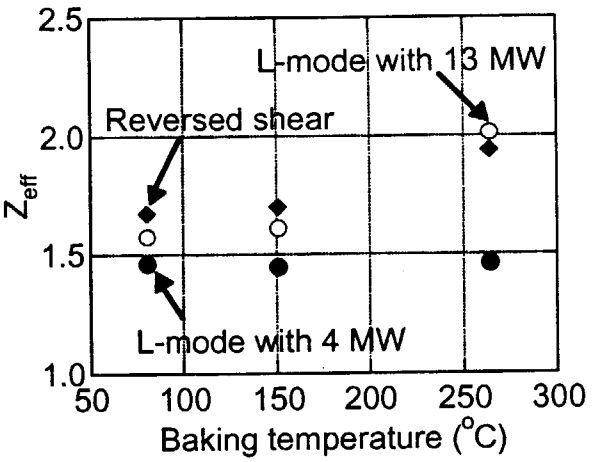

Fig.1 Plasma effective charge (Z_{eff}) as a function of baking temperature in hydrogen discharges. Closed circles show Z_{eff} for L-mode discharges with 4 MW NB heating, open circles for L-mode with 13 MW and diamonds for reversed shear.

Figure 2 (a) shows the CH_4/CD_4 sputtering yields as a function of ion flux density at the outer strike point. Each sputtering yield shows a decreasing trend with increasing ion flux up to 1.3 x 10^{23} $m^{-2}s^{-1}$ for each surface temperature and hydrogen isotopes. Regression analysis of the CH_4/CD_4 sputtering yield (Y) with a function of $Y \propto \Gamma_{ion}^{a}$ results in a ~ -0.05 to -0.40 with errors of ~ 0.2, where Γ_{ion} is the ion flux to the divertor plates. Figure 2 (b) and (c) show the C_2H_x/C_2D_x and the total sputtering yield defined as $Y_{total} = Y_{CH4/CD4} + 2 \times Y_{C2Hx/C2Dx}$ as a function of ion flux density. Similar analysis for the C_2H_x/C_2D_x and the total sputtering yield leads to a ~ -0.07 to -0.37 and a ~ -0.12 to -0.37 (except for the total sputtering yield by deuterium ions at the surface temperature of 150 °C, a ~ - 0.6), respectively. Since it is difficult to separate clearly the dependence of the chemical sputtering yields on an ion flux and on an incident ion energy, the above analysis results in only an apparent dependence of the sputtering yields on the ion flux. In order to investigate the dependence, the total sputtering yields have been analyzed by a regression analysis with a function of $Y \propto T_e^{a}$, where T_e is the electron temperature at the strike point. Figure 3 shows the total sputtering yields as a function of electron temperature. Assuming an ion temperature is equal to the electron temperature, corresponding impact energy range is from ~ 30 eV to ~ 90 eV due to a sheath

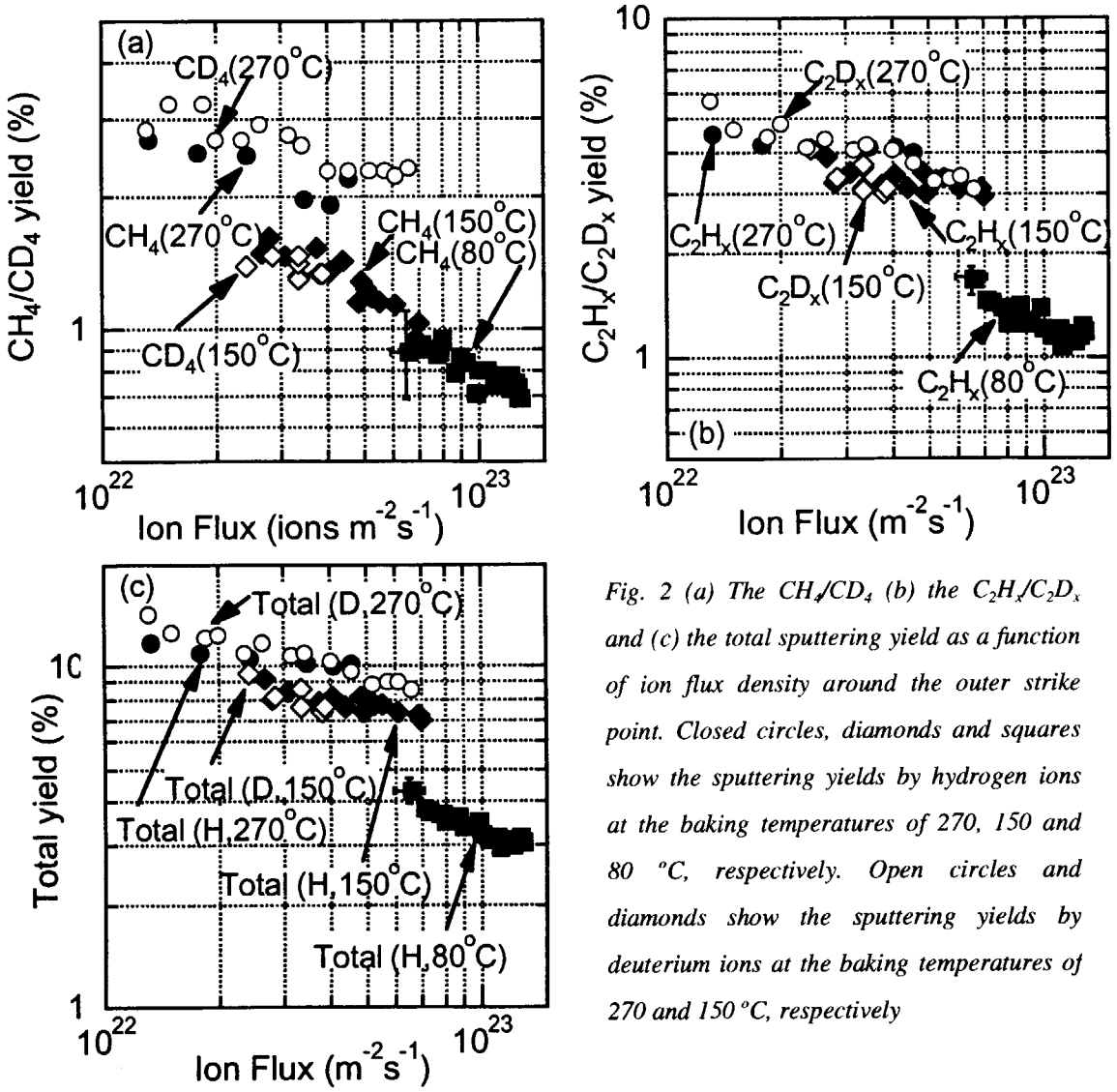

Fig. 2 (a) The CH_4/CD_4 (b) the C_2H_x/C_2D_x and (c) the total sputtering yield as a function of ion flux density around the outer strike point. Closed circles, diamonds and squares show the sputtering yields by hydrogen ions at the baking temperatures of 270, 150 and 80 °C, respectively. Open circles and diamonds show the sputtering yields by deuterium ions at the baking temperatures of 270 and 150 °C, respectively

acceleration. The regression analysis for the yields with a function of $Y \propto T_e^a$ results in $a \sim 0.24 - 1.1$ with errors of ~ 0.2. Similar results are obtained from the regression analyses for the CH_4/CD_4 and C_2H_x/C_2D_x yields. Assuming that the incident ion energy is proportional to the electron temperature and chemical sputtering yields do not depend on the ion flux, the results from the regression analysis with a function of $Y \propto T_e^a$ (a ~ 0.24 – 1.1) agree with the result from PISCES-B [5]. In particular, the most reliable regression analysis due to the largest number of data points for the CH_4 and C_2H_x and the total sputtering yield at the surface temperature of 80 °C results in ~ 0.5, and the result is in good agreement with the result from PISCES-B [5]. Therefore, the reducing dependence of the chemical sputtering yields on the ion flux is considered to be due to the decrease of the incident ion energy. The dependence of the chemical sputtering on a surface temperature is estimated with a help of the results from the regression analysis

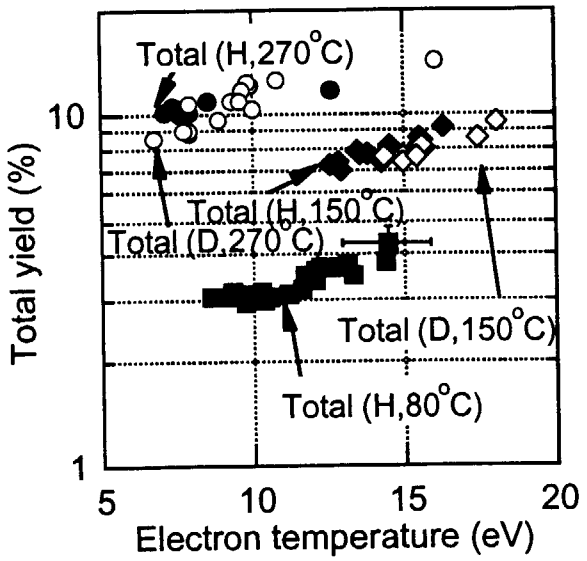

Fig. 3 The total sputtering yield as a function of electron temperature. Symbols are similar to Fig. 2.

for the sputtering yields with a function of $Y \propto T_e^a$. To avoid serious errors due to extrapolation, comparison is limited in the electron temperature range from 10 eV to 15 eV. The resultant ratio of the chemical sputtering yield at the surface temperature of 270, 150 and 80 °C is about 1 : 0.5 – 0.6 : 0.3. Similar analyses result in the ratio of 1 : 0.4 : 0.3 for the CH_4/CD_4 yields and the ratio of 1 : 0.5 - 0.7 : 0.3 for the C_2H_x/C_2D_x yields.

In Fig. 2 and 3, the difference between the chemical sputtering yields by hydrogen ions and deuterium ions is also compared. The sputtering yield by deuterium ions was similar to the sputtering yield by hydrogen ions.

4. Summary

The plasma effective charge (Z_{eff}) was successfully decreased in L-mode discharges with 13 MW NB heating and reversed shear discharges by lowering a baking temperature from 270°C, usual baking temperature, to 150 and 80 °C. This might result from the lower chemical sputtering yield at the lower surface temperature. The measured chemical sputtering yield showed apparent dependence on an ion flux, i.e., $Y \propto \Gamma_{ion}^{-0.05 - -0.40}$. However, the regression analysis with a function of $Y \propto T_e^a$ indicated that the reducing dependence of the chemical sputtering yields on the ion flux was considered to be due to the decrease of the incident ion energy. The chemical sputtering yield also showed clear dependence on the surface temperature. The ratio of the chemical sputtering yield at 270 and 150 and 80 °C was about 1 : 0.4 - 0.7 : 0.3. The sputtering yield by deuterium ions was similar to the sputtering yield by hydrogen ions.

References

[1] Mech.B.V., et al., J.Nucl.Mater. **241-243**, 1147 (1975).

[2] Nakano T., et al., Nucl. Fusion **42**, 689 (2002).

[3] Yamada R., J. Nucl. Mater. **145-147**, 359 (1987).

[4] Pospieszczyk A., et al., UCLA report PPG-1251 (1989).

[5] White, D.G., et al., Nucl. Fusion **41**, 47 (2001).

8. Divertor/SOL Plasmas

8.1 Volume recombination in detached divertor plasmas

H. Kubo and T. Nakano

1. Introduction

The detached divertor regime is attractive for mitigating the severe problem of concentrated power loading of the divertor plates. The volume recombination is considered to be important in reducing the ion flux to the divertor plates and detaching the plasma from the divertor plates [1-3]. This paper describes a study of the volume recombination in detached divertor plasmas by observation of Balmer lines of hydrogen atoms and continuum.

2. Experimental

The diagnostics for the present divertor study is shown in Fig. 1. Using a filter optics with a 60ch optical fiber array, the spatial profiles of H_α and C II 658 nm line emission were measured. Using a visible spectrometer, spectra around a wavelength of the Balmer series limit of H I were observed. With the spectrometer, we could simultaneously observe the spectra for 16 viewing chords selected from a 60ch optical fiber array. In two identical discharges, spectra for 30 viewing chords were observed by changing the fiber selection. Figure 2 shows a spectrum of the Balmer series lines. The Balmer series lines with the upper levels of n = 7 - 11 were identified. Profiles of electron density and temperature were measured with Langmuire probes at the divertor target plates and in the vicinity of the X point, as shown in Fig. 1. The electron density at the divertor target plates might be underestimated by a factor of ~2 due to erosion of the Langmuir probes.

Figure 3 shows time evolution of an L-mode discharge (hydrogen plasma, NBI power: 4 MW) to be investigated. By a feedback technique using a H_2 gas puffing, the electron density was raised and kept 52 % of the Greenwald density limit. After the onset of an X-point MARFE at 7.9 s, the gas-puffing rate decreased. Time evolution of the intensities of H_α and H_ε line emission is shown in (b) and (c). The intensities were integrated over the inner and outer divertor plasmas. The intensities increased with the electron density, and the intensities in the outer divertor increased rapidly at the MARFE onset. Spatial profiles of emission of H_α, H_ε, and C II lines are shown in Fig. 4. At 6.4 s: before the MARFE onset, the emission profiles had peaks around the inner and outer strike points. At 8.5 s: when the MARFE appeared, not only the C II profile but also H_α and H_ε profiles had peaks around the X point besides the peaks around the inner and outer strike points. In Fig. 3 (d), time evolution of the ion fluxes to the divertor plates is shown. The ion fluxes were derived from the target probe measurement. The ion fluxes to the inner and outer divertor plates rolled over around 6.3 and 7.2 s, respectively. They decreased drastically, when the MARFE appeared. Therefore, partial

detachment started gradually before the MARFE onset, and the detachment became pronounced by the MARFE onset. Spatial profiles of electron density, temperature, and pressure measured with the target and X-point probes are shown in Fig. 5. It seems that the inner and outer divertor plasmas had already been detached partially near the strike points at 6.4 s: before the MARFE onset. The width of the detached region was ~ 1 cm. Since the reduction of the ion flux in the detached region was small for the outer divertor, the total ion flux to the outer divertor plates did not decrease at 6.4 s as seen in Fig. 3 (d). The detachment was clearly seen at 8.5 s: after the MARFE onset. The width of the detached region was ~ 0.5 cm in the outer scrape-off layer near the X point, and the width was ~ 2 cm at the divertor plates. The electron density and temperature in the attached region just outside of the detached region were ~ 1.2×10^{20} m^{-3} and ~ 30 eV near the X point, respectively. The electron density and temperature were ~ 1.5×10^{19} m^{-3} and ~ 5 eV at the divertor plates, respectively.

3. Analysis and Discussion

From the intensities of the Balmer series lines with the upper levels of n = 7 - 11, it was found that the populations of n > 7 levels could be explained by the Saha-Boltzmann distribution. Therefore, the population of the n = 7 level was attributed to the recombination component. When we assume that the populations of the n = 3 and 7 levels are attributed to the recombining components, using a collisional radiative model, the intensity ratio is estimated to be 0.05 - 0.3 in the region of $n_e = (1 - 10) \times 10^{19}$ m^{-3} and $T_e = 0.3 - 100$ eV. The ratio of the H_ε line intensity to the H_α line intensity is shown in Fig. 4 (d). The intensity ratio was lower than 0.01, and it suggests that most of the population of the n = 3 level was ascribed to the ionization component. When the population of the n = 7 level is attributed to the recombination component, the recombination rate is almost proportional to the H_ε line emission rate in the region of $n_e = (1 - 10) \times 10^{19}$ m^{-3} and $T_e = 0.5 - 10$ eV [3]. In the region, the ratio of the recombination rate to the H_ε line emission rate is ~ 135. From the profile of the H_ε line emission shown in Fig. 4 (b), it is suggested that the recombination rate was high around the both divertor plates before the MARFE onset. When the X-point MARFE appeared, the recombination rate was also high around the X point. In Fig. 3 (c), the recombination ion flux, which was derived from the intensity of the H_ε line emission on the assumption that the ratio of the recombination rate to the H_ε line emission rate was 135, can be seen by referring to the right scale. The recombination ion flux increased gradually with the electron density. The increase with the MARFE onset was notable in the outer divertor. When the MARFE appeared, the recombination ion flux was estimated to be 25 % of the divertor plate ion flux at ~ 7.5 s: before the MARFE onset. The ratios of the recombination ion flux to the ion flux to the divertor plates were 1 and 0.5 in the inner and outer divertor, respectively.

To explain the spectroscopic observation, the electron temperature measured with the Langmuir probes was too high and the electron density measured with the Langmuir probe

was too low. At the present stage, the reason has not been known. The Langmuir probe measurement might have a problem for low-temperature plasmas. Molecular activated recombination [3], which has not been considered in the present analysis, might play important roles. Effect of line integration for the spectroscopic measurement should also be considered [2].

4. Summary

From the profile of the H_ε line emission, it was suggested that the recombination rate was high around the both divertor plates before the MARFE onset. When the X-point MARFE appeared, the recombination rate was also high around the X point. The recombination ion flux increased gradually with the electron density. With the MARFE onset, the increase in the recombination ion flux was notable in the outer divertor. When the MARFE appeared, the recombination ion flux was estimated to be 25 % of the divertor ion flux before the MARFE onset. The ratios of the recombination ion flux to the ion flux to the divertor plates were 1 and 0.5 in the inner and outer divertor, respectively. To explain the spectroscopic observation, the electron temperature measured with the Langmuir probes was too high and the electron density measured with the Langmuir probe was too low. Further investigation is necessary to understand the volume recombination.

References

[1] Lumma D. et al., Phys. Plasma **4**, 2555 (1997).

[2] Kubo H. et al., Proc. of 1998 Int. Conf. on Plasma Physics and 25th EPS Conf. on Cotr. Fusion and Plasma Physics, (Prague, 1998), Vol. 22C, 427 (1998).

[3] Kubo, H. and Sawada K., J. Plasma and Fusion Research **74**, 562 (1998).

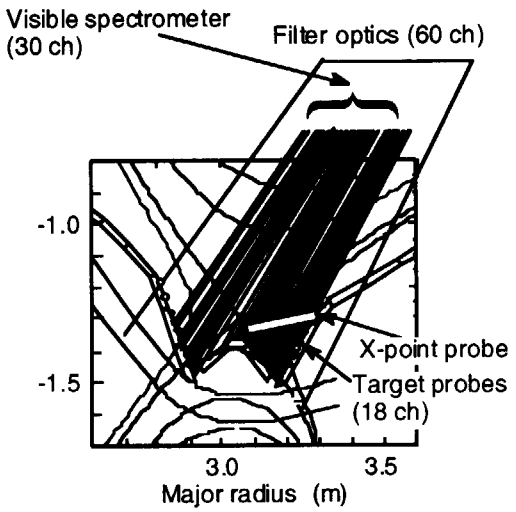

Fig. 1. Diagnostics for the present divertor study.

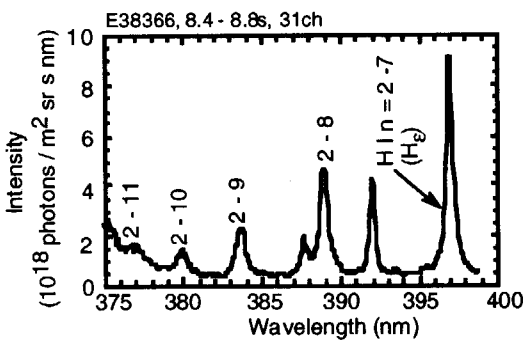

Fig.2. Spectrum around a wavelength of the Balmer series limit. The spectrum was observed with the chord viewing the X point in a detached divertor plasma with an X-point MARFE (8.6 s in Fig. 3).

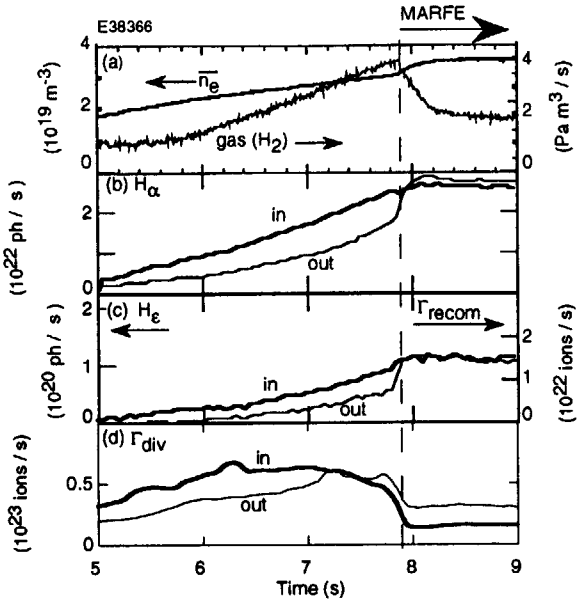

Fig.3. Time evolution of an L-mode discharge (plasma current: 1.5 MA, toroidal magnetic field: 3.5 T, NBI heating power: 4 MW). (a) Electron density in the main plasma and H_2 gas puff rate, (b) intensity of H_α line emission from the inner and outer divertor plasmas, (c) intensity of H_ε line emission from the inner and outer divertor plasmas, and (d) ion flux to the inner and outer divertor plates. In (c), the recombination ion flux, which was derived by multiplying the H_ε line intensity by 135, can be referred to the right scale.

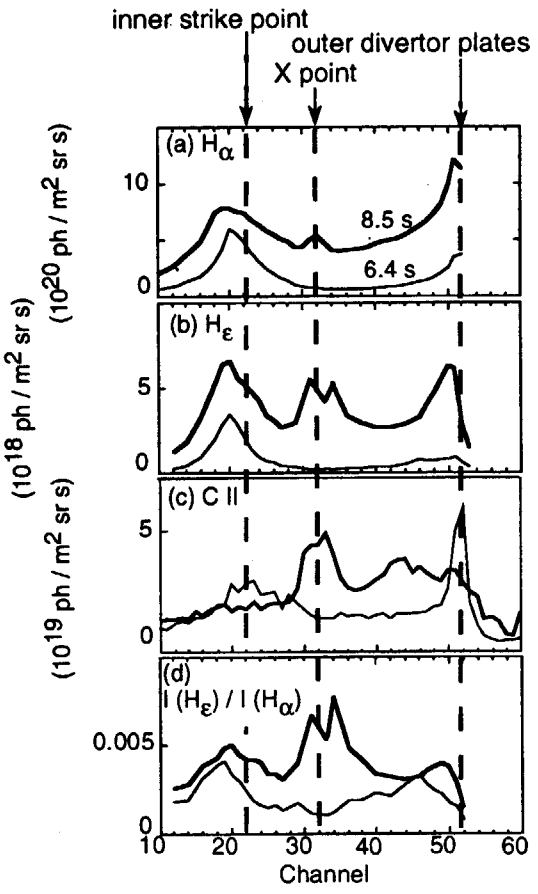

Fig. 4. Spatial profiles of emission of (a) H_α, (b) H_ε, and (c) C II 658 nm lines and (d) ratio of the H_ε line intensity to the H_α line intensity.

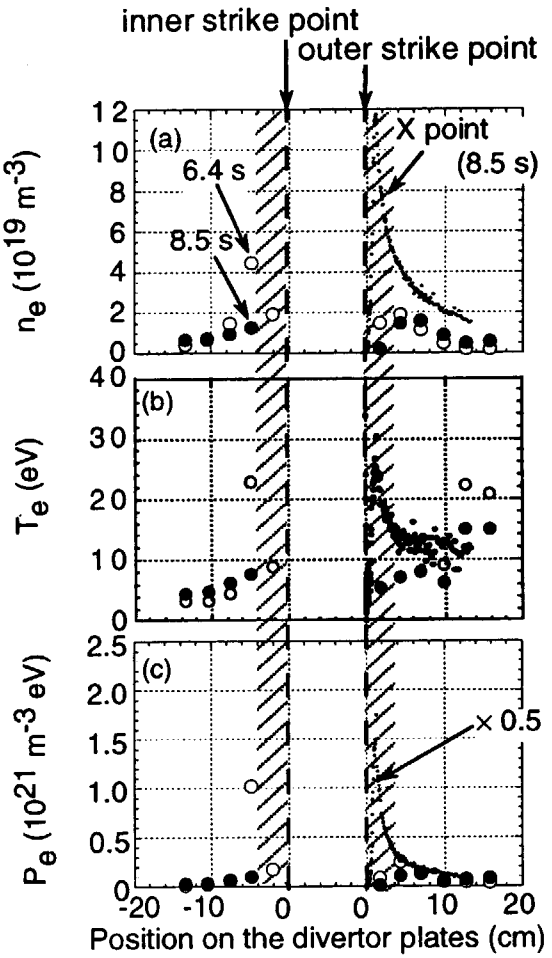

Fig. 5. Spatial profiles of (a) electron density, (b) temperature, and (c) pressure measured with the target (large symbols) and X-point (small symbols) probes. For the X-point probe, the data are plotted against the position that the flux surfaces struck on the divertor plates.

8.2 Pumping effect on plasma flow and divertor detachment[1]

N. Asakura, S. Sakurai, H. Tamai, Y. Koide, Y. Sakamoto, O. Naito, K. Masaki

Control of the plasma flow in the scrape-off layer (SOL) and divertor, using a divertor pumping system, is considered important because of its implications for the exhaust of helium ash and impurity retention in the divertor. However, there were few measurements of the SOL plasma flow, and the effect on the plasma flow pattern is not understood. In 2000, the SOL plasma flow for the case of pumping at the down-stream sides (both inner and outer divertor private flux region) was investigated under the partical detachment condition, using the reciprocating Mach probes installed at the outer midplane and the x-point[2]. The neutral recycling in the divertor region was also measured.

Pumping effect on divertor detachment

Profiles of T_e and j_s in the SOL were measured in the L-mode plasmas where $I_p = 1.6-1.7$ MA, $B_t = 3.5$ T, $q_{95} = 3.5$, and plasma density, $\bar{n}_e$, was scanned on a shot-to-shot basis. An improvement of the divertor operation is observed for the both-side pumping case. Partial-detached plasma at both divertor targets without causing the x-point MARFE (i.e. plasma detached below the x-point) is maintained at $\bar{n}_e$ of $(2.3-2.6)\times10^{19}$ m^{-3}. The onset $\bar{n}_e$ of the x-point MARFE (2.75×10^{19} m^{-3}) is higher than that for the inner divertor pumping, where the partial-detached plasma is observed at $\bar{n}_e = 2.45\times10^{19}$ m^{-3} and the x-point MARFE appears at $\bar{n}_e = 2.6\times10^{19}$ m^{-3}.

Under the partial-detached plasma at both divertor targets without the x-point MARFE, T_e^{Xp} decreases to 10−30 eV and p_e^{Xp} is maintained at 230−340 Pa while $2p_{e,out}^{div}$ decreases. The ratio of $2p_{e,out}^{div}/p_e^{Xp}$ is smaller than that for the inner-side pumping case, which is mostly due to a large reduction in the ion flux at the divertor target, while T_e^{div} of 5−10 eV is comparable. The larger plasma flow just below the x-point for the both-side pumping is produced by larger reduction in $p_{e,out}^{div}$. The neutral source at the separatrix is reduced by the divertor pumping from the private flux region. The larger reduction in $p_{e,out}^{div}$ is also observed during the x-point MARFE, where the detachment region extends to the up-stream (x-point) and the outer flux surfaces.

In-out asymmetry in divertor recycling

For attached divertor condition at high $\bar{n}_e$, in particular, $\Phi_{D\alpha}^{div,in}$ (recycling flux in the inner divertor) is enhanced 2−3 larger than $\Phi_{D\alpha}^{div,out}$. Both recycling flux in the divertor and the in-out asymmetry are similar for the inner-side and both-side pumping cases. Neutrals from the inner divertor to outer divertor through the bypath is small so that the in-out asymmetry does not change.

When plasma detachment occurs at the inner divertor separatrix, $\Phi_{D\alpha}^{div,out}$ increases with $\bar{n}_e$, and then outer divertor plasma is detached. For the detached divertor without x-point MARFE, in-out symmetries in recycling flux, neutral pressure and ion flux are observed. For the both-side pumping, larger values of $\Phi_{D\alpha}^{div,in}$ and $\Phi_{D\alpha}^{div,out}$ are observed in the detached divertor, compared to those for the inner-side pumping cases.

Summary

With application of both inner and outer divertor pumping, the both-side pumping was favorable for the partial-detached plasma, which can be maintained without appearance of x-point MARFE. Under the partial-detached divertor condition, an increase in the plasma flow at the x-point was observed for the both-side pumping due to a reduction in the down-stream plasma pressure.

References

[1] N. Asakura, *et al.*, J. Nucl. Mater. **290-293** (2001) 825.
[2] N. Asakura, *et al.*, Nucl. Fusion **39** (1999) 1983.

8.3 Fast measurement of SOL flow and plasma profile in ELMy H-mode

N. Asakura, S. Sakurai, K. Itami, H. Tamai

Fast measurement of heat and particle fluxes in SOL during an ELM is crucial for evaluating convection and conduction of ELM power flow. At the same time, measurements of the ELM flow pattern is important to understand the particle and impurity exhaust in ELMy H-mode. The plasma flow in SOL of the ELMy H-mode plasma was measured using reciprocating Mach probes installed at the outer midplane and the divertor x-point. ELM heat load on the divertor plates was measured with IRTV of fast sampling (250μs per profile). Plasma parameters were I_p=1MA, B_t=2T, δ=0.32, κ=1.4, P_{NB}= 4.3MW. Line-averaged electron density was $1.8\times10^{19}\,m^{-3}$, and additional gas puff was not supplied during measurements, where ELM frequency was 30-40Hz. Since reciprocating period of the probe is about 1s, about 10 ELM events are measured near the separatrix (<10cm).

1. SOL plasma flow

Time evolutions of ion saturation currents, j_s, at up-stream side of the midplane and the x-point probes, and j_s ratio, j_s(down-stream side)/j_s(up-stream side), are shown in Fig.1. Figure 1(a) shows that two ELMs occur and increment of j_s at up-stream side of the probe is an order of magnitude both at midplane and x-point. Values of j_s both at up-stream side and down-stream side of the probe are increased. However, time evolutions of j_s ratio are different for the two locations as shown in Fig.1(b). j_s(down)/j_s(up) at the midplane is decreasing to unity (i.e. flow velocity zero) just after ELM event. On the other hand, j_s(down)/j_s(up) near x-point is decreased to 0.1 (i.e. flow velocity increases towards divertor) and, then, it is increased to unity (i.e. flow velocity zero).

Enlarged figures in the period of 2 ms are shown in Fig.2. Figure 2(a) shows that j_s both at up-stream and down-stream sides of midplane are increased to the maximum values just after the ELM event and that values of j_s for the two sides become comparable in 1 ms. The change shows that increment of j_s is caused by radial diffusion or poloidal drift rather than the parallel transport along the field lines. Figure 2(b) shows that j_s at the up-stream side near the x-point is increased faster than j_s at down-stream side and that it reaches a peak in ~200μs after the j_s peak at the midplane. The time delay between j_s peaks at the midplane and the x-point is explained by the parallel convective flow. Transit time of ions from the midplane to the x-point is about 130μs (connection length = 26m/ acoustic speed = 2×10^5m/s assuming pedestal ions and electrons are exhausted into SOL, where T_i = 800eV and T_e = 600eV are measured at

pedestal).

Figure 2(c) shows that flow velocity near the x-point becomes large during ~200μs of j_s peak. Then j_s(down)/j_s(up) increased in 1ms larger than that between ELMs, i.e. flow velocity decreases. It may be caused by an increase in the plasma pressure near the divertor target.

Profiles of Mach number at the midplane and near the x-point are shown in Fig.3(a) and (b), respectively. At the midplane, flow reversal between ELMs is reduced just after ELM (at j_s peak), and flow velocity becomes zero over the SOL region. In particular, SOL flow towards the divertor is observed only at 1cm outside of the separatrix. As a result, increment of j_s at outer flux surfaces may be caused by the radial diffusion. Near the x-point, flow velocity is increased from ~0.5 to 0.8-1.0 just after ELM (at j_s peak) only within 1-1.5cm outside of the separatrix, while flow velocity is reduced in the outer flux surfaces. Thus, the parallel convective flow is observed just after ELM within 1 - 1.5cm of SOL. The increment of j_s at outer flux surfaces may be caused by the radial diffusion similar to that at the midplane.

An increase in the plasma pressure near the divertor target may be caused by the ionization of neutrals. Figure 4 (b) shows time evolution of D_α brightness at midplane and divertor. A rapid increase in D_α brightness at outer divertor is observed during the large convective flow.

2. Target heat load

Figure 5 shows a superimposed plot of 8 time evolutions of ELM heat flux to the divertor, which are normalized by each maximum value. Most ELM heat fluxes are extended over 2-3 time frames of the fast IRTV measurements. This fact suggests that deposition time of ELM heat flux corresponds to 1-2 *x* frame (250μs) = 250-500 μs.

Figure 6 shows time evolutions of ELM heat flux and j_s, j_s-ratio and floating potential measured with the x-point Mach probe. The period of the peak heat flux corresponds to that of the enhancement of the plasma flow (j_s is increased, j_s-ratio is decreased), 250μs. Fast electrons and ions reached to the x-point Mach probe at the start of the heat flux enhancement (faster than at the peak). This fact suggests that most of energy flow to the divertor is transported by the parallel convective flow.

Profiles of ELM heat flux are measured with the fast IRTV, and 8 ELMs are superimposed in Fig. 7. At the outer divertor, FWHM of the ELM heat flux profiles ranged in 1.3+-0.2cm, and multi-peaks are sometimes seen in the profile. The FWHM of 1.3cm is in good agreement with area (1-1.5cm) for enhancement of the ELM SOL flow. At the inner divertor, FWHM of the ELM heat flux profiles ranged in 1.7+-0.6cm, and multi-peaks are very often seen in the profile. Thus, deposition width of ELM heat flux is wider than 1.7cm.

Summary

Particle flux and SOL flow caused by ELM events were measured using Mach probes at outer midplane and near the divertor x-point. Enhancement of the SOL flow velocity towards the divertor was observed near the x-point, which occurred ~200μs after the increase in the particle flux at midplane. Duration of heat deposition at the outer divertor target (~250μs) was comparable to that for the enhancement of the SOL flow (~200 μs). These results show that the convective transport plays an important role on heat transport at ELMs. Density and power scans are planned in 2001 to investigate the transport of ELM heat and particle fluxes.

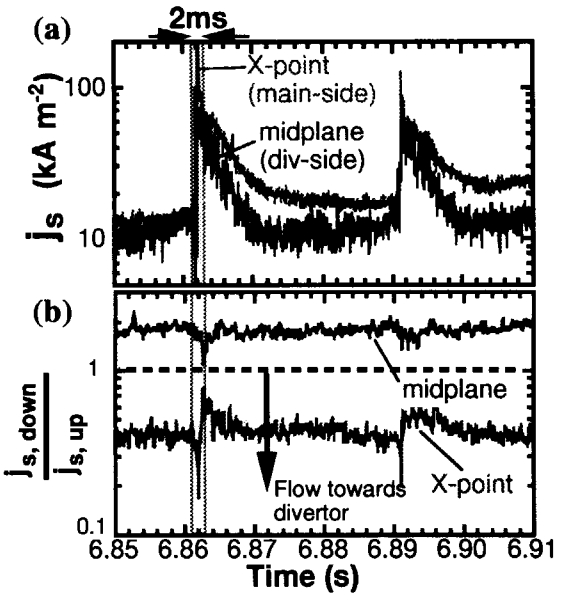

Fig1. Time evolutions of (a) j_s at up-stream side of probes, (b) j_s ratios at midplane and x-point.

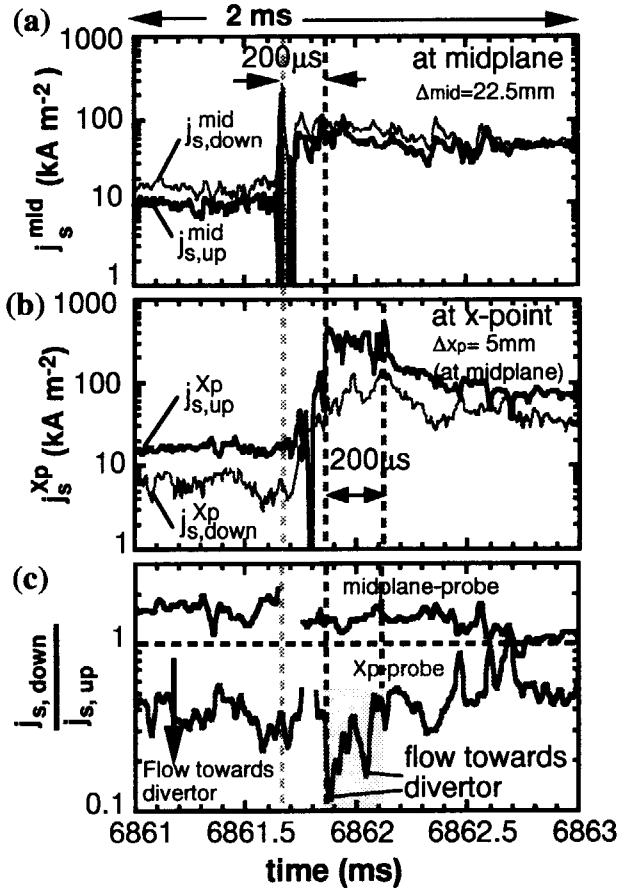

Fig2. Evolutions of (a) j_s at midplane, (b) j_s at x-point, (c) j_s ratios at midplane and x-point during an ELM.

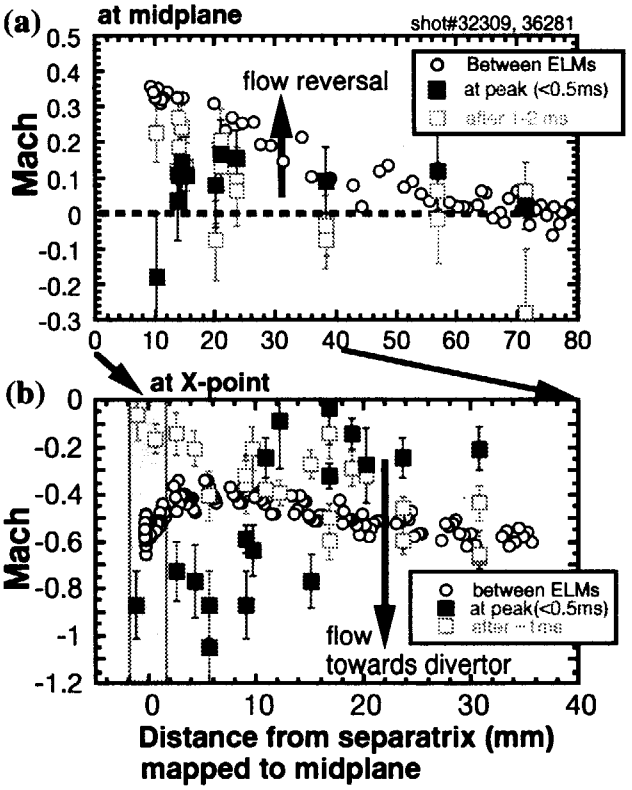

Fig3. Radial profiles of Machnumbers (a) at midplane (b) near x-point.

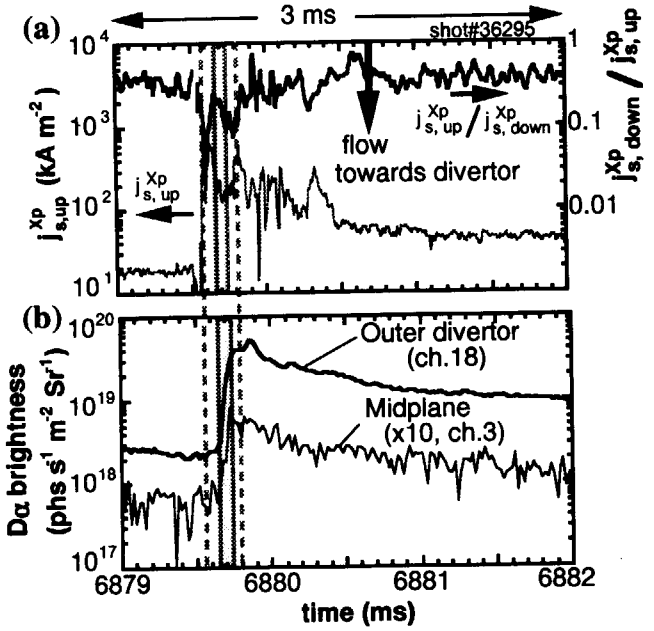

Fig4. Evolution of (a) j_s (upstream-side), j_s ratio at x-point, (b) D_α brightness at midplane and outer divertor.

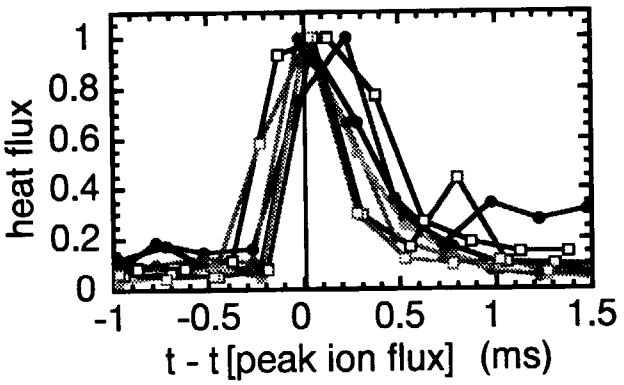

Fig5. Time evolution of heat load at outer divertor target, which are normalized at each peak (8 ELMs are overplotted).

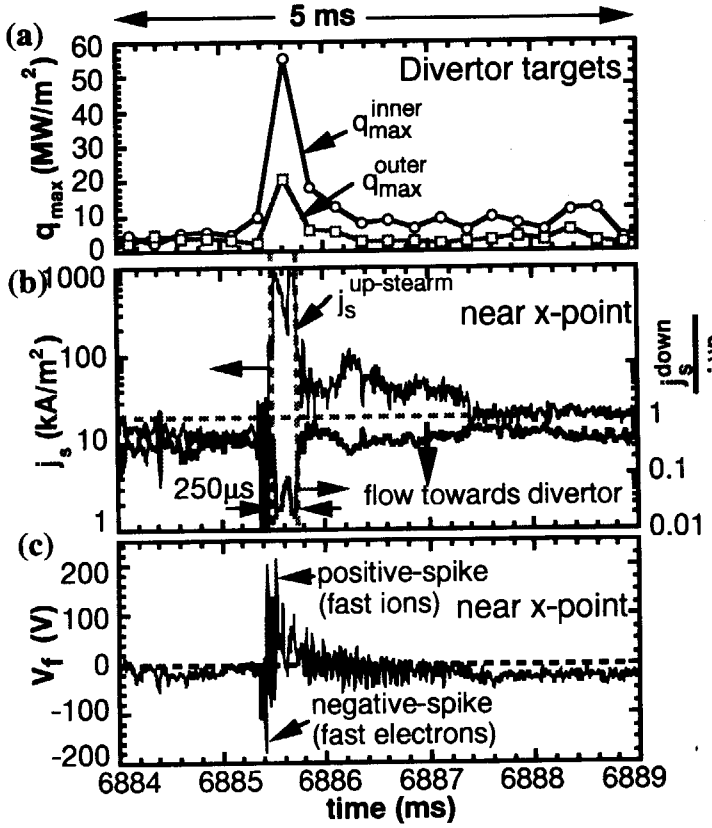

Fig6. Time evolution of heat load at inner and outer divertor target, (b) j_s and j_s ratio near x-point, (c) floating potentiol near x-point.

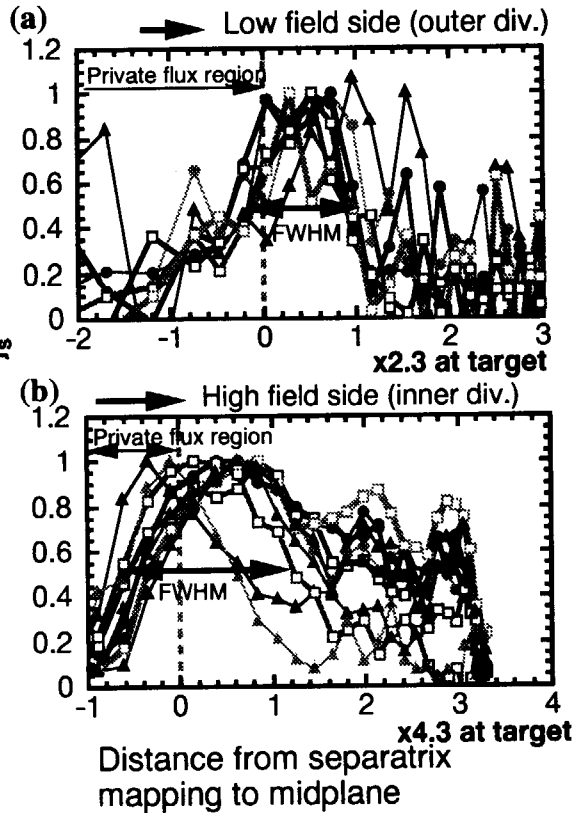

Fig7. ELM heat flux profiles at (a) inner and (b) outer targets (8ELMs are overplotted)

8.4 Fast measurement of SOL flow and plasma profile in pellet injection

N. Asakura, S. Sakurai, H. Takenaga

Fast measurement of particle flux in SOL during pellet injection was performed, for the first time, to investigate perturbations of density profile and SOL flow pattern. The plasma flow in SOL was measured using reciprocating Mach probes, similar to that for the ELMy H-mode plasma (Sec. 8.3), installed at the outer midplane and near the divertor x-point. Plasma parameters were I_p=1MA, B_t=2T, δ=0.32, κ=1.4, P_{NB}= 3.5MW for hydrogen L-mode plasma. Line-averaged electron density was 1.3×10^{19} m^{-3}, and additional gas puff was not supplied during the pellet injections (PI). Pellets were injected from two locations: horizontally from the outer midplane port (outboard pellet injection, O-PI) and vertically from the inner upper port (upper-inboard pellet injection, UI-PI).

1. SOL profile measurements

Profiles of electron density and temperature are measured with applying a triangle waveform of voltage (from -200 to +200V, a period of 2ms). Figure 1 shows time evolution of ion saturation current measured at upstream-side of the x-point Mach probe, $j_{s,up}^{Xp}$, and distance from the separatrix (mapping to midplane). Pellets are injected from outer midplane with the frequency of ~10Hz, and one pellet is not injected (this is the best case). Reciprocating period of the probe is about 1s, and about 3-6 pellet events are actually measured. Value of $j_{s,up}^{Xp}$ is increased rapidly after pellet injection, in particular, near the separatrix. It should be noted that an increase in $j_{s,up}^{Xp}$ is observed in the private flux region (large increase in $j_{s,up}^{Xp}$ was not observed for the SOL plasma measurements of ELM events in ELMy H-mode plasma). For the case of PI, SOL plasma density is also increased in the private flux region.

Figure 2 shows profiles of $j_{s,up}$ and $T_{e,up}$ at up-stream side of the x-point Mach probe for O-PI and UI-PI. For the two cases, increments of $j_{s,up}$ are roughly 30-50% near the separatrix. $T_{e,up}$ does not change in the time resolution of voltage scan (2ms), except for near separatrix (<1mm at midplane distance) of UI-PI case, where $T_{e,up}$ is decreased from 70 to 45 eV.

Figure 3 shows time evolutions of the ion saturation current measured at upstream-side of the midplane Mach probe, $j_{s,up}^{mid}$, and distance from the separatrix. Increment of $j_{s,up}^{mid}$ is observed near the separatrix (0.8 cm). Profiles of $j_{s,up}$ and $T_{e,up}$ at the up-stream side of the midplane Mach probe are shown in Fig. 4 for O-PI and UI-PI. Increment of $j_{s,up}$ is relatively small and slow at the outer midplane, as shown in Fig. 4(a), even for O-PI. The midplane Mach probe did not move in 38369(UI-PI), and pellets were not well injected in 38367 (increment of $j_{s,up}$ was not clearly seen either for UI-PI).

2. Fast changes in j_s and plasma flow in pellet injection

Figure 5 shows the time evolutions of $j_{s,up}^{Xp}$ and $j_{s,up}^{mid}$, for O-PI with applying a constant

voltage of −160V, and fast sampling time of 5μs. The value of $j_{s,up}^{Xp}$ is increased rapidly by a factor of 3-5 just after PI (<0.1ms). However, it is reduced within 1ms, and increment of $j_{s,up}^{Xp}$ is actually by 20-50%, and it is decreased to the background level in 40-80ms. On the other hand, change in $j_{s,up}^{mid}$ is not observed at the midplane.

Figure 6 shows time evolutions of $j_{s,up}^{Xp}$ and $j_{s,up}^{mid}$, for UI-PI during the probe insertion. The value of $j_{s,up}^{Xp}$ is increased by 30% at 6.85s after PI (0.2-0.4 ms). $j_{s,up}^{Xp}$ is increased largely just outside the x-point (at 6.91s) by a factor of 2, and it is decreased to the background level in 40-60ms. Rapid and large increases (a factor of 2-3) in $j_{s,up}^{mid}$ are observed at the midplane for UI-PI. After the rapid increase, $j_{s,up}^{mid}$ is decreased in 0.4-1ms to the background one.

The pellet injector, the x-point and midplane Mach probes are located at P-10, P-9 (-20 degree) and P-18 (+160 degree), respectively. Since magnetic field lines do not connect between the midplane Mach probe and the outboard pellet injector, increment of ion density ablated by O-PI may not affect the midplane SOL at P-18. Connection of magnetic field lines between two points should be identified by equilibrium analysis.

Figure 7(a) shows time evolutions of the j_s^{Xp} ratio, $j_{s,up}^{Xp}/j_{s,down}^{Xp}$, for UI-PI. Value of $j_{s,up}^{Xp}/j_{s,down}^{Xp}$ increases just after PI shows that SOL flow velocity towards the divertor. Values of $j_{s,up}^{Xp}/j_{s,down}^{Xp}$ after 1ms (cross-squares) and between PI(circles) are picked up, and the profiles of Mach number are shown in Fig.7(b) from 3 UI-PI shots, where the Mach number is estimated from the Hutchinson's formula, $0.35\ln[j_{s,up}^{Xp}/j_{s,down}^{Xp}]$. A large increase in SOL flow velocity is observed near separatrix and private flux region (<2mm mapping to midplane). Plasma flow in the outboard SOL, except for near the separatrix and private region, is not affected by UI-PI.

Figure 8(a) shows time evolutions of $j_{s,up}^{Xp}/j_{s,down}^{Xp}$ for O-PI. SOL flow velocity is increased just after PI, corresponding to the $j_{s,up}^{Xp}$ peaks in Fig.5(a). Values of $j_{s,up}^{Xp}/j_{s,down}^{Xp}$ just after PI(darken squares), 1ms after PI(cross-squares) and between PIs (circles) are picked up, and profiles of Mach number are shown in Fig.8(b) from 3 O-PI shots. A large increase in the flow velocity towards the divertor is observed just after PI in relatively wide SOL region (< 2.6cm mapping to midplane). However, it is decreased rapidly, and at 1ms after PI an increase in SOL flow is seen only near the separatrix and private flux region (similar to UI-PI case).

3. Summary

Increases in $j_{s,up}^{Xp}$ and the SOL flow velocity were observed, in particular, near the x-point. Those are similar between UI-PI and O-PI, except for large peaks just after O-PI (< 1ms). Net increment of the plasma density near the x-point is 20-50% but it is decreased to the background level in 40-80ms. The large and rapid peaks in $j_{s,up}^{Xp}$ near the x-point and no change in $j_{s,up}^{mid}$ for O-PI may be caused by local increase in the plasma density.

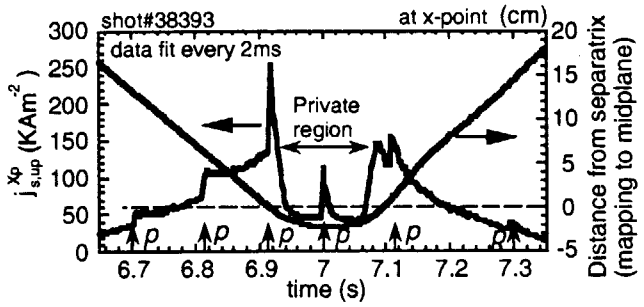

Fig1. Time evolutions of j_s at up-stream side of x-point Mach probe and distance from separatrix.

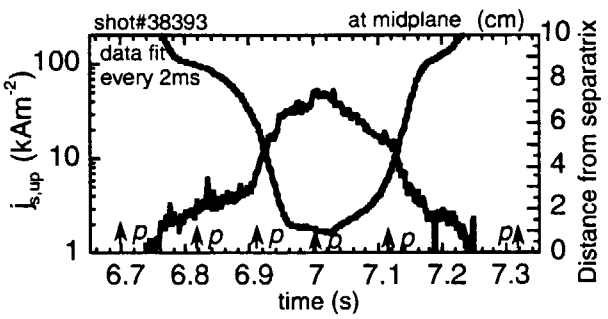

Fig3. Time evolutions of j_s at up-stream side of midplane Mach probe and distance from separatrix.

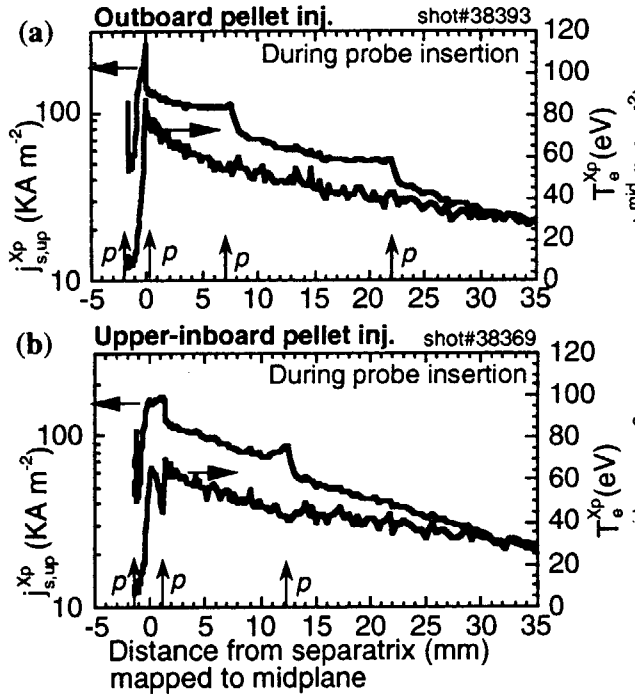

Fig2. Profiles of j_s and T_e at up-stream side of x-point Mach probe, (a) for outboard PI, (b) for upper-inboard PI.

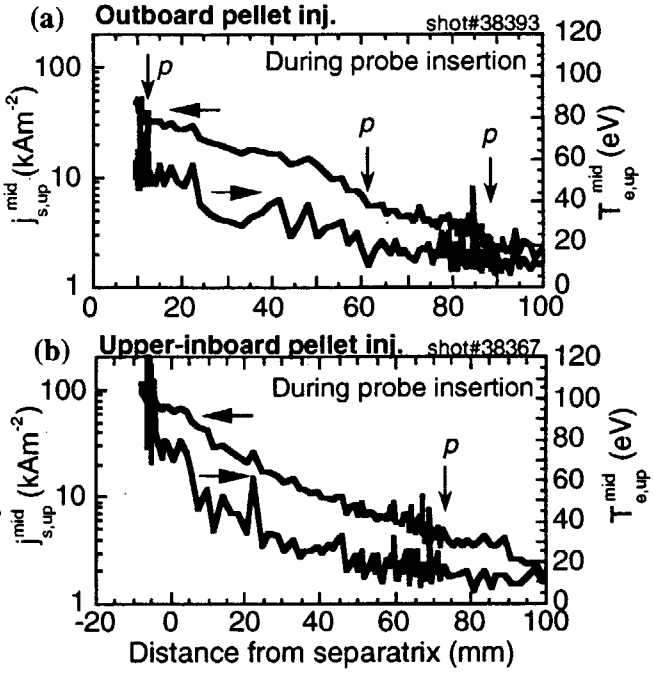

Fig4. Profiles of j_s and T_e at up-stream side of midplane Mach probe, (a) for outboard PI, (b) for upper-inboard PI.

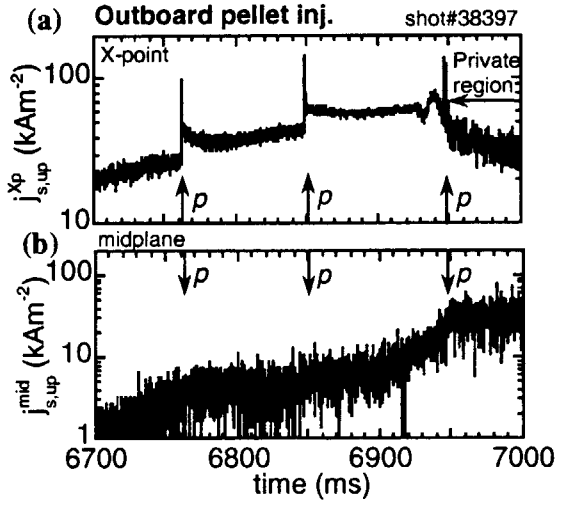

Fig5. Time evolutions of j_s at up-stream side of (a) x-point, (b) midplane Mach probes for Outboard PI.

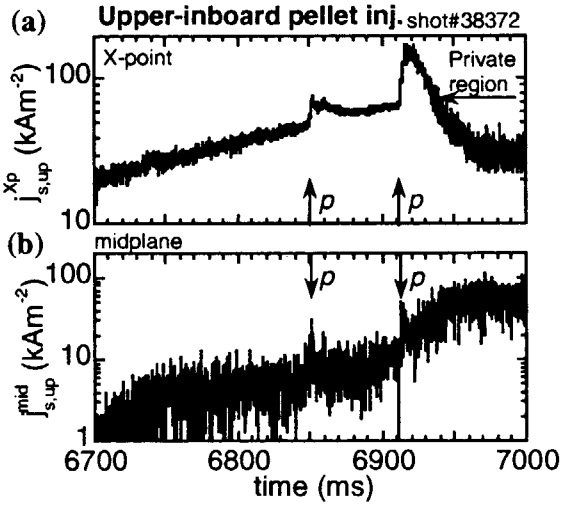

Fig6. Time evolutions of j_s at up-stream side of (a) x-point, (b) midplane Mach probes for Upper-inboard PI.

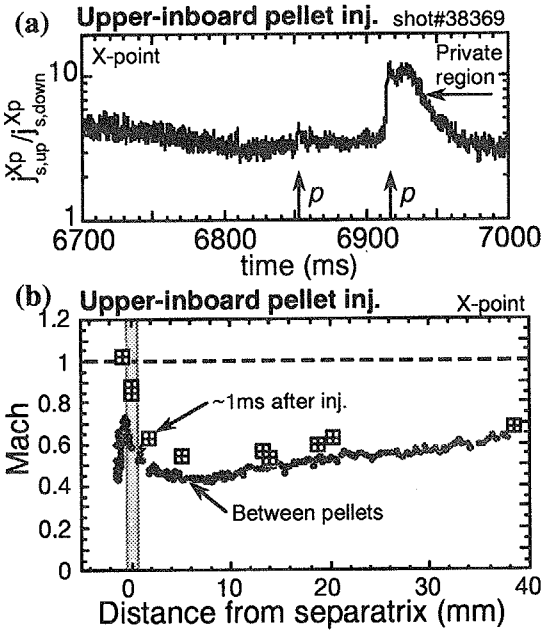

Fig7. (a) Time evolutions of j_s^{Xp} ratio near x-point, (b) profile of Mach number for Upper-inboard PI.

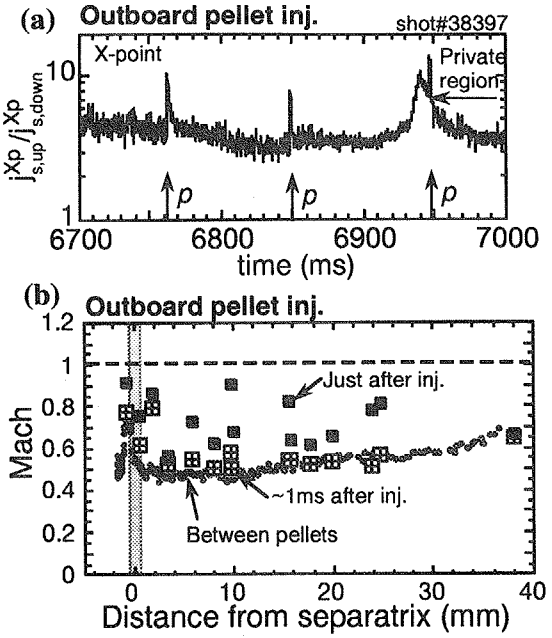

Fig8. (a) Time evolutions of j_s^{Xp} ratio near x-point, (b) profile of Mach number for Outboard PI.

9. Plasma Diagnostics and Heating System

9.1 Infrared laser polarimetry for electron density measurement in tokamak plasmas [1]

Y. Kawano, S. Chiba, and A. Inoue

The infrared CO_2 laser polarimetry for electron density measurement based on the tangential Faraday rotation has been progressed in JT-60U tokamak. The reliability of polarimetry in a pellet-injected plasma was confirmed. The Faraday rotation was measured with good angle resolution of ~0.01° under the sufficiently fast temporal resolution of 4 ms. Electron density evaluated from the tangential Faraday rotation measured by polarimetry shows good agreement with that measured by interferometry for an identical probing laser beam. The long-time continuous measurement up to ~7 hours was successful with good stability and accuracy. The basic feasibility of the infrared CO_2 laser polarimetry for electron density measurement in long-time and steady-state operation in large fusion devices was demonstrated.

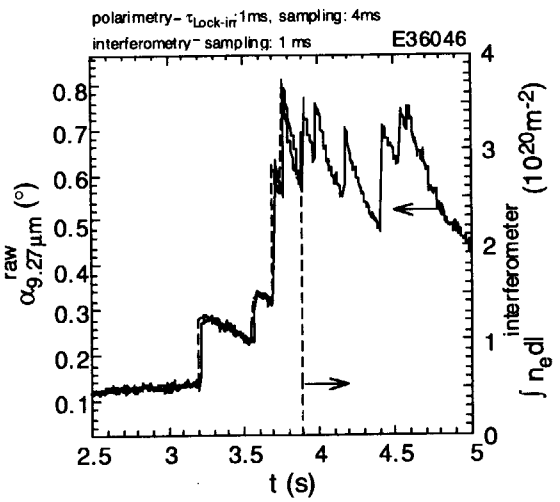

Fig. 1 Comparison between the raw Faraday rotation angle (λ=9.27 μm) and the line integrated electron density measured by interferometry.

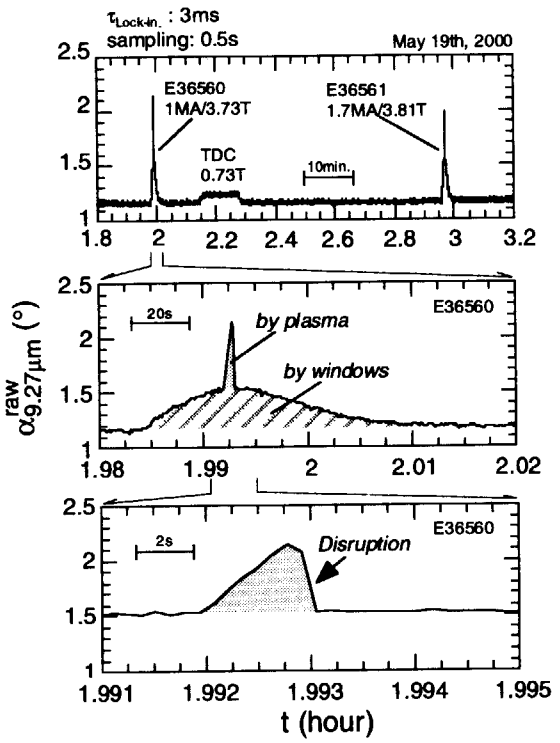

Fig. 2 Detail from long-time continuous measurement (~7h) of the CO_2 laser polarimetry.

[1] Y. Kawano, S. Chiba, and A. Inoue, Rev. Sci. Instrum. **72**, 1068 (2001).

9.2 Development of a 20-channel electron cyclotron emission detection system for the grating polychromator [1]

A. Isayama, N. Isei, S. Ishida and M. Sato

1. Introduction

In JT-60U, there are three kinds of ECE diagnostic systems [2, 3], which are the Fourier transform spectrometer [4], the grating polychromator [5] and the heterodyne radiometer [6, 7]. The grating polychromator is advantageous in that the measurement point can be changed by changing the grating mirror angle, and it is used to measure electron temperature and its perturbations. There has been a 20-channel ECE detection system for the grating polychromator, where indium antimonide (InSb) detectors are cooled at 4.2 K by a refrigerator. From the viewpoint of maintenance work, a refrigerator is better than a cryostat which holds liquid helium because there is no need to refill the liquid helium. However, large noise from the refrigerator sometimes makes it difficult to measure small perturbations. In the grating polychromator system, three out of twenty channels are used only for noise measurement. Furthermore, typical channel separation of the grating polychromator is about 6-8 centimeters in major radius, which is not enough to measure the electron temperature near the internal transport barrier. In 2000, a new ECE detection system was installed in order to measure electron temperature more precisely with narrower channel separation.

2. System specifications

The new ECE diagnostic system is composed of 20 waveguides, a 20-channel InSb detector system, preamplifiers, filter amplifiers, analog-to-digital converters and electrical-optical converters. Schematic diagram of this system is shown in Fig. 1. Detailed specifications of the waveguides, the InSb detector system and the preamplifiers, which are specially designed and fabricated for the new system, are described in next subsections.

2.1 Waveguides

Frequency-resolved ECE is led to the InSb detector system through waveguides. They are composed of an L-shape WR-51 (12.954 mm×6.477 mm) rectangular waveguide and a rectangular-to-circular waveguide transition from WR-51 to ϕ12.7 mm. The waveguides are made with silver plated brass. Measured transmission loss of the L-shape waveguide and the waveguide transition are 3.8 dB and 0.1 dB at 170 GHz, respectively. The waveguide array is inserted between the existing waveguides, which enables reduction of channel separation (Fig. 2).

2.2 Twenty channel InSb detector system

Since electron cyclotron emission from a JT-60U plasma is transmitted through 40 m waveguides, its intensity is reduced to about -11 dB in the frequency rage of 100-300 GHz. In order to detect the ECE signal with a high signal-to-noise ratio, detector system with good responsivity is required. In the existing detector system, InSb detectors are cooled by a refrigerator, where mechanical noise sometimes makes it difficult to measure small perturbations. Thus, we adopted an InSb detector system with a cryostat. Schematic drawing of the cryostat which holds InSb detectors is shown in Fig. 3. Diameter and height of the cryostat are about 500 mm and 660 mm, respectively. In the cryostat, there is a 30-liter can for liquid helium and a 25-liter can for liquid nitrogen. At the bottom of the 30-liter can, twenty InSb detectors are aligned in a row. Boil-off rate of liquid helium is monitored by

measuring the flow rate of helium gas from the cryostat. Time trace of the flow rate after the first fill is shown in Fig. 4. While the flow rate is high just after the start-up phase of the cryostat, it becomes stable after a few days. Typical flow rate in a stable phase is 0.3-0.4 liter per minute, which corresponds to about 6 - 7 weeks' hold-time. Height of the liquid nitrogen is monitored by a level meter, and the liquid nitrogen is automatically refilled every 2 days.

2.3 Preamplifiers

Detected ECE signal is led to the preamplifier. DC-coupled amplifiers are used in order to improve gain characteristics in low frequency region. Since offset voltage changes in time in a DC-coupled amplifier, a circuit to cancel the offset voltage is needed to be installed. In the preamplifier system, two of the trigger signals, which are originally used to control the other CAMAC (computer-aided measurement and control) systems, are used to control the offset cancellation circuit: One signal, S1, is received one minute before the discharge, and the other signal, S2, is received at end of the discharge. The sequence of the operational status is shown in Fig. 5. When the preamplifier receives the S1 signal, an internal timer is turned on. After T1 second, the circuit in the preamplifier is closed to cancel the offset voltage. When the preamplifier receives the S2 signal, the circuit is opened. Even when the preamplifier does not receive the S2 signal, the gate is opened after T2 second. In the preamplifier system, T1 and T2 is set at 50 seconds and 30 seconds, respectively. Voltage gain is manually changed from 1000 to 10000. Error in output gain is within ±0.1 dB in the frequency region of DC to 100 kHz. Typical noise voltage is measured to be 1 $nV/Hz^{0.5}$, which is lower than that in the existing preamplifiers (typically 4 $nV/Hz^{0.5}$). Offset drift is measured to be about 0.5 mV/s even for the worst case. Since output voltage is typically 5V, the offset drift during a discharge (15 seconds) is very small. It has been confirmed in experiment that the offset voltage is canceled as expected, and that the offset drift during a discharge is negligibly small.

3. Measurement of electron temperature

Time evolution of electron temperature in a reversed shear discharge measured by the new ECE detection system is shown in Fig. 6 (a). Note that electron temperature is not measured from 4.95 s to 5.05 s because a shutter located at the input of the polychromator is closed to measure the offset voltage in the old system. At t=4.4 s, electron temperature of channel 10 increases while electron temperature of channel 11 does not, which suggests the formation of internal transport barrier. After the mini-collapse at t=4.9 s, a large collapse occurs at t=5.5 s, and the central electron temperature decreases from 5 keV to 1.5 keV. From Fig. 6(a), we can see that these collapses are observed after the increase of the electron temperature of channel 10. Time evolution of electron temperature near the collapse at t=5.5 s is shown in Fig. 6(b). It can be seen from this figure that there are two phases in the collapse. At the first collapse at t=5.485 s, decrease in electron temperature at the peripheral region (CH10-CH12) is much larger ($\delta T_e/T_e \approx -100\%$) than that near the center (CH5; $\delta T_e/T_e \approx -10\%$). At the second collapse at t=5.502 s, decrease in electron temperature (CH5-CH7) near the center is observed. From this measurement, we can see that the timing and location of ITB formation and the process of a collapse can be measured by the new ECE detection system.

4. Summary

A new 20-channel ECE detection system was installed in 2000. Since the detector is cooled by liquid helium held by a cryostat, no mechanical noise is observed. This enables

measurement of small electron temperature perturbations. Furthermore, a 20-channel DC-coupled preamplifier is used to improve gain characteristic in the low frequency region. It was confirmed that the offset cancellation circuit worked as expected, and that the change in the background noise was negligible. Since there is no need to measure the background noise, all channels can be used for electron temperature measurement, and thus precise measurement of the structure of ITB and the process of a collapse became possible.

References

[1] Isayama A., Isei N., Ishida S. and Sato M. : to be published in Rev. Sci. Instrum..
[2] Sato M., Ishida S., Isei N., Isayama A., Shirai H., Oyevaar T., Teranishi M., Iwama N. and Uchino K. : Fusion Eng. and Design **34–35** 477 (1997).
[3] Isei N., Isayama A., Ishida S., Sato M., Oikawa T., Fukuda T., Nagashima A., Iwama N. and the JT-60 team : Fusion Eng. and Design **53** (2001) 213.
[4] Sato M., Isei N. and Ishida S. : JAERI-M 93-057, "Development of Fourier Transform Spectrometer System", 359 (1993).
[5] Ishida S., Nagashima A., Sato M., Isei N., and Matoba T. : Rev. Sci. Instrum. , **61** (1990) 2834.
[6] Isei N., Sato M., Ishida S, Uchino K., Nagashima A., Matoba T. and Oyevaar T. : Rev. Sci. Instrum. **66** (1995) 413.
[7] Isayama A., Isei N., Ishida S., Sato M., Kamada Y., Ide S., Ikeda Y., Takahashi K., Kajiwara K., Hamamatsu K., JT-60 Team : Fusion Eng. Design **53**, 129 (2001).

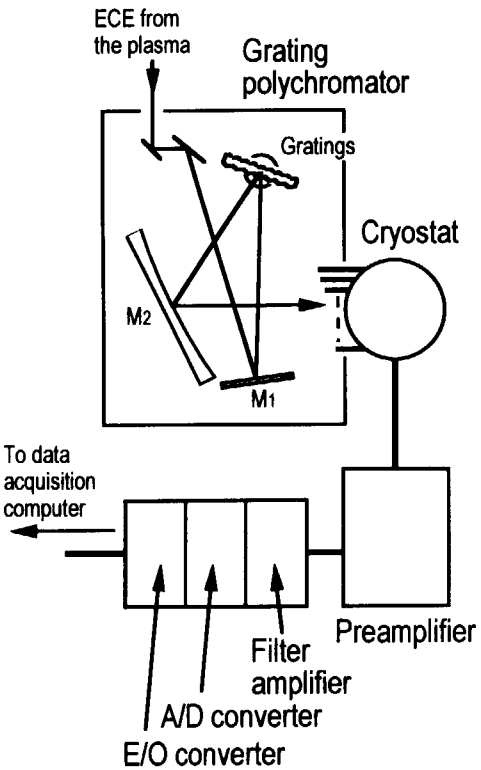

Fig. 1: Schematic diagram of the grating polychromator system.

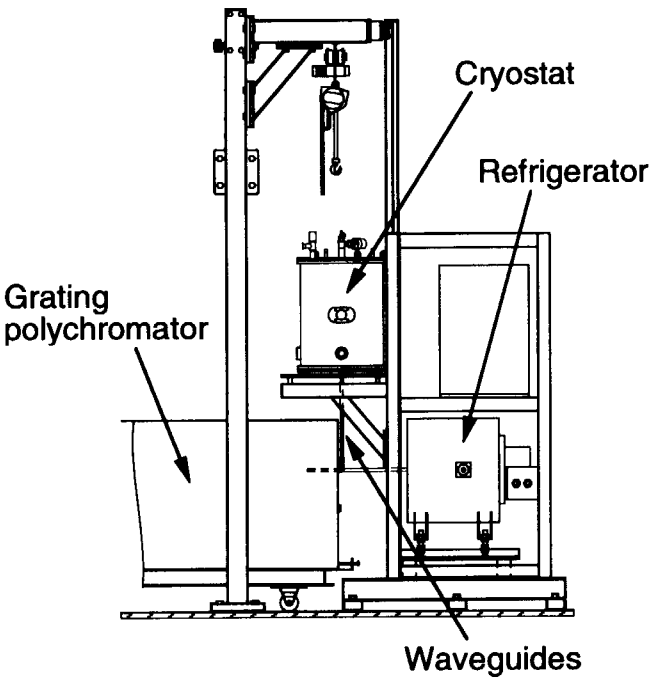

Fig. 2: Schematic drawing of the upgraded grating polychromator system.

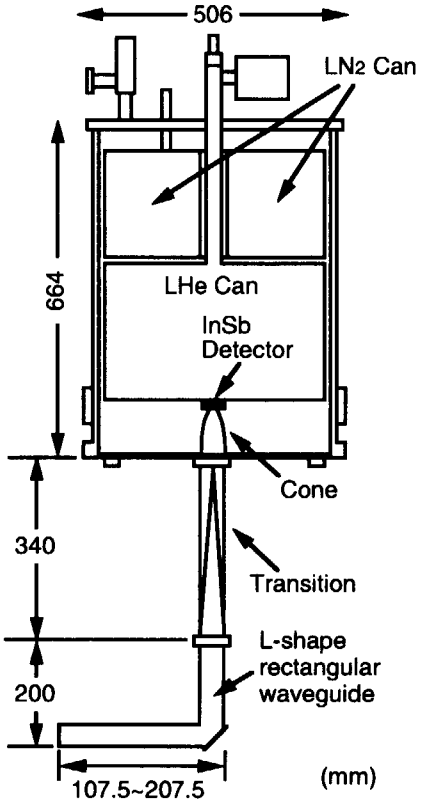

Fig. 3: Schematic drawing of the cryostat.

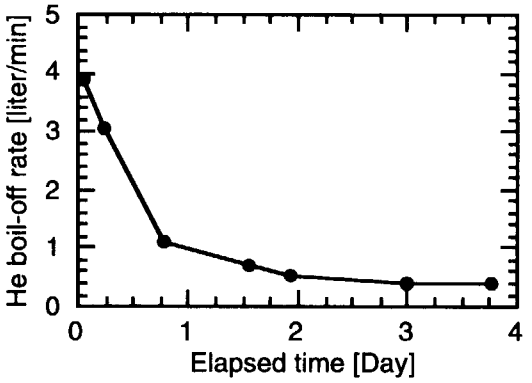

Fig. 4: Time evolution of helium boil-off rate after the first fill of liquid helium.

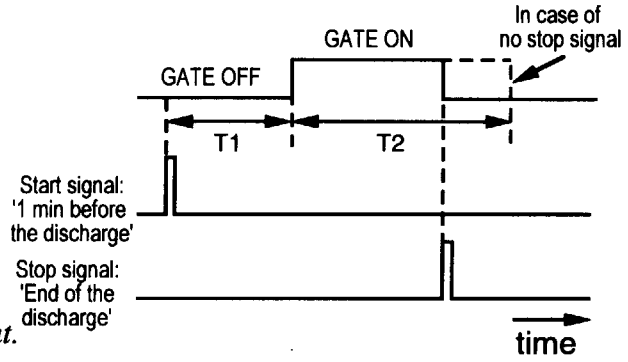

Fig. 5: Time chart of cancellation of offset voltage in the preamplifier.

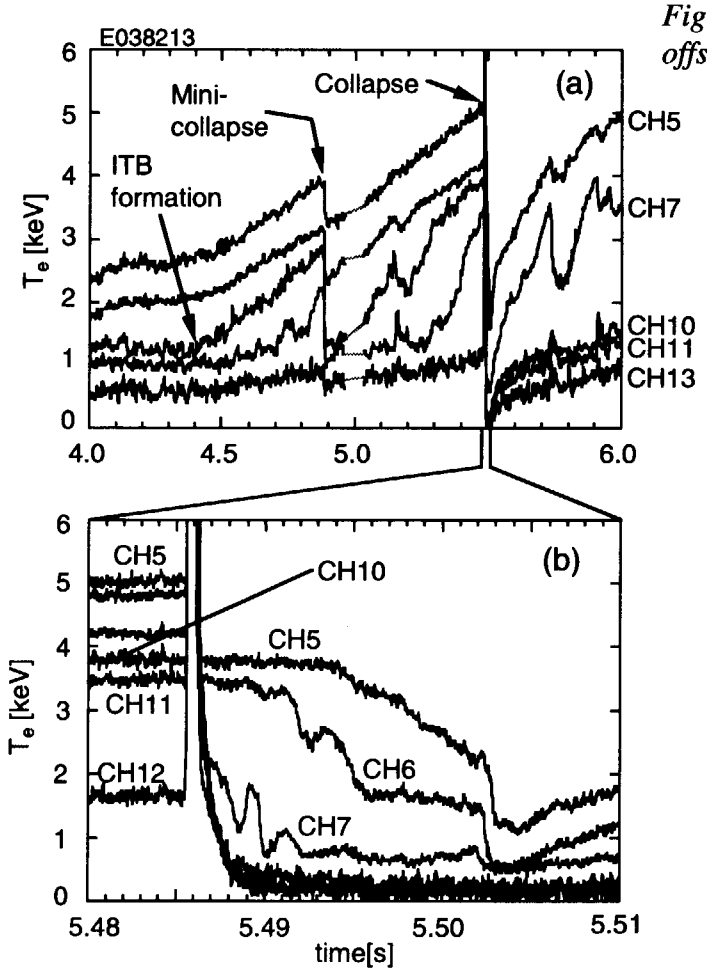

Fig. 6: Time evolution of electron temperature in a reversed shear discharge.

9.3 Collective Thomson scattering using a pulsed CO_2 laser in JT-60U[1]

T. Kondoh, and S. Lee

A collective Thomson scattering (CTS) diagnostic system using a carbon dioxide (CO_2) laser has been developed for the purpose of establishing measurement technique of ion temperature and fast alpha particle in a fusion reaction plasma. A pulsed CO_2 laser (15J, 1μs at 10.6 μm) and a heterodyne receiver with a stray-light notch filter has been successfully installed. The noise equivalent power (NEP) of the heterodyne receiver is below 9 x 10^{-19} W/Hz up to a frequency of 8 GHz. A six-channel filter bank analyzes spectrum of the scattered light in the frequency range from 0.4 GHz to 4.5 GHz to measure ion temperature and to detect fast ions generated by negative-ion source neutral beam (N-NB) injection of the JT-60U plasmas. Test of the CTS system by injecting the CO_2 laser into the vacuum vessel of JT-60U has started. Stray light signal around the JT-60U vacuum vessel was detected and optimization of the optical alignment was proceeded.

Reference

[1] T. Kondoh, S. Lee D. P. Hutchinson, and R. K. Richards, Rev. Sci. Instrum. **72**, 1143 (2001).

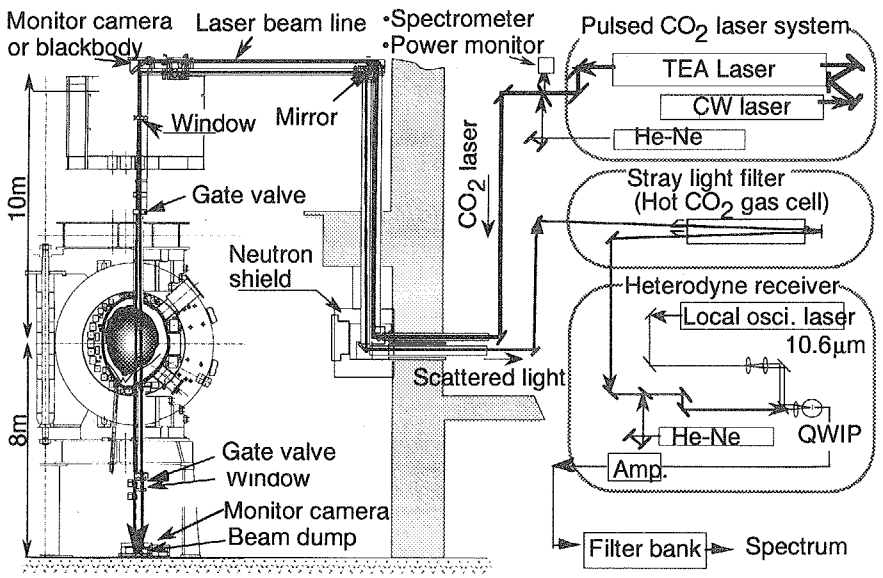

Fig. 1 Schematic view of the Collective Thomson scattering system in JT-60U.

9.4 A filter bank system for scattered spectrum analysis in collective Thomson scattering diagnostic on JT-60U [1]

S. Lee, T. Kondoh, Y. Yonemoto and Y. Miura

In JT-60U, collective Thomson scattering (CTS) diagnostic system has been developed to measure ion temperature and velocity distribution of fast ions to demonstrate feasibility of measurements of confined alpha particles. In order to resolve frequency distribution of pulsed scattered light (1μs), we developed a wide band filter bank system (0.4 - 4.5 GHz, Fig. 1) for scattered spectrum analysis. The detector bandwidth and frequency resolution are both designed based on the calculation results of expected scattered spectrum in JT-60U. In order to realize wide band multichannel detection, cascade connected seventh order simultaneous-Chebyshev (elliptic) bandpass filters were adopted(Fig. 2(b)). Signal to noise ratio (S/N) based on the noise-equivalent-power (NEP) of quantum-well infrared photodetector receiver and laser pulse length are also evaluated. Horizontal step line in Fig.2(a) shows the required signal level to obtain a sufficient S/N value (S/N=2). The calculation shows that sufficient scattered power from bulk ions is expected in JT-60U experiment. The bandpass filter of ΔB=2GHz was also prepared in order to measure fast ions (6ch). A wide band filter will improve the S/N ratio.

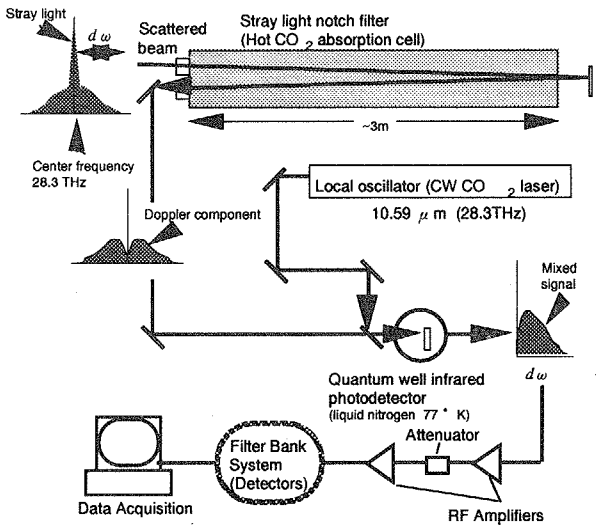

Fig. 1: Schematic diagram of CTS heterodyne receiver system using a stray light filter (hot CO_2 absorption cell).

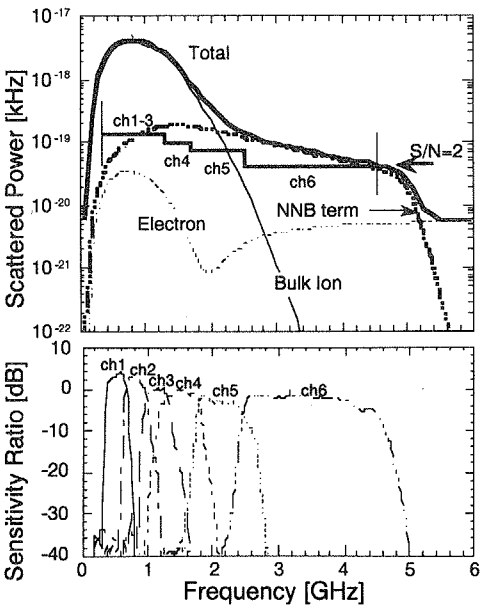

Fig. 2: (a)Expected scattered power for NNB heated plasma. (b)Transmission rate and bandwidth of each detectors.

Reference

[1]S. Lee, T. Kondoh, Y. Yonemoto1 and Y. Miura, Rev. Sci. Instrum. 71,(2000)4445.

9.5 Neutron emission profile monitor on JT-60U

Y. Shibata[1], T. Nishitani, A. Morioka and M. Ishikawa[2]
[1] Department of Nuclear Engineering, Nagoya University, Nagoya, 464-8603, Japan
[2] Plasma Research Center, University of Tsukuba, Tsukuba, 305-8577, Japan

1. Introduction

Fusion neutron measurement is one of the most promising techniques for diagnostics on burning plasmas and is necessary for the future fusion devices such as ITER [1]. Especially, measurements of neutron emission profiles are useful to study the transport of bulk and high-energy ions [2]. We have developed a neutron emission profile monitor for deuterium-deuterium plasmas in JT-60U.

2. Measurement system of neutron emission profile monitor

The neutron emission profile monitor has a neutron collimator (3m × 3m × 1m), which has 6 fan-shaped channels made of polyethylene and lead. The collimator is installed in oblique downward of the vacuum vessel and is located 5 m away from the plasma center (see Figs. 1 and 2). The detector of the system is an NE213 organic liquid scintillator (ϕ 1" × 1").

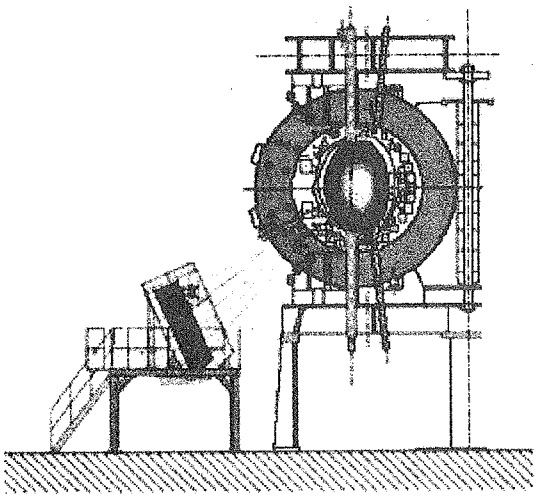

Fig. 1 Position of the measurement system

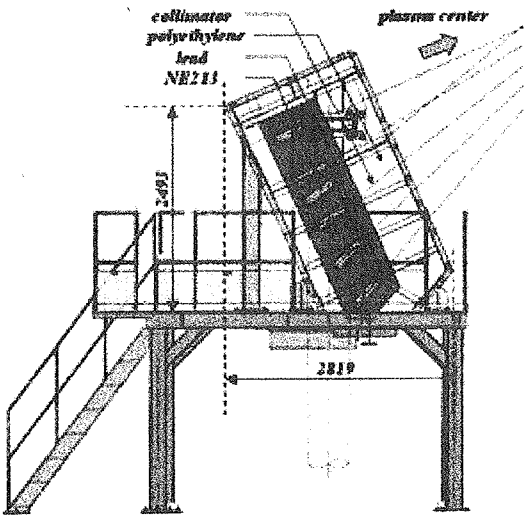

Fig. 2 Neutron Collimator of the measurement system

3. Primary results and discussion

3.1 Test of the performance of the detector

The performance of an NE213 organic scintillator detectors was tested with 2.45 MeV neutrons at the FNS (Fusion Neutron Source) neutron generator in JAERI Tokai. In this experiment, we calibrated the six detectors for 2.45 MeV DD neutron measurement. An experimental system is shown in Fig. 3. As shown in Fig. 4, the width of the neutron energy spectrum is around 310 keV at FWHM. From these relative calibrations, we decided relative

detection efficiency between each detector.

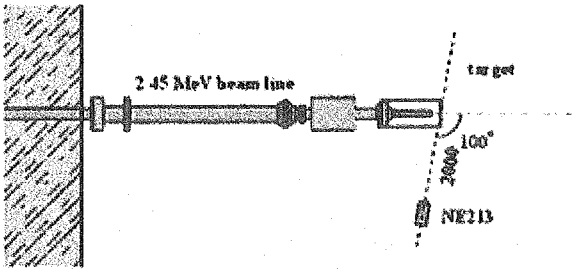

Fig. 3 NE213 position in FNS experiment

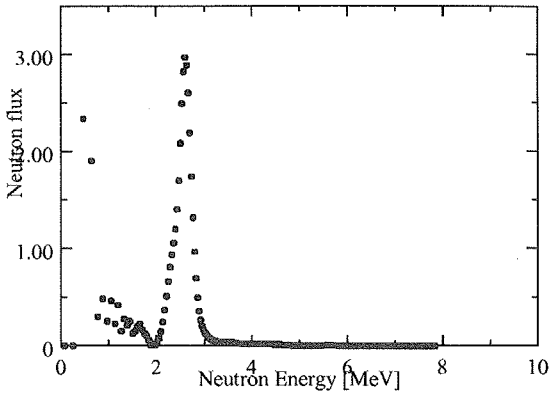

Fig. 4 Energy Spectrum of NE213 in FNS experiment

3.2 First measurement in JT-60U

We applied the neutron emission profile monitor to JT-60U experiments. Firstly, we confirmed the linearity of the NE213 detector of the profile monitor. Figure 5 shows that the count rate of the NE213 detector is linearly proportional to the neutron flux from the ^{235}U fission chamber (FC). We can see that the count rate of the NE213 detector was deviated from the linearity at a neutron flux of 1.0×10^{16} neutrons/s of the FC. We confirmed that the neutron emission profile measurements are reliable up to the neutron flux of 1.0×10^{16} neutrons/s of the FC in the present setup.

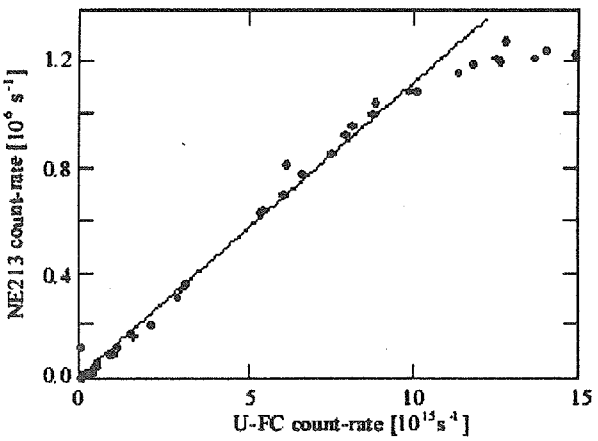

Fig.5 The relativity between count-rate from NE213 and ^{235}U-FC in JT60U NBI experiment

The neutron emission profile during the NBI (Neutral Beam Injection) was measured. Figure 6 shows measured count rates of individual channels. Since these values are line-integrated neutron emission rate, we have to employ the Abel inversion method to obtain a neutron emission profile. The method converts the line-integrated values to local neutron emission on the magnetic flux surfaces. The neutron emission is calculated from

$$C_i = \sum_j l_{ij}\phi_j$$

where C_i is the measurement values (line-integrated value), l_{ij} is the length of line chord (weight coefficient), and ϕ_i is the neutron emission. The result is shown in Fig.7. The shape of profiles seems to be

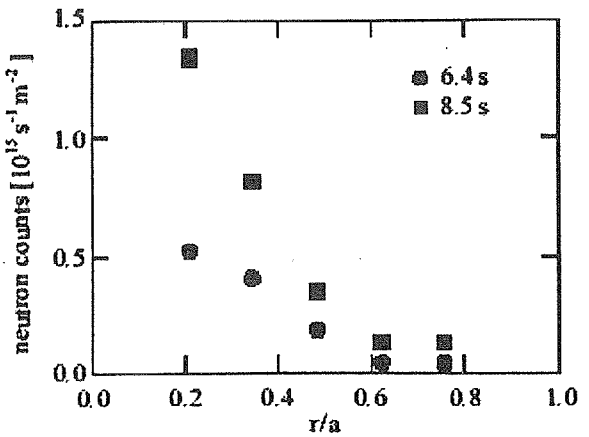

Fig.6 Neutron counts (line integrated values) of each channel in E37838, t=6.4, 8.6s

reasonable. The obtained neutron emission profile will be compared with those from analysis codes (TOPICS and OFMC).

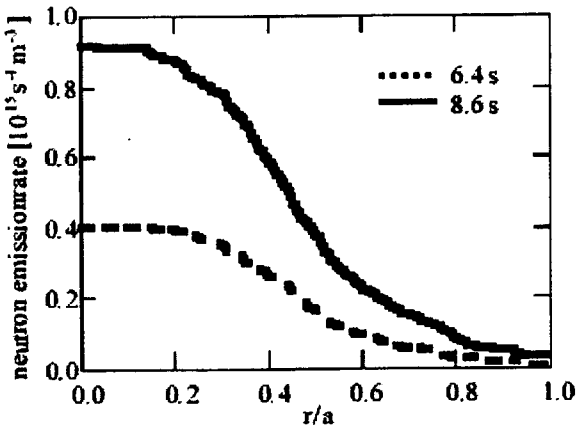

Fig.7. Neutron emission profile after Abel inversion in E37838, t=6.4, 8.6s

Summary

We have developed a neutron emission profile monitor with a 6 fan-shaped channel neutron collimator. We have adopted NE213 organic liquid scintillator and calibrated the detectors at FNS JAERI Tokai.

We have found that the profile monitor is reliable up to the neutron flux of 1.0×10^{16} neutrons/s of the FC in the present setup. In the NBI measurements, we have obtained neutron emission profiles by Abel inversion of the line-integrated values measured with this system. We confirmed that the neutron emission profile monitor operates well in the typical DD plasma experiments of the JT-60U.

In the future, we will measure and analyze the DD plasma routinely with the system, compare the measured profiles with those from analysis codes, and investigate a correlation between the neutron emission profile and other plasma parameters.

References

[1] J. M. Adams et al., Nucl. Inst. Methods, **A329**, 277 (1993).

[2] B. Wolle, Phys. Reports, **312**, 1 (1999).

9.6 Multichordal charge exchange recombination spectroscopy on the JT-60U tokamak [1]

Y. Koide, A. Sakasai, Y. Sakamoto, H. Kubo and T. Sugie

Recent development of the JT-60U charge exchange recombination spectroscopy (CXRS) diagnostic system is reported. The measurements of the radial profiles of the ion temperatures (Fig. 1(a)), the toroidal and poloidal rotation velocities (Fig. 1(b)) and the impurity density (Fig. 2(a)) are based on CXR spectra of fully stripped carbon ions induced by neutral beam injection. Radial electric field profile is estimated based on momentum balance equation (Fig. 2(b)). Measurements are made simultaneously at 59 spatial points (23 toroidal and 36 poloidal) with a time resolution of 1/60 second throughout the full discharge pulse of 15 seconds. It should be noted that apparent velocity, especially for poloidal velocity, is induced due to the energy dependence of cross-section of charge exchange reaction. Therefore precise information on the cross-section is crucial for the estimation of radial electric field; however it is still under discussion.

Reference

[1] Y. Koide, A. Sakasai, Y. Sakamoto, H. Kubo and T. Sugie, Rev. Sci. Instrum. **72** (2001) 119.

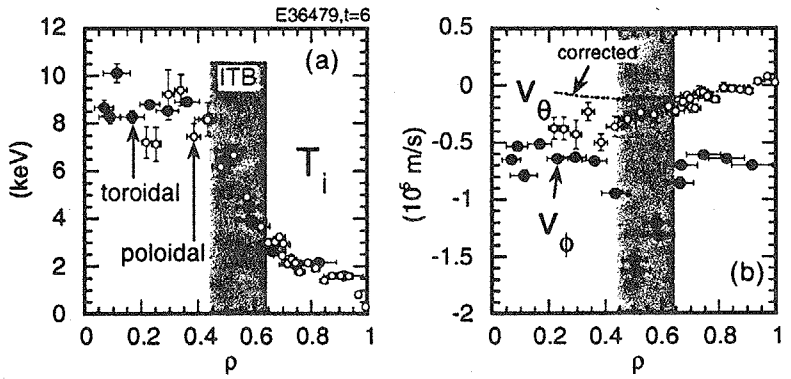

Fig. 1 (a) ion temperature from toroidal and poroildal field of view, (b) toroidal and poloical rotation velocity.

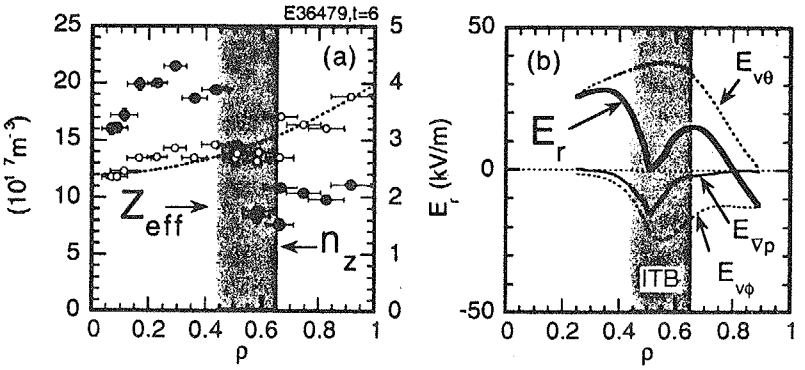

Fig. 2 (a) carbon density (n_z) and deduced effective ionic charge (Z_{eff}), (b) radial electric field (E_r) deduced from momentum balance equation.

9.7 Improvement in MHD equilibrium reconstruction code with MSE data

T. Fujita, T. Oikawa, T. Suzuki

1. Introduction

In the MHD equilibrium reconstruction code with MSE (motional Stark effect diagnostics) data in JT-60U, the current density profile was assumed to be a polynomial function of normalized poloidal flux [1]. However, since it had a small number of free parameters, difficulties were frequently encountered to fit the MSE data satisfactorily. The fitting was poor especially in reversed shear plasmas which had the bootstrap current peaked at the internal transport barrier (ITB) layer. To improve the ability of fitting of MSE data, the functional form for current density profile has been extended.

2. Function for current profile in the previous code

In an axisymmetric MHD equilibrium, which is represented by the Grad-Shafranov equation, the current density is given by a function of Ψ and R, where Ψ is the poloidal flux function and R is the major radius;

$$j(R, \Psi) = Rp'(\Psi)+(1/\mu_0 R)*F(\Psi)F'(\Psi).$$

The profiles of current density and pressure, $j(\rho)$ and $p(\rho)$, are mainly determined by two functions, $p(\Psi)$ and $F(\Psi)$. Here ρ is the normalized radius; $\rho = 0$ at the axis and $\rho = 1$ at the last closed flux surface. In the MHD equilibrium code in JT-60U to fit the MSE data, $p'(\Psi)$ and $F(\Psi)F'(\Psi)$ are assumed to be similar functions of normalized poloidal flux ψ, $Y(\psi)$;

$$p'(\Psi) = c*\beta_{pc}*Y(\psi), \qquad (1/\mu_0)*F(\Psi)F'(\Psi) = c*(1-\beta_{pc})* R_p^2*Y(\psi)$$

then

$$j(R,\psi) = c*(R*\beta_{pc} +(1-\beta_{pc})*R_p^2/R)*Y(\psi),$$

where $\psi=0$ at the magnetic axis, $\psi=1$ at the last closed flux surface, R_p is the plasma major radius, and β_{pc} is a constant close to the poloidal beta; c and β_{pc} are determined to adjust the total plasma current and the poloidal beta (or plasma stored energy) to given values.

In the previous code, $Y(\psi)$ was assumed to be a polynomial function of ψ;

$$Y(\psi) = 1+c_3+c_1\psi+c_2\psi^2-(1+c_1+c_2)\psi^3. \qquad (1)$$

The coefficient c_3, which represents the amount of surface current, is fixed and is given in an input file. Coefficients of c_1 and c_2 can be determined in a code to adjust q(0) and l_i to given values or can be fixed and given in an input file. An example of MHD equilibrium reconstruction using the MSE data in reversed shear plasma (Fig. 1) with this function is shown in Fig. 2 (a). Here, the plasma current is 0.8 MA, the plasma major radius (R_p) is 3.4 m, toroidal field at R_p is 3.4 T, the plasma minor radius is 0.80 m and q_{95} is ~9. The data of channel 4 to 8 in the MSE collection optics viewing a counter NB (#7B) are used to fit and shown in Fig. 2 (a). These channels cover $\rho = 0.35$ to 0.85 in this configuration. At the top, a projected pitch angle γ_p of magnetic field line along the #7B beam line is shown.

Rectangular symbols denote the MSE data (γ_p^{MSE}) while a solid line is a calculated one from the equilibrium obtained with the code. The dotted line denotes a projected pitch angle for a vacuum toroidal field, γ_{p0}. The solid line crosses the dotted line where the #7B beam line is closest to the magnetic axis. In the outer region where $R>R_{axis}$, γ_p becomes smaller than γ_{p0} due to the poloidal field. The magnitude of poloidal field is proportional to an absolute value of $\gamma_p-\gamma_{p0}$. Roughly speaking, the slope of γ_p reflects the current density there; the slope becomes steeper when the current density there is larger. Our purpose is to find an equilibrium that has a profile of γ_p as close as to that of MSE data. The fitted curve was obtained with $c_1 = 12.92$, $c_2 = -24.92$ and $c_3 = 0$. It can be seen that the slope between channel 5 and 8 is too gentle, which means that the current density at $\rho \sim 0.5$-0.7 is too small. With this functional form, it is impossible to make a narrow peak at a half radius because $Y''(\psi)$ is a linear function of ψ which increases or decreases monotonically with ψ. At the bottom is shown the q profile. The solid line denotes the q profile of equilibrium while symbols are calculated as $q^*(\gamma_p-\gamma_{p0})/(\gamma_p^{MSE}-\gamma_{p0})$ assuming that the q is inversely proportional to the $\gamma_p-\gamma_{p0}$.

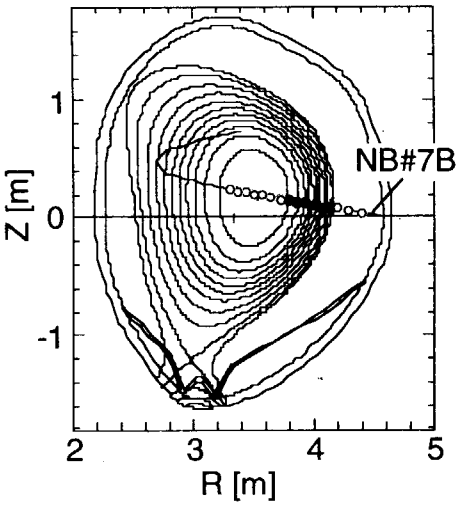

Fig. 1. Plasma configuration for the test of equilibrium code. MSE points (cirlces) and the beam line of #7B are also shown. Closed symbols denote the points used for the fitting in Fig. 2 (channel 4 to 8).

3. New functions for current profile

Two kinds of new functions have been installed into the equilibrium code. One is a polynomial function + Gaussian function of ψ and the other is a spline function of ρ.

3.1 Polynomial + Gaussian

Here, a Gaussian function $\exp(-\alpha(\psi- c_5)^2)$ is added to the polynomial function (1) to represent an off-axis peak;

$$Y(\psi) = 1+c_3+c_1\psi+c_2\psi^2-(1+c_1+c_2)\psi^3+ c_4*\exp(-\alpha(\psi- c_5)^2). \quad (2)$$

The location, width and height of peak are given by c_5, α and c_4, respectively. These parameters are fixed and are given in an input file. An example of using this function is shown in Fig. 2 (b) for the same MSE data as Fig. 1 (a). By adding a Gaussian function located at $\rho \sim 0.55$ with full-width-of-half-maximum of ~0.18 in ρ, the steep slope of channel 5 to 8 are fitted well. It is noted that the current density at $\rho=0.55$ (0.7 MA/m^2) becomes 1.4 times as large as that in Fig. 1 (a) (0.5 MA/m^2). The bootstrap current peaked at the ITB layer is well represented. Accordingly, the deep hollow in the q profile around q_{min} is obtained; a large positive shear at $\rho \sim 0.75$ and a large negative shear at $\rho \sim 0.45$. However, the outermost

channel (channel 4) cannot be fitted well by this function.

3.2 Spline function

The spline function can represent any shape, in principle, by adjusting the number and the position of knots. Here, $Y(\psi)$ is represented by a third-order spline function of ρ, $g(\rho)$;

$$Y(\psi) = g(\rho(\psi)). \quad (3)$$

The number of knots, N_k, positions of knots, ρ_i ($i = 1,\ldots, N_k$), and values of Y at each knot, Y_i ($i = 1,\ldots, N_k$) are given in an input file. The function $\rho(\psi)$ is calculated by tracing the poloidal flux surfaces at $\psi = \psi_i = i/N_\rho$ ($i=1,\ldots, N_\rho$) at each step of iteration to solve the Grad-Shafranov equation, where N_ρ is typically 50. An example is shown in Fig. 2 (c). Here, a spline function with 8 knots is used. To fit a positive slope between channel 4 and 5, it is required to reduce the current density between them ($\rho \sim 0.8$) than that in Fig. 2 (b). All five channels (4 to 8) are well fitted in Fig. 2 (c). In the current profile, a small peak near the surface appears since the current at $\rho \sim 0.8$ has been moved to $\rho \sim 0.9$. This can be interpreted as the bootstrap current in the H-mode pedestal. As mentioned above, the pressure profile in the equilibrium code is automatically determined from the current profile and cannot be fit. However, the pressure profile in Fig. 2 (c) has a typical feature of reversed shear plasma with an H-mode edge; steep gradient at the ITB layer, flat portion inside and outside the ITB, and the edge pedestal. This is because the bootstrap current is dominant in this discharge (~80%). The bootstrap current becomes large where the pressure gradient is large while, in the equilibrium code, the pressure gradient is mainly proportional to the current density since both are proportional to $Y(\psi)$.

Typically one knot per one section between neighboring channels is put in addition to two points at $\rho = 0$ and $\rho = 1$. More knots are required to make a large change in the gradient in Y. Since no algorithm to adjust the value at knots is equipped in the code, one has to adjust the values and/or positions of knots by hand looking at the previous results. Typically ~20 iterations are required to obtain a satisfactory result.

4. Summary and discussion

Two kinds of new functions have been installed into the equilibrium code; polynomial function + Gaussian function of ψ and a spline function of ρ. The spline function is very powerful and can fit almost any shape of current profile. By using these new functions, the real shape of current profile in JT-60U reversed shear plasmas, which is characterized by the bootstrap current peaked at the ITB layer, has been obtained for the first time. This enables us to do deeper analysis, for instance the calculation of bootstrap current density, the estimation of loop voltage profile [2] and so on in reversed shear plasmas.

References

[1] Fujita, T., et al., Fusion Eng. Design **34-35**, 289 (1997).
[2] Fujita, T., et al., Phys. Rev. Lett. **87**, 085001 (2001).

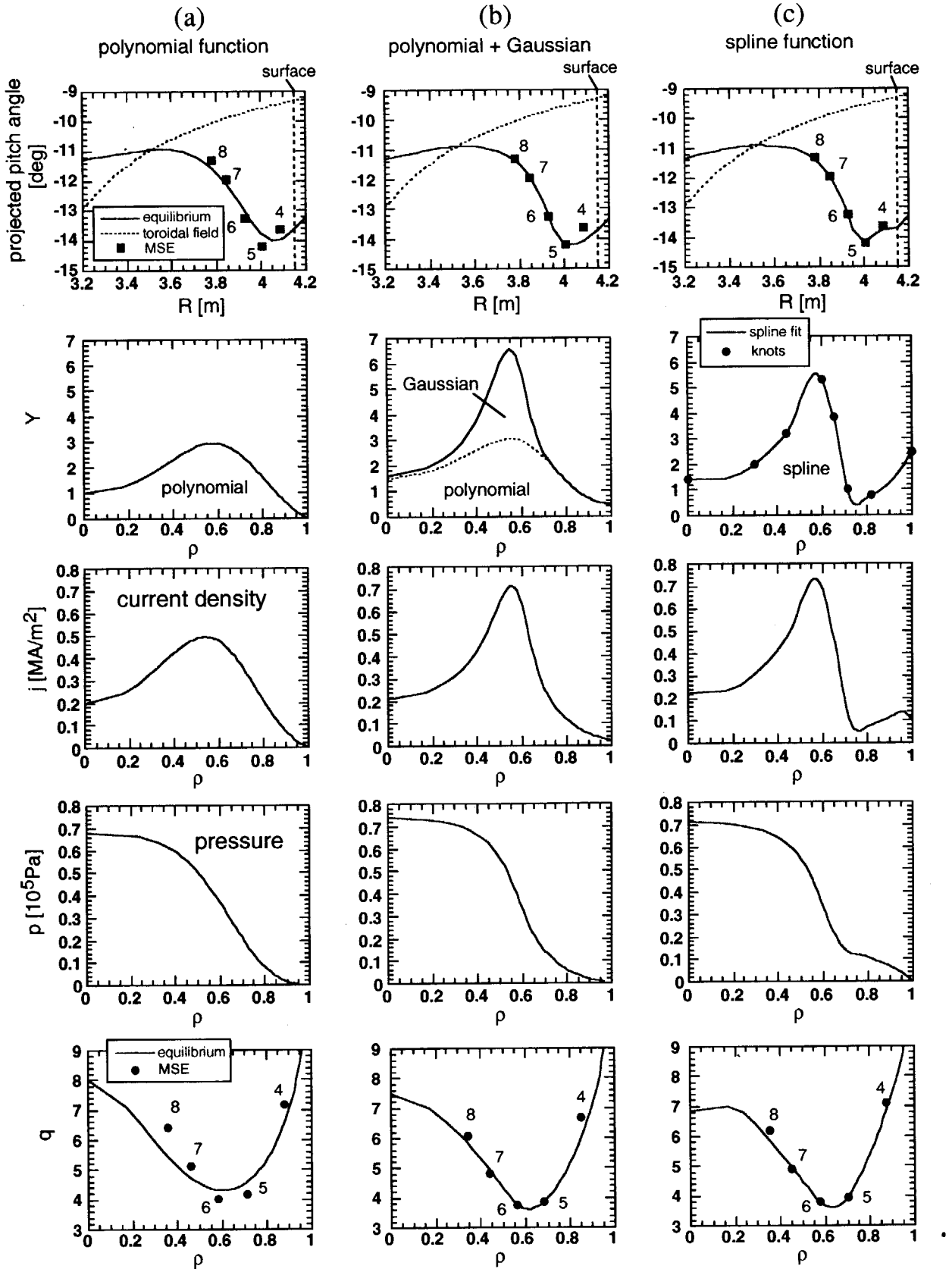

Fig. 2. Examples of equilibrium reconstruction with MSE data using different types of function for the current profile; (a) polynomial, (b) polynomial + Gaussian, (c) spline. From the top, projected pitch angle, Y, current density, pressure and q.

9.8 Improvement of LH-coupling by neutral gas injection

M. Seki

It is very important to obtain good coupling for LHCD performance, because an optimized spectrum for high current drive efficiency is launched under the condition of low reflection coefficient. In order to realize good coupling, a thin plasma for propagation of LH wave is required in front of an LH antenna. The density of the plasma should be higher than the cut-off density (~5 x 10^{16} m^{-3}) for the LH wave of 2 GHz. This means that outer plasma surface must be close to the LH antenna so as to obtain an enough density for good coupling. On the other hand a large clearance between the outer plasma and the first wall should be kept for low enough heat load on the LH antenna mouth. Therefore an active method, for example neutral gas injection, must be established for good coupling at a long plasma-antenna distance. This long distance coupling allows wide flexibility in LHCD operation, for instance in the reverse magnetic shear plasma.

Preliminary coupling properties of LH were reported in ref [1, 2] without neutral gas injection after modification of the divertor to a semi-closed W-shaped one. In this campaign coupling properties are systematically examined such as dependence on the amount of neutral gas, dependence on the gas species and dependence on the toroidal magnetic field. Figure 1 shows a reflection coefficient of the LH antenna located at an equatorial port versus a distance δ_7 between the outer plasma surface and the first wall near the LH antenna. By increasing the amount of neutral gas injection from 1 to 3 Pa•m^3/s, the critical distance allowing a low reflection coefficient less than 10 % is extended from 6 to 8 cm. The improvement of coupling for gas injection of 1 Pa•m^3/s is small compared with no gas injection. A higher toroidal magnetic field leads to a longer critical distance. The density profile measured by a fast moving probe in front of the LH antenna is consistent with the coupling property. No major difference of the critical distance is observed for some species of gas such as H_2, He and CH_4. However gas injection of CH_4 shows a possibility of suppressing rf breakdown at higher LH power. This effect will be confirmed in the next campaign. The neutral gas injection does not degrade good confinement of the reverse magnetic shear plasma up to ~5 Pa•m^3/s

In summary, it was found possible to maintain a low reflection coefficient at a large clearance by using a neutral gas feed. The neutral gas injection near the LH antenna can be an active method to improve coupling of LH.

References

[1] M. Seki, JAERI Review 98-019, pp.13-14, (1998).
[2] O. Naito, M. Seki, S. Ide, T. Kondoh, K. Ushigusa, JAERI Research 98-039, pp.105, (1998).

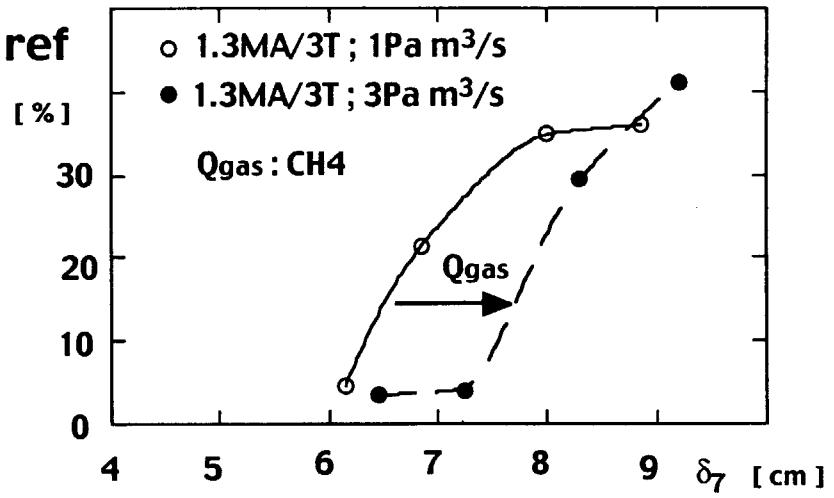

Fig. 1 Reflection coefficient vs plasma - wall distance.

9.9 Behavior of reflected X-mode electron cyclotron wave [1]

K. Kajiwara, Y. Ikeda, S. Moriyama, M.Seki and T. Fujii

The behavior of the unwanted X-mode was studied on JT-60U when the fundamental EC wave was launched from the low field side. The power fraction of the X-mode component was changed from ~10 to ~60 % using a pair of polarizes. The poloidal injection angle of the EC beam was also changed from the center (poloidal angle:~40°) to the edge (poloidal angle:~0°) using a steerable antenna mirror. It was found that the pressure at an NBI port adjacent to the ECRF antenna increased in the case of the poloidal injection angle of 19°-23° at the plasma density of ~2.5×10^{19} m^{-3}. The pressure increase for the injected X-mode power of 0.54MW x 3-sec was about seven times higher than that for the normal NBI operation. A large reduction of the liquid helium in the cryo-panel at the NBI port was also observed in this condition, where the reduction of the liquid helium was in proportion to the injected X-mode energy. It was found that the reduction of the liquid helium depended on the plasma density. When the plasma density was ~3.5×10^{19} m^{-3}, no reduction of the liquid helium was observed even though the poloidal injection angle was set at 19°.

It is well known that the fundamental X-mode launched from the low field side reflects at the cut-off layer, whose position depends on the plasma density. Since the injected EC beam was well focused within the diameter of ~0.1 m, the reflected point at the cut-off layer was changed with the poloidal injection angle and the reflected X-mode might keep its locality. Therefore, it seemed that the reduction of the liquid helium was caused by the local invasion of the reflected X-mode into the NBI port. Indeed, the diagram of the poloidal injection angle and the plasma density, where the reduction of the liquid helium was observed, is well explained by a ray tracing code. The calculation shows that the EC wave with the poloidal injection angle of 19° is guided into the NBI port after the reflection at the cut-off layer when the plasma density is less than 2.5×10^{19} m^{-3}, while the reflected X-mode is not guided into the NBI port for the plasma density more than 2.5×10^{19} m^{-3}.

Though it has not been clearly understood how much energy of the invaded X-mode was acceptable for the NBI cryo-pumping system, the NBI operation was sometimes terminated by the pressure interlock at the NBI port. The fundamental O-mode launched from the low field side is the proposed scheme for electron cyclotron current drive in ITER. The deigned EC beam is well focused for local current drive. Since the position of the cut-off layer depends on the plasma parameters and the O-mode power fraction depends on the angle between the magnetic field line and the EC wave vector at the plasma edge, the development and optimization of the real time control of the O-mode power fraction are required in response to the plasma parameters and the injection angle during a long pulse and/or steady state operation in ITER.

Reference

[1] K. Kajiwara, Y. Ikeda, S. Moriyama, M. Seki and T. Fujii, to be submitted to Fusion Eng. Design.

Acknowledgments

The authors wish to acknowledge dedicated efforts of the members of Japan Atomic Energy Research Institute in support of the JT-60 program. They also wish to express their gratitude for domestic and international collaborations for the JT-60 experiments.

This is a blank page.

国際単位系 (SI) と換算表

表 1　SI 基本単位および補助単位

量	名称	記号
長さ	メートル	m
質量	キログラム	kg
時間	秒	s
電流	アンペア	A
熱力学温度	ケルビン	K
物質量	モル	mol
光度	カンデラ	cd
平面角	ラジアン	rad
立体角	ステラジアン	sr

表 2　SI と併用される単位

名称	記号
分，時，日	min，h，d
度，分，秒	°，′，″
リットル	l，L
トン	t
電子ボルト	eV
原子質量単位	u

1 eV = 1.60218 × 10^{-19} J

1 u = 1.66054 × 10^{-27} kg

表 5　SI 接頭語

倍数	接頭語	記号
10^{18}	エクサ	E
10^{15}	ペタ	P
10^{12}	テラ	T
10^{9}	ギガ	G
10^{6}	メガ	M
10^{3}	キロ	k
10^{2}	ヘクト	h
10^{1}	デカ	da
10^{-1}	デシ	d
10^{-2}	センチ	c
10^{-3}	ミリ	m
10^{-6}	マイクロ	μ
10^{-9}	ナノ	n
10^{-12}	ピコ	p
10^{-15}	フェムト	f
10^{-18}	アト	a

表 3　固有の名称をもつ SI 組立単位

量	名称	記号	他の SI 単位による表現
周波数	ヘルツ	Hz	s^{-1}
力	ニュートン	N	m·kg/s^2
圧力，応力	パスカル	Pa	N/m^2
エネルギー，仕事，熱量	ジュール	J	N·m
工率，放射束	ワット	W	J/s
電気量，電荷	クーロン	C	A·s
電位，電圧，起電力	ボルト	V	W/A
静電容量	ファラド	F	C/V
電気抵抗	オーム	Ω	V/A
コンダクタンス	ジーメンス	S	A/V
磁束	ウェーバ	Wb	V·s
磁束密度	テスラ	T	Wb/m^2
インダクタンス	ヘンリー	H	Wb/A
セルシウス温度	セルシウス度	℃	
光束	ルーメン	lm	cd·sr
照度	ルクス	lx	lm/m^2
放射能	ベクレル	Bq	s^{-1}
吸収線量	グレイ	Gy	J/kg
線量当量	シーベルト	Sv	J/kg

表 4　SI と共に暫定的に維持される単位

名称	記号
オングストローム	Å
バーン	b
バール	bar
ガル	Gal
キュリー	Ci
レントゲン	R
ラド	rad
レム	rem

1 Å = 0.1 nm = 10^{-10} m

1 b = 100 fm^2 = 10^{-28} m^2

1 bar = 0.1 MPa = 10^5 Pa

1 Gal = 1 cm/s^2 = 10^{-2} m/s^2

1 Ci = 3.7 × 10^{10} Bq

1 R = 2.58 × 10^{-4} C/kg

1 rad = 1 cGy = 10^{-2} Gy

1 rem = 1 cSv = 10^{-2} Sv

（注）

1. 表 1 − 5 は「国際単位系」第 5 版，国際度量衡局 1985 年刊行による。ただし，1 eV および 1 u の値は CODATA の 1986 年推奨値によった。
2. 表 4 には海里，ノット，アール，ヘクタールも含まれているが日常の単位なのでここでは省略した。
3. bar は，JIS では流体の圧力を表わす場合に限り表 2 のカテゴリーに分類されている。
4. EC 閣僚理事会指令では bar，barn および「血圧の単位」mmHg を表 2 のカテゴリーに入れている。

換　算　表

力	N(=10^5 dyn)	kgf	lbf
	1	0.101972	0.224809
	9.80665	1	2.20462
	4.44822	0.453592	1

粘度　1 Pa·s(N·s/m^2) = 10 P(ポアズ)(g/(cm·s))

動粘度　1 m^2/s = 10^4 St(ストークス)(cm^2/s)

圧力	MPa(=10 bar)	kgf/cm^2	atm	mmHg(Torr)	lbf/in^2(psi)
	1	10.1972	9.86923	7.50062 × 10^3	145.038
	0.0980665	1	0.967841	735.559	14.2233
	0.101325	1.03323	1	760	14.6959
	1.33322 × 10^{-4}	1.35951 × 10^{-3}	1.31579 × 10^{-3}	1	1.93368 × 10^{-2}
	6.89476 × 10^{-3}	7.03070 × 10^{-2}	6.80460 × 10^{-2}	51.7149	1

エネルギー・仕事・熱量	J(=10^7 erg)	kgf·m	kW·h	cal(計量法)	Btu	ft·lbf	eV
	1	0.101972	2.77778 × 10^{-7}	0.238889	9.47813 × 10^{-4}	0.737562	6.24150 × 10^{18}
	9.80665	1	2.72407 × 10^{-6}	2.34270	9.29487 × 10^{-3}	7.23301	6.12082 × 10^{19}
	3.6 × 10^6	3.67098 × 10^5	1	8.59999 × 10^5	3412.13	2.65522 × 10^6	2.24694 × 10^{25}
	4.18605	0.426858	1.16279 × 10^{-6}	1	3.96759 × 10^{-3}	3.08747	2.61272 × 10^{19}
	1055.06	107.586	2.93072 × 10^{-4}	252.042	1	778.172	6.58515 × 10^{21}
	1.35582	0.138255	3.76616 × 10^{-7}	0.323890	1.28506 × 10^{-3}	1	8.46233 × 10^{18}
	1.60218 × 10^{-19}	1.63377 × 10^{-20}	4.45050 × 10^{-26}	3.82743 × 10^{-20}	1.51857 × 10^{-22}	1.18171 × 10^{-19}	1

1 cal = 4.18605 J（計量法）

= 4.184 J　（熱化学）

= 4.1855 J　（15 °C）

= 4.1868 J（国際蒸気表）

仕事率　1 PS（仏馬力）

= 75 kgf·m/s

= 735.499 W

放射能	Bq	Ci
	1	2.70270 × 10^{-11}
	3.7 × 10^{10}	1

吸収線量	Gy	rad
	1	100
	0.01	1

照射線量	C/kg	R
	1	3876
	2.58 × 10^{-4}	1

線量当量	Sv	rem
	1	100
	0.01	1

（86 年 12 月 26 日現在）

Review of JT-60U Experimental Results in 2000